

UNIVERSITY OF BIRMINGHAM

INVESTIGATION OF THE PRESSURE VARIATION GENERATED BY FREIGHT TRAIN PASSING THROUGH A TUNNEL

by

ZHEN LIU

A thesis submitted to the University of Birmingham for the degree of

DOCTOR OF PHILOSOPHY

Fluids Research Group

School of Engineering

College of Engineering and Phyiscal Sciences

University of Birmingham

October 2023

UNIVERSITY OF
BIRMINGHAM

University of Birmingham Research Archive

e-theses repository

This unpublished thesis/dissertation is copyright of the author and/or third parties. The intellectual property rights of the author or third parties in respect of this work are as defined by The Copyright Designs and Patents Act 1988 or as modified by any successor legislation.

Any use made of information contained in this thesis/dissertation must be in accordance with that legislation and must be properly acknowledged. Further distribution or reproduction in any format is prohibited without the permission of the copyright holder.

© Copyright by ZHEN LIU, 2023

All Rights Reserved

Abstract

As a train passes through a railway tunnel is creates a series of pressure waves, which travel at the speed of sound within the tunnel environment. These pressure waves not only generate aerodynamic loads on freight train body and tunnel infrastructures, but also have an adverse effect on the comfort of people on the train or within the tunnel as the train passes through. There are a range of methods by which to predict the magnitude of these pressure waves, most notably numerical approaches through 1-dimensional (1d) codes.

The bluff nature of a freight train, coupled with large gaps between wagons and loaded goods, influence the pressure wave pattern generated by it passing through a tunnel. This research addresses the intricate challenges associated with predicting pressure wave patterns caused by freight trains passing through tunnels. The accurate resolution of separation regions at the train nose, within containers, and at unloaded gap sections is essential for precise predictions. Achieving this accuracy demands exceptional mesh quality, significant computational resources, and the careful selection of numerical models. This study evaluates various numerical models to capture these complexities in separation regions. It quantitatively analyses how alterations in train head shape and loading configurations influence resulting pressure patterns within tunnels. These insights are synthesised into an advanced 1d computational framework designed to accurately simulate pressure waves generated by partially loaded freight trains. To achieve these goals, firstly a 1d program is developed, validated against published research, and successfully models pressure wave propagation and reflection. The program's accuracy is further enhanced by integrating a separation bubble model. A comprehensive parameterisation study explores the relationship between train head bluntness, blockage ratio, and separation bubble

model parameters. These equations are validated and applied to various train types and tunnel configurations. The programme is extended to consider the discontinuities of the train body by implementing a new mesh system and boundary conditions into the 1d programme, and results are validated against LES data. A parameterisation study for different loading configurations improves program adaptability, and the relationship between predetermined parameters and gap length is investigated. This research bridges the gap in freight train tunnel aerodynamics, offering a versatile 1d computational tool for accurate pressure wave prediction.

Acknowledgements

I extend my deepest gratitude to my supervisors, Dr. David Soper and Prof. Hassan Hemida, for their exceptional guidance, unwavering patience, and constant encouragement throughout my doctoral journey. Their mentorship helped me navigate the course of my research and provided reassurance during moments of confusion and stress. And their belief in my potential have been the driving forces that steered me through the academic challenges and uncertainties, particularly during the demanding period of the COVID-19 pandemic.

In addition to my supervisors, I would like to express my sincere appreciation to my independent academic reviewer Dr. Bruño Fraga, to academic member Dr. Mike Jesson, my colleagues and fellow researchers, namely Dr. Zijian Guo, Dr. Syeda Hashmi, Dr. Giulio Vita, and Mr. Mohammed Amar. Their valuable contributions, engaging discussions, and shared expertise significantly enriched the depth and breadth of my research. Moreover, their companionship and collaborative spirit made this academic endeavor profoundly fulfilling.

Moreover, my heartfelt thanks go to my family and my boyfriend Dr. Boyang Chen for their encouragement, love, and understanding during this academic journey. Their support provided the emotional foundation I needed to persevere and reach this significant milestone.

Lastly, I would like to acknowledge the financial support received from University of Birmingham and China Scholarship Council that made this research possible.

Contents

Abstract i

Acknowledgements iii

Contents v

List of Figures xi

List of Tables xvii

List of Acronyms xix

List of Terms xxi

List of Subscript xxiii

1 Introduction 1

1.1 Outline of Studies 1

1.2 Research Background & Motivation 2

1.3 Aims and Objectives 5

1.4 Thesis Structure 6

2 Literature Review 9

2.1 Introduction 9

2.2 Railway Aerodynamics 10

2.2.1 Introduction . . . 10
2.2.2 Characteristic Flow Regions In the Open Air . . . 11
2.2.3 Fields of Train Aerodynamics . . . 13
2.3 Train Aerodynamics in Tunnels . . . 15
2.3.1 Pressure Wave . . . 15
2.3.2 Aerodynamic Drag . . . 16
2.3.3 Standards . . . 19
2.4 Research Methodology . . . 21
2.4.1 Three-Dimensional Numerical Method . . . 21
2.4.2 One-Dimensional Numerical Method . . . 25
2.4.3 Full-scale Experiments . . . 28
2.4.4 Model-scale Experiments . . . 29
2.5 Bluff Body Aerodynamics . . . 31
2.5.1 Freight Trains . . . 31
2.5.2 Other Bluff Bodies . . . 34
2.6 Conclusions . . . 36

3 One Dimensional Numerical Method 39
3.1 Introduction . . . 39
3.2 Governing Equations . . . 39
3.3 MOC Method . . . 42
3.3.1 Characteristic Equations . . . 42
3.3.2 Numerical Scheme . . . 44
3.4 Mesh System . . . 44
3.5 Boundary Conditions . . . 46
3.5.1 Tunnel Portal . . . 47
3.5.2 Train Head . . . 48
3.5.3 Train Tail . . . 53
3.6 Flow Chart . . . 53

3.7 Pre-determined Parameters 54
3.8 Validation 55

4 Three Dimensional Numerical Method **57**
4.1 Introduction 57
4.2 Tunnel 58
4.2.1 Numerical Model 58
4.2.2 Geometry 60
4.2.3 Computational Domain and Boundary Conditions 61
4.2.4 Mesh 62
4.2.5 CFD Solver Set Up 63
4.2.6 Model Validation 63
4.3 Open Field 65
4.3.1 Numerical Model 65
4.3.2 Geometry 67
4.3.3 Computational Domain and Boundary Conditions 69
4.3.4 Mesh 70
4.3.5 Solver Set Up 71
4.3.6 Model Validation 72
4.4 Summary of Numerical Cases 74

5 Pressure Wave Induced by Blunt Train Nose **77**
5.1 Introduction 77
5.2 Comparison of RANS to LES results for the Separation Bubble Development . 78
5.2.1 Open Track Considerations 78
5.2.2 Tunnel 79
5.3 Modification of the One Dimensional Code 80
5.4 Reference Case 82
5.4.1 Traditional 1d Code 82

5.4.2 Wall Shear Stress and Flow Field for the Class 66 Locomotive Entering a Tunnel . . . 83
5.4.3 Implementation of the Parameters into the Modified 1d Code . . . 84
5.5 Parameterisation Study on Nose Bluntness . . . 87
5.5.1 Wall Shear Stress . . . 88
5.5.2 Velocity Field . . . 90
5.5.3 Vortex Structures . . . 94
5.6 Influence of Blockage Ratio . . . 96
5.7 Summary of the Parameters to be Used in 1d Code . . . 100
5.8 Methodological Contributions . . . 106

6 Pressure Wave Induced by Loading Configurations 109

6.1 Introduction . . . 109
6.2 Modification of the 1d Code . . . 110
6.2.1 Mesh System . . . 110
6.2.2 Boundary Conditions . . . 110
6.3 Reference Case . . . 112
6.3.1 Wall Shear Stress . . . 113
6.3.2 Velocity Field and Vortex Structure . . . 114
6.3.3 Pressure Field and Pressure Waves . . . 119
6.3.4 Implement the Parameters in the Modified 1d Code . . . 124
6.4 Parameterisation Study on Loading Configurations . . . 128
6.4.1 Streamline and Velocity field . . . 128
6.4.2 Pressure Distribution . . . 139
6.5 Summary of the Parameters to be used in 1d Code . . . 141
6.5.1 Parameterisation Equations . . . 141
6.5.2 Validation of the Model . . . 143
6.6 Methodological Contributions . . . 146

7 Conclusions and Future Work **149**

7.1 Introduction 149

7.2 Conclusions 150

7.3 Limitations and Future Works 158

References **161**

A Authors publications **179**

List of Figures

1.1 The alignment of HS2 Phase 2 [1] 3

2.1 The generation, propagation and emission of pressure wave [2] 16
2.2 Pressure time histories and the wave propagation processes of a passenger train passing through a tunnel [3] 17
2.3 Diagram of the influence of pressure waves on friction drag (Liu et al. [4]) . . . 19
2.4 Properties of measured TPS signal (CEN [2]) 20
2.5 Characteristic region of BARC flow (Rocchio.et al., 2020) 35

3.1 Diagram of the flow model 40
3.2 Mesh system of three phases (a) phase1: train enter the tunnel (b) phase 2: train completely inside tunnel (c) phase3: train exit the tunnel 46
3.3 Diagram of boundary condition at train head (a) train head inside tunnel (b) characteristic variables at train head in duct1 (moving reference frame) 48
3.4 Diagram of boundary condition at train head(a) train head enter tunnel (b) train head exit tunnel 52
3.5 Flow chart 54
3.6 Comparison of experimental results and 1d predicted pressure time history curves. 56

4.1 Dimensions of the freight train CAD model (a) Class 66 locomotive (b) FEA-B wagons with containers 61
4.2 Computational domain of freight train passing through a tunnel and boundary conditions (dimensions in the figure are given as full-scale). 62

4.3 Mesh around tunnel portal (a) mesh on train and tunnel surface (b) mesh on the clip Y=0 m. 63

4.4 Pressure history curve at measuring points (a) position of measuring points (b) comparison of pressure variation on train and tunnel surface between $k-\omega$ SST URANS and Experimental results 64

4.5 Different freight locomotive types 67

4.6 Different head shapes of generic freight loco for parameterisation study 68

4.7 Different loading configurations for parameterisation study (a) fully loaded train (b) 20 feet gap (c) 40 feet gap (d) 60 feet gap (1 carriage empty) 68

4.8 Computational domain of the freight train operating in the open field and generic freight locomotive (dimensions in the figure are given as full-scale and in meters). 69

4.9 The blocking structure around the 33 % partially loaded freight train 70

4.10 Mesh size and distribution around the 33 % partially loaded freight train 71

4.11 Mesh size and distribution (a)The blocking structure around the train head and mesh on train surface (b) instantaneous wall Y^+) 72

4.12 Comparison between the medium and fine mesh on train roof (a) TKE (b) time-averaged velocity profile. 73

4.13 Comparison of pressure distribution on train surface between LES and Experimental results 74

5.1 Comparison of the separation bubble at top of the freight train predicted by RANS and LES (a) RANS (b) LES 79

5.2 Velocity contour obtained from LES simulation and streamline obtained from URANS simulation when a freight train enters a tunnel 80

5.3 Boundary condition when train nose enters a tunnel (variables marked in red are the unknowns that need to be solved) 81

5.4 Comparison of pressure history curve obtained from the traditional 1d result and experiment. 82

5.5 Flow field around Class 66 locomotive (a) before entering the tunnel (b) after entering the tunnel. 84

5.6 Separation bubble size at top, side and bottom of the train nose (a) before entering the tunnel (b) after entering the tunnel. 84

5.7 Separation bubble model at the head of loco 66 (a) effective blockage area (b) effective bubble length (c) parameters of the size of the separation bubble adopted in the code. 85

5.8 Comparison of pressure history curve obtained from 1d result and experiment (measuring points at (a) 2m (b) 4m (c) 8m (d) 16m to tunnel portal) (CH1: the first compression wave induced by the train head entering the tunnel; EH: Expansion wave when CH1 reflected back from the tunnel exit; CH2: the second compression wave when EH1 reflected from the tunnel entrance; H: the head of the train). 86

5.9 Top view of time-averaged trace lines on train body. 89

5.10 Side view of time-averaged trace lines on train body. 89

5.11 Time-averaged streamline at plane Y=0. 91

5.12 Time-averaged streamline at plane Y=0.4W. 92

5.13 Time-averaged streamline at plane Z=0.6H. 92

5.14 Time-averaged streamline at plane Z=0.9H. 93

5.15 Time-averaged velocity profile above the train roof (a) influence of α (b) influence of β (c) influence of $\alpha + \beta$. 94

5.16 Mean λ_2 at the top of the train (a) 0+0 (b) 15+0 (c) 30+0. 95

5.17 Mean λ_2 at the side of the train (a) 30+0 (b) 30+15 (c) 30+30. 95

5.18 PSD of velocity fluctuations at positions near average shear layer edge (a) 0+0 (b) 15+0 (c) 30+0. 97

5.19 H_R inside the tunnel (a) 30 m^2 (b) 45 m^2 (c) 60 m^2 (d) 75 m^2. 98

5.20 H_{S1} inside the tunnel (a) 30 m^2 (b) 45 m^2 (c) 60 m^2 (d) 75 m^2. 98

5.21 H_{S2} inside the tunnel (a) 30 m^2 (b) 45 m^2 (c) 60 m^2 (d) 75 m^2. 99

5.22 Fitting domain for the height of separation bubble and bluffness (a) relationship between H_R and α, β (b) relationship between H_S and α, β. 101

5.23 Fitting domain for the height and length of the center of the separation bubble and bluffness (a) relationship between H_c and α, β (b) relationship between L_c and α, β. 102

5.24 Influence of the blockage ratio on the scale factor. (a) Configuration of the tunnel cross section (dimensions given as full-scale) (b) Relationship between C_b and β_E. 103

5.25 Comparison of pressure history curve obtained from 1d prediction model and simulation (a) 2m to the tunnel portal (b) 4m to the tunnel portal (c) 8m to the tunnel portal (d) 16m to the tunnel portal. 104

5.26 The Class 70 validation case locomotive. (a) Class 70 locomotive (b) the CFD mesh and key dimensions, given here in the reduced 1/25th scale in m. 106

5.27 Comparison of pressure time history curves for a Class 70 locomotive passing through a tunnel obtained from the 1d prediction model and CFD simulation for measuring positions (a) 8 m from the tunnel entry portal and (b) 16 m from the tunnel entry portal. 106

6.1 Mesh system for a partially loaded train. 110

6.2 New boundary condition at the ends of containers for a partially loaded train. . 111

6.3 Side view of variations in wall shear stress on the train surface at different time instants during the train's entry into the tunnel. 115

6.4 Top view of variations in wall shear stress on the train surface at different time instants during the train's entry into the tunnel. 116

6.5 Side view of velocity distribution on plane Y = 0 m at different time instants during the train entry into the tunnel. 117

6.6 Top view of velocity distribution on plane Z = 0.09 m at different time instants during the train entry into the tunnel. 118

6.7 Side view of iso-surface of $\lambda_2 = -80000$ at different time instants during the train entry into the tunnel. 120

6.8 Top view of iso-surface of $\lambda_2 = -80000$ at different time instants during the train entry into the tunnel. 121

6.9 Side view of pressure distribution on plane Y = 0 m at different time instants during the train entry into the tunnel. 122

6.10 Top view of pressure distribution on plane Y = 0 m at different time instants during the train entry into the tunnel. 123

6.11 Pressure history curve generated by a locomotive with four 33% partially loaded freight train at 4 m inside tunnel (C_{H1}: the first compression wave induced by the train head entering the tunnel;e_L: Expansion wave generated by the rear of the locomotive entering the tunnel; c_{C1}: Compression wave generated by the front of the containers entering the tunnel; e_{C1}: Expansion wave generated by the rear of the containers entering the tunnel; E_{H1}: Expansion wave when C_{H1} reflected back from the tunnel exit; C_{H2}: the second compression wave when E_{H1} reflected from the tunnel entrance; H: the head of the train). 125

6.12 Comparison of pressure history curve obtained from 1d result and LES simulation (a) 2 m (b) 4 m (c) 8 m (d) 16 m. 127

6.13 Velocity field of the locomotive at contour Y=0 m (From top to bottom corresponding to gap distances of 1 L_{car}, 0.66 L_{car}, and 0.33 L_{car} respectively) (a) mean u and streamline (b) TKE. 129

6.14 Velocity field of the locomotive at contour Z=0.09 m (From top to bottom corresponding to gap distances of 1 L_{car}, 0.66 L_{car}, and 0.33 L_{car} respectively) (a) mean u and streamline (b) TKE. 129

6.15 Velocity field of the second container at contour Y=0 m (a) mean u and streamline (b) TKE. 130

6.16 Velocity field of the second container (a) at contour Z=0.09 m (b) at contour Z=0.12 m (c) at contour Z=0.15 m. 131

6.17 Comparison of velocity distribution at different measuring lines inside the gap (a) position of the 12 measuring lines (b) $\bar{u}$ (c) $\bar{w}$ (blue dash line: Gap = 33% L_{car}; red line: Gap = 66% L_{car};black line: Gap = 1 L_{car}). 132
6.18 Velocity field of the second container at contour Y=0 m (From top to bottom corresponding to gap distances of 1 L_{car}, 0.66 L_{car}, and 0.33 L_{car} respectively) (a) mean u and streamline (b) TKE. 134
6.19 Velocity field of the second container at contour Z=0.09 m (From top to bottom corresponding to gap distances of 1 L_{car}, 0.66 L_{car}, and 0.33 L_{car} respectively) (a) mean u and streamline (b) TKE. 134
6.20 Position of measuring lines relative to the locomotive and container 136
6.21 Distribution of mean u at different lines positioned along the train (a) 1 container empty (b) 0.66 container gap (c) 0.33 container gap. 136
6.22 Pressure distribution around the locomotive (From top to bottom corresponding to gap distances of 1 L_{car}, 0.66 L_{car}, and 0.33 L_{car} respectively). 138
6.23 Pressure distribution around the first container (From top to bottom corresponding to gap distances of 1 L_{car}, 0.66 L_{car}, and 0.33 L_{car} respectively). 138
6.24 Pressure distribution around the second container (From top to bottom corresponding to gap distances of 1 L_{car}, 0.66 L_{car}, and 0.33 L_{car} respectively). . . . 139
6.25 Distribution of mean pressure on train surface (a) 1 container empty (b) 0.66 container gap (c) 0.33 container gap. 140
6.26 Distribution of mean pressure at different lines positioned along the train (a) 1 container empty (b) 0.66 container gap (c) 0.33 container gap. 141
6.27 Diagram of flow characteristics inside the gap. 142
6.28 Estimation of the container's effective area 143
6.29 Surface mesh of freight train for validating loading configuration 144
6.30 Comparison of pressure history curve for the validation case predicted by the redeveloped 1d programme and LES simulation (a) 2 m (b) 4 m (c) 8 m (d) 16 m from tunnel entrance. 145

List of Tables

2.1 Maximum tunnel characteristic pressure changes (CEN [2]) 20

3.1 Freight train parameters used in the traditional 1d code. 55
3.2 Tunnel parameters used in the traditional 1d code. 55
3.3 Train parameters to be used for validation of the 1d code. 56
3.4 Tunnel parameters to be used for validation of the 1d code. 56

4.1 Summary of numerical cases for the investigation on locomotive head shape. . . 76
4.2 Summary of numerical cases for the investigation on loading configurations. . . 76

5.1 The length of separation bubble at train roof and side. 90
5.2 The size of the separation bubble of 6 train bluffness at different planes. 93
5.3 Fitting parameters for the parameterisation equation. 101
5.4 The relative position of the vortex core with respect to the full height and length of the vortex (%). 102

6.1 The height of the separation bubble at the top and height of the container. . . . 133

List of Acronyms

1d 1 Dimensional. 1

3d 3 Dimensional. 1

BARC Aerodynamics of a Rectangular 5:1 Cylinder. 34

CFD Computational Fluid Dynamics. 1

DES Detached-eddy Simulation. 21

EN European codes of practice. 9

LES Large-eddy Simulation. 7, 21

MMR Moving Model Rig. 3

MOC method of characteristics. 42

RANS Reynolds-averaged Navier-Stoke. 7, 21

SGS subgrid-scale. 23

TKE Turbulent kinetic energy. 59

TPS Tunnel pressure signature. 20

TSI Technical Specifications for Interoperability. 9

WALE Wall-Adapting Local Eddy-Viscosity. 65

List of Terms

A Speed of sound non-dimensioned by c_R. 43

C_p Pressure coefficient. 64

C_p Specific constant of air ($\mathrm{J\,kg^{-1}\,K^{-1}}$). 41

E Cross-sectional area ($\mathrm{m^2}$). 41

H_R, W_S, W_B Separation bubble height at train roof/side/bogie (m). 85

L Length of the train (m). 73

L_b Length of the separation bubble (m). 85

R Gas constant for air ($\mathrm{J\,kg^{-1}\,K^{-1}}$). 42

Re Reynolds number. 61

S Perimeter of duct (m). 41

T Temperature K. 41

U Gas velocity non-dimensioned by c_R. 43

V Speed of train ($\mathrm{m\,s^{-1}}$). 17

W Width of the train/cube (m). 33

X Distance coordinate non-dimensioned by X_R. 43

Z Time non-dimensioned by X_R/c_R. 43

β_E Blockage ratio. 28

κ Ratio of specific heats. 42

$\lambda, \beta, A_{\mathbf{A}}$ Characteristic parameters. 43

H Train height (m). 61

R Resistance (N). 16

$\mathcal{g}$ Friction term (N). 40

$\mathcal{q}$ Heat-transfer term ($\mathrm{W\,m^{-2}\,K^{-1}}$). 40

$\mathcal{w}$ Work-transfer term (J). 40

ρ Density ($\mathrm{kg\,m^{-3}}$). 41, 42

τ Wall shear stress (Pa). 40

ζ Loss coefficient. 49

c Speed of sound ($\mathrm{m\,s^{-1}}$). 43

f Friction coefficient. 41

h Heat convection coefficient. 41

p Pressure (Pa). 20, 21, 42

p_0 Stagnation pressure (Pa). 49

s Entropy of the gas ($\mathrm{J\,K^{-1}}$). 43

t time (s). 40

u Gas velocity ($\mathrm{m\,s^{-1}}$). 41, 42

List of Subscript

1 Duct 1. 40, 49

2 Duct 2. 41, 49

HP Head pass by measuring point. 21

N Nose of the train. 20, 49

P Tunnel portal. 53

R Reference value. 43

T Tail of the train. 20

an Annulus between train and tunnel. 41

car Carriage. 125

con Container. 86, 112

fr Frictional effect. 20

gap Gap between loaded containers. 112

tr Train. 41

tu Tunnel. 40

Chapter 1

Introduction

1.1 Outline of Studies

This thesis has developed an improved one-dimensional (1d) numerical programme that is able to predict the unique pressure wave pattern generated when a freight train enters into a tunnel. Modifications are made to the traditional 1d modelling approach to consider the separation bubble induced by the blunt freight train head, and the series of pressure waves generated by spaces/gaps between wagons or partially loaded containers along the length of the train. These modifications were supported through a series of three-dimensional (3d) computational fluid dynamics (CFD) simulations for a Class 66 locomotive entering a tunnel, with a view to characterising the shape of the separation bubble at the locomotive nose, to calculate the pressure losses and the change of effective cross sectional area caused by the separation in the gaps between wagons. These parameters are implemented in the 1d code. Furthermore, in order to encompass a diverse array of freight locomotive types and operational scenarios, parameterisation studies were carried out. These studies involved the exploration of a generic freight train model with varying leading edge separation angles and loading configurations. The objective was to quantitatively analyze the relationship between predetermined parameters and bluntness/gap, aiming for a broader applicability of the 1d program.

1.2 Research Background & Motivation

Railway lines for high speed trains and metros are requiring more and more tunnels to be built, for reasons ranging from siting to avoid densely populated areas, to the desire of straighter operation lines to achieve higher train speeds. Meanwhile, in many countries around the world rail transportation speeds are not able to meet the capacity demand, thus leading to the requirement for a higher operation speed [5, 6].

In the UK, the planned High Speed 2 railway (HS2) requires the development of several tunnel sections, with a total length of over 30 km for only the section from London to Birmingham, as shown in Figure 1.1. The desired operation speed increase to above 299 km/h, reaching up to 360 km/h along the Birmingham route. In the Central Shinkansen project in Japan, 86% of the line from Tokyo to Nagoya (286 km) are planned to be built underground, with a desired operating speed up to 505 km/h.

In addition to moving passengers, railway networks are also used to transport freight. The GB rail freight industry plays a vital role for the UK economy in the transportation of goods, but also supports the Government policy on decarbonisation [7]. In line with this importance, the UK government aims to double the volume of rail freight cargo on the UK rail network by 2030 [8]. Opportunities highlighted to achieve this aim include the introduction of dedicated high-speed freight, new paths and routes for freight. However, increasing train speeds cause a series of aerodynamic problems, including slipstream effects for platform passengers and trackside workers, as well as tunnel pressure magnitudes. For example, the amplitude of the pressure change increases approximately proportional to the square of train speed [9]. Furthermore, aerodynamic problems are more obvious when the train is running in a confined space, such as a tunnel [4].

As the train head enters a tunnel, the nose of the train pushes the air ahead of it, generating a compression wave that propagates to the tunnel exit with the speed of sound [10, 11]. This compression wave leads to a sudden pressure rise where it passes. Numerous studies over the concern of pressure behaviour of trains in tunnels have been carried out since the 1960s, mainly in UK, Japan, Germany, France and China in relation to developments in rail systems. These



Figure 1.1: The alignment of HS2 Phase 2 [1]

studies have assessed the problem through a range of methodologies including 1d theoretical methods, numerical simulations, moving model rig (MMR) tests and full-scale experiments. Among all of the methods presented to analyze the pressure variations in tunnels, full-scale experiments are considered to be the most accurate and offer an excellent base for validating other methods. However, full-scale methods are the most expensive and limited by the uncontrollable environment and working conditions. Compared to full-scale experiments, scaled MMR tests are less expensive and more flexible, but the difference in scale associated with lower Reynolds number must be considered. The drawback of MMR methods is the requirement for powerful drive capability for train models and high speed to be achieved [12, 13].With the improvement of computing ability, massive simulations can be undertaken using CFD software to achieve a better knowledge of the flow field when trains pass through tunnels [4, 10, 14, 15]. However, the simulation of a moving train is very computationally expensive and time-consuming. Now, since the length of the tunnel is much larger than the diameter of the tunnel section, the pressure fluctuation over a certain cross-section of the tunnel can be neglected compared to its variation

with time [16]. Subsequently many researchers have developed 1d programmes to calculate a quick, less computationally intensive solution to the pressure variation in tunnels [17, 18, 19]. Compared to 3d simulations, which can take days/months to simulate a train passing through a tunnel, it may only take a matter of seconds or minutes for a 1d code to obtain an accurate result of the pressure variations. Besides, it has been shown to provide reasonable results for project demands, especially having the advantage of being able to model train crossing and extra-long tunnels [20]. Such simulations can easily be run in a batch form, enabling a range of parameters to be considered relatively quick and cheaply. This is therefore an invaluable technique for testing many different scenarios in the initial design of new trains and/or tunnels.

Though numerous studies have been conducted to consider the aerodynamics of trains in tunnels, the majority has purely focused on passenger trains due to the speed at which these vehicles travel. However, although freight trains travel at generally slower speeds to passenger rolling stock, the shape of a freight train typically looks very different to that of a passenger train, for which these 1d studies have been traditionally undertaken. As a freight train passes through a tunnel, it generates a unique characteristic set of pressure wave patterns that different from passenger trains, due to the blunt nose shape of freight trains, and the loading configurations of goods carried. Additionally, the separation bubble induced by the blunt head of freight train potentially increases the effective cross sectional area of the train body [21]. It generates a noticeable pressure rise and drop when the train head enters the tunnel, which significantly increases the initial pressure wave. It also has a lasting impact on the subsequent pressure changes as the pressure wave propagates inside the tunnel. As will be shown, this phenomenon is not able to be fully well predicted in traditional 1d methodologies, since the influence of the train nose shape on compression wave is reflected only by a pressure loss coefficient and the effective cross-sectional area. Besides, the influence of the train body on pressure variation is calculated using frictional coefficient, train length and cross-sectional area in traditional 1d method. The varying cross-sectional area and the intermittent flow pattern between loaded and unloaded wagons, resulting from the diverse load configurations, render the 1d methods inadequate for analysis in the context of freight trains. Therefore, this method is incapable of

predicting the series of pressure waves generated by the big gaps between containers loaded onto intermodal freight trains, as the individual wagon/container enters into the tunnel, especially for partially loaded freighted trains. As a result, though traditional 1d methodologies have prominent advantage on predicting pressure variation inside tunnel fast and accurately, they are not not suitable for freight trains in the current form, especially for partially loaded freight trains.

Hence, to address these limitations, this research conducts the redevelopment of a 1d program. The aim is to refine and enhance its predictive capabilities, making it apt for the specific characteristics of freight trains, particularly the challenges posed by blunt head shape and partially loaded freight trains.

1.3 Aims and Objectives

The aim of this research is to understand the development of flow field as an intermodal container freight train passes through a tunnel, and to create a 1d flow model that is capable of predicting the pressure waves generated. To achieve this aim the following objectives are to be completed,

1. Undertake a comprehensive literature review on freight train aerodynamics, and previous research on how freight train has been considered in relation to pressure waves when it passes through a tunnel.

2. Write a code based on 1d unsteady compressible non-homotropic model, which is able to calculate the tunnel pressure wave generated by a passenger train. The accuracy of the code is validated by comparing with results presented in published research.

3. Conduct 3d CFD simulations for freight trains entering a tunnel and validate results by comparing with the experimental results. The flow field around the blunt freight train head is analysed for the separation bubble model to be built into the 1d code.

4. Modify the 1d code to consider the effective area change caused by the separation bubble. The pressure history curve measured from the modified 1d code is compared with experimental result.

5. A parameterisation study is done using generic freight train head model to obtain the relationship between the bluntness of train head and the parameters used in the separation bubble model. The applicability of the model is tested and validated.

6. To understand the flow field at the large gaps between containers and how it influences the pressure wave, 3d CFD simulations of a partially loaded freight train entering a tunnel are conducted using different numerical models.

7. Add new boundary conditions and change the mesh and coordinate systems of the 1d code to simulate the discontinuities of the train body. The result obtained after modification is compared with validated LES result.

8. A parameterisation study is undertaken using a freight train with different loading configurations, to investigate the relationship among the predetermined parameters and the distance of the gap.

1.4 Thesis Structure

This section outlined the the structure of the thesis and a brief summary of each Section

1. Chapter 2 presents a review of literature related to the investigations on pressure wave pattern inside tunnel and aerodynamic characteristics of bluff bodies. The review starts from a fundamental introduction on the aerodynamic phenomenon of trains passing through a tunnel and the regulations related to this. Then previous investigations on this phenomenon using 1d and 3d numerical method and experiments are summarised separately. The development and timeline of how these methods are applied on train/tunnel aerodynamics are presented, which provides a guideline on the numerical settings of the simulations and a foundation of the physical model adopted in the 1d code in this research. Finally, the aerodynamic research related to freight trains and bluff body are analysed in comparison with passenger trains and streamlined body, highlighting the importance of this research

and the reason why there are limitations to traditional 1d code in calculating pressure wave pattern generated by freight trains.

2. Chapter 3 introduces the numerical method adopted to write the 1d program that is able to predict the pressure variation of a passenger train passing through a tunnel. The governing equations, physical model and the numerical method to solve equations are introduced first. Then the expanding and contracting mesh system that used to simulate a moving train inside tunnel is illustrated. The boundaries at mesh ends are categorised and the equations used to solve them are deducted. Finally a flow chart of the calculation process is given for a better understanding of the 1d code. This Chapter provides a theoretical basis and platform for the further modifications on the 1d code in relation to objectives 3 and 6. Since the code is self-developed based on previous research, its accuracy is validated by comparing with the result predicted by a commercial 1d programme.

3. Chapter 4 introduces all the 3d numerical methodology adopted in the simulations carried out in this research. For simulations used to analyze the development of the flow field when a freight train entering a tunnel that used to modify the 1d code, $k-\omega$ SST Reynolds-averaged Navier-Stokes (RANS) model is adopted. The pressure time history curve measured from the simulation is compared with experimental results to validate the numerical model and settings. Large-eddy Simulation (LES) is adopted for the parameterisation study which is conducted on open track. The governing equations for the two numerical model, geometry for reference case and parameterisation study, computational domain, mesh and numerical settings for the two working conditions are illustrated in detail.

4. Chapter 5 builds a separation bubble model to describe the effective area change caused by blunt freight train head and implement in the 1d code. The pressure history curve inside tunnel calculated from the modified 1d code is compared with experimental result to show the improvement after considering the separation bubble. A parameterisation study is done to obtain the relationship between the parameters used in the separation

bubble model and the bluntness of the head, which is controlled by a combination of the angles between different regions at train head. The applicability of the parameterisation equation is tested and validated on different train head shapes. The content of this chapter is to fulfill the requirements of objectives 2, 3 and 4.

5. Chapter 6 discusses the flow characteristics between the gaps of partially loaded freight trains, and the implementation of a gap model in the 1d code from the simulation results. Firstly the flow field development of a partially loaded freight train entering a tunnel is analysed for the gap model to be built. After validation of the gap model, a parameterisation study is done to obtain the relationship between the length of the gap and the parameters (pressure loss coefficients and effective gap area) used in the model. This chapter is to meet the requirements of objectives 5,6 and 7.

6. Chapter 7 provides a concise synthesis of the primary findings extracted from the antecedent chapters. The distinctive contributions and innovative aspects of this research are underscored prominently. Furthermore, the chapter evaluates the utility and constraints of the proposed 1d program, offering insights into its potential applications and inherent limitations. This discussion unveils the evolving landscape for further advancements in addressing aerodynamic challenges specific to freight trains in tunnels.

Chapter 2

Literature Review

2.1 Introduction

This section presents a review of relevant studies for freight train aerodynamics and the aerodynamic phenomenon induced by a train passing through a tunnel. Firstly a general overview of railway aerodynamics is introduced by understanding the flow characteristics in a series of distinct flow regions around the train in sections 2.2.1 -2.2.2. The specific topics of train aerodynamics when trains operate on open line and confined spaces are briefly introduced in Chapter 2.2.3, drawing upon train aerodynamics in tunnels which is the main problem investigated in this research. Thus the studies relevant to this area are summarised in detail in Chapter 2.3.1 ~ 2.3.3 by discussing the main train/tunnel aerodynamic problems including aspects of the formation of pressure wave system, the generation of micro-pressure wave at tunnel exit, the drag increase caused by pressure change and the related Technical Specifications for Interoperability (TSI) and European codes of practice (EN) limitations. In order to provide the fundamental basis of the numerical method developed in this paper, the development of the approaches adopted to study railway aerodynamics are summarised in Chapter 2.4. The pros and cons of these methodologies are discussed in detail in relation to their applicability on this study. Finally, due to the bluff nature of freight trains which generates very different flow field comparing with streamlined passenger trains, a study of previous research on bluff body

aerodynamics is carried out in Chapter 2.5. The specific characteristics of bluff body flow and how it brings limitations on its application on 1d code are discussed in Chapter 2.5.1.

2.2 Railway Aerodynamics

2.2.1 Introduction

Railway aerodynamics entails the comprehensive examination of the airflow phenomena surrounding trains during their motion through the atmosphere, investigating the consequences on the trains themselves, as well as the surrounding environment through which the train is passing. Extensive research efforts have been dedicated to studying the aerodynamic performance, encompassing slipstream velocity, aerodynamic noise, and pressure distribution around trains, through a combination of computational simulations and experimental approaches. The emergence of these aerodynamic phenomena is intricately tied to the flow patterns arising from the passage of air around trains, which can also be categorised as bluff bodies. Consequently, this chapter commences by presenting a concise overview of the characteristic flow regions created by a train (chapter 2.2.2), aiming to establish a fundamental comprehension of the flow field encompassing trains.

Past studies have widely acknowledged the division of the flow field around trains into five distinct regions: the upstream region, nose region, boundary layer region, and wake regions (including near and far wake regions), each exhibiting distinct characteristics of velocity and pressure time histories. Among the aforementioned regions, the upstream region is recognised as an inviscid flow area, that holds relatively less significance regarding aerodynamic concerns. Consequently, it is not extensively elaborated upon in the subsequent chapters. The objectives of these researches encompass a comprehensive and fundamental analysis of aerodynamic drag to enhance fuel efficiency, improve operational safety and comfort, and mitigate noise pollution. Given that different operating conditions and environments exert influence on the flow development around trains, the specific areas of concern pertaining to railway aerodynamics during train operation in open field, crosswind conditions, and tunnel environments are individually

discussed in chapter 2.2.3.

2.2.2 Characteristic Flow Regions In the Open Air

Nose Region

The nose region, defined within the time range 0 < t < 0.25 (where t is normalised by the train's speed and length) according to Baker et al. [22], exhibits a notable phenomenon of increasing velocity as the flow passes over the train nose. Extensive experimental investigations on both passenger trains and freight trains have confirmed the presence of a velocity peak in this region [23, 24]. Notably, studies on freight trains have observed significantly larger velocity and pressure magnitudes in the nose region compared to previous findings on passenger train slipstream studies [24]. Numerical simulations have been employed to visualize the streamline patterns in the nose region and elucidate the underlying mechanisms of this velocity change. Consistently, various types of trains exhibit a common observation in the nose region, characterised by a high stagnation pressure forming at the front of the nose as the air is displaced aside. In the case of streamlined train heads, the flow accelerates as it moves over the curved surface, maintaining good attachment to the nose region throughout the process [25, 26]. In contrast to passenger trains, the flow around the nose of a freight train exhibits a detachment due to its bluff nature, resulting in the formation of a recirculation region. This recirculation phenomenon leads to a double peak behavior at the nose and a negative longitudinal velocity at a measuring point located within the recirculation zone in the nose region [27]. Furthermore, in comparison to passenger trains, a higher velocity peak is generated at locations outside the recirculation zone around the head of a freight train.

Boundary Layer Region

The boundary layer region refers to the area where the boundary layer forms along the length of the train, either on the top or side surfaces. The characteristics of this region, such as boundary layer displacement, turbulence intensity, and slipstream peak values, are influenced by

factors such as train length, operating velocity, and on-body structures (e.g., inter-carriage gaps, pantograph). Studies have shown that inter-carriage gaps stimulate boundary layer development, leading to peaks in the slipstream profile. Trains with smoother bodies exhibit a more gradual growth of the boundary layer, lower turbulence intensity, and pressure coefficients close to zero [23]. On the other hand, freight trains, especially partially loaded ones, with rougher body surfaces experience higher turbulence intensity in the boundary layer and exhibit different slipstream profiles, due to the vortices generated in the gaps between wagons for containers on intermodal freight train types [24]. Larger spaces between loaded containers cause increased velocities along the train, resulting in a thicker boundary layer along its side.

Wake Region

The wake region of a train can be divided into two distinct regions based on flow characteristics and slipstream profile: the near wake region and the far wake region. The near wake region is primarily influenced by large-scale vortices that detach from the train tail, and their size and shedding frequency are highly sensitive to the train's shape [28, 29]. Studies have shown that trains with pointed noses have a thinner boundary layer and experience a sudden increase in slipstream velocity in the near wake, whereas trains with rounded noses promote faster boundary layer development with a less intense flow [30]. Furthermore, apart from the boundary layer separation at the rear of the train, a significant amount of turbulence is generated at the bottom of the train, due to relatively unshielded bogies and undercarriage equipment, contributing to the overall turbulence in the wake. This leads to a high level of turbulence within the flow of the wake. In the near wake region, the average slipstream velocity exhibits notable peaks caused by the presence of large-scale wake vortices. As for the far wake region, which extends beyond the near wake, the turbulent effects diminish, resulting in a more stable and uniform flow. The velocity decay in the far wake region can be described by a power law relationship, where the velocity U decays as a function of the distance X from the rear of the train, typically represented as $U = a(X)^n$, with the exponent n around -0.5 ± 0.15 [30].

2.2.3 Fields of Train Aerodynamics

Train aerodynamics encompasses several areas of study that have been extensively explored in previous research. These areas can be classified based on the specific operating conditions and environments. In summary, the following distinct areas of train aerodynamics have been commonly investigated and briefly introduced as below:

1. Open Field Aerodynamics: This area of study is dedicated to exploring the aerodynamic behavior of trains operating in unobstructed open environments. It encompasses the investigation of various phenomena aimed at improving operational safety, energy efficiency, and passenger comfort. Key aspects studied include the reduction of aerodynamic drag, analysis of slipstream velocity patterns, examination of head pressure pulses, and the characterization of aerodynamic noise generation [31].

   Studies have demonstrated that aerodynamic drag and pressure are directly proportional to the square of operational velocity [20]. As the demand for higher operational speeds in passenger trains increases, these aerodynamic issues become more pronounced. To address these challenges, significant efforts have been made to optimize the aerodynamic properties of trains. Strategies include lengthening the nose of trains [32, 33, 34, 28], implementing smoother on-body structures [35], and incorporating cover-bogie structures [36, 37], etc. These optimizations aim to minimize drag, enhance energy efficiency, and improve overall train performance.

2. Crosswind conditions present significant challenges and are a matter of crucial concern in train aerodynamics, particularly with regard to train operational safety, stability, and passenger comfort. Extensive research efforts have been dedicated to comprehending the intricate effects of lateral wind forces and yaw angles on the aerodynamic and dynamic characteristics of trains under crosswind conditions [38, 39, 40, 41, 42]. The assessment of crosswind stability entails the determination of force and moment coefficients through experimental investigations or computational fluid dynamics (CFD) methodologies, followed by their incorporation into multi-body dynamic simulations for comprehensive

analysis [43, 44]. It has been observed that each carriage exhibits distinct characteristics in terms of force coefficients. Furthermore, investigations have revealed substantial disparities in the slipstream patterns surrounding trains under crosswind compared to those unaffected by crosswind. These disparities can be attributed to the generation of vortices on the leeward side of the train, which significantly impact the local airflow velocity [40]. The position, number, and trajectory of these vortices demonstrate heightened sensitivity to factors such as yaw angle, nose length, and train length. Findings indicate that models featuring shorter noses exhibit increased production of unsteady vortices, consequently leading to higher vibration frequencies of the side force when compared to models with longer noses [45, 38]. These relevant research endeavors conducted in this domain aim to develop effective strategies for mitigating the adverse effects of crosswinds, ensuring the safe and comfortable operation of trains across a range of wind conditions.

3. Confined space: The confined environment, such as bridges, windbreak walls, and tunnels, exacerbate aerodynamic challenges for trains and trackside structures. Recent studies have examined pressure loads on trackside structures and compared them with relevant gauging conditions, shedding light on changes in pressure fields around trains [46, 47, 48, 49, 45, 36, 50]. These measurements have revealed higher pressure due to flow constraints, in contrast to open air conditions, with variations depending on the train type. Further investigations have explored the impact of higher constraint levels and operating speeds, leading to increased pressure transients on trackside structures and higher velocity peak values at measurement points.

   Tunnel aerodynamics entails specific challenges arising from the propagation and emission of pressure waves. Measures to alleviate these issues have been undertaken, including optimising head shapes, designing tunnel hoods, and incorporating ventilation shafts. Section 2.3 provides detailed investigations on tunnel aerodynamics, encompassing the formation mechanism of pressure waves, research methodologies, and mitigation measures.

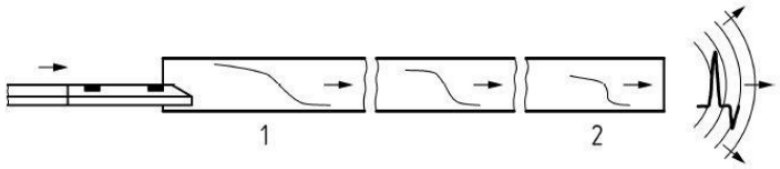
Each of these areas of train aerodynamics demands meticulous attention and research to gain comprehensive insights into the specific aerodynamic characteristics and challenges encountered under different operating conditions. Through the systematic investigation of these areas, researchers strive to enhance the operational efficiency, safety, passenger comfort, and environmental sustainability of railway systems.

2.3 Train Aerodynamics in Tunnels

2.3.1 Pressure Wave

The formation and transportation of pressure waves are one of the most important issue that has been particularly focused on and investigated over the past decades. When the head of train enters the tunnel, the air pressure ahead of the train nose rises abruptly due to its flow motion restricted by the tunnel wall, and forms a compression wave [51, 10]. This compression wave propagates forward at approximately the speed of sound. When it reaches the tunnel exit, part of it reflects back as expansion wave, the rest expands and generates an infrasound wave called micro-pressure wave, as illustrated in Figure 2.1[2]. The amplitude of the pressure pulse is largely related to pressure gradient of the pressure wave. The emission of micro-pressure wave at tunnel portals can cause environmental problems around tunnel portals. Then when the tail of the train enters the tunnel, large quantity of air outside the tunnel is sucked into the rear of the train and an expansion wave forms at tunnel portal. To get a better illustration of this typical phenomenon, a pressure wave diagram and pressure time-history curve from measuring points inside tunnel when a single train passes through a tunnel is shown in Figure 2.2 [3]. The measuring points are located at 1200 m and 1400 m inside tunnel, represented by the orange and blue horizontal lines in Figure 2.2(a). When the horizontal lines intersect with the train and pressure waves, a pressure change occurs. The pressure time histories can be divided into two regions in relation to the moment that the train exits the tunnel. Before this moment, the pressure is affected by both the train and pressure waves, and after that, it is only affected by pressure wave and varies periodically. For example, the trace line of train head intersect with measuring point

at 1400 m inside tunnel at point B, resulting in a sudden pressure drop. Similarly, when the trace line of train tail intersect with measuring point at point C, the pressure at this point increases. In general, compression and expansion wave (solid and dash lines) are generated at the instant of train nose and tail entering the tunnel separately. These waves propagate at approximately 340 m/s (the speed of sound). Due to the sudden change of cross sectional area at tunnel portals, there is a mismatch of acoustic impedance [52]. It leads to the pressure waves reflecting back once they reach the tunnel portal and causing pressure fluctuations within the tunnel — observed as an increase in pressure when compression wave reaches and decrease when expansion wave reaches [53]. In addition, this pressure wave pattern becomes more complicated when more trains enter and intersect in tunnel [54].



Key

1 tunnel entrance portal

2 tunnel exit portal

Figure 2.1: The generation, propagation and emission of pressure wave [2]

2.3.2 Aerodynamic Drag

The total running resistance of a train is composed by rolling resistance, mechanical resistance which is proportional to operation velocity and aerodynamic resistance which is 'approximately' proportional to the square of operation velocity. Thus the general formula of the running resistance (R) can be deduced as Equation. 2.1, commonly known as the Davis equation [55]. The parameters A and B are train mass-related. Some empirical relationships for these parameters are investigated and summarized in Rochard et al. [55].

$$\mathrm{R} = A + BV + CV^2 \tag{2.1}$$

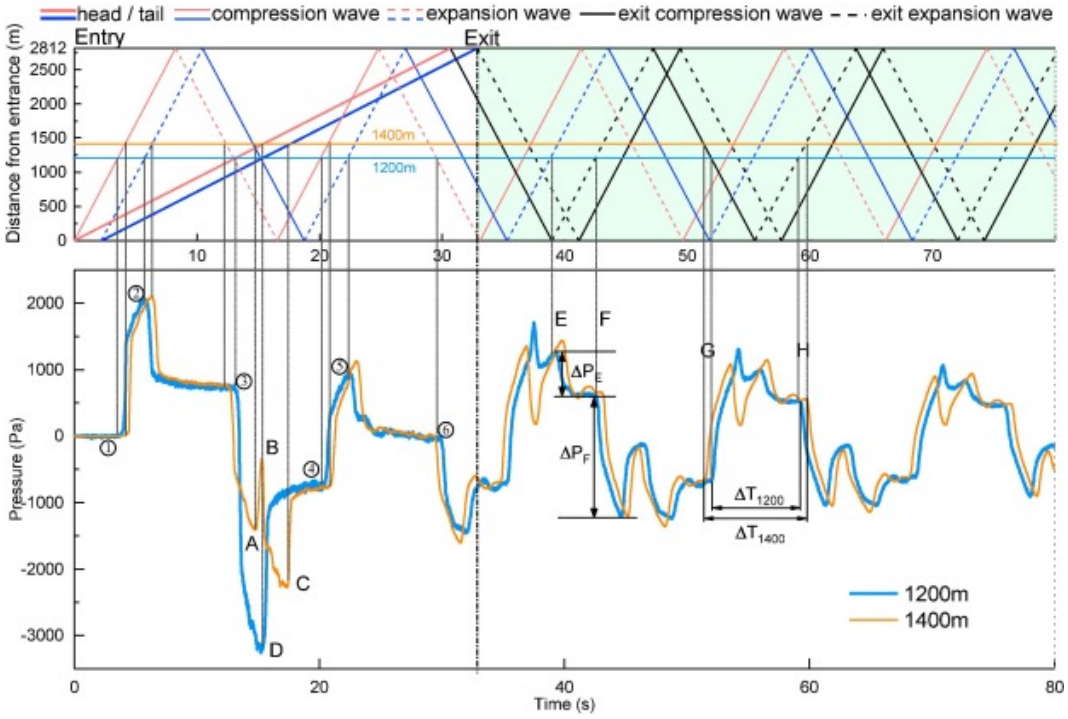


Figure 2.2: Pressure time histories and the wave propagation processes of a passenger train passing through a tunnel [3]

V is the speed of train. Since aerodynamic resistance is approximately proportional to the square of train speed, it can contribute more than 90% to the total resistance for very high-speed trains [56]. The aerodynamic drag on a moving train is composed of pressure and friction drag, in which pressure drag is force caused by the pressure difference along the reverse running direction act on the front and tail surface [57]. Thus, pressure drag is calculated by summing up the pressure force act on train surface as shown in Equation. 2.2, in which $p$ix is the pressure force along the reverse running direction acting on train surface and dS_P is the area perpendicular to train moving direction [58]. From the definition of pressure drag, it can be deduced that pressure force is sensitive to the factors that influences pressure distribution on the head and rear of the train, such as train nose length, operating velocity, etc. Research indicates that the pressure distribution for a streamlined train head is different from that for a blunt head [59, 28, 4]. Friction drag is the sum of the shear stresses and can be obtained by integration along the entire train surface as shown in Equation. 2.3. From the definition, it can be deduced that frictional force is mainly influenced by the velocity and length of the train. Previous research

shows that frictional drag is not sensitive to the shape of nose shape. Increasing nose length can only reduce pressure drag, but frictional drag is almost fixed [60].

$$F_{px} = \oint p_{ix} dS_P \tag{2.2}$$

$$F_{\tau x} = \oint \tau_{ix} dS_F \tag{2.3}$$

When a train operates inside a tunnel, additional resistance (R_{at}) is generated due to the confined space and propagation of pressure wave. $R_{at} = R_t - R_0$ in which R_t is the total train resistance inside tunnel and R_0 is that for the open line. Studies show that both pressure and frictional drag increases when trains operating inside a tunnel compared to those in open line [4, 61]. The aerodynamic drag of a high-speed train triples when the blockage ratio reaches 0.45 [61]. The influence of the tunnel geometry on the pressure drag is straightforward and mainly contains two parts: (a) the confined space potentially increases the upcoming velocity and thus increase the stagnation pressure on the upfront surface of the train (b) the propagation of pressure waves influence the pressure where it passes and further influence the pressure drag. The influence of the tunnel geometry on frictional drag is analyzed in detail in by Liu et al. [4]. The increase of upcoming velocity due to the confined space increases the wall shear stress along the train body, thus increasing the frictional drag. Furthermore, the pressure waves slightly influences the velocity where it passes which depends on its moving direction, as shown in Figure 2.3. When the change on velocity caused by pressure waves has the same direction as the upcoming velocity, the frictional drag increases, and decreases otherwise[4].

High aerodynamic drag inside a tunnel can cause problems including energy loss and subsequently higher energy/fuel consumption, operating discomfort on passengers and an inability to not achieve design speeds. Numerous studies have been conducted to reduce the aerodynamic drag of a train as it passes inside a tunnel by optimizing the shape of the train, as well as the addition of tunnel infrastructures (airshafts, pressure relief portals, etc). Chen et al. [32] investigated the the aerodynamic performance of high-speed trains passing through tunnels with different lengths of streamlined head. Results show that with the increase of the head length, both the

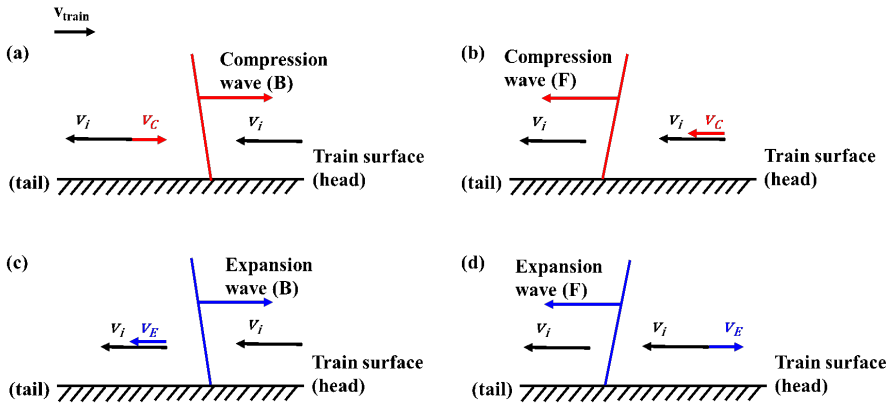


Figure 2.3: Diagram of the influence of pressure waves on friction drag (Liu et al. [4])

lateral force and resistance of the train and pressure amplitude of the measured points on the tunnel wall and train surface decrease. The total aerodynamic resistance reduces by 50% when the nose of the train increases from 0.5m to 10m [60]. Munoz-Paniagua et al. [33] optimized the shape of the train head using genetic algorithm (GA) optimization model to minimize the maximum pressure gradient and aerodynamic drag at the same time. Additionally, covering the inter-gap between carriages and using bogie skirt can also decrease the aerodynamic drag to some extent [62, 63].

2.3.3 Standards

The Technical Specifications for Interoperability [64], contains the requirements for an interoperable train in a solo-run formation within a non-inclined tube-like tunnel. A similar approach is taken in the Locomotive and Passenger National Technical Specification Notice (LOC&PAS NTSN), published by the Secretary of State on 1 January 2021 pursuant to regulation 3B of the Railways (Interoperability) Regulations 2011. This NTSN replaces and substantially reproduces the provisions of Commission Regulation (EU) 1302/2014 (the LOC&PAS TSI), and includes relevant amendments made by Commission Implementing Regulation (EU) 2019/776 which came into force in June 2019. Further limitations are contained in the BS EN 14067-5 [2] regarding the assessment of characteristic pressure and limitation of pressure gradient generated by train entering the tunnel. It's defined in the BS EN 14067-5 [2] that pressure differential

exceeding 10 kPa peak-to-peak is not permitted for aural safety during passage through the tunnel.

The procedure of the assessment and the related limitations of maximum characteristic pressure are summarized here. A tunnel pressure signature (TPS) is shown in Figure 2.4 to determine the distinct pressure amplitude. The steep pressure rise is caused by the train head entering the tunnel, identified as $\Delta\, p_N$. Then due to the frictional effect when train body enters the tunnel, the pressure continues to rise by an amplitude of $\Delta\, p_{fr}$. There is then a pressure drop, caused by the train tail entering the tunnel, defined as $\Delta\, p_T$ in Figure 2.4. The entry pressure history curve is divided by these characteristic points, and used to calculate the amplitude of these pressure changes. Details of how to extract these characteristic points (A ~ F) and offset pressure could be found in the BS EN 14067-5 [2].The obtained amplitude of these pressure changes are then compared with the limit values contained in the NTSNs in Table 2.1 to check if the accessed train fulfills the requirements.

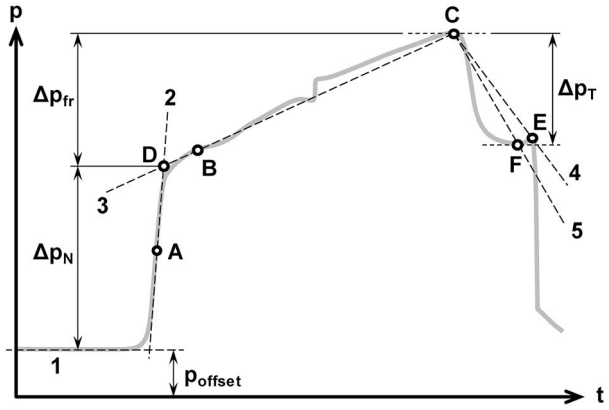


Figure 2.4: Properties of measured TPS signal (CEN [2])

Train Type	Reference Case		Criteria for the Reference Case		
	$V_{tr}\ km/h$	$A_{tu}\ m^2$	$\Delta p_N\ Pa$	$\Delta p_N + \Delta P_{fr}\ Pa$	$\Delta p_N + \Delta P_{fr} + \Delta P_T\ Pa$
$V_{tr,\max} <$ 250 km/h	200	53.6	$\leq$ 1750	$\leq$ 3000	$\leq$ 3700
$V_{tr,\max} \geq$ 250 km/h	250	63	$\leq$ 1600	$\leq$ 3000	$\leq$ 4100

Table 2.1: Maximum tunnel characteristic pressure changes (CEN [2])

In Table 2.1, V_{tr} is the reference velocity of the rolling stock, Δp_N is the sharp first increase in pressure caused by the entry of the nose of the train into the tunnel, Δp_{fr} is the second

increase in pressure due to friction effects caused by the entry of the main part of the train into the tunnel and Δp_T is a drop in pressure caused by the entry of the tail of the train in the tunnel. The maximum pressure variation caused by the passage of a train running at the maximum permissible speed in the tunnel, must not exceed 10 kPa. In cases where the maximum pressure variation cannot be directly measured, it is approximated as $\Delta p_{\max} = \Delta p_N + \Delta p_{fr} + \Delta p_T + \Delta p_{HP}$,in which $\Delta\ p_{HP}$ is the pressure drop caused by the train head passing through the measuring point. These values are estimated based on the worst conditions. While European countries may have established acoustic regulations for railway operations, there are currently no standardized rules that comprehensively address micro-pressure emissions. For instance, Germany has a specific guideline concerning infrastructure assessment and acoustic criteria. The simulation procedures demonstrated here align with the BS EN 14067-5 [2]. Initially, a simulation involving the reference vehicle entering the designated tunnel at a speed of 250 km/h is carried out to compute the maximum entry pressure gradient. To validate the simulation settings, this gradient should fall within the range of $[8,800\ \text{Pa/s}, \leq\ 9,500\ \text{Pa/s}]$. Subsequently, the simulation employs the same validated numerical settings to determine the maximum pressure gradient of the evaluated train as it enters the reference tunnel. The evaluated vehicle successfully undergoes the homologation procedure if its maximum pressure gradient is lower than that of the reference train. Finally, micro-pressure wave emissions are calculated based on the entry pressure wave signature and compared with specified limit values.

2.4 Research Methodology

2.4.1 Three-Dimensional Numerical Method

RANS

At present, the 3d numerical methods applied to studying train aerodynamics mainly includes RANS (Reynolds-averaged numerical simulation), LES (Large-eddy simulation) and DES (Detached-eddy simulation), etc. However, since the compressibility of the air and the rel-

ative motion between the train and tunnel need to be considered when simulating trains entering the tunnel, the required computational resources increase significantly. Therefore, RANS is the most widely adopted numerical method to investigate the train-tunnel aerodynamic problem. A large number of simulations have been carried out using RANS and many factors that could affect the aerodynamic characteristics inside a tunnel have been studied. These predominantly include: (a) blockage ratio (b) train speed (c) the shape of train head and tunnel portals (d) the length of train and tunnel (e) the facilities in tunnel (platform, ventilation, track type, etc.) (f) multiple trains

Among which, (a) blockage ratio and (b) train speed were the two main factors that affected the first pressure wave generated by the train entering the tunnel [65]. These two factors are also referred as "two primary factors influencing pressure transients in tunnel" by Ko et al. [66]. It is evident and well-known that pressure disturbance in a tunnel is approximately proportional to the square of (b) train speed, therefore the effect of (a) blockage ratio is important to be investigated. Zhang et al. [67] and Cross et al. [15] studied the influence of train speed, blockage ratio, tunnel features and train length on the ventilation rate and piston wind. A sensitivity analysis showed that the blockage ratio had the greatest influence. Munoz-Paniagua et al. [33] studied the impact of nose length, nose shape and blockage on the first compression wave and aerodynamic drag. It is concluded that the cross-sectional area has a significant impact on the maximum pressure and drag.

Factors (c)~(e) can be grouped as the features of train and tunnel. Since the interaction of train and tunnel has the greatest impact on the first compression wave, therefore among these factors, the shape of train nose [20, 33] and tunnel portals [68, 69, 70] are mostly considered. Train nose length is found to play a key role on the maximum pressure gradient [69, 33, 4]. Xiang et al. [71] compared the effect of nine continuous tunnel hoods to reduce the maximum pressure gradient, with the optimal shape shown to effectively reduce the pressure gradient by 43%. Similar studies have been carried out by Liu et al. [72], and discontinuous hoods and trains intersection considered. It was shown that there is a reasonable relationship between the length and the cross-sectional area of the hood on the peak pressure value. Uystepruyst et al. [73] uses

an in-house 3d numerical solver to further investigate the effective length and cross-sectional area of the hood compared to that of the train nose. The findings indicate that the influence of the rarefaction wave is significant in determining the optimal hood section Additionally, studies have considered the number and position of airshafts, cross-passage and other "discontinuities" in the tunnel and found these changes in geometry to have effect on the pressure amplitude and environment in tunnels, in particular subway tunnels, where the blockage ratio between the train and tunnel is higher than traditional railway systems [74, 75, 76, 20]. These types of infrastructure can either generate or influence pressure wave formation and development, and could release the piston effect to some extent. In terms of long tunnels, the effect of the tunnel wall surface friction and track type can influence the steepening of the pressure wave. There are however only a small number of simulations/studies conducted to address this issue, primarily due to the large computational resource required for the case of a long tunnel.

Since RANS modelling techniques average the fluctuating velocity components, it is not able to observe the instantaneous flow characteristics. However, for some aerodynamic problems (e.g. gust peak), the peak of instantaneous velocity is much higher than that of the averaged one and therefore is important to be considered. Furthermore, although RANS is relatively time-efficient due to its simplification, the hypothesis that the turbulence model used to calculate the mean averaged components inherently imports additional error in accuracy at the same time. To overcome these problems, researchers have applied DES and LES modelling techniques to simulate the air flow around trains. Since DES and LES require a higher mesh resolution and thus more computational resources, it is more commonly be used to simulate trains on the open line, rather than tunnels[29]. Literature regarding these two methods are summarised separately as follows.

LES

The underlying principle of the LES model involves fully resolving the large-scale turbulent structures while modelling the less energetic small-scale structures using a subgrid-scale (SGS) model. To reduce the impact of time averaging on unsteady structures, LES models employ

spatial filtering rather than temporal filtering. The turbulence spectrum can be used to filter the size of vortices in the flow field, distinguishing between small-scale and large-scale vortices. In the LES approach, the mesh in the flow field is divided into two parts based on its resolution: (a) meshes that are used to directly solve the Navier-Stokes equation to capture the large-scale model, and (b) meshes that are used to solve the small-scale vortices after applying a filtering technique and constructing a turbulence model (sub-grid model).

Previous discussions have highlighted the computational resource requirements of LES compared to RANS, especially for high Reynolds number simulations. As a result, LES implementation in train aerodynamics has primarily focused on train operating conditions on open field. To reduce computational costs, researchers have often employed simplified train models that preserve the main flow characteristics while neglecting detailed on-body structures. For example maintaining the shape of the train head but neglecting smaller details such as windscreen wipes, radio antenna and pipework. Examples of such simplified models can be found in studies by Krajnovic et al. [77], Krajnović et al. [78, 79], Zhuang et al. [80], and Hemida et al. [40]. Hemida et al. [38] utilised LES to investigate the influence of nose length on a generic train model with different yaw angles, at a Reynolds number of approximately 3×10^5. The results revealed differences in flow characteristics between long-nose and short-nose models, with the absence of a small vortex near the nose and a more streamlined flow towards the train body. The flow remained attached along most of the surface on the roof-side face. A similar study has also been done by Zhuang et al. [80] at a Reynolds number of 2×10^5. The averaged flow patterns, turbulent statistics and the surface forces of a simplified CRH3 train with two different yaw angles are studied. Results show that increasing the yaw angle leads to higher lift and side forces, along with a broader frequency range for the time-dependent aerodynamic forces. He et al. [81] compared numerical simulations of LES, Improved Delayed Detached Eddy Simulation (IDDES), and RANS with experimental data, using a simplified high-speed train model at a Reynolds number of 6×10^4. It was concluded that well-resolved LES was the most accurate method for predicting flow around high-speed trains. Furthermore, it was shown that IDDES and Unsteady RANS (URANS) were suitable for capturing mean flow, but IDDES

was not effective in predicting near-wall flow instability. Finally, Maleki et al. [82] assessed the capabilities of RANS, ELES and SAS on predicting the flow characteristics (pressure and velocity variation, aerodynamic drag) around a freight wagon. The results obtained from ELES and SAS simulations are validated and analysed quantitatively, with both models indicating good agreement with experimental techniques. However, whilst the steady RANS model is capable of predicting the trend in pressure, it performed badly for individual drag prediction [82].

With advancements in computational capabilities, researchers have begun to utilise the Large Eddy Simulation (LES) method to study aerodynamics problems induced by a moving train, such as train-tunnel interactions and wind break effects. Liu et al. [83] employ LES and dynamic grid techniques to investigate the aerodynamic characteristics of trains passing through different semi-enclosed noise barrier systems. The aerodynamic load characteristics are analysed, as well as the spatial and spectral characteristics of the aerodynamic pressure in various scenarios. In a similar vein, Yang et al. [84] focus on the aerodynamic performance of high-speed trains on tunnel-bridge sections using a sliding mesh technique. A comparison of results obtained from different turbulence models and find that, overall, the IDDES and LES models exhibit consistent aerodynamic load changes, while the URANS model yields higher values. Notably, the primary discrepancy in the simulated aerodynamic forces among the turbulence models is observed in the side force experienced by the head carriage.

2.4.2 One-Dimensional Numerical Method

With the improvement of computing ability, massive simulations can be undertaken using commercial software to achieve a better knowledge of the flow field when trains pass through tunnels [4, 10, 14, 15]. However, the simulation of a moving train is very computationally expensive and time-consuming [4]. Since the length of tunnel is much larger than the diameter of tunnel section, the flow pattern inside tunnel can essentially be considered as a simple “duct flow”, where the pressure fluctuation over a certain tunnel section could be neglected compared to its variation with time [16]. Subsequently many researchers have developed 1d programmes to calculate a quick, less computationally intensive solution to the pressure variation in tunnels

[17, 18, 19]. Compared with 3d simulations, which can take days/months to simulate a train passing through a tunnel, it may only take a matter of seconds or minutes for a 1d code to obtain an accurate result of the pressure variations. This is therefore an invaluable technique for testing many different scenarios the initial design of new trains and/or tunnels. The approach can be easily run in a batch form, enabling a wide range of tunnel, train and operational configurations to be analysed. The underlying method which is commonly adopted to solve the hyperbolic equations in these programmes is based on the method of characteristics. Different 1d flow models have been developed in recent decades. In 1968, a model (model (a)) is presented by Yamamoto [85] considering that the air density is constant but the feature of wave propagation is retained by the use of a finite speed-of-sound. Schultz [86] adopted an unsteady, compressible, homentropic (uniform and constant entropy) flow model (model (b)) to predict transient pressure waves for short tunnels without the consideration of frictional effects. Based on this model, Kage et al. [87] investigate the effect of train nose length and cross-sectional area ratios with the consideration that the area of tube to be changed with time and distance. However, frictional effect could be considerable for long trains and tunnels, and is necessary to be calculated. Therefore, homentropic flow model with frictional effects (model (c)) is developed by adding a term of viscous friction in momentum conservation equation [19, 88], and is further modified by considering the leakage and compressibility of the train [89]. In this model, variables are solved by coupling continuity and momentum equations in conjunction with the law of homentropic flow. In general, friction coefficients on the tunnel and train walls are assumed constant. However, technically, local friction changes occur due to the effect of pressure waves on the boundary layer surrounding the moving train. Some researchers investigated the effect of unsteady friction to vary with time, but the results indicate limited improvement on the prediction of pressure fluctuations [90, 91]. Since model (c) is based on the assumption that the flow is adiabatic, that is, the heat transfer between air and walls is neglected, there could be discrepancy on air temperature and might lead to errors particularly for high speed trains and long tunnels [92]. Hence a non-homentropic flow model (model (d)) is presented, which strictly obeys the conservation of mass, momentum and energy equations. Based on this model, Woods et al. [16]

presents a comprehensive method that could model the effects involving the considerations listed above, as well as mass transfer, locomotive heat release, and vehicle leakage and gravity body forces. This method is validated with full-scale experiment data, suggesting that the numerical method can predict temperature, velocity and pressure variations accurately. Many researchers adopt this model to build into computer programmes, and simplify it according to specific demands to investigate the effects of airshafts, branches, perforated walls, etc [18, 93, 94, 92, 95]. Though model (d) is academically more accurate to the flow conditions, model (c) is much simpler (a set of characteristic lines fewer) and is more flexible for the predictions in terms of multi-trains and tunnel with airshafts and branches [92]. Moreover, the results obtained from model (c) give good agreement with experiments and is acceptable for most conditions. The commonly used railway tunnel simulation programme "ThermoTun", which is widely used in European countries, offers both model (c) and (d) in its latest version [96]. The important input parameters required for the 1d model include the following:

1. pressure loss coefficients for head and tail of the train
2. tunnel discontinuities
3. frictional coefficients of train and tunnel
4. average cross-sectional area/perimeters/lengths of train and tunnel
5. operation velocity
6. vehicle leakage area, initial velocity and temperature

The specific definitions of which are illustrated in Vardy [58]. Some of these parameters could be given or obtained directly from the geometry of train and tunnel, but others are empirical quantities. The empirical parameters are in general deduced from experiments or from standard texts on pipe-flow losses. A range of widely used parameter values are summarised as follows [16]:

1. loss coefficient of 0.5 for tunnel portals

2. friction factor of 0.005 for well-maintained brick surface of tunnel; friction factor of 0.006 for a tunnel with slab track construction.

Different methods are presented for the determination of friction factors and loss coefficients of train head. Vardy [97] obtained the best fit values through a 'trial and error' methodology using experiment data, deduced from the relationship between blockage ratios when the tunnel changes [17, 97, 98] determine the values from the pressure rise occasioned during train entry by using weak-wave theory. In addition, the loss coefficient of train tail are approximately ${\beta_E}^2$ and $(\frac{\beta_E}{1-\beta_E})^2$ deduced based on two different assumptions, presented by Vardy [97] and Woods et al. [16] respectively, where β_E represents the blockage ratio.

2.4.3 Full-scale Experiments

The significance of comprehending overpressures in tunnels escalated in Europe during the 1990s with the emergence of high-speed railway lines. To tackle the aerodynamic challenges associated with train speeds surpassing 200 km/h, a collaborative project called TRANSAERO was launched. This initiative focused on conducting comprehensive experimental tests, encompassing both full-scale and small-scale experiments, to investigate time-dependent phenomena such as cross-winds, train pressure pulses, and tunnel waves [46]. Concurrently, numerical simulations, including CFD and 1d codes like TETUN [18], were developed to optimise the design of trains and tunnels while simulating train crossings. However, achieving accurate replication of all the intricate details and phenomena, including factors like roughness and scale, using wind tunnel or model-scale experiments remains a persistent challenge. As a result, full-scale experimental tests continue to serve as the fundamental basis for validating the design and acceptance of trains and tunnels [2].

Several notable studies have been conducted to investigate the effects of different factors on pressure wave patterns during train passages. For instance, a comprehensive full-scale campaign was carried out on Italian high-speed railway lines by Somaschini et al. [99]. This campaign explored the influence of train interactions, varying speeds, and tunnel parameters on pressure wave patterns. The findings highlighted the significant impact of the initial tunnel

environment on pressure wave signals, emphasising the importance of considering these factors in computational analysis.

Furthermore, Liu et al. [100] conducted measurements of transient aerodynamic pressure during the passage of high-speed trains through double-track tunnels. The analysis focused on peak-to-peak pressure values at different measuring points during tunnel entry and exit. The results revealed a periodic attenuation of pressure values after leaving the tunnel, while the implementation of a Bamboo-truncating portal hood contributed to a reduction in peak-to-peak pressure after multiple cycles. In another study by Martinez et al. [101], a comprehensive series of tests were carried out on the Madrid-Barcelona high-speed line in Spain. The primary objective was to validate the efficiency of air conditioning systems in seven distinct high-speed train models, utilising pressure sensors placed both inside and outside the trains. The initial findings unveiled a self-similar pattern in train pressure, with noticeable variations between the entrance and exit of tunnels due to changes in altitude.

Although full-scale experiments provide crucial data for validating numerical methods, acquiring field experimental data for diverse operating scenarios remains a challenging endeavor due to environmental limitations and high economic costs. Nonetheless, continued research efforts in this domain are vital to enhance our understanding and optimise train and tunnel designs for improved safety and performance.

2.4.4 Model-scale Experiments

Reduced-scale/physical modelling experiments through moving-model techniques have the ability to reproduce the relative motion between trains and tunnel, as well as the meeting of passing trains. Furthermore, compared to full-scaled experimental approaches, scaled model experiments can be less expensive to conduct, and more flexible to control the environment and change the parameters. Compared to computational simulations, scaled experiments have the ability to reveal the real flow pattern, which may be difficult to be accurately obtained by numerical simulations. Therefore, it has certain advantages on investigating the aerodynamic performance of trains passing through tunnels and providing validation data for numerical simulations.

Due to the limitations of power system and test devices in the early years of railway aerodynamics research, researchers utilised pressure wave generators to reproduce wave front similar to that generated when train enters the tunnel. However, it was found that the pressure gradient of the wave front was difficult to control. After that, scaled train-tunnel simulation were conducted with reduced-scale models, at relatively low speeds and with highly simplified train shapes, such as cylinder or block. In the 1990s, Japanese researchers used a 1/250th scaled train-tunnel simulator to reproduce the first compression wave and the shock wave at tunnel exit. The effect of different tracks and wall types on the attenuation and propagation of the wave were investigated [102, 103] using a 200mm-long cylindrical piston to experimentally reproduce the impulse pressure wave when train enters the tunnel. Results shows that hood at tunnel exit and porous material on the exit wall could effectively reduce the pressure gradient and sonic boom. A 1/250th scaled tunnel-train simulator is used to study the wave characteristics and pressure variations for two train speed Zonglin et al. [104]. The results are used to validate a numerical simulation, and further to investigate how train length, train-tunnel configurations and blockage ratio affect the wave processes. Ricco et al. [105] studied the influence of different parameters on the initial pressure wave and the pressure periodicity inside the 1:87 scaled tunnel experimentally and numerically. The results showed that the first compression wave reproduced by one-dimension code fits well with the scaled experimental data with and without airshafts.

With the development of experimental techniques, the acceleration and deceleration sections were constructed based on more effective driving and braking mechanisms, which are capable to accelerate larger scale train model to the required higher operating speed. A test rig developed by [106] was able to accelerate a 1/77th scaled model to Mach number reaching 0.34 by using an airgun [51]. Compared to the full-scaled test of single ETR 500/2 train passing through and trains intersecting in Terranuova tunnel, the magnitude of compression wave reproduced by this scaled test only deviates less than 4% and 10% and the time span also fits well [77]. Similarly, using the airgun principle for acceleration, a number of scaled train-tunnel devices were built to investigate the wave patterns, pressure characteristics in tunnel and micro-pressure wave, for various high speed trains. Similarly, an alternative approach for the acceleration system of

MMR facilities in Central South University and University of Birmingham is to power the train by a set of rubber ropes. The former one allows to accelerate 1:20 scaled train to a maximum speed of 500 km/h. Based on this MMR facility, Zhou et al. [107] investigated the pressure characteristics when a high-speed train passing through and two high-speed trains intersecting at stations, and further analyze the effect of train speed, crossing position on the pressure variation of the platform screen doors. The effect of various types of tunnel portals on transient pressure and micro-pressure waves are also studied [67, 11, 108]. Using the same device, MMR tests of metro-train, inter-city train and high-speed train passing through tunnels are conducted, to study the aerodynamic phenomena including flow velocities, pressure variations and aerodynamic drag [109]. The MMR facility in Derby, UK is capable of firing $1/25^{th}$ scaled train models at speed up to 270km/h, depending on the weight of train model. [110, 50] studied the pressure-loading patterns near to the tracks when train runs in tunnels, partially enclosed or confined spaces. Furthermore, a wide variety of investigations have been carried out on this facility to study the train aerodynamics in tunnels, including the effect of train geometries, relief ducts, buffer structure at tunnel portals, etc., providing a wealth of data for the validation of various numerical simulations[111, 112, 113, 114].

2.5 Bluff Body Aerodynamics

2.5.1 Freight Trains

Though numerous studies have been conducted to consider the aerodynamics of trains in tunnels, the majority have purely focused on passenger trains due to the speed at which these vehicles travel[115]. Freight trains however typically look very different to passenger trains, for which these 1d numerical techniques and studies have been traditionally designed/undertaken for. Due to the blunt nose shape of freight trains and discontinuities along the train length, these vehicles generate a unique characteristic pressure wave pattern, that is different from that of a passenger train as they pass through a tunnel [21]. The separation bubble induced by the blunt head will increase the effective blockage ratio, and further notably increase the magnitude of the initial

pressure rise [21]. It also has a lasting impact on the subsequent pressure changes as the pressure wave propagates inside the tunnel. These phenomena are not able to be well predicted through traditional 1d methods, since the influence of the train nose shape on the compression wave is represented only by pressure loss and cross-sectional area. Furthermore, for passenger studies the cross-sectional area of the train body is considered a constant value in the traditional method, which is often not the case for freight trains with a range of wagon types and/or container loading patterns. As a result and as will be initially shown in this study, the pressure change caused by the separation bubble at the bluff train head and discontinuity of the partially loaded containers is not able to be accurately predicted in traditional 1d methods.

The aerodynamic flow around a freight train can be considered as a bluff body flow. As air flows over an "elongated" bluff body, the flow will separate at the leading edge, followed by reattachment along the body [116]. Investigations on flow patterns and force coefficients for freight trains with bluff train head and wagon shapes have been conducted using a range of experimental and computational techniques [116, 38]. It is found that complex flow structures and separations, which are different from the flow around passenger trains, are formed around freight wagons [38]. Recent studies have categorized flow regions in the open air around a freight train [24] as follows:

1. Upstream and Nose Region: Marked by an increase in flow velocity before the train's front, strongly influenced by the train's shape.

2. Boundary Layer Region: Represents a highly turbulent area developing along the train's sides.

3. Near Wake Region: Boundary layer velocity in the slipstream gently decreases, without a distinct tail peak commonly observed in passenger trains.

4. Far Wake Region: Exhibits turbulent flow with shedding vortices.

Separation bubbles are observed on the roof and side of the train, which is similar to what occurs on the cube and generic bluff-body [116]. The separation bubble on the roof was found to be

around 1.75W in length and 0.35W in height (W is the width of the train) for the single wagon with a Reynolds number of 10^5. Apart from numerical simulations, experiments have also been carried out to study the leading edge flow separation [117]. The leading edge separation at the freight train nose is analysed using the vertical and lateral velocity data measured by model scale experiment [110]. A positive, then negative velocity peak is observed at the freight train nose and container leading faces, indicating a flow reversal zone caused by separation. Previous research indicates that the leading separation angle, which also acts as an indicator to the bluffness of a geometry, plays an important role in the formation of the leading edge separation bubble [117]. Li, Chao, et al. Li et al. [118, 119] investigate the flow topology of a double-stacked container wagon subject to different combinations of front and rear gap sizes. Results indicate that the leading edge separation zone at each container is similar to flow over a surface-mounted cube. Furthermore, the pressure distribution across the train surface and the separation reattachment length are measured, which have been subsequently used by modellers for validation purposes [82, 120].

Apart from the separation bubble formed at the blunt nose of the freight train and the front section of the container, another notable distinction between container-type freight trains and passenger trains lies in the wake vortices produced due to boundary layer separation at the rear of the preceding container. Current studies on container type freight train mainly focused on influence of loading configuration on pressure distribution and force coefficients in the open air [24, 27, 121, 118, 122, 123]. Maleki et al. [120] used the ELES approach to simulate the flow around a model freight train loaded with different configurations of double-stacked containers. Increasing the front or base gap sizes around the test wagon increased its drag, with the front gap having a stronger effect. The near-wake consisted of symmetric and asymmetric vortices, and a front gap size of approximately 1.77 times the wagon width allowed for flow across to the downstream wagon. However, a front gap size of 3.23 times the wagon width caused wake closure and impinged the shear layers, resulting in higher drag. Increasing the front gap size while keeping the base gap constant contracted the recirculation zone and increased the curvature of the shear layers [120, 82]. Östh et al. [116] used Large Eddy Simulation to analyze the flow

around a generic container freight wagon model. Two cases were numerically studied: a single wagon and a wagon submerged in a train set by using periodic boundary condition. The study observed oscillations in the separation bubble and upper shear layer, synchronised by vorticity waves. Counter-rotating vortices in the wagon gaps reduced drag in the train set, inhibited lateral oscillations, and caused dominant oscillations in the side force signal.

2.5.2 Other Bluff Bodies

.

The early research on bluff body flow is mainly focused on basic fundamental investigations in low Re number [124, 125, 126, 127]. Among all the research on bluff body flow, a benchmark study aimed at investigating the aerodynamic characteristics of rectangular cylinders with an aspect ratio of 5:1 was announced [128]. Known as the Benchmark on the Aerodynamics of a Rectangular 5:1 Cylinder (BARC), this benchmark problem sought to provide a standardised test case for evaluating the complex flow features surrounding elongated rectangular cylinders, which are of significant interest in the field of civil engineering, and clearly have applications to block freight train shapes. The flow region of a BARC configuration is characterised and depicted as shown in Figure 2.5 [129]. The top part of the figure is the averaged streamline and the bottom part shows the instantaneous vortices. Despite its relatively simple geometry, the BARC configuration is characterised by a multifaceted flow regime. The flow around the front face of the elongated rectangular cylinder is characterised by the development of a boundary layer, which then separates from the upstream edges to form a separated shear layer (region I). Subsequently, the shear layer starts to roll-up, resulting in the formation of vortical structures of varying sizes (region II). The corresponding mean flow is shown in the upper part of Fig. 1, where a recirculation region terminates with mean flow reattachment close to the trailing edge (region III). A wide range of experiments have been carried out to study the leading edge flow separation [117]. Results indicate that the leading separation angle, which also acts as an indicator to the bluffness of a geometry, plays an important role in the formation of the leading edge separation bubble [117]. With the development of computational capability, computational

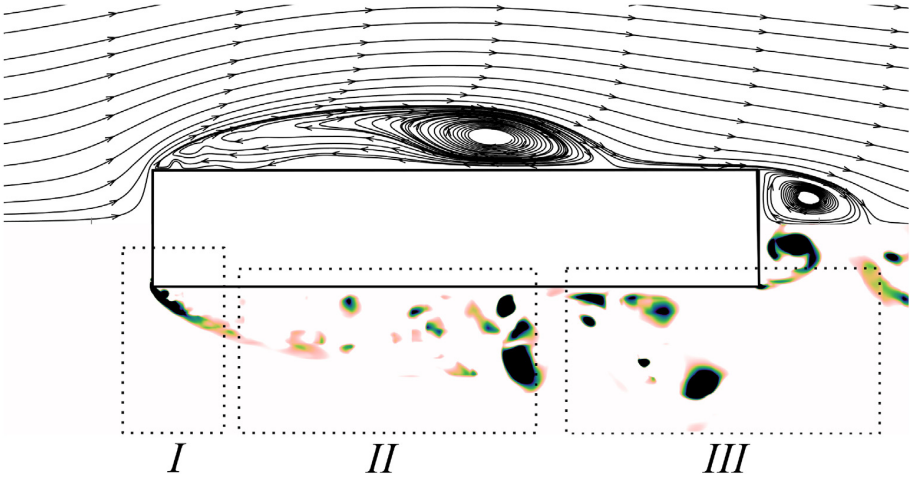


Figure 2.5: Characteristic region of BARC flow (Rocchio.et al., 2020)

methods have been developed and implemented to explore the flow around a bluff-body, in which LES has been shown to be very suitable for addressing this type of flow and widely implemented to study the flow structures around basic models (e.g. cubes, square cylinders [124, 130, 77] buildings [131] and generic bluff ground vehicles (e.g. bus, Ahmed body, etc ([132, 78]). This is not only due to the flow field around the bluff body being dominated by large-scale vortices generated as the air flows over its sharp edges, but also due to the relatively Reynolds number being very small at this this type of separation region, resulting in a relatively low mesh resolution requirement.

In addition to the considerable body of literature investigating the flow characteristics around isolated bluff bodies, research efforts have been dedicated to studying the wake interference phenomenon (buffeting) arising from the arrangement of two or more bluff bodies with varying sizes and gap lengths. Notably, Havel et al. [133] conducted experimental investigations on surface-mounted cubes with varying the gap length, under a Reynolds number of 22,000. Three regimes are summarised and briefly described as below,

1. Bi-stable Regime: At a gap length of approximately 1.5W (W is the width of the cube), the shear layer can either reattach or separate, resulting in low or high-frequency vortex shedding. Drag on the downstream body increases gradually, while the upstream body experiences a minimum drag at a gap length of 2W.

2. Lock-in Regime: Occurring at a gap length of 1.5W–2.3W, the upstream shear layer attaches to the downstream body, generating a strong vortex within the gap. Shedding frequency is locked to the resonance of the cavity, leading to a plateau in the front cube drag value and gradual drag increase in the rear cube.

3. Quasi-isolated Regime: Characterised by a large gap separation, a single shedding frequency occurs in the gap and downstream of the second body. With increasing gap size, the interaction between the gap flow and wake decreases, resulting in completely asynchronous vortex shedding. At a gap size of approximately 6W, the drag on both bodies reaches a constant value similar to an isolated body.

Similar flow regimes are identified and analysed for various upstream and downstream dimensions of different bluff bodies [134, 133, 135]. While these studies offer valuable reference data for sharp-edged three-dimensional objects like wagons, it should be noted that the Reynolds numbers considered in most of these studies are significantly lower than those encountered in train flows.

2.6 Conclusions

The literature review presented in this chapter reveals a notable disparity in the treatment of train tunnel coupled aerodynamic issues induced by freight trains as opposed to passenger trains. While extensive research exists for the latter, there is a marked scarcity of research focusing on freight trains. This discrepancy can be attributed to the complexity of numerically predicting pressure waves induced by freight trains passing through tunnels, which necessitates accurate simulation of the separation region. Consequently, meticulous considerations regarding mesh precision, computational resources, and the selection of an appropriate numerical model become paramount. Moreover, the inadequacies of previous 1d models in accounting for the influence of a blunt train nose and substantial gaps on pressure waves underscore the necessity for this research. The primary objective is to bridge these gaps by evaluating various numerical models and their efficacy in addressing aerodynamic challenges posed by freight trains passing through

tunnels. Additionally, the research endeavors to develop an enhanced 1d program capable of accurately simulating the pressure waves generated by freight trains, utilising the proposed novel model.

Chapter 3

One Dimensional Numerical Method

3.1 Introduction

This chapter will present the development of a 1d programme, written to solve the pressure wave pattern induced by a passenger train entering a tunnel. Much of this programme is based on previous research, but the initial development is vital to form a platform from which to redevelop the model and include freight train considerations. The structure for this chapter is as follows: firstly the governing equations for the 1d model and numerical calculation method are presented in detail. Then a flow chart of the programme is given in Chapter 3.6 to illustrate the programming and calculation process. Finally the accuracy of the 1d solver is validated and presented in Chapter 3.8.

3.2 Governing Equations

According to 2.4.2, four approaches to the development of a 1d numerical model have been introduced for solving the pressure variation inside tunnel. Among these models, Model (d), an unsteady, compressible, non-homentropic flow model, is the most complete 1d model for simulating air flow in a tunnel. This model has been previously validated in comparison to full-scale experimental data, suggesting that it can predict temperature, velocity, and pressure variations accurately [93, 16]. Therefore Model (d) is adopted as the foundation for the 1d

programme presented in this study. In this model, heat transfer and friction effect between air and train/tunnel walls are considered, and the air inside tunnel is modelled as ideal-gas. The continuity, momentum and energy equations are given as Eq. 3.1, Eq. 3.2 and Eq. 3.3 and the diagram of this flow model is given in Figure 3.1 for further illustration.

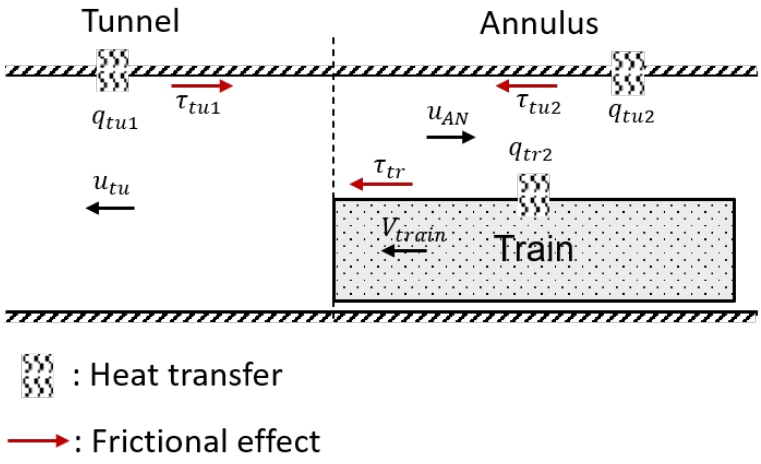


Figure 3.1: Diagram of the flow model

$$\frac{\partial \rho}{\partial t} + u\frac{\partial \rho}{\partial x} + \rho\frac{\partial u}{\partial x} = 0 \tag{3.1}$$

$$\frac{\partial u}{\partial t} + u\frac{\partial u}{\partial x} + \frac{1}{\rho}\frac{\partial p}{\partial x} + g = 0 \tag{3.2}$$

$$\left(\frac{\partial p}{\partial t} + u\frac{\partial p}{\partial x}\right) - a^2\left(\frac{\partial \rho}{\partial t} + u\frac{\partial \rho}{\partial x}\right) = (q - w + ug)\rho(\kappa - 1) \tag{3.3}$$

Here g represents the friction term, q is the heat-transfer term and w is the work-transfer term.

The calculation method of these additional terms will be briefly deducted here. According to previous research, the unsteady friction effect mainly has an influence on the steepening of the pressure wavefront and a distortion of the wave as the wave propagates inside tunnel [136, 56, 137]. Therefore when the tunnel is sufficiently long, or the train operates in a high speed and high blockage ratio situation, it is feasible to see that the influence of unsteady friction must be considered. Since the focus of this research is on the initial pressure wave pattern when a freight train enters a tunnel, the unsteady frictional effect is not a crucial parameter, thus the frictional force in this code is calculated by only considering the steady wall shear stress ($\tau_{tu\,1}$

in Figure 3.1).

$$\tau \approx \frac{1}{2} f \rho u |u| \tag{3.4}$$

ρ is the density of the air and f is friction coefficient. Thus giving the equation to calculate the frictional force acting on per unit mass of air in an empty tunnel,

$$\mathcal{g}_{tu} = \frac{S_{tu}}{2E_{tu}} f_{tu} u |u| \tag{3.5}$$

S is the perimeter and E is the cross-sectional area. Now, for the air in the annulus between a train and tunnel, the fictional force can be considered as the sum of the force acting on the tunnel and train surface (τ_{tu2} and τ_{tr} in Figure 3.1) [16]. The relative velocity between the air and train is $u-V$, in which V is the speed of the train. Thus the equation for the frictional force in the annulus $\mathcal{g}_{an}$is given by,

$$\mathcal{g}_{an} = \frac{S_{tu}}{2E_{an}} f_{tu} u |u| + \frac{S_{tr}}{2E_{an}} f_{tr} (u - V) |u - V| \tag{3.6}$$

The heat convection between the air and tunnel surface, as well as the air and train surface is considered in this flow model, as it will contribute the most to the heat transfer term. According to the Newton's law of cooling [138], heat convection is proportional to the temperature difference between air and wall surface,

$$Q = hA \left(T_w - T_\infty\right) = hSL \left(T_w - T_\infty\right) \tag{3.7}$$

in which T_w and T_∞ are wall and air temperature separately. h is heat convection coefficient calculated using Reynolds' analogy method [139],

$$h = \frac{1}{2} \rho f \left|u'\right| C_p \tag{3.8}$$

in which C_p is the specific constant of air and u' is the air velocity relative to the wall. Together

this leads to the heat transfer term in empty tunnel and annulus between the tunnel and train,

$$q_{tu} = \frac{S_{tu}}{2E_{tu}} \frac{\kappa R}{\kappa - 1} f_{tu} |u| \left(T_{tu} - T\right) \tag{3.9}$$

$$q_{an} = q_{tu} + q_{tr} = \frac{S_{tu}}{2E_{an}} \frac{\kappa R}{\kappa - 1} f_{tu} |u| \left(T_{tu} - T\right) + \frac{S_{tr}}{2E_{an}} \frac{\kappa R}{\kappa - 1} f_{tr} |u - V| \left(T_{tr} - T\right) \tag{3.10}$$

κ is the ratio of specific heats and R is the gas constant for air. The work transfer term refers to the work on the control element done by the moving wall surface of the train. Since there is no relative motion between the tunnel wall surface and control element in the ground coordinate system, the work transfer term in empty tunnel can be expressed as Equation 3.11.

$$w_{tu} = 0 \tag{3.11}$$

For the annulus between train and tunnel, the work on the control element done by the frictional force of moving train surface per unit time, per unit mass is given as Equation 3.12,

$$w_{an} = \frac{S_{tr}}{2E_{an}} f_{tr} V (u - V) |u - V| \tag{3.12}$$

Hence we get the full expression of the terms in continuity, momentum and energy equation for the 1d flow model.

The next section will illustrate the numerical method to solve the variables (ρ, p, u) in these equations.

3.3 MOC Method

3.3.1 Characteristic Equations

The mathematical method to solve the set of quasilinear hyperbolic partial differential equations is the method of characteristics (MOC). Firstly, these equations are non-dimensionalised by reference quantities (the reference speed of sound and the reference length) and replace the

variables with pseudo-Riemann variables λ, β, A_A [16]. The generalized Riemann variables are defined from Equation 3.13 to 3.14,

$$\lambda = \frac{c}{c_R} + \frac{\kappa - 1}{2}\frac{u}{c_R} = A + \frac{\kappa - 1}{2}U \tag{3.13}$$

$$\beta = \frac{c}{c_R} - \frac{\kappa - 1}{2}\frac{u}{c_R} = A - \frac{\kappa - 1}{2}U \tag{3.14}$$

U is non-dimensioned gas velocity and A is non-dimensioned speed of sound, and a_A is defined as the speed of sound when the airflow undergoes isentropic expansion to the reference pressure. It is a function of the entropy of the gas (s), calculated from Equation 3.15,

$$a_A = c_R e^{(\frac{s - s_R}{2C_p})} \tag{3.15}$$

It can be seen that a_A reflects the entropy of the flow. As the value of a_A increases, the entropy of the airflow also increases. Finally, A_A is a_A non-dimensionalised by the reference speed of sound (c_R),

$$A_A = \frac{a_A}{c_R} \tag{3.16}$$

Then Equations. 3.1 to 3.3 can be transformed to the characteristic equations. This involves consideration of the direction conditions for these three families of characteristic curves and the corresponding compatibility equations.The direction conditions and the calculation of corresponding compatibility conditions of the disturbance characteristics (λ and β) are given in Equation 3.17 and 3.18.

$$\left(\frac{\mathrm{d}X}{\mathrm{d}Z}\right)_{\substack{\lambda \\ \beta}} = U \pm A \tag{3.17}$$

$$\begin{aligned} d^{\lambda}_{\beta} &= \Delta^{\lambda}_{\beta_{A_A}} + \Delta^{\lambda}_{\beta_E} + \Delta^{\lambda}_{\beta_f} + \Delta^{\lambda}_{\beta_h} = \frac{\lambda + \beta}{2}\frac{d_A}{A_A} - \frac{(\lambda + \beta)(\lambda - \beta)}{4E}\frac{\mathrm{d}E}{\mathrm{d}X}\,\mathrm{d}Z \\ &\mp \frac{\kappa - 1}{2}\left[1 \mp 2\frac{(\lambda - \beta)}{(\lambda + \beta)}\right]\frac{l_R}{c_R^2}q\mathrm{d}Z + \frac{(\kappa - 1)^2}{(\lambda + \beta)}\frac{(q - w)}{c_R^3}l_R dZ \end{aligned} \tag{3.18}$$

Here $\Delta^{\lambda}_{\beta_{A_A}}$, $\Delta^{\lambda}_{\beta_E}$, $\Delta^{\lambda}_{\beta_f}$, $\Delta^{\lambda}_{\beta_h}$ refer to the change on disturbance characteristics influenced by entropy, cross-sectional area, frictional effect and heat transfer respectively. Similarly, the

direction condition and the equation to calculate the compatibility condition for the path line characteristic A_A are given as follows:

$$\left(\frac{dX}{dZ}\right)_{A_A} = U \tag{3.19}$$

$$\begin{aligned} dA_A &= \Delta A_{Af} + \Delta A_{Ah} \\ &= 2\frac{(\lambda-\beta)}{(\lambda+\beta)^2}\frac{1}{c_R^2}q\,dZ + \frac{2(\kappa-1)}{(\lambda+\beta)^2}\frac{(q-w)}{c_R^3}l_R dZ \end{aligned} \tag{3.20}$$

Note that the uppercase letter in these equations refers to non-dimensionalised variables. When the Riemann variables at the previous moment Z are known, the discrete Reimann variables can then be calculated through the Equations. 3.18 and 3.20. Thus the variables at next time step $Z + \Delta Z$ can be deduced by interpolation, using a 'mesh method' [16]. The numerical scheme applied to solve these variables is briefly introduced in Section 3.3.2. Readers may find a more detailed overview on solving the characteristic variables using the MOC method in Benson et al. [140].

3.3.2 Numerical Scheme

3.4 Mesh System

The boundaries illustrated in Chapter 3.5 are considered as non-continuous boundaries. Therefore the tunnel can be divided into several separated ducts. The length of these ducts changes with the train passing through the tunnel. Each duct has a fixed left-hand end and a moving right-hand end. This idea was introduced in Woods et al. [141]. It is commonly adopted by many researchers for solving the problem of moving mesh when train passes through a tunnel and has been further refined to consider a range of infrastructure types [16, 93, 92]. According to the different mesh systems, the whole process for the most simplistic system of a train passing through a tunnel is divided into three phases. The three phases are demonstrated in Figure 3.2. Blue mesh refers to the annulus between the train and tunnel, and black mesh refers to the empty

tunnel. Details are illustrated as below:

- Phase 1 is the period from the train head entering the tunnel to train tail entering the tunnel. It contains 2 mesh systems: duct1 is an empty tunnel that contracts in length and duct2 is an annulus that expands in length. Both have a moving end that is the nose of train head. The fixed left-hand ends are the tunnel exit and entrance. The characteristic variables at inner mesh points of each duct are calculated using the MOC method. The contracting and expanding mesh marked in the figure are used to solve the train head boundary. The equations that are applied to solve the characteristic variables for the points at the end of each duct are deduced in Chapter 3.5.

- Phase 2 is the period from the train tail entering the tunnel to the train head leaving the tunnel exit. The whole train is completely inside the tunnel during this process, which contains 4 mesh systems. Duct1 and duct4 are the empty tunnel in front of the train head and behind the train tail respectively. The annular space is divided into two ducts by a selected cross-section, given by the distance between the train and the tunnel wall. This section is chosen near the mid-point of the annulus and is moving from time to time. Overall, mesh is contracting in duct 1 and 3 and expanding in duct 2 and 4. The method to solve the inner mesh points and boundary mesh points are similar to that illustrated in Phase 1.

- Phase 3 is the period from train head leaving the tunnel to train tail leaving the tunnel. The tunnel is divided by the tail of the train into 2 ducts. Duct1 is an annulus that contracts in length and duct2 is an empty tunnel that expands in length. The mesh system is similar to that of phase 1, but the moving-end changing from the nose of the train to the tail of the train.

The coordinate system with this mesh system in this approach is relative to the ground. That is, the position of the grid points around the train It can be seen that the train needs to be divided into an expanding and a contracting duct in between the two discontinuities (head and tail of the train). However, for the case presented in this study for a partially loaded intermodal freight

train, there are many discontinuities on train body due to the large gaps that exist between loaded containers. Therefore to avoid excessive extending and expanding mesh, the mesh system of the annulus between freight train and tunnel is converted to a coordinate system that is stationary relative to the train. Details of the mesh system designed for the freight train with different container loading configurations will be illustrated in Chapter 6.2.

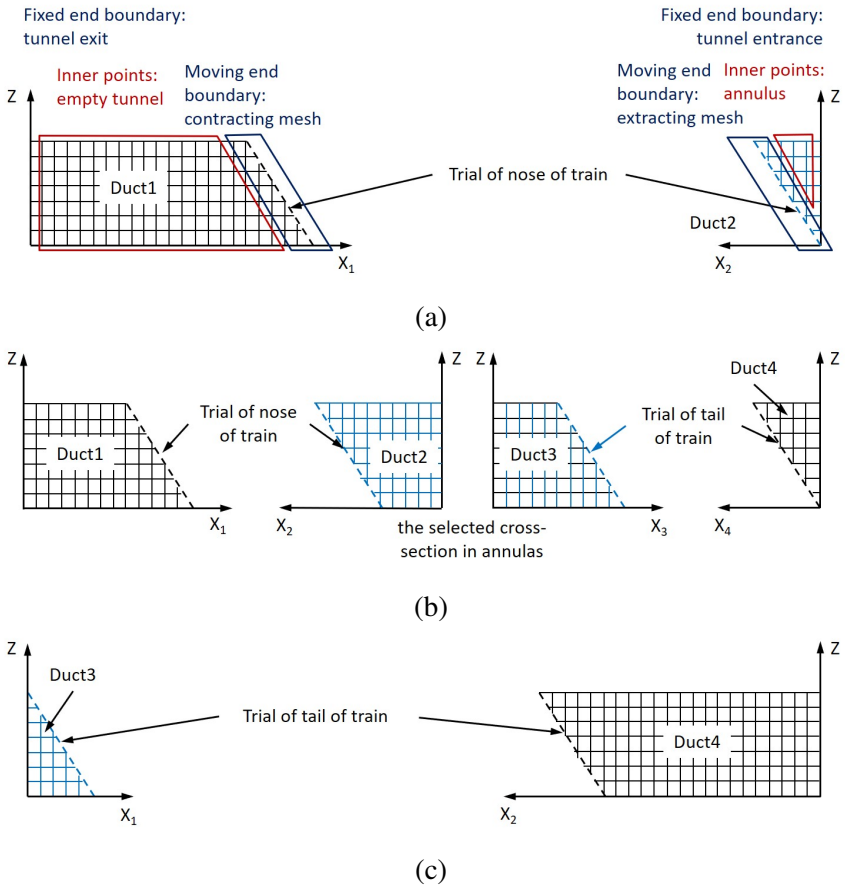


Figure 3.2: Mesh system of three phases (a) phase1: train enter the tunnel (b) phase 2: train completely inside tunnel (c) phase3: train exit the tunnel

3.5 Boundary Conditions

The characteristic variables at all the inner points in each duct can be calculated using the MOC, introduced in Chapter 3.3. The boundaries at the end of each mesh (tunnel portals and train head/tail) need to be calculated separately by the flow equations in conjunction with the characteristic equation. The boundary conditions for a single train passing through a tunnel are

summarized and divided into three types as below, to be illustrated separately in this Section The boundary at tunnel portal (a) is a fixed-end boundary and the boundaries related to the moving train ends are moving boundaries (b) ~ (c)[16].

(a) inflow/outflow at the tunnel portal

(b) train head enter/inside/leave tunnel the entrance/tunnel/exit

(c) train tail enter/inside/leave tunnel the entrance/tunnel/exit

The flow at tunnel portals that connect a duct and atmosphere are considered to be adiabatic and not necessarily reversible [142]. The condition and variables of the atmosphere are known and the characteristic variables only need to be considered and solved for the other one duct. Therefore boundary (a) is introduced and deduced first due to its simplicity, compared with the other boundaries related to the train ends.

3.5.1 Tunnel Portal

The boundary conditions at tunnel portals connect the flow between the tunnel/annulus and the atmosphere. The atmospheric pressure is set to 1 atm and the temperature is 20°C, which is the same as the initial pressure and temperature inside tunnel. Note that these values are adjustable to accommodate varying operational scenarios. Therefore, only the three characteristic variables in the tunnel/annulus need to be solved. The flow type at tunnel portal can be divided into two types,

(I) outflow: from tunnel/annulus to atmosphere

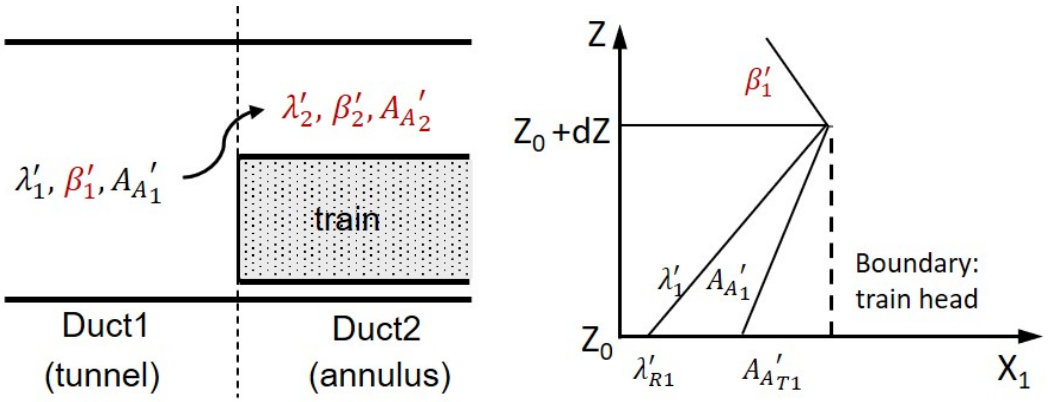
(II) inflow: from atmosphere to tunnel/annulus

From Chapter 3.3.2, it can be seen that the characteristic direction and the interpolation position of A_A is determined by the positive and negative sign of the air velocity. Specifically, for the inflow condition where air flows from the atmosphere to the tunnel/annulus, the unknown variables are solved by combining the momentum equation, thermodynamic relationship equation, and

characteristic equation[16]. For the outflow condition where air flows from the tunnel/annulus to the atmosphere, the characteristic variables A_A and λ can be directly solved from the characteristic equations. The characteristic variable β is obtained from the flow outside. To be more specific, it could be calculated from the pressure at the tunnel portal, which is equal to atmospheric pressure.

3.5.2 Train Head

The boundary at the train head connects the flow between the tunnel and the annulus, which requires six characteristic variables to be solved for both ducts as shown in 3.3. Note that the subscript 1, 2 in the figure refers to duct1 (tunnel) and duct2 (annulus) separately. Variables marked in red are the unknowns that need to be solved. The physical model at the train head adopted in this programme is similar with the one proposed in Woods et al. [16], but without considering the heat release generated from the locomotive engine. Generally, the unknown Riemann variables are solved by three flow equations in conjunction with the characteristic equation, in which the flow equation involves the steady-flow energy equation, the continuity equation and an empirical equation which expresses the loss of total pressure across the boundary. To build the flow equations across the train head, the flow at the train head needs to be considered



(a) (b)

Figure 3.3: Diagram of boundary condition at train head (a) train head inside tunnel (b) characteristic variables at train head in duct1 (moving reference frame)

quasi-steady relative to the train. The transformation form of Reimann variables that are relative

to the train are given as follows:

$$\lambda' = \lambda - \frac{\kappa - 1}{2}\frac{V}{c_R} \tag{3.21}$$

$$\beta' = \beta + \frac{\kappa - 1}{2}\frac{V}{c_R} \tag{3.22}$$

$$A'_A = A_A \tag{3.23}$$

As shown in 3.3(b), $\lambda_1{}'$ and $A_{A1}{}'$ on boundary grid point at $Z_0 + \Delta Z$ can be calculated by interpolation from the known characteristic variables at Z_0. Thus there are four variables ($\beta_1{}'$, $\lambda_2{}'$, $\beta_2{}'$, $A_{A2}{}'$) that are left unknown and need to be solved. The continuity equation of the flow from duct 1 to duct 2 is,

$$\rho_1 E_1 u'_1 = \rho_2 E_2 u'_2 \tag{3.24}$$

and the energy equation for quasi-steady flow is

$$c_1^2 + \frac{k-1}{2}u_1'^2 = c_2^2 + \frac{k-1}{2}u_2'^2 \tag{3.25}$$

According to the definition of the head pressure loss,

$$p_{01} - p_{02} = \frac{1}{2}\rho_2 {u'_2}^2 \zeta_N = \frac{1}{2}\kappa p_2 (\frac{u'_2}{c'_2})^2 \zeta_N \tag{3.26}$$

in which p_{01} and p_{02} are the stagnation pressure in duct 1 and 2, and ζ_N is head pressure loss. Thus by dividing both sides of Equation 3.26 by p_{02}, this leaves:

$$\frac{p_{01}}{p_{02}} = \frac{1}{2}\kappa\zeta_N \frac{\left(\frac{u'_2}{c_2}\right)^2}{\left(1 + \frac{\kappa-1}{2}\left(\frac{u'_2}{c_2}\right)^2\right)^{\frac{\kappa}{\kappa-1}}} + 1 \tag{3.27}$$

By investigating the correlation between the entropy ratio and the stagnation pressure ratio, we can derive the subsequent equation:

$$\frac{A_{A_2}}{A_{A_1}} = \left(\frac{p_{01}}{p_{02}}\right)^{\frac{\kappa-1}{2\kappa}} = \left\{1 + \frac{\frac{\kappa}{2}\left(\frac{\boldsymbol{u}_2'}{c_2}\right)^2 \zeta_N}{\left[1 + \frac{\kappa-1}{2}\left(\frac{\boldsymbol{u}_2'}{c_2}\right)^2\right]^{\frac{\kappa}{\kappa-1}}}\right\}^{\frac{\kappa-1}{2\kappa}} \tag{3.28}$$

Thus we get the three equations describing the flow from duct1 to duct 2: the continuity equation 3.24, the energy equation 3.25 and entropy change 3.28. According to the relationship between physical quantities and Riemann variables,

$$U = \frac{\lambda - \beta}{\kappa - 1}, A = \frac{\lambda + \beta}{2}, \frac{p}{p_R} = (\frac{A}{A_A})^{\frac{2\kappa}{\kappa-1}} \tag{3.29}$$

substitute the equations. 3.29 to obtain the three flow equations expressed by characteristic variables,

$$\left(\lambda_1' + \beta_1'\right)^2 - \left(\lambda_2' + \beta_2'\right)^2 + \frac{2}{\kappa - 1}\left[\left(\lambda_1' - \beta_1'\right)^2 - \left(\lambda_2' - \beta_2'\right)^2\right] = 0 \tag{3.30}$$

$$\left(\lambda_1' - \beta_1'\right)^2 \left(\lambda_1' + \beta_1'\right)^{\frac{2}{\kappa-1}} \left(\frac{A_{A_2}}{A_{A_1}}\right)^{\frac{2\kappa}{\kappa-1}} - \frac{E_2}{E_1}\left(\lambda_2' - \beta_2'\right)\left(\lambda_2' + \beta_2'\right)^{\frac{2}{\kappa-1}} = 0 \tag{3.31}$$

$$\frac{A_{A_2}}{A_{A_1}} = \left\{1 + \frac{\frac{2\kappa}{(\kappa-1)^2}\left(\frac{\lambda_2' - \beta_2'}{\lambda_2' + \beta_2'}\right)^2 \zeta_N}{\left[1 + \frac{2}{\kappa-1}\left(\frac{\lambda_2' - \beta_2'}{\lambda_2' + \beta_2'}\right)^2\right]^{\frac{\kappa}{\kappa-1}}}\right\}^{\left(\frac{\kappa-1}{2\kappa}\right)} \tag{3.32}$$

Since there are four characteristic variables to be solved, the equations are not closed. Thus, an additionally equation is used to reflect the relationship between the characteristic variables at the boundary for duct 2,

$$\beta_2' = \beta_{2S}' + C_1' A_{A_2} + \delta C_f + \delta C_h + \delta C_a \tag{3.33}$$

in which β_{2S}' is calculated by interpolation of the known β' values from last time step. $C_1' A_{A_2}$, δC_f, δC_h and δC_a refer to the change caused by entropy, fictional effect, heat transfer and cross-

sectional area respectively. Each term can be calculated from Equation 3.18. Finally we have the four Equation 3.30 ~ 3.33 to solve the four unknown characteristic variables. The equations are solved using the Newton-Raphson method with a convergence criteria lower than 10^{-6}.

The boundary conditions when the train head enters and exits the tunnel are similar as the train head inside tunnel. The flow equations 3.30 ~ 3.32 that describe the flow from duct 1 to duct 2 across the train head are the same. However, since the length of one of the ducts is not long enough for interpolation, the characteristic Equation 3.33 for this duct needs to be replaced when the train head is in the phase of just entering/exiting the tunnel[142]. A diagram of this process is illustrated in Figure 3.4. As shown in Figure 3.4(a), the length of the duct2 (annulus) is smaller than the mesh size ($l < \Delta x$). Therefore it can be assumed that the distance l is sufficiently small that the density is uniform over the element ($\rho_2 = \rho_3$). Therefore according to the continuity equation, the velocity over the element is constant ($u_2 = u_3$). Thus, the momentum equation can be written as,

$$(p_2 - p_3) E_2 - \tau_{tu} l S_{tu} - \tau_{tr} l S_{tr} = \left(\rho_2 u_2^2 - \rho_3 u_3^2\right) E_2 = 0 \tag{3.34}$$

According to the relationship between wall shear stress and frictional coefficient (Equation 3.4), it is possible to substitute the wall shear stress τ_{tr} and τ_{tu} into Equation 3.34 by frictional coefficient f_{tr} and f_{tu}. Therefore, by reorganizing and expressing the equation in terms of characteristic variables,

$$\begin{aligned} \left(\frac{\lambda_2' + \beta_2'}{2A_{A_2}}\right)^{\frac{2\kappa}{\kappa-1}} = \frac{1}{p_R}\Bigg\{ p_3 + \frac{\rho_3 l c_R^2}{2\left(E_{tu} - E_{tr}\right)} \\ \left[f_{tu} S_{tu} \left(\frac{\lambda_2' - \beta_2'}{\kappa - 1} + \frac{V}{c_R}\right)^2 + f_{tr} S_{tr} \left(\frac{\lambda_2' - \beta_2'}{\kappa - 1}\right)^2 \right] \Bigg\} \end{aligned} \tag{3.35}$$

Thus the four unknown characteristic variables in boundary condition of train entering a tunnel can be solved from Equation 3.30 ~ 3.32 in conjunction with Equation 3.35.

Similarly, when train head is reaching the tunnel exit as shown in Figure 3.4(b), the length of duct1 is smaller than mesh size ($l < \Delta x$). The flow across this short element is regarded as incompressible flow. The entropy of the duct is considered uniform, which is the mean entropy

in duct1 from previous time step ($A_{A_1} = \bar{A_A}$). The momentum equation for duct1 can therefore be written as,

$$(p_1 - p_3)E_1 - \tau_{tu} l S_{tu} = 0 \tag{3.36}$$

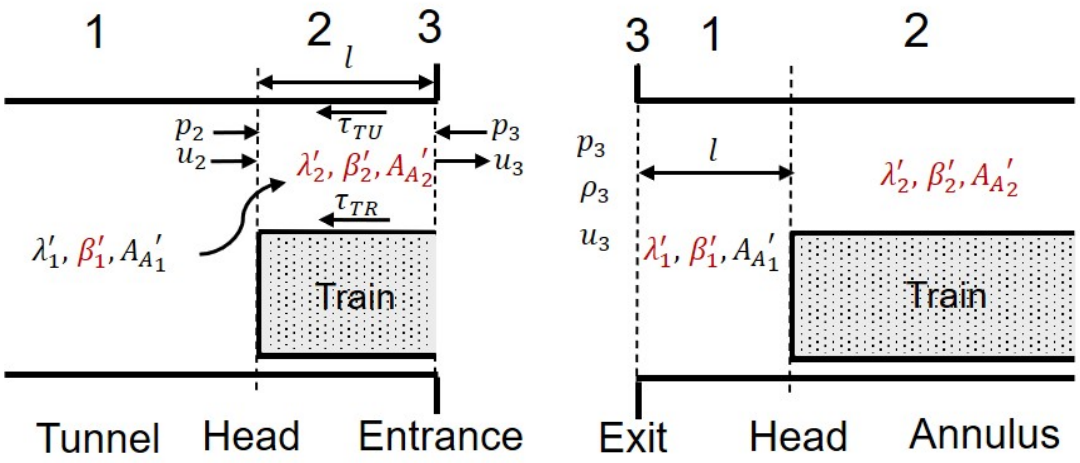
in which $\tau_{tu} = \frac{1}{2} f_{tu} \rho_3 \bar{u}^2$, $\bar{u}$ is the mean velocity in duct1 calculated from previous time step. From the relationship between pressure and characteristic variables,

$$\frac{p_1}{p_R} = \left(\frac{\lambda_1' + \beta_1'}{2A_{A_1}} \right)^{\frac{k}{k-1}} \tag{3.37}$$

and from the definition of characteristic variables, the relationship between Riemann variables λ_1' and β_1' is

$$\beta_1' = \lambda_1' - (\kappa - 1)\frac{u_1'}{c_R} \tag{3.38}$$

in which p_1 is calculated from Equation 3.36 and A_{A_1} is known. Thus the rest of characteristic variables at position 1 (λ_1' and β_1') can be obtained from Equation 3.37 and 3.38. Finally, the unknown characteristic variables at position 2 (λ_2' , β_2' and A_{A_2}) can be calculated by substituting λ_1' , β_1' and A_{A_1} into Equation 3.30 ~ 3.32



(a) (b)

Figure 3.4: Diagram of boundary condition at train head(a) train head enter tunnel (b) train head exit tunnel

3.5.3 Train Tail

The deduction of boundary conditions at the train tail is similar to that at the train head. The flow of the train head inside the tunnel can be simplified as airflow entering from a duct of larger cross-sectional area to a smaller one, while the train tail is the opposite [94]. Similarly, Equations 3.30 through 3.32 and 3.33 can also be utilized to solve the flow from the annulus space of the train tail to the tunnel. The subscripts 1 and 2 in these equations denote the variables at the annulus space of the train tail and inside the tunnel, respectively. In Equation 3.32, ζ_N needs to be replaced by the pressure loss at the train tail, denoted as ζ_T. When the train tail enters the tunnel, Equations 3.30 to 3.32 remain unchanged. Additionally, Equation 3.39 is required to close the system of unknown equations, describing the flow in the short tunnel duct from the train tail to the tunnel entrance. The assumption and derivation of this equation are similar to those for the boundary condition when the train head enters the tunnel, as elaborated in detail in Chapter 3.5.2. ζ_P is the pressure loss at tunnel portal.

$$\left(\frac{\lambda_2' + \beta_2'}{2A_{A_2}}\right)^{\frac{2\kappa}{\kappa-1}} = \left[1 - \frac{1}{2}\kappa\left(\frac{\lambda_2' - \beta'}{k-1} + \frac{V}{c_R}\right)^2\left(\frac{1}{A_A}\right)^2 \xi_P\right] \times \left[A_A^2 + \frac{\kappa-1}{2}\left(\frac{\lambda_2' - \beta'}{k-1} + \frac{V}{c_R}\right)^2\right]^{\frac{\kappa}{\kappa-1}} \tag{3.39}$$

3.6 Flow Chart

Through the approach taken using the 1d unsteady, compressible, non-homentropic numerical model built in Chapter 3.2 ~ 3.5, a computational programme is written in the Matlab environment to calculate the pressure and velocity of a train passing through a tunnel. The programme flow chart is shown as Fig. 3.5. The main programme is to monitor the position of the train and call the corresponding subroutine. The input variables includes: atmospheric pressure and temperature; cross-sectional area, perimeter and total length of the tunnel, frictional parameter of tunnel surface, pressure loss coefficient of tunnel portal; train speed, cross-sectional area,

perimeter and length of the train, frictional parameter of train surface, pressure loss coefficient of train head and tail; reference velocity of sound, reference length, reference pressure and grid size.

For each subroutine, the calculation process is similar. First is to judge type of the mesh and obtain the characteristic value at moment Z on every grid point. Then calculate the time step ΔZ, choosing the minimum ΔZ to keep it consistent among all the ducts. Time step is calculated based on Courant–Friedrichs–Lewy (CFL) criterion $\frac{\delta Z}{\delta X} \leq \frac{1}{A+|U|}$. Then by considering the direction of velocity, determine the position of interpolated points and further calculate the characteristic value of all the inner points at $Z + \Delta Z$. The characteristic value of boundary grids are calculated according to the corresponding boundary conditions. Then pressure and velocity can be obtained based on the relationship between Riemann variables and thermodynamics. Finally, assign the value of $Z + \Delta Z$ to Z, and execute the loop until the phase end.

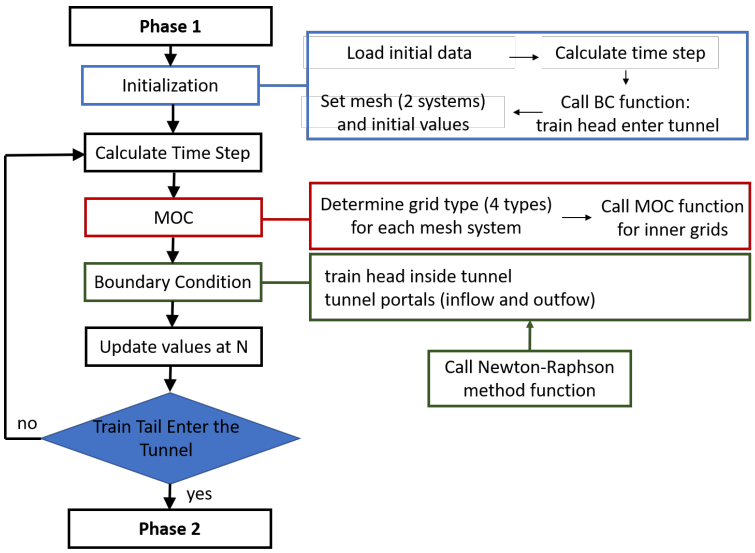


Figure 3.5: Flow chart

3.7 Pre-determined Parameters

As can be seen from the equations given in the introduction to the 1d numerical model, some input parameters of describing the train and tunnel need to be pre-determined, including areas, perimeters, length, frictional coefficients of the train and tunnel, as well as the pressure loss

coefficient at head/tail of the train and tunnel portals. According to Vardy et al. [17], the empirical parameter of head loss coefficient ζ_N for passenger trains is 0.05 ± 0.025, and that for freight trains is 0.1. According to the Borda-Carnot relationship, the tail loss coefficient ζ_T is $(\beta_E)^2$, in which β_E is the blockage ratio [17]. The pressure loss coefficient at a tunnel portal is often estimated at around 0.5, which is similar to the dynamic head of a pipe inlet in a plane wall based on previous research [16]. Details for the other parameters used in the 1d simulation of a Class 66 freight locomotive entering a tunnel are given in Table 3.1 and 3.2.

Name	Length	Area	Perimeter	Friction coefficient	Head Loss	Tail loss	Velocity
Loco66	182 m	10.5 m^2	9.82 m	0.01	0.1	β_E^2	33.5 m/s

Table 3.1: Freight train parameters used in the traditional 1d code.

Name	Length	Area	Perimeter	Friction coefficient	pressure loss at entrance and exit
Tunnel	574.5 m	45 m^2	24 m	0.01	0.5

Table 3.2: Tunnel parameters used in the traditional 1d code.

3.8 Validation

To validate the accuracy of the 1d code developed in this work, the pressure wave of a Talgo1 train passing through a tunnel predicted by this code is compared with results presented in a previous paper. The parameters adopted in the code are defined in detail by Vardy et al. [17]. For ease, the speed of the train is 129.5 km/h and the other main parameters of importance are listed in Table 3.3 and 3.4. Compared to measured and previous 1d results as shown in Figure 3.6, it can be seen that the code developed in this work is able to predict the magnitude and pressure wave pattern as presented by Vardy et al. [17]. All significant pressure signals are well predicted using this 1d code, including the compression and expansion waves caused by the entry of train head and tail, the frictional effect of train and tunnel surface, and reflection of pressure waves at tunnel portal and the propagation of pressure waves inside the tunnel. The

difference in the pressure wave shape between the result obtained from this code and in previous research can be contributed to the utilization of different cross-sectional areas for the locomotive of the passenger train and the containers in Vardy's research. Thus it is concluded that the boundary conditions, the mesh system, the transient scheme and MOC method are successfully applied to this 1d programme.

Name	Length	Area	Perimeter	Friction coefficient	Head Loss	Train loss
Talgo1	146 m	10 m^2	12 m	0.003	0.075	β^2

Table 3.3: Train parameters to be used for validation of the 1d code.

Name	Length	Area	Perimeter	Friction coefficient	pressure loss at entrance and exit
Grauhoz	6298 m	62 m^2	32 m	0.006	0.5

Table 3.4: Tunnel parameters to be used for validation of the 1d code.

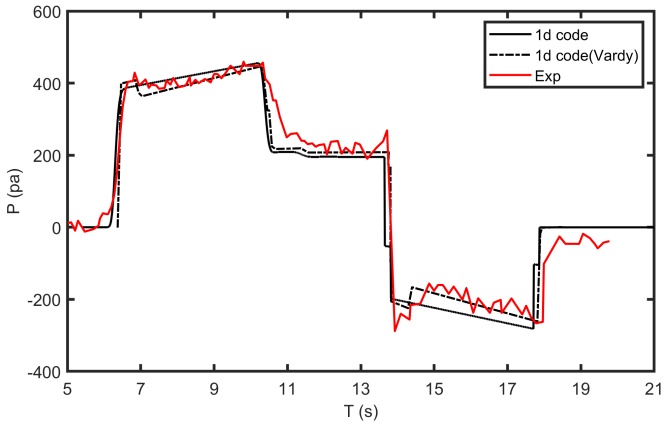


Figure 3.6: Comparison of experimental results and 1d predicted pressure time history curves.

Chapter 4

Three Dimensional Numerical Method

4.1 Introduction

Fundamental to the development of a simplified 1d model for freight passage through a tunnel is an understanding of the characteristic aerodynamic flow pattern and appreciation of the size of flow separation around the bluff body. In this work, both Large Eddy Simulation (LES) and SST k-ω Reynolds Averaged Navier-Stokes (RANS) models are adopted to simulate and analyze the flow field and to predict the development of the separation bubble. The simulations are conducted using the pressure-based solver of the commercial software Fluent. With a freight train operating at a speed of 33.5 m/s, corresponding to a Mach number of 0.1, the flow is treated as incompressible when the train operates on open track. However, when the train passes through tunnels, the air is simulated as a compressible gas to model the generation of pressure waves. This chapter will outline the governing equations in compressible format, the numerical settings for these simulations, as well as the geometries and boundary conditions.

4.2 Tunnel

4.2.1 Numerical Model

To obtain an understanding of the 3-dimensionality of the flow field around a freight train and the clear shape of the separation bubble as the train enters into the tunnel, URANS (Unsteady Reynolds-averaged Naiver-Stokes) is adopted. Indeed, this technique is also adopted over the LES technique, as whilst it is understood that URANS is more dissipative than LES, the URANS technique is adopted to avoid the generation of a high number of turbulent flow and transient coherent structures, which mask the overall shape/size of the core separation bubble, which is the main feature creating the effective shape of the freight locomotive nose entering into a tunnel. Thus the URANS approach was used for the simulation with the tunnel, including the reference simulation and the simulations to investigate the influence of blockage ratio. The applicability of investigating the separation bubble and loading configuration using URANS model is investigated in Chapter 4.2.6 through a comparison with experimental and LES numerical results.

URANS

The compressible RANS equations are written as,

$$\frac{\partial \bar{\rho}}{\partial t} + \frac{\partial}{\partial x_j}(\bar{\rho}\hat{u}_j) = 0 \tag{4.1}$$

$$\frac{\partial(\bar{\rho}\hat{u}_j)}{\partial t} + \frac{\partial}{\partial x_j}(\hat{u}_j\bar{\rho}\hat{u}_i) = -\frac{\partial p}{\partial x_i} + \frac{\bar{\sigma}_{ij}}{\partial x_j} + \frac{\tau_{ij}}{\partial x_j} \tag{4.2}$$

$$\frac{(\bar{\rho}\hat{E})}{\partial t} + \frac{\partial}{\partial x_j}(\hat{u}_j\bar{\rho}\hat{H}) = \frac{\partial}{\partial x_j}(\bar{\sigma}_{ij}\hat{u}_i + \overline{\sigma_{ij}u_i''}) - \frac{\partial}{\partial x_j}(\bar{q}_j + c_p\overline{\rho u_j''T''} - \hat{u}_i\tau_{ij} + \frac{1}{2}\overline{\rho u_i''u_i''u_j''}) \tag{4.3}$$

where

$$\hat{H} = \hat{E} + \bar{p}/\bar{\rho} \tag{4.4}$$

$$\bar{q}_j = -\overline{k_T \partial T/\partial x_j} \approx -\frac{c_p \hat{u}}{Pr} \frac{\partial \hat{T}}{\partial x_j} \tag{4.5}$$

$\bar{\sigma}_{ij}$ is the viscous stress tensor, which can be calculated using equation. 4.6.

$$\bar{\sigma}_{ij} \approx 2\hat{\mu} \left(\hat{S}_{ij} - \frac{1}{3} \frac{\partial \hat{u}_k}{\partial x_k} \delta_{ij} \right) \tag{4.6}$$

The Reynolds stress term $\tau_{ij} \equiv \overline{\rho u_i'' u_j''}$, which will be modelled using k-ω SST model as given in Section 4.2.1. The conventional time-average mean is denoted by the overbar, indicating an averaging time scale assumed to be long relative to turbulent fluctuations but short compared to unsteadiness in the mean flow. In contrast, the hat symbolizes the Favre (density-weighted) average. $\hat{f} = \frac{\overline{\rho f}}{\bar{\rho}}$ and that $f = \bar{f} + f' = \hat{f} + f''$. Furthermore, we have the equation of state (equation. 4.7),

$$\bar{p} = (\gamma - 1) \left(\bar{\rho}\hat{E} - \frac{1}{2}\bar{\rho}(\hat{u}^2 + \hat{v}^2 + \hat{w}^2) - \bar{\rho}k \right) \tag{4.7}$$

where k is the local turbulent kinetic energy (TKE), $k = \frac{1}{2}(\hat{u''^2} + \hat{v''^2} + \hat{w''^2})$. γ is the heat capacity ratio which is, taken as 1.4 for air. The other terms that also need to be modelled are given as follow,

$$c_p \overline{\rho u_i'' T''} \approx -\frac{c_p \hat{u}_t}{Pr_t} \frac{\partial \hat{T}}{\partial x_j} \tag{4.8}$$

$$\overline{\sigma_{ij} u_i''} - \frac{1}{2} \overline{\rho u_i'' u_i'' u_j''} \approx \left(\hat{\mu} + \frac{\hat{\mu}_t}{\sigma_k} \right) \frac{\partial k}{\partial x_j} \tag{4.9}$$

k-ω SST URANS

Compared to other RANS models, k-ω SST model is expected to predict a better result for the separation bubble since it can eliminate the adverse free flow issues of the Wilcox model, and avoid overprediction of the shear stress at the train surface [143]. Since this investigation includes the requirement of solve the separation regions around freight trains, thus k-ω SST

URANS model is accepted in this study.

The two-equations k-ω SST in conservation form are given as equation. 4.10 and 4.11 [144],

$$\frac{\partial(\rho k)}{\partial t} + \frac{\partial(\rho u_j k)}{\partial x_j} = P - \beta^* \rho \omega k + \frac{\partial}{\partial x_j}\left((\mu + \sigma_k \mu_t)\frac{\partial k}{\partial x_j}\right) \tag{4.10}$$

$$\frac{\partial(\rho \omega)}{\partial t} + \frac{\partial(\rho u_j \omega)}{\partial x_j} = \frac{\gamma}{\nu_t} P - \beta \rho \omega^2 + \frac{\partial}{\partial x_j}\left((\mu + \sigma_\omega \mu_t)\frac{\partial \omega}{\partial x_j}\right) + 2(1 - F_1)\frac{\rho \sigma_{\omega 2}}{\omega}\frac{\partial k}{\partial x_j}\frac{\partial \omega}{\partial x_j} \tag{4.11}$$

of which

$$P = \tau_{ij}\frac{\partial u_i}{\partial x_j} \tag{4.12}$$

$$S_{ij} = \frac{1}{2}\left(\frac{\partial u_i}{\partial x_j} + \frac{u_j}{\partial x_i}\right) \tag{4.13}$$

$$\tau_{ij} = 2\mu_t\left(S_{ij} - \frac{1}{3}\frac{\partial u_k}{\partial x_k}\right) - \frac{2}{3}\rho k \delta_{ij} \tag{4.14}$$

Furthermore, the turbulent eddy viscosity μ_t is computed using equation. 4.15,

$$\mu_t = \frac{\rho a_1 k}{max(a_1 \omega, \Omega F_2)} \tag{4.15}$$

F1 and F2 correspond to the blending functions in the SST model. Detailed equations can be referenced in Liu et al. [145].

4.2.2 Geometry

A 1/25 scale Class 66 freight locomotive connected to simplified FEA-B flatbed wagons with containers is used in this study as shown in Figure 4.1. The features and shape of the nose and underbody are kept consistent with the model used in the experiment [21] as much as possible. A number of simplifications have been made in the bogie region to facilitate the division of structured mesh and enable a higher mesh quality [77, 115]. However, the overall

length and height of the bogies and position/diameter of the wheels are the same as those used in the experiment, to keep the blockage area unchanged. The dimensions of the scale locomotive are height H=0.16 m and width W = 0.107 m. These dimensions will be used in the parameterisation study for the non-dimensionalisation of the separation bubble size. Further details and dimensions of the train type and CAD model are demonstrated in Flynn et al. [27].

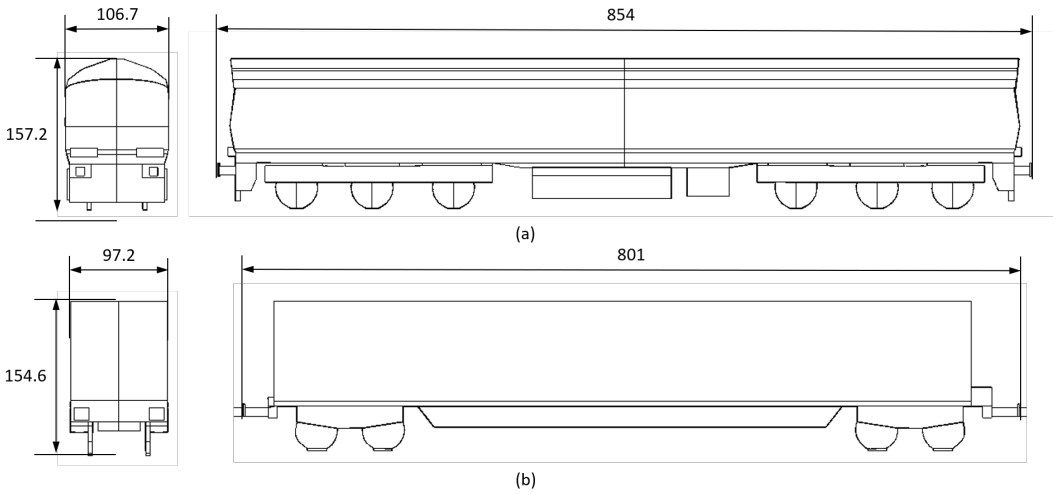


Figure 4.1: Dimensions of the freight train CAD model (a) Class 66 locomotive (b) FEA-B wagons with containers

4.2.3 Computational Domain and Boundary Conditions

The commercial software Fluent (pressure-based solver) is used to solve the 3d flow field and pressure wave pattern induced by a freight train entering a tunnel. A sliding mesh method is used to simulate the relative motion between the train and the tunnel. Using this method, the whole computational domain is composed of a stationary region that contains the tunnel and a sliding mesh region (the yellow region in Figure 4.2) that contains the freight train and moves in the longitudinal direction with train speed 33.5 m/s. According to the expression of Reynolds number: $Re = \frac{ul}{v}$, and taking the train height H as the reference length, H = 0.16 m, the Reynolds number of the flow field around the freight train in this study is approximately 3.82×10^5. The whole computational domain is symmetrical with respect to xz plane and the freight train is located at the symmetry plane. The dimensions of the computational domain and

boundary conditions are illustrated in Figure 4.2. In order to validate these simulations against previous experimental results, the tunnel configuration is selected to be the same as that used in the moving model experiment carried out by Iliadis et al. [21]. The cross-sectional area of the tunnel is 45 m^2 and the length of which is 574.5 m at full-scale. Interfaces of the stationary and sliding regions enable the information exchange between the stationary and moving regions. The ground, tunnel and train surfaces are set as non-slip walls.

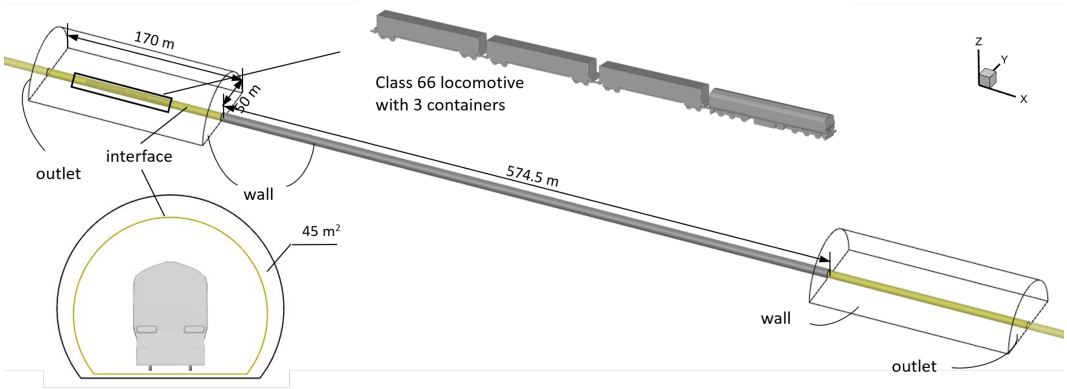
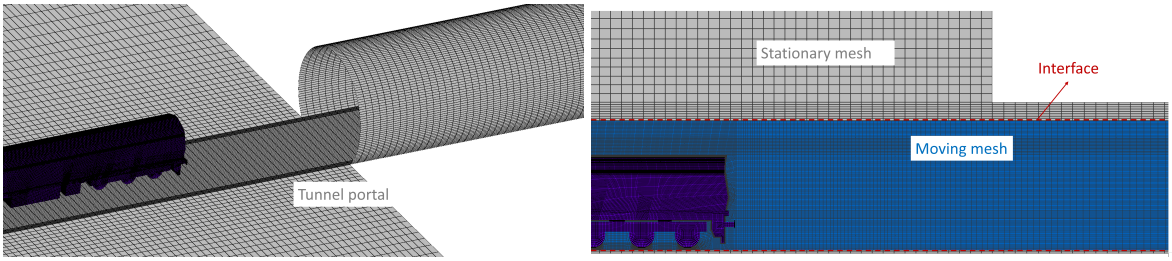


Figure 4.2: Computational domain of freight train passing through a tunnel and boundary conditions (dimensions in the figure are given as full-scale).

4.2.4 Mesh

The mesh near the freight train for cases of passing a tunnel is the same as that on the open field. The detail and the requirements of the block strategy of dividing the mesh and the mesh size around the freight locomotive and the containers are presented in Chapter 4.3.4. In this chapter, only the diagram of mesh around the tunnel portal and at interfaces between are given as shown in Figure 4.3. For illustration, the tunnel shown in the figure is a 45 m^2 tunnel, and the mesh size and division for tunnels of other cross-sectional areas in this study are the same. The mesh size in the stationary region around the tunnel portal is refined, with a span-wise size of approximately 6 mm and a stream-wise size of approximately 15 mm. Specifically, for a tunnel with a cross-sectional area of 45 m^2, this results in a cell count of approximately 3.16 million in the stationary region. For the sliding region involving a freight locomotive 66 with four fully loaded containers, and another with four 33% loaded containers, the respective cell counts are



(a) (b)

Figure 4.3: Mesh around tunnel portal (a) mesh on train and tunnel surface (b) mesh on the clip Y=0 m.

approximately 31 million and 43 million.

4.2.5 CFD Solver Set Up

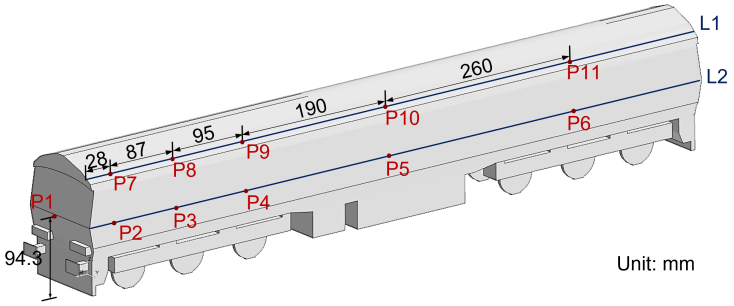
To reduce the error caused by discretisation, a second-order upwind scheme is used for the discretisation of the convection and diffusion terms [115]. The relevant control equations are solved using the CFD software Fluent based on the finite volume method, and a PISO pressure-velocity coupling method is also adopted. The time derivative is discretized using the bounded second-order implicit scheme for the unsteady calculation. The time step Δt is set as 4×10^{-5}, estimated by CFL$\leqslant$1 ($CFL = \Delta t \cdot v/\Delta x_{\min}$, where v is the train operating speed and $\Delta x_{\min}$ is 0.0015m).

4.2.6 Model Validation

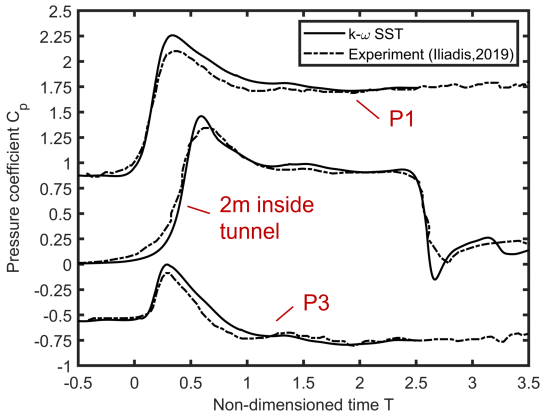
Comparison of Pressure History Curve with Experimental Results

The simulation of the freight train entering a tunnel using $k-\omega$ SST RANS model is validated against experimental data measuring using the University of Birmingham Transient Aerodynamic Investigation (TRAIN) rig moving model facility. The experimental setup utilises a 1/25th scale Class 66 locomotive connected to four FEA-B flatbed container wagons in a fully loaded container configuration (there are no unused container loading spaces on the wagons) passing through a 45 m^2 tunnel. Further details of the experimental settings can be found in Iliadis et al. [21]. The position of surface pressure measuring points across model train surface

are illustrated in Figure 4.4(a). To validate the computational simulations, pressure time-history curves at the measuring positions on train surface (P1 and P3) and on the tunnel wall 2 m inside the tunnel entrance are compared with the experimental results, as shown in Figure 4.4(b). P1 and P3 are measuring points at train nose and train side located inside the separation bubble region. The pressure coefficient is calculated by $C_p = \frac{p-p_\infty}{0.5\rho v^2}$ and time is non-dimensionalised by $\frac{L}{v}$, where L is the length of the locomotive.



(a)



(b)

Figure 4.4: Pressure history curve at measuring points (a) position of measuring points (b) comparison of pressure variation on train and tunnel surface between $k-\omega$ SST URANS and Experimental results

The results illustrate that the pressure at measuring points P1 and P3 before and after the train enters the tunnel are very well predicted, indicating an accurate prediction of the flow separation in this region. The maximum pressure caused by the initial pressure rise as the train enters into the tunnel is a little overpredicted by the $k-\omega$ SST model, by an error around 6 %, which is typical in comparison to other studies [146, 147, 148]. This may be attributed to the assumption of isotropy and equilibrium of turbulence of the RANS model, which tends to overestimate the

size of separation bubbles. Although the $k-\omega$ SST RANS model performs better in predicting separation and reattachment of the boundary layer than other RANS models, previous research has shown that it still tends to overpredict the separation length and exhibit a lagging recovery after attachment [149]. In general, the computational approach performs well in predicting the effect of the separation bubble on the change of pressure wave. The results indicate that the $k-\omega$ SST model is capable of simulating the flow field pattern, providing correct flow field information (e.g. the size of separation bubble) to be fed in the parameterisation study and support the development of the 1d code for freight trains, as shown in Chapter 5.4.3.

4.3 Open Field

4.3.1 Numerical Model

Since the fluctuating quantities are averaged and modelled using the URANS model, LES numerical model is used in the case of trains operating in an open field, including the parameterisation study due to its ability on providing more accurate predictions of vortex separation [132, 77, 38]. Therefore the LES method is adopted to conduct the parameterisation study of the separation bubble size by simulating freight trains with various head shapes operating on an open field.

LES

From Chapter 4.2.1 URANS model divided the variables into time-averaged and fluctuating components, where the latter one is modelled in the simulation. In the LES methodology, a filter is employed to distinguish between the larger scales and smaller ones. Consequently, all variables such are divided into grid and sub-grid components. Upon filtering the variables within the compressible Navier-Stokes equations, the resulting equation at the instantaneous filtered level manifests in the subsequent equations. The governing equations for LES method based on Wall-Adapting Local Eddy-Viscosity (WALE) model is illustrated as follow.

$$\frac{\partial \bar{\rho}}{\partial t} + \frac{\partial}{\partial x_i} \cdot (\rho \tilde{u}_i) = 0 \tag{4.16}$$

$$\frac{\partial \bar{\rho}\tilde{u}_i}{\partial t} + \frac{\partial}{\partial x_i}(\bar{\rho}\tilde{u}_i\tilde{u}_j) + \frac{\bar{\rho}}{\partial x_i} = \frac{\partial}{\partial x_i}\left(-\bar{\tau}_{ij} + u_\tau(\frac{\tilde{u}_i}{\partial x_j} + \frac{\tilde{u}_i}{\partial x_i}) + \frac{\delta_{ij}}{3}T_{kk}\right) \tag{4.17}$$

$$\frac{\partial \bar{\rho}\tilde{h}}{\partial t} + \frac{\partial}{\partial x_i}(\bar{\rho}\tilde{u}_i\tilde{h}) = \frac{D\bar{p}}{Dt} + \frac{\partial}{\partial x_i}\left((\frac{\mu}{Pr} + \frac{\mu_t}{Pr})\frac{\partial \tilde{h}}{\partial x_i}\right) \tag{4.18}$$

where the symbols ˜ and ¯ refer to filtered (volume averaged) Favre and filtered quantities. The term u, p, ρ, h and δ denote to the velocity vector, pressure, flow density, enthalpy and the Kronecker delta. In addition, T_{kk} is the isentropic contribution and can be absorbed into the filtered pressure.

WALE

A Wall-Adapting Local Eddy-Viscosity (WALE) model is adopted for the subgrid-scale (SGS) model in this study. Previous research illustrate that the WALE model performs well in resolving complex flows, including those with separation regions [150], such as the flow created about the bluff freight train. The subgrid scale kinetic energy can be computed as follow,

$$\frac{\partial K_t}{\partial t} + \frac{\partial \tilde{u}_j K_t}{\partial x_i} = \frac{\partial}{\partial x_i}\left(\frac{\mu_t}{\bar{\rho}Pr_t}\frac{\partial K_t}{\partial x_i}\right) - \tau_{ij}\frac{\partial \tilde{u}_j}{\partial x_i} - \epsilon_t \tag{4.19}$$

where ϵ_t and τ_{ij} represent the subgrid scale dissipation and stress tensor, and μ_t is the eddy-viscosity that is calculated based on WALE model,

$$\mu_t = \rho L_s^2 \frac{(S_{ij}^d S_{ij}^d)^{3/2}}{(\bar{S}_{ij}\bar{S}_{ij})^{5/2} + (S_{ij}^d S_{ij}^d)^{5/4}} \tag{4.20}$$

where the parameter S_{ij} and L_s denote to the rate-of-strain tensor and mixing length for subgrid scale strain rate. Moreover, S_{ij}^d can be computed as follow,

$$S_{ij}^d = 0.5\left((g_{ij})^2 + (g_{ji})^2\right) - \delta_{ij}(g_{kk})^2 \tag{4.21}$$

in which, the term $g_{ij} = \frac{\partial \bar{u}_i}{\partial x_j}$.

4.3.2 Geometry

Parameterisation Study of Nose Bluntness

To identify an appropriate methodology for conducting a parameterization study on the influence of locomotive shape, we have taken into account a diverse range of freight locomotive types, as illustrated in Figure 4.5. These locomotives have been divided into distinct regions, namely the roof, windshield, and coupling sections. The degree of bluntness can be finely regulated by adjusting the parameters α and β, as depicted in Figure 4.6.α is the angle between roof region and cross-sectional plane of the train body, and β is the angle between windshield region and cross-sectional plane of the train body. Among the various locomotive types and shapes, Class 90 emerges as the most aerodynamically streamlined. The characteristic controlling angles for Class 90 locomotives typically fall within the range of approximately 30 degrees. Consequently, for our parameterization study concerning nose bluntness, we initially simplify the Class 66 locomotive into a generic freight locomotive. Subsequently, we further divide it into three distinct regions: the roof, windshield, and coupling. The governing angles, α and β, are constrained within the interval [0, 30] degrees. Six unique combinations of these angles have been selected to facilitate the parameterization study, encompassing values of 0+0, 15+0, 15+15, 30+0, 30+15, and 30+30, as visually represented in Figure 4.6.



Figure 4.5: Different freight locomotive types

Parameterisation Study of Loading Configurations

For the parameterisation study of container loading configurations on intermodal flatbed wagons, four loading configurations are used in this investigation. The flatbed wagon chosen for this

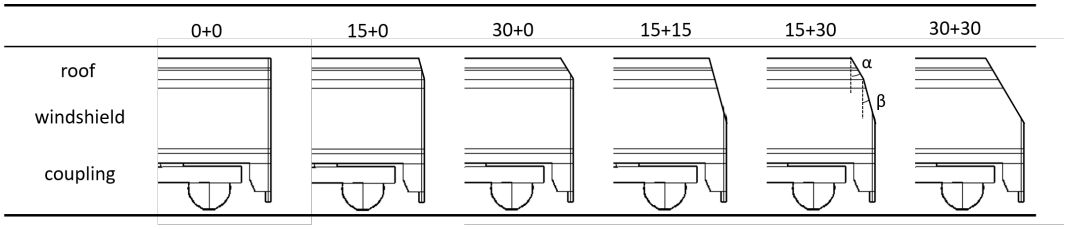


Figure 4.6: Different head shapes of generic freight loco for parameterisation study

study is the FEA-B type, with a 18.2 m (60 foot) loading deck, as used in previous aerodynamic studies [24, 21]. According to standard International Shipping Organisation (ISO) designs, two types of container are designed with a size of 12.192m × 2.438m × 2.590m (40 foot) and 6.096m × 2.438m × 2.590m (20 foot). Thus by adjusting the position and the number of containers, five loading configurations are obtained to study the influence of the gap ranging from 0 m to 18.2 m (0 to 60 foot) on flow parameters in the gaps (Figure 4.7). More specifically, the first working condition used both a 40 foot and a 20 foot containers, known as the fully loaded case. The second and third working conditions used one 40 foot and one 20 foot container for the second carriage of the train, which is empty for the fourth case.

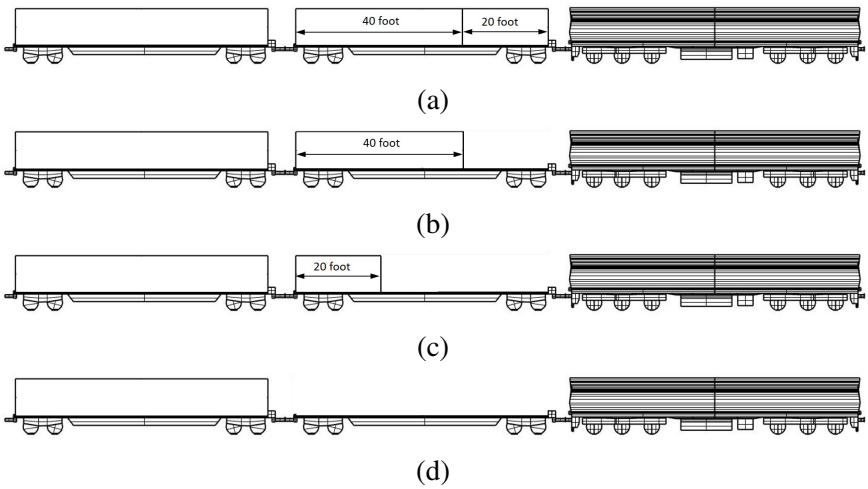


Figure 4.7: Different loading configurations for parameterisation study (a) fully loaded train (b) 20 feet gap (c) 40 feet gap (d) 60 feet gap (1 carriage empty)

4.3.3 Computational Domain and Boundary Conditions

In order to get the time-averaged flow information from the LES method that will be utilised in the parameterisation study, simulations for this aspect were carried out in the open field. It is appreciated that the separation bubble will change when the train enters into a tunnel; however, results indicate that the bubble size can be scaled to the size when train head just enters the tunnel using a scale factor obtained from the reference simulation case. Therefore, this approach to conduct a single simulation in the open field, removes the technical difficulties and requirement for many additional simulations within tunnels when considering a wide array of train designs.

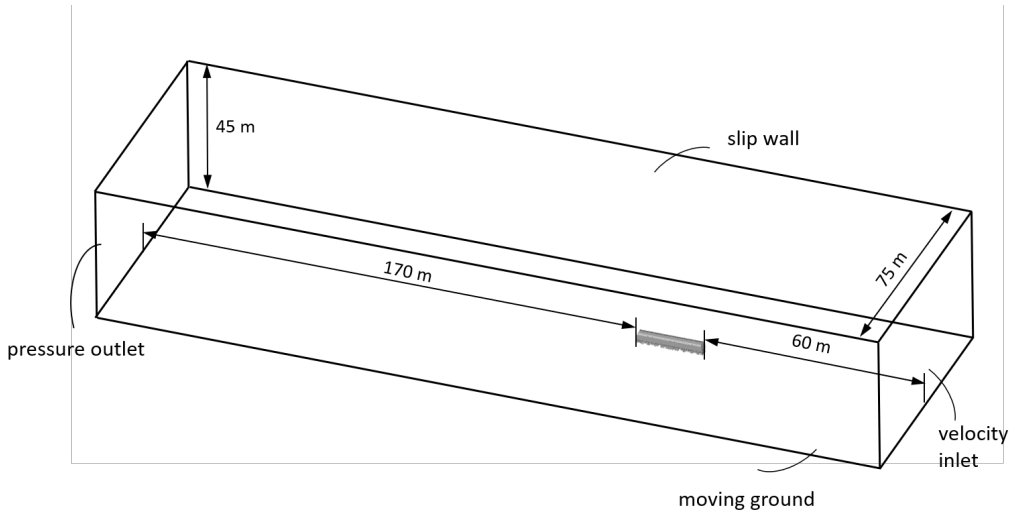


Figure 4.8: Computational domain of the freight train operating in the open field and generic freight locomotive (dimensions in the figure are given as full-scale and in meters).

The dimensions of the computational domain, boundary conditions and the generic freight locomotive used in parameterisation study are illustrated in Figure 4.8. The ground is set as a moving wall with the velocity set to be the same as train velocity (33.5 m/s), to simulate the relative movement between the train and ground. The boundaries at both sides and top planes of the open field around the train are set as a slip wall type, to avoid the formation of boundary layers which may influence the overall flow development at these boundaries [115]. The distance from velocity inlet/pressure outlet to the nose/tail of the freight train are set as 15/40 H respectively, to ensure the full development of the flow field. These distances are similar to that used in previous studies and as indicated in the Euronorm standards [151]

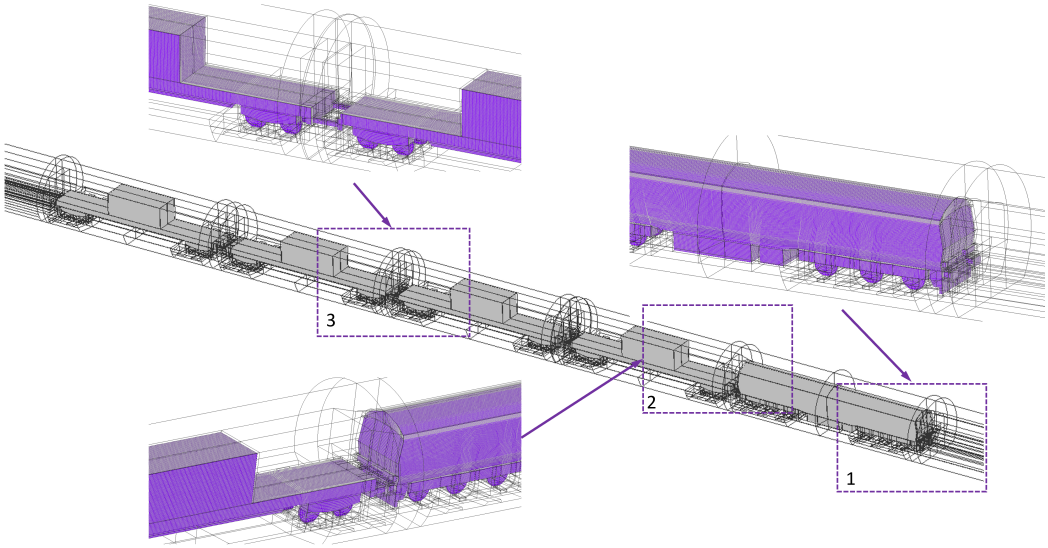


Figure 4.9: The blocking structure around the 33 % partially loaded freight train

4.3.4 Mesh

Since the prediction of the separation bubble is very sensitive to the mesh quality, and subsequently the numerical model chosen, the whole computational domain is divided by a structured mesh to increase the overall mesh quality [77, 115].The entire computational domain has been meticulously divided into hundreds of hexahedral block regions. In contrast to automatically generated meshes controlled by predefined parameters, the utilization of a manually crafted structured mesh allows for precise control over the quality of each element. This approach mitigates the occurrence of poor-quality meshes, particularly at sharp edges or areas with significant curvature changes. Remarkably, more than 99.5% of the mesh exhibits a skewness quality lower than 0.54. Moreover, mesh at the region that forms after the flow separates over the leading edges of the train head is refined further to resolve all motion down to the inertial subrange. Similarly for partially loaded freight train, the mesh at the unloaded gap is also refined. For the case of freight train with 4 33% loaded containers, the blocking structure and the mesh around the train are shown in Figure 4.9 and 4.10.

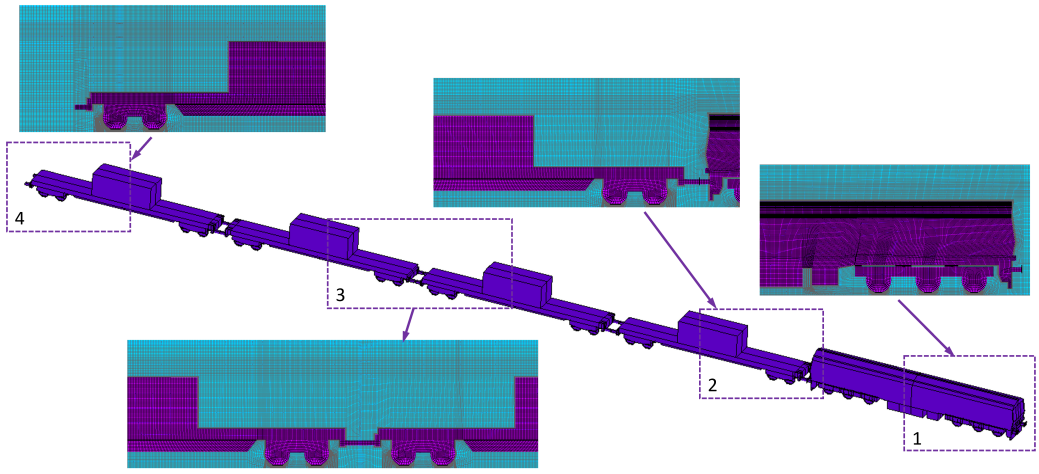


Figure 4.10: Mesh size and distribution around the 33 % partially loaded freight train

In order to better simulate the velocity distribution in the viscous flow region of the train, the first layer of the wall of the train surface (except the bogies) is estimated with $y^+ \approx 8$ ($y^+ = \Delta y/\lambda^+$), with 17 prism layers and a total thickness of around 4 mm. According to previous research, the cell size adjacent to the wall in the spanwise and streamwise direction are $\Delta s \approx 50\lambda^+$ and $\Delta x \approx 100\lambda^+$ [116, 79]. Figure 4.11(b) illustrates the instantaneous wall y^+ on the locomotive's surface. Notably, y^+ on the train surface (excluding the bogies) remains below approximately 5 [152, 79, 153], placing it within the viscous sub-layer of the boundary. This positioning ensures accurate velocity computation within the boundary layer. To further confirm the adequacy of mesh resolution, a thorough validation has been conducted. In Chapter 4.3.6, the velocity and TKE profiles surrounding the separation region are cross-validated using a finer mesh. Additionally, the pressure distribution on the train surface has been validated against experimental results in Chapter 4.3.6.

4.3.5 Solver Set Up

The bounded central differencing scheme is used for the discretization of the convection terms to ensure the accuracy and stability of the simulation. The rest of the solver set up are kept the same as that used in Section 4.2.5.

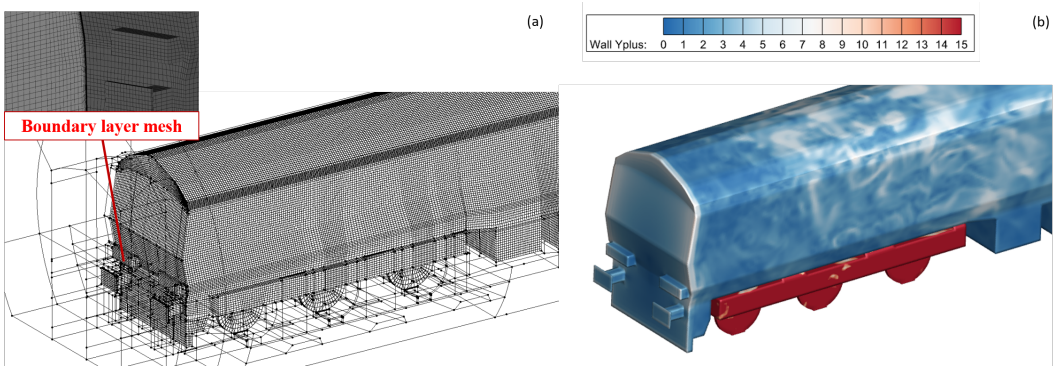


Figure 4.11: Mesh size and distribution (a)The blocking structure around the train head and mesh on train surface (b) instantaneous wall Y^+)

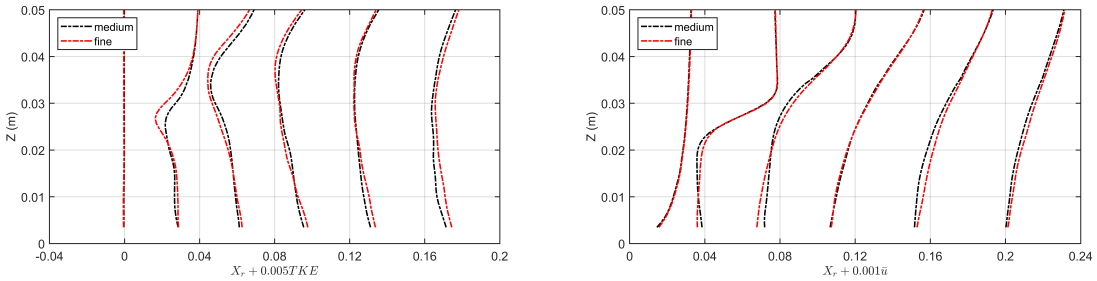
4.3.6 Model Validation

Mesh Sensitivity

To ensure the grid size is capable of providing a sufficiently fine spatial resolution, especially in areas where the separation bubble forms, a mesh independence validation is conducted by comparing the velocity profile above the train roof with a finer mesh. For the finer mesh, the first layer of the wall is refined to $y^+ \approx 5$ with 25 prism layers. Similarly, the mesh on the train surface is refined to $\Delta s \approx 50\lambda^+$ and $\Delta x \approx 80\lambda^+$. The total cell count of the medium and fine meshes are 29 million and 36 million respectively. Figure 4.12 shows a comparison of the performance of fine and medium mesh sizes in predicting the flow field using turbulence kinetic energy (TKE) and mean velocity profile. Specifically, TKE is calculated using $0.5 \times (u'^2 + v'^2 + w'^2)$, which is used to evaluate the accuracy in predicting turbulence properties between the two mesh sizes. To provide a comprehensive analysis, data was extracted from six vertical lines located above the train roof. The x-axis values in Figure 4.12(a) and (b) are obtained using the following functions: $x = x_r + 0.005 \times TKE$ and $x = x_r + 0.001 \times \bar{u}$, where x_r represents the distance from the vertical line to the leading edge, and the Z axis represents the distance to the train roof. The six vertical lines are positioned at x_r values of 0/0.04/0.08/0.12/0.16/0.2 m, respectively.

Figure 4.12(a) reveals that the medium mesh size slightly under predicts turbulence generation at $x_r = 0.04\ m$, but the TKE data from the medium mesh size generally agree with those obtained from the fine mesh at these locations above the roof. The mean velocity profile

presented in Figure 4.12(b) displays minor discrepancies in the recirculation velocity within the separation bubble between the fine and medium mesh models, which yields a maximum difference less than 3 % at $x_r = 0.08\,m$. Overall, both mesh yield identical predictions regarding the position of the boundary layer (where $\bar{u} = 0.99 \times u_{train}$) and the size (height and length) of the recirculation region, which are the parameters of interest in this paper. Therefore, the medium mesh size is adopted in this paper to complete the parameterisation study. To further confirm the adequacy of the mesh resolution and the turbulence model utilised in this study, the pressure coefficients obtained from the medium mesh are compared with the experimental results for measuring points on the train surface in Section 4.3.6.



(a) (b)

Figure 4.12: Comparison between the medium and fine mesh on train roof (a) TKE (b) time-averaged velocity profile.

Compare Pressure with Experimental Result

To validate the numerical settings and mesh resolution adopted for LES simulations, experimental results of surface pressure located at a set of measurement points along the roof and side of the locomotive are used to compare with the numerical results. Experimental data is obtained from the moving model experiments presented in [21]. The data is recorded by onboard data logger systems as the model train moves down the track. The data is then time averaged for each measurement location, in the measuring section before the train enters the tunnel [21]. The position of the measuring points (P2 ~ P11 and L1~L2) used for validation is illustrated in Figure 4.4(a) and the comparison of results is shown in Figure 4.13. The X-axis is non-dimensioned by L, as per the previous definition. The pressure from the leading edge of the

train head to around 0.3 ~ 0.4 L is negative, indicating the separated flow region around the train nose. Measuring points P2 and P7 are located just after the leading edge separation, P3 and P8 are inside the separation region, and P4 and P9 are close to where the flow reattaches to the train body. Results show that the pressure distribution along L1 and L2 (lines located at the roof and side of the train) extracted from the LES simulation fit well with the experimental data at these points, with a percentage error below 5%. A similar conclusion can be observed at P5 ~ P6, P10 ~ P11 located out of the separation bubble region. Therefore, it is concluded that the simulation settings and mesh resolution adopted in the LES numerical simulations can accurately calculate the flow field information and separation region of the area of interest around the train.

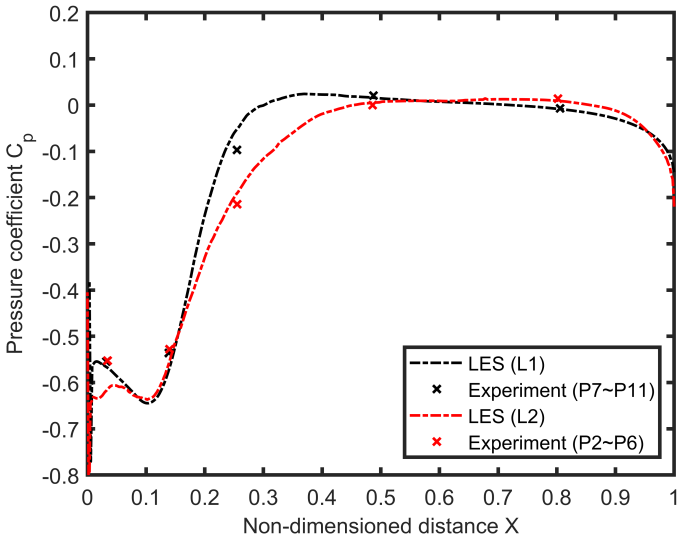


Figure 4.13: Comparison of pressure distribution on train surface between LES and Experimental results

4.4 Summary of Numerical Cases

Given the different numerical approaches adopted for the various modelling and parameterisation studies conducted in this research, in order to facilitate comparison between cases considered, Tables 4.1 and 4.2 have been constructed as a point of reference for numerical simulations in the results and discussion, regarding to the investigation of head shapes and loading configurations separately. The operating conditions, as shown in Table 4.1, including tunnel/open-field

simulations and the corresponding boundary conditions, are consistent with those depicted in Figures 4.2 and 4.8, respectively. All cases throughout this research have been conducted for a train speed of 33.5 m/s, corresponding to a Mach number of approximately 0.1, with all geometries scaled to 1/25th reduced-scale. The Reynolds number calculated using the feature length H, as defined earlier, results in an approximate value of 3.82×10^5 across all cases. Additionally, to minimise variations attributable to meshing, a consistent blocking strategy and mesh size have been utilised for each train type and head shapes to the greatest extent possible.

Case 1 and 2 are the reference cases. To be more specific, case 2 is used to propose the separation bubble model and generate the parameters required by the 1d numerical method. The proposed model is then fed into Case 1 to test the modified 1d numerical model. Cases 3 to 8 are proposed to analyze the influence of head bluffness on flow field and to parameterise the relationship of leading separation angles and the height of length of separation bubble. Similarly, Cases 9 to 12 are to analyze the influence of tunnel cross-sectional area on flow field and to parameterise the relationship of blockage ratio and the effective cross sectional area of separation bubble. Finally, to validate the applicability of the parameterisation equations and the proposed separation bubble model, two sets of validation cases were conducted. The results obtained from the modified 1d method (Cases 13 and 15) are compared with the results obtained from the 3d simulations (Cases 14 and 16). Case 17 to 19 serve as the references cases for investigating various loading configurations. They evaluate the effectiveness of LES and URANS models in simulating the pressure wave generated when partially loaded containers enter a tunnel. These results form the basis is used for constructing the physical model in the 1d program and validating the outcomes of the modified 1d code. Subsequently, Cases 20 to 23 focus on a parameterization study of loading configurations. This involves analysing how the unloaded gap impacts the effective cross-sectional area within the gap and the size of the separation bubble formed at the leading edge of the trailing container. The insights gained from this parameterization study are then incorporated into the 1d program (Case 24) to simulate the pressure wave generated when a freight train entering a tunnel, where the first carriage is fully empty.

Case	Geometry		Operating Condition	Numerical Model	Description
	Train	Tunnel			
1	Class 66 with 4 containers	45 m^2	Tunnel	1d model	Reference
2	Class 66 with 3 containers	45 m^2	Tunnel	URANS	Reference
3~8	Generic locomotive 0+0/15+0/15+15/30+0/30+15/30+30	/	Open Field	LES	Parameterisation on nose bluntness
9~12	Generic locomotive 20+20	30/45/ 60/75 m^2	Tunnel	URANS	Parameterisation on blockage ratio
13	30+10	45 m^2	Tunnel	1d model	Validation
14	30+10	45 m^2	Tunnel	RANS	Validation
15	Class 70 locomotive	65 m^2	Tunnel	1d model	Validation
16	Class 70 locomotive	65 m^2	Tunnel	URANS	Validation

Table 4.1: Summary of numerical cases for the investigation on locomotive head shape.

Case	Geometry		Operating Condition	Numerical Model	Description
	Train	Tunnel			
17	Class 66 with 4 33%$loaded$ containers	45 m^2	Tunnel	1d model	Reference
18~19	Class 66 with 4 33%$loaded$ containers	45 m^2	Tunnel	LES and URANS	Reference
20~23	Class 66 with 2 containers, with the first container fully loaded/20/40/60 foot gap	45 m^2	Inside tunnel (steady)	LES	Parameterisation on Loading configurations
24~25	Class 66 with 2 containers, with the first container unloaded and second container 20 foot gap	70 m^2	Tunnel	LES and 1d model	Validation on proposed model

Table 4.2: Summary of numerical cases for the investigation on loading configurations.

Chapter 5

Pressure Wave Induced by Blunt Train Nose

5.1 Introduction

This chapter conducts a comprehensive comparative analysis of the flow field acquired from both LES and URANS simulations. The effectiveness of the two models in accurately simulating the effects of a separation bubble on pressure wave patterns is evaluated. To establish a solid foundation, the validated methodology is adopted to conduct a reference case, allowing us to discern the intricate influence of freight locomotives on pressure wave change. Subsequent to this comparison, as delineated in Chapter 5.3, the modifications made to the boundary conditions at the train head and the equations to accommodate the changing effective cross-sectional area induced by flow separation at the bluff train head are illustrated. A separation bubble model built into our 1d numerical methodology is introduced based on the characteristics of the geometry and the separation region. Then an extensive parameterisation study is conducted, incorporating varying leading edge separation angles and tunnel cross-sectional areas. The proposed model and the associated parameterisation equations are subjected to validation through independent simulations. Class 70 locomotive is used, as elucidated in Chapter 5.7, ensuring the robustness and accuracy of our computational framework.

5.2 Comparison of RANS to LES results for the Separation Bubble Development

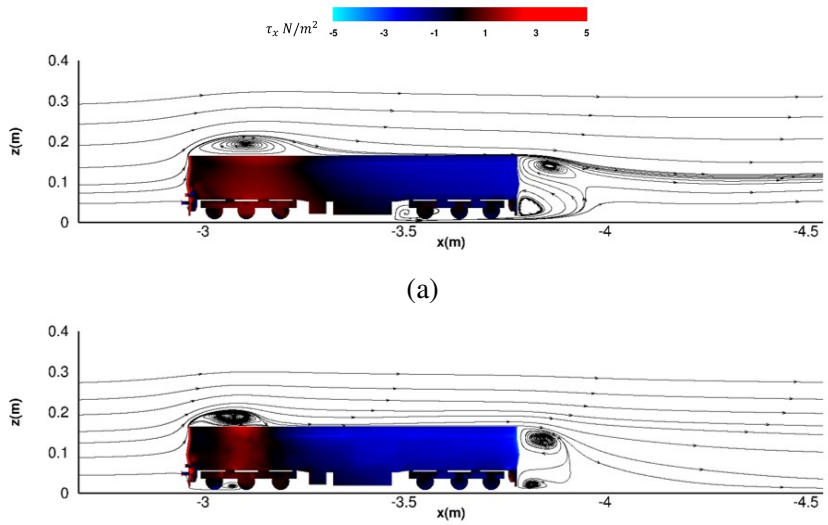
In this section both LES and SST $k-\omega$ RANS models are adopted to visualize the flow field, to enable an assessment of the capability of RANS to predict the development of the separation bubble. The SST $k-\omega$ model is chosen because it provides a better prediction of flow separation than most RANS models and also accounts for its good behaviour in adverse pressure gradients [143]. It has the ability to account for the transport of the principal shear stress in adverse pressure gradient boundary layers [154]. Given its high accuracy to computational cost ratio, it is very commonly used in simulations of train aerodynamics [155, 131, 156]. The pressure and velocity distribution predicted by LES and SST $k-\omega$ RANS models are compared in the following sections. The comparison considered results of train operating on open track and passing through a tunnel.

5.2.1 Open Track Considerations

The results obtained from LES and RANS simulations are shown in Figure 5.1, primarily indicating the streamlines to show the development of separation bubbles at the lead and trailing edges of the Class 66 locomotive. The streamlines in Figure 5.1(a) are calculated using mean u and w and the surface of the train is coloured by mean x-wall shear stress, which reflects the separation and reattachment points. It can be seen that the RANS simulation is capable of capturing the height of the separation bubble, but tends to overpredict the length of the bubble. A similar phenomenon appears on the prediction of boundary layer separation at the tail of the train. That being said, overall the SST $k-\omega$ RANS approach provides gives a reasonable prediction of the shape of the separation bubble when compared to the LES simulations. Therefore, considering that using the LES method to simulate the process of a train entering a tunnel requires extensive computing resources, the SST $k-\omega$ RANS model is adopted to simulate the freight train passing through a tunnel for this study. The results from the subsequent CFD simulations enable a development of knowledge which could be fed into the 1d code to verify

its validity for predicting the maximum pressure.

Although this approach works well for a single locomotive type entering a tunnel, it becomes very complicated and computationally expensive when considered in the frame of a parameterisation study to consider a wide variety of train types and shapes. To combat this, the approach adopted for the parameterisation study of the separation bubble and loading configurations is to simulate these conditions in the open track and apply a squeezing function (5.4.3) based on the tunnel geometry. These simulations in the open track require much less computational resource, but an greater accuracy of the separation bubble shape and size is required to support the parameterisation study. Therefore LES methodology is used for the parameterisation study to provide a more accurate observation and analysis of the separation region.



(a)

(b)

Figure 5.1: Comparison of the separation bubble at top of the freight train predicted by RANS and LES (a) RANS (b) LES

5.2.2 Tunnel

In order to show the difference of the separation bubble size inside tunnel predicted between URANS and LES model more clearly, the results obtained from both models are compared in the same Figure As shown in Figure 5.2, the velocity contour (effectively the coloured background) is calculated from LES numerical model, whereas the streamline is calculated from URANS.

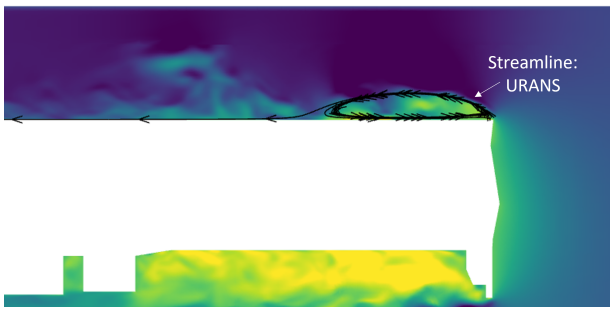


Figure 5.2: Velocity contour obtained from LES simulation and streamline obtained from URANS simulation when a freight train enters a tunnel

The results is plotted at the moment after the train head enters the tunnel. It can be seen that there is very little difference on the prediction of bubble height between the two models, giving good confidence in the URANS methodology for this application. Both the height and length of the separation region predicted from URANS model are well fitted with LES model. The fluctuating quantities are averaged using the URANS model, which enables clear identification of the separation bubble shape at different moments when the train enters a tunnel. However, if using LES method, the transient flow field around the train head at every moment is highly turbulent and contains unsteady coherent structures when a train enters a tunnel, as shown in Figure 5.2. As a result, for this case, a clear separation bubble shape cannot be identified using LES. Additionally, the k-ω SST RANS models have been demonstrated to effectively predict the impact of separation bubbles on pressure waves when compared to experimental results. The precision of the separation bubble size obtained from URANS is sufficient to support the development of the 1d code. Thus, in order to feed the empirical parameters into the 1d code, URANS model was applied for working conditions of train entering a tunnel.

5.3 Modification of the One Dimensional Code

The differences in solving the flow field at the train head caused by considering the separation bubble are presented in this section and a novel methodology illustrated to enable consideration of bluff freight train shapes. Figure 5.3 illustrates the modified boundary condition at train head

at the region as it just enters a tunnel. Similar to the boundary condition at train head illustrated in section 3.5.2, there are six Riemann variables that need to be solved for flow from 1 (tunnel) to 2 (annulus), in which λ_1' and A_A' can be interpolated and calculated from the previous time step. The rest of the other four unknown variables are marked red in the Figure Since the separation bubble only influences the flow model in the annulus between train and tunnel, the continuity, momentum equation and the thermodynamic relationship equation for the quasi-steady flow from duct 1 to duct 2 are the same as the traditional equations (3.30 ~ 3.32). For the flow from 2 (head of the train inside annulus) to 3 (tunnel entrance), equation 5.1 is introduced and derived from the continuity and momentum equation of the flow from 2 to 3, as shown in Equations 5.2~5.3. At this point we assume that the distance l is sufficiently small such that the density is uniform over the element ($\rho_2 = \rho_3$).

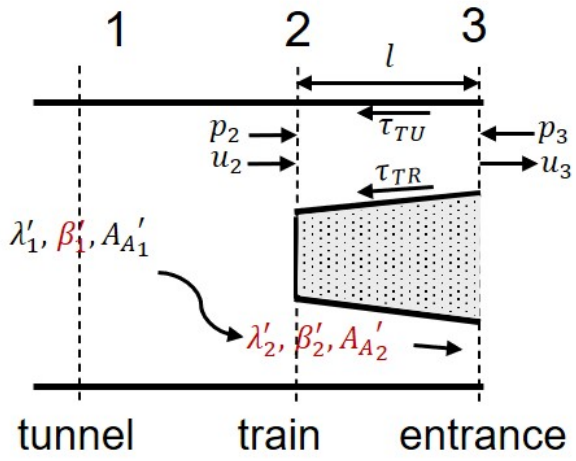


Figure 5.3: Boundary condition when train nose enters a tunnel (variables marked in red are the unknowns that need to be solved)

$$\left(\frac{\lambda_2' + \beta_2'}{2A_{A_2}}\right)^{\frac{2\kappa}{\kappa-1}} = \frac{1}{p_R}\left\{\frac{p_3}{\phi} + \rho_3 c_R^2(\phi-1)\left(\frac{\lambda_2' - \beta_2'}{\kappa-1} + \frac{V}{c_R}\right)^2 + \frac{\rho_3 l c_R^2}{2E_2}\left[\frac{f_{tu}S_{tu}}{4}\left[(\phi+1)\left(\frac{\lambda_2' - \beta_2'}{\kappa-1} + \frac{V}{c_R}\right)\right]^2 + \frac{f_{tr}S_{tr}}{4}\left[(\phi+1)\left(\frac{\lambda_2' - \beta_2'}{\kappa-1}\right)\right]^2\right]\right\} \tag{5.1}$$

$$\rho_2 E_2 u_2 = \rho_3 E_3 u_3 \tag{5.2}$$

$$p_2E_2 + \rho_2E_2u_2^2 = p_3E_3 + \rho_3E_3u_3^2 + 0.5\rho_3 l\left[f_{tu}\bar{u}^2S_{tu} + f_{tr}\left(\bar{u} - V_{tr}\right)^2 S_{tr}\right] \tag{5.3}$$

5.4 Reference Case

5.4.1 Traditional 1d Code

Firstly, the pressure change induced by a Class 66 locomotive with eight fully loaded flatbed containers entering a tunnel is predicted using the traditional 1d method without considering the separation bubble model. Here we will be considering measuring locations at 2 m and 8 m inside the tunnel. The parameters (pressure loss coefficients, cross-sectional area, etc) of Class 66 locomotive and the tunnel that used in the 1d code are summarised in Table 3.1 and Table 3.2. The result is then compared with experimental data as measured by Iliadis et al. [21] as shown in Figure 5.4.

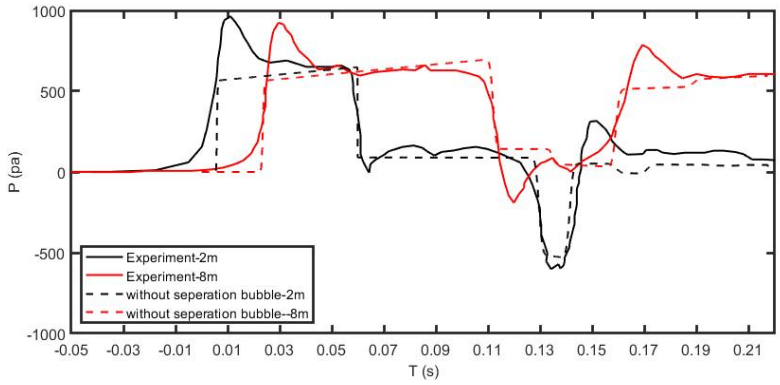


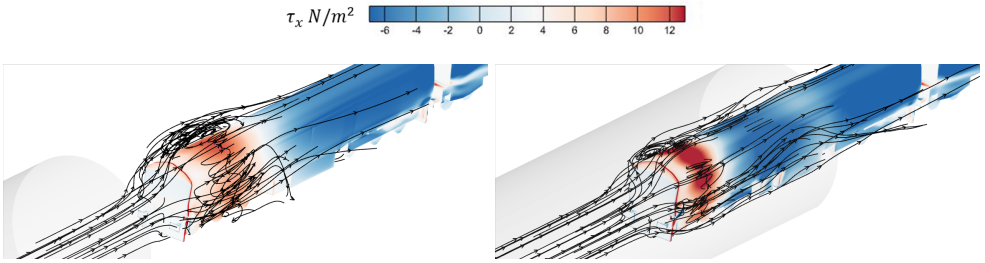
Figure 5.4: Comparison of pressure history curve obtained from the traditional 1d result and experiment.

It can be seen that the traditional 1d method is able to roughly predict the trend of pressure change induced by the pressure waves and friction effect. However, as expected, a large discrepancy occurs for the magnitude and shape of the initial pressure rise and the subsequent pressure change when reflected pressure waves pass by the measuring points, due to fact that the effective area including the separated flow at the blunt locomotive is not considered. The maximum pressure rise calculated by the traditional 1d method is about 563 pa, resulting in an error of 43% compared to that obtained from the experiment. Clearly without considering the

separation bubble, it failed to predict the maximum pressure. To understand the development of the separation zone at the nose of the Class 66 locomotive, and the influence this has on the pressure wave formation in the tunnel, a 3d simulation was undertaken to visualize the flow field at the blunt train nose.

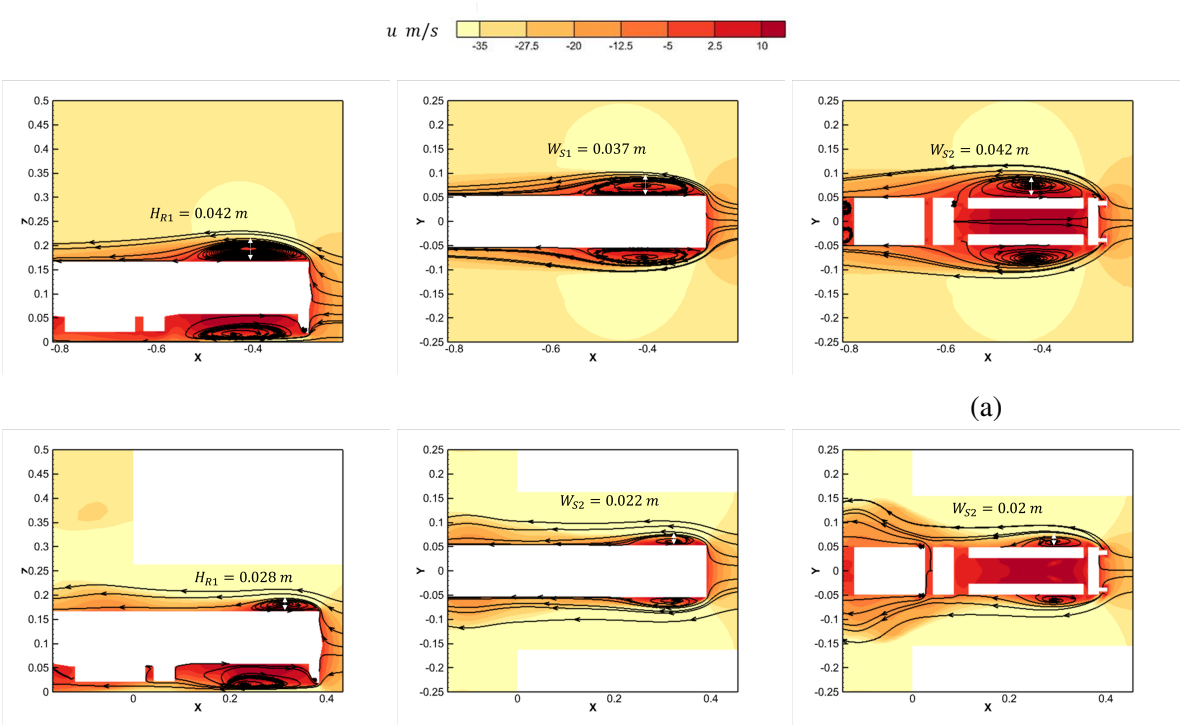
5.4.2 Wall Shear Stress and Flow Field for the Class 66 Locomotive Entering a Tunnel

To understand the development of the separation zone at the nose of the Class 66 locomotive, and the influence this has on the pressure wave formation in the tunnel, a 3d simulation was undertaken to visualise the flow field at the blunt train nose. The streamlines around the nose of the locomotive are plotted to visualize the development and changing of the separation region as shown in Figure 5.5 and 5.6. The velocities used to plot the streamline visualisation are stationary relative to the train. Velocity contours at the top ($y = 0\ m$), side ($z = 0.1\ m$) and bottom ($z = 0.05\ m$) of the train are analysed to obtain the bubble size that is developed at the blunt locomotive nose. It can be seen that part of the flow in the separation bubble is blocked by the tunnel entrance as the head entering tunnel. It not only significantly decreases the bubble size (height), but also decreases the effective length influenced by separation bubble. The bubble size before and after the train nose enters into the tunnel are measured as shown in Figure 5.6. These dimensions can be fed into the development of a separation bubble model. It can be seen that the vortices' size at these positions are significantly squeezed and reduced to different extents. Specifically, the roof and windshield regions experienced a reduction of 33.3% and 40.5% respectively, while the bogie region had a larger reduction percentage of 52%. As the position approaches the ground, a larger portion of the airflow's motion inside the separation bubble is blocked at the tunnel entrance due to the floor as well as the tunnel wall which is closer to the train due to the tunnel shape considered, resulting in a more prominent reduction in the bubble size after it enters the tunnel.



(a) (b)

Figure 5.5: Flow field around Class 66 locomotive (a) before entering the tunnel (b) after entering the tunnel.



(a)

(b)

Figure 5.6: Separation bubble size at top, side and bottom of the train nose (a) before entering the tunnel (b) after entering the tunnel.

5.4.3 Implementation of the Parameters into the Modified 1d Code

The results obtained from these simulations are then used to develop a description for the shape of the separation bubble in the 1d code. A simplified model is built, as shown in Figure 5.7, to calculate and parameterise the maximum effective blockage area. The separation region at the roof/windshield/coupling are simplified as half circle/rectangular/rectangular, as shaded by

blue, green and gray region in the Figure. To get the input parameters used to calculate the area of each region, $\overline{H_R}$, $\overline{W_S}$, $\overline{W_B}$ are estimated by averaging the bubble width (H_R, W_S, W_B) inside tunnel obtained from the simulation. Thus the maximum effective blockage area E_{max} can be calculated by adding these parameters together. The train radius, r_t, is determined from the equation $E_{tr} = \pi {r_t}^2$, where E_{tr} represents the cross-sectional area of the train obtained from the train geometry model. Consequently, the equivalent separation bubble radius, r_b, can be derived from $E_{max} = \pi(r_t + r_b)^2$.

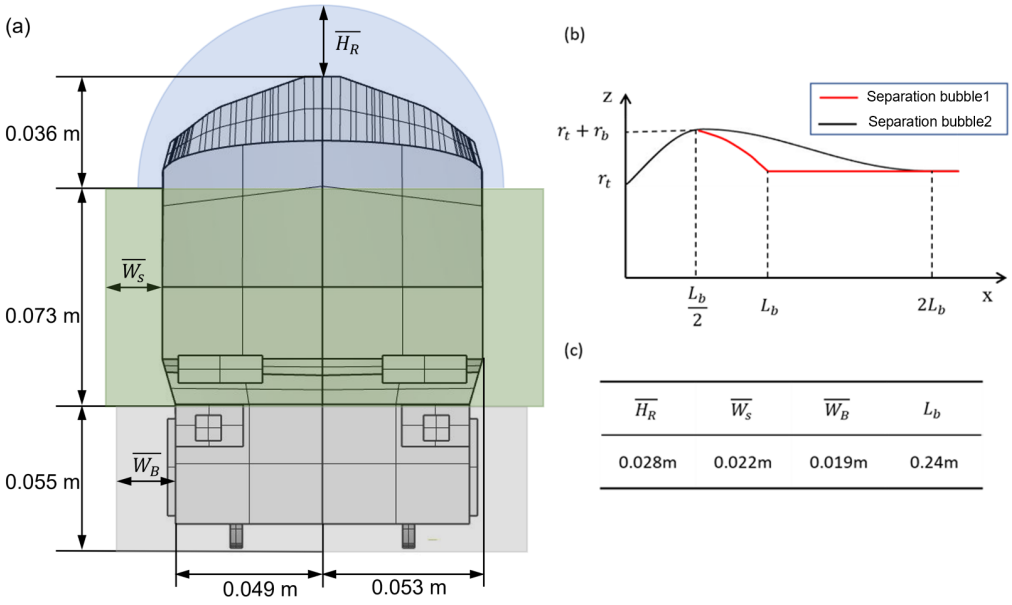


Figure 5.7: Separation bubble model at the head of loco 66 (a) effective blockage area (b) effective bubble length (c) parameters of the size of the separation bubble adopted in the code.

The shape of the bubble in the streamwise direction is described as a sine function or a combination of two sine functions, as illustrated in Figure 5.7(b). The choice of this approach was based on a best fit study whereby a sine function was shown to provide the best and most consistent fit. L_b is the bubble length around the nose averaged from the simulation, and the maximum effective cross-sectional area is set as $x = L_b/2$. The separation bubble length L_b is estimated by the distance from the leading edge of the train head to the point where the wall shear stress reaches zero. The real length of the separation bubble recovered from E_{max} to E_{train} is around $L_b/2$, labelled as separation bubble1. However, considering the suppression on

the separation bubble caused by the tunnel entrance, the recovering length when freight train enters the tunnel is longer than the real length of the separation bubble. Therefore the shape of separation bubble2 uses a recovering length of $3L_b/2$, which makes the total effective bubble length of $2L_b$. The parameters of the size of the separation bubble are given in the table in Figure 5.7. Other parameters of the locomotive and tunnel are the same as those presented in Table 3.1 and Table 3.2. Furthermore, from the dimensions of side view of the freight train given in Figure 4.1, the cross sectional area of a fully loaded container is smaller than the locomotive. Therefore a smaller effective area, $E_{con} = 9.5\,\mathrm{m}^2$, is adopted for the containers.

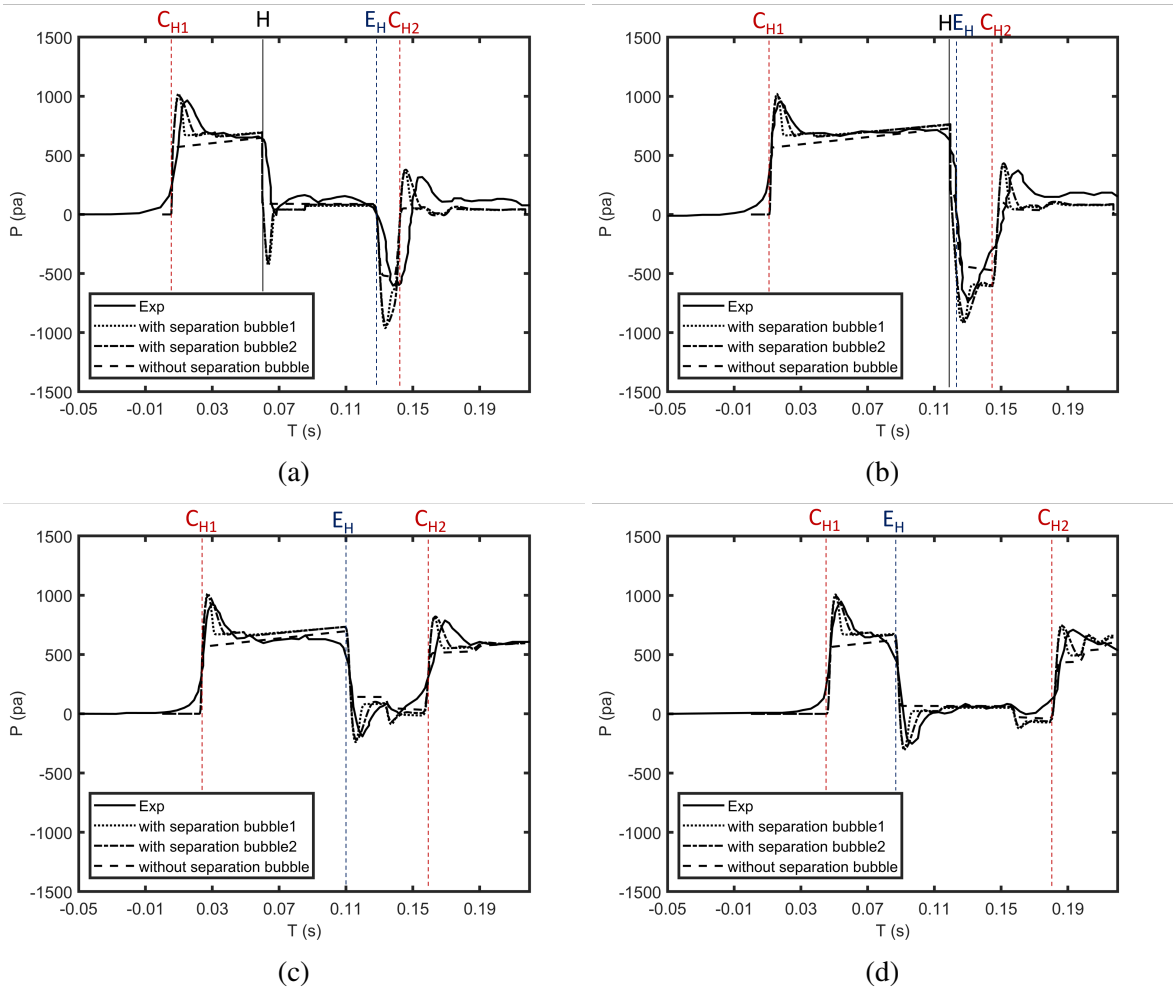


Figure 5.8: Comparison of pressure history curve obtained from 1d result and experiment (measuring points at (a) 2m (b) 4m (c) 8m (d) 16m to tunnel portal) (CH1: the first compression wave induced by the train head entering the tunnel; EH: Expansion wave when CH1 reflected back from the tunnel exit; CH2: the second compression wave when EH1 reflected from the tunnel entrance; H: the head of the train).

Now the 1d code is adapted to consider the influence of the separation bubble, the code is rerun as per the earlier configuration to consider the pressure variation at different measuring points inside the tunnel at 2 m/4 m/8 m/16 m to tunnel portal. The results are again compared with the experimental results presented in [21] for a 1:25 reduced-scale freight train with eight fully loaded flatbed wagons entering the tunnel as shown in Figure 5.8. The red/blue dashed vertical line represent the pressure change caused by compression/expansion wave generated by freight train nose entering the tunnel and the reflected component when pressure wave reaches tunnel portals. Black vertical lines represent the head of the locomotive passing the measuring positions. It can be seen through considering the influence of the separation bubble, the error of the maximum initial pressure rise is reduced to 4%, less than the 43% previously observed. Furthermore, the subsequent pressure change caused by the reflected pressure wave from tunnel exit is also well predicted. The pressure drop when the head passes the measuring point at 2 m is slightly overpredicted by the 1d code. This is due to the big difference in pressure variation over the separation bubble caused by the strong 3-dimensional effect of the flow separation at the train nose as it passes the measuring point and at the same time very close to tunnel entrance, which is not able to be reflected in a 1d code. When the measuring location is positioned further into the tunnel, for example 4 m after the tunnel entrance, the difference between the experiment and 1d code on predicting the pressure drop caused by train head is greatly reduced.

5.5 Parameterisation Study on Nose Bluntness

From the results obtained in Chapter 5.4, it can be seen that the prediction of maximum pressure rise for a blunt train shape can be greatly improved by implementing the size of separation bubble in the 1d code. Now, clearly so far this approach has been developed for a particular train type, in this case the Class 66 locomotive, which is quite restrictive in terms of being able to model a wide variety of freight rolling stock. Therefore to improve the 1d code and offer applicability to various types of freight trains, a parameterisation study of the separation bubble is conducted by investigating the effect of the bluffness of the locomotive on the size, shape and development

of the nose separation bubble. It is acknowledged that this approach is initially computationally expensive; however, the ability to accurately numerically model pressure waves through a 1d code will enable a wider range of train types and tunnel configurations to be examined. As discussed in Chapter 4.3.2, the summary of different shapes of freight locomotive heads can be divided into three parts: roof, windshield, and coupling region, in line with standards on train design and gauging. A wide variety of simulations and analysis was then conducted to investigate the influence of characteristic angles connecting each part on the height and width of the separation bubble. The geometry used for parameterisation study is given in Chapter 4.3.2.

5.5.1 Wall Shear Stress

Time-averaged trace lines and wall shear stress on the surface of different locomotives on the roof and side are presented in Figure 5.9 and Figure 5.10 respectively. These figures clearly show the difference in the direction of the flow and the position of the separation bubble caused by the change of bluffness. From the figures, it is possible to observe the bifurcation lines, where "the lines are drawn in the flow toward which the trajectories are asymptotic" [157] . More specifically, positive bifurcation lines (PBL: flow separate from the line) and negative bifurcation lines (NBL: flow goes into the line) indicate where flow is separated or is attached. The PBL and NBL for 30+15 case are depicted in Figure 5.9 and Figure 5.10(e) for the illustration of those lines. The length of the separation bubble is defined as the length from the leading edge to where the mean shear stress of x-direction equals to zero. The results are measured and summarised in Table 5.1. Subscript R1 and S1 represent the position at plane Y=0W and Z=0.6H separately.The X-axis represents the direction of the train's length, the Y-axis represents the direction of the width, and the Z-axis represents the direction of the height.The flow velocity is positive along the X-axis (from train tail to head). The lengths of the separation bubble on the roof (L_R) is non-dimensioned by the height of the train, similarly, the length of the separation bubble on the side (L_S) is non-dimensioned by the width of the train.

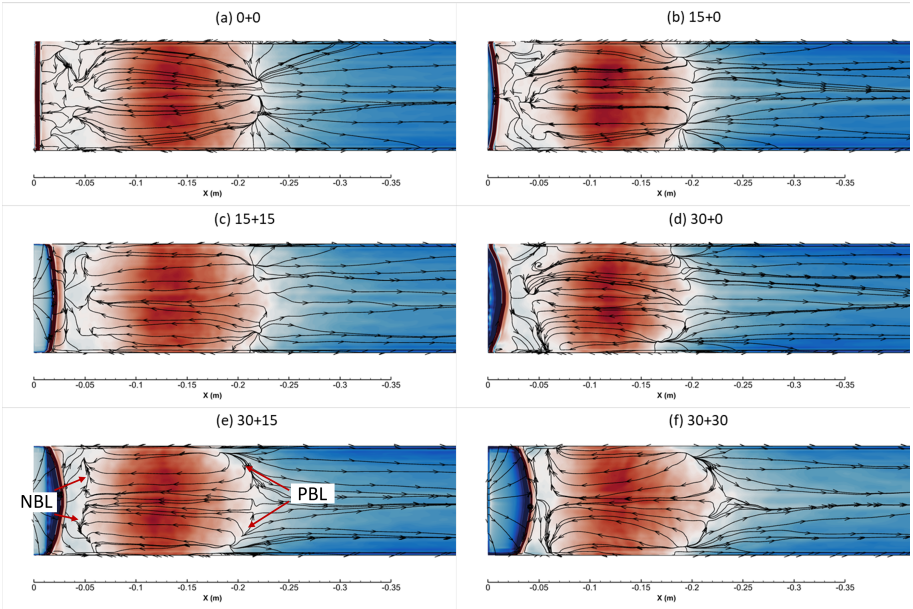


Figure 5.9: Top view of time-averaged trace lines on train body.

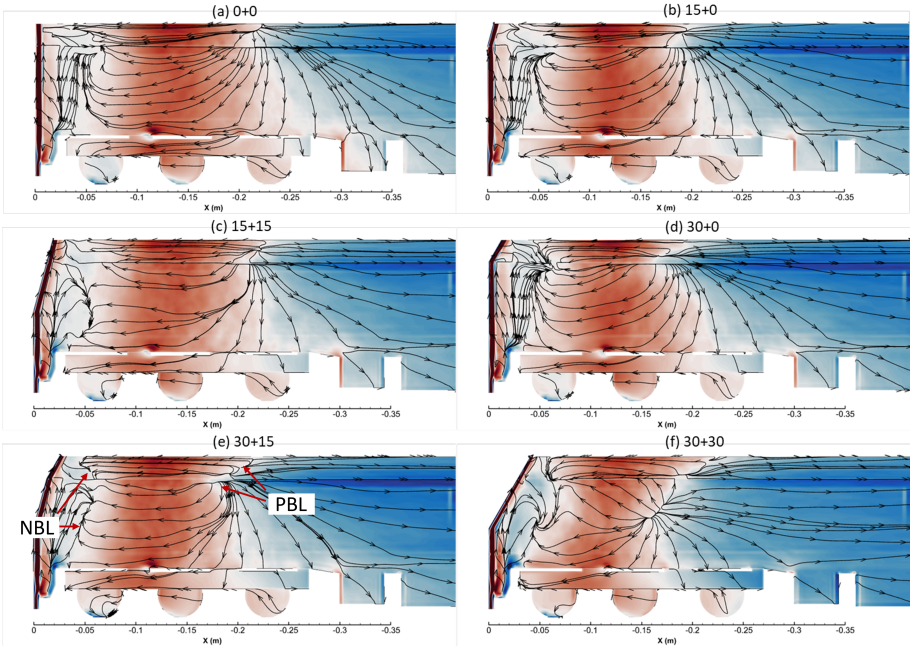


Figure 5.10: Side view of time-averaged trace lines on train body.

It can be seen from Figure 5.9 that the bluffness doesn't show much impact on the composition of the flow region on the train roof, but has a certain impact on the strength of the reverse flow and the length of the separation bubble. In general, as the air flows over the leading edge, it follows with a thin recirculation region, in which a distinct separation bubble region between PBL and NBL is formed, where wall shear stress shows as red in the figures. Comparing

Figure 5.9 (a)(b)(d) and (c)(e)(f), the recirculation region exhibits strong instability when the windshield region is perpendicular to the coming flow and is more uniform and stable when the sub-angle (β) increases. With the increase of the leading separation angle (α), the colour where the separation bubble exists is lighter, indicating a smaller reflow velocity close to the train surface and a weaker vortex strength. Besides, the unstable node (UN) moves sideward. From Table 5.1, it can be seen that in general, the length of the separation bubble on the roof (L_R) decreases as the leading edge angle (α) increases. However, it shows a trend of slightly increasing as the sub-angle (β) increases. This might be due to the longer slope accelerating the air before it reaches the leading separation edge. Further analysis regarding this will be conducted by extracting the velocity profile along the roof in Chapter 5.5.2.

From the side view of the time-averaged trace lines on the train body, a more obvious difference can be observed when the sub-angle (β) increases. As marked in Figure 5.10(c) that when β increases, the position of NBL changes from the top corner to the middle height of the locomotive. Unlike other cases, a more significant difference is that for the 30+30 case, in that the stable node transforms into a stable spiral at the front of the locomotive. Besides, the position of the node source, where the length of the side separation bubble is the shortest, moves from the upper corner to the middle height of the train as shown in Figure 5.10(f).

	0+0	15+0	15+15	30+0	30+15	30+30
L_{R1}/W	2.008	1.788	1.951	1.694	1.737	1.735
L_{S1}/W	1.782	1.521	1.632	1.483	1.381	1.035

Table 5.1: The length of separation bubble at train roof and side.

5.5.2 Velocity Field

The time-averaged streamlines at the front of the locomotive with different bluffness are compared on four planes (Y=0, Y=0.4W, Z=0.6H, Z=0.9H) to visualize the distribution of the separation bubble, as shown in Figures. 5.11~5.14, in which W and H are the width and height of the train. The flow field is coloured by mean velocity in the longitudinal x-direction. The

region coloured in red is where the speed is positive, indicating a backflow region or a separation region.

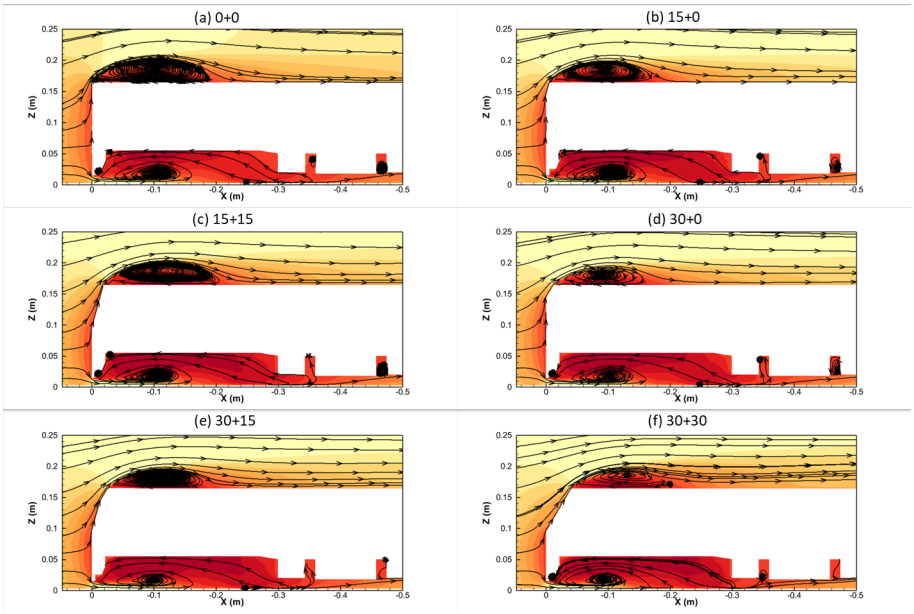


Figure 5.11: Time-averaged streamline at plane Y=0.

The height of the separation bubble in the middle at the top of the train is larger than that on the Y= 0.4W plane. Similarly, except for the 30+30 case, the width of the vortex on the middle height of the train is larger than that on the Z=0.9H plane (near the corner). This phenomenon is consistent with the previous result of the trace lines on the train body that except for the 30+30 case, the shortest vortex length is at the upper corner of the train. To quantitatively compare the difference among different bluffness and get the relationship between the bubble size and angles, the results of the bubble size are measured from the figures and summarised in Table 5.2. Subscript R1, R2, S1,S2 represent the position at plane Y=0, Y=0.4W, and Z=0.6H, Z=0.9H separately. The sizes of the separation bubble are non-dimensionaled by the width of the train.

Among all cases, the separation bubble generated by case 1 is the largest at all the planes investigated. The height of the vortex at the top and side of the locomotive decreases when the leading separation angle α increases. Comparing the size of the separation bubble on the middle of the roof (H_{R1}) under cases 2, 3, and cases 4, 5, and 6, it can be seen that H_{R1} is not sensitive to sub-angle β. However, H_{S1}, which is the width of the bubble at around the mid-height plane Z=0.6H, significantly decreases with the increase of sub-angle β. This trend is the opposite for

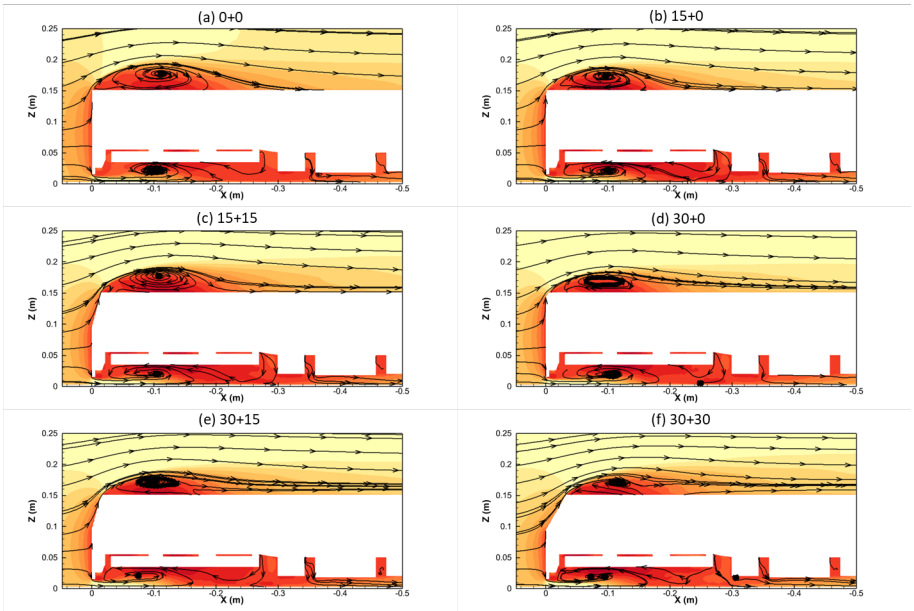


Figure 5.12: Time-averaged streamline at plane Y=0.4W.

H_{S2} at plane Z=0.9H, which is the upper corner of the locomotive. This might be related to the source point on the train roof moving sidewards when increasing sub-angle β (as shown in Figure 5.9).

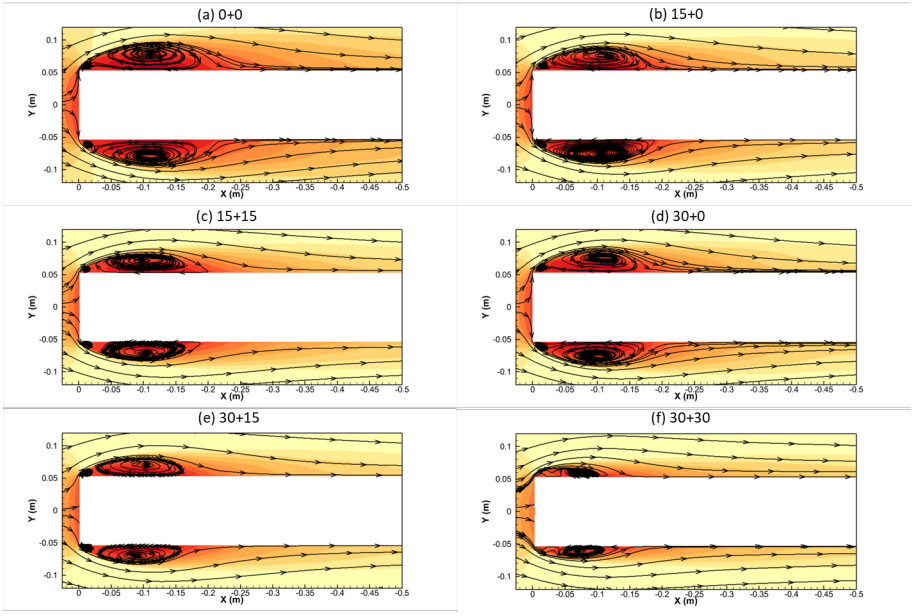


Figure 5.13: Time-averaged streamline at plane Z=0.6H.

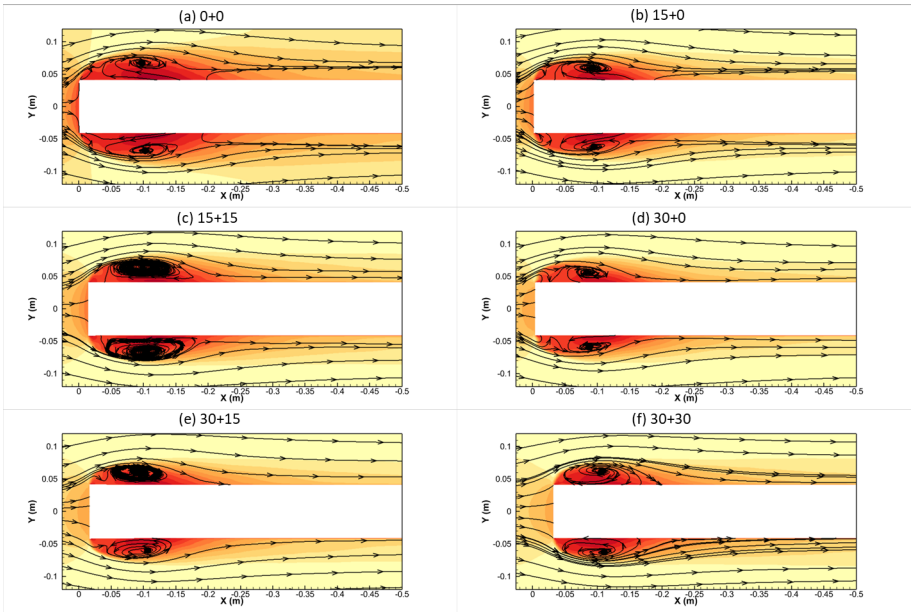


Figure 5.14: Time-averaged streamline at plane Z=0.9H.

$\alpha+\beta$	0+0	15+0	15+15	30+0	30+15	30+30
H_{R1}/W	0.406	0.331	0.350	0.285	0.294	0.275
H_{R2}/W	0.257	0.219	0.238	0.145	0.154	0.135
W_{R1}/W	0.429	0.382	0.336	0.359	0.299	0.196
W_{R2}/W	0.280	0.196	0.280	0.149	0.215	0.243

Table 5.2: The size of the separation bubble of 6 train bluffness at different planes.

In order to further analyze how the angles influence the flow and the formation of the separation bubble, the mean velocity distribution along a set of vertical lines above the roof are compared in Figure 5.15. It can be seen that changing the bluffness of the head mainly influences the velocity at 0.04 m to the leading edge, where the flow has just separated. Figure 5.15(a) shows that increasing α can significantly decrease the height of the recirculation area, but increases the recirculation velocity. A similar conclusion can be deducted from Figure 5.15(c) when β and α increases at the same time. Increasing β will increase the recirculation velocity and at the same time slightly increase the height of the separation region close to the leading edge. This might be due to the acceleration of the airflow caused by the longer slope at train head.

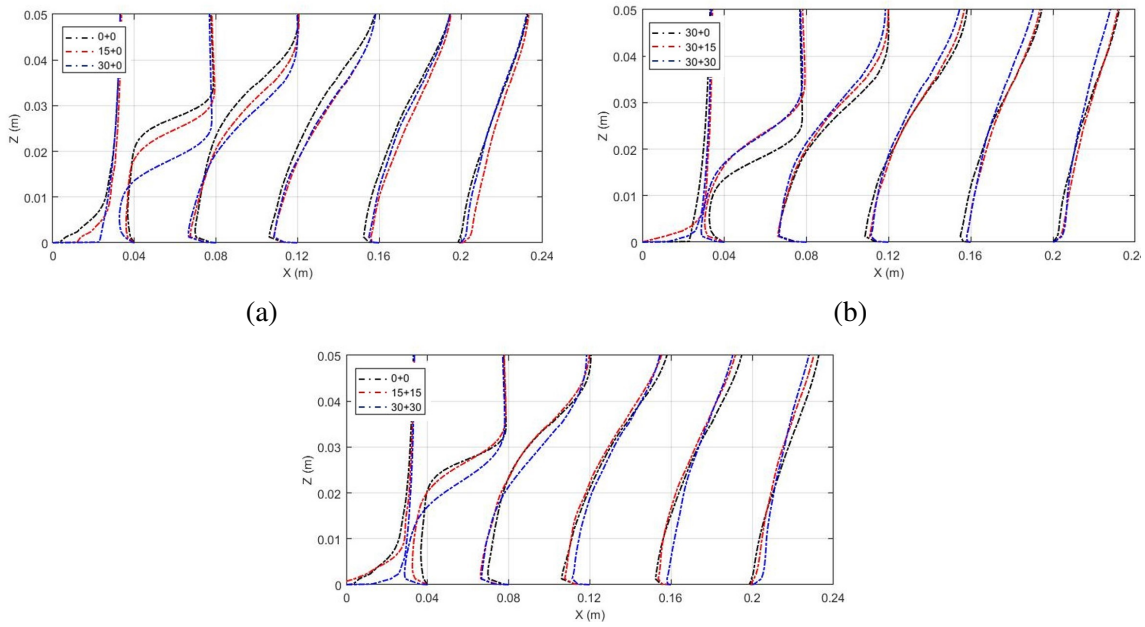


Figure 5.15: Time-averaged velocity profile above the train roof (a) influence of α (b) influence of β (c) influence of $\alpha + \beta$.

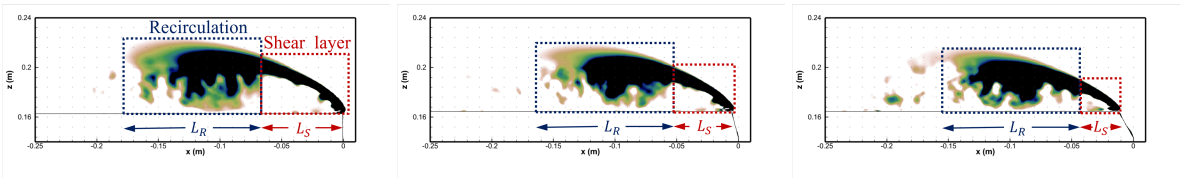
5.5.3 Vortex Structures

Previous literature has elucidated the physical phenomenon of the separation and reattachment of flow around bluff bodies [129]. Briefly, the flow initially separates from the upstream leading edges, leading to the formation of a separated shear layer (Region I). This separated layer subsequently undergoes roll-up, generating instantaneous vortex structures of varied sizes, resulting in a recirculation region (Region II) in mean flow visualisation. These regions are demarcated by red and blue dotted squares in Figure 5.16 and 5.17.

The time-averaged λ_2 [158] is calculated to identify the vortex structures on the top and side of the train. The Lambda-2 criterion involves analysing the second eigenvalue of the velocity gradient tensor, which reflects local rotation and stretching of fluid elements. The steps to calculate λ_2 is illustrated as follow. Firstly a velocity gradient tensor J is defined as,

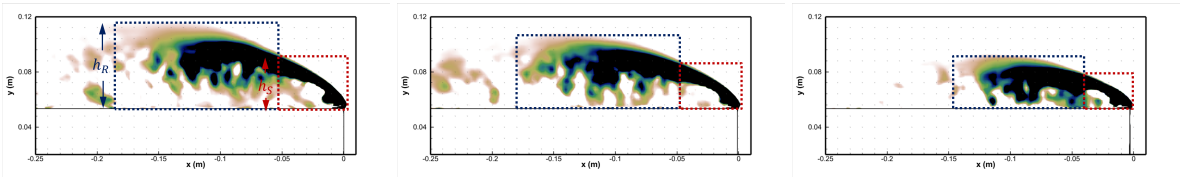
$$J \equiv \nabla u = \begin{pmatrix} \partial_x u_x & \partial_y u_x & \partial_z u_x \\ \partial_x u_y & \partial_y u_y & \partial_z u_y \\ \partial_x u_z & \partial_y u_z & \partial_z u_z \end{pmatrix} \tag{5.4}$$

The velocity gradient tensor is composed by the symmetric part $S = \frac{1}{2}(J + J^T)$ and the antisymmetric part $\Omega = \frac{1}{2}(J - J^T)$. The three eigenvalues of $S^2 + \Omega^2$ are calculated and ordered in a descending order, so that we have $\lambda_1 \geq \lambda_2 \geq \lambda_3$. Since a point in the velocity field can be identified as a vortex core only if at least two of the eigenvalues are negative, thus we have the Lambda-2 criterion is to find the region where the second eigenvalue λ_2 is negative and the magnitude of the velocity gradient tensor is large. Given that the results above have indicated that the vortex on the roof is more susceptible to changes in α, while the vortex on the side of the train is more sensitive to variations in β, comparisons for the former are made by varying α in Figure 5.16, whereas the latter is performed by varying β in Figure 5.17. As anticipated, the observed results demonstrate that the increase in α has a notable impact on reducing the length of the shear layer region (l_s) and the height of the recirculation region (l_h). More specifically, the l_s is observed to decrease from 0.07 m to 0.045/0.03 m when α increases from 0 to 15/30°. On the other hand, the impact of β on the vortices observed at the side of the train is found to be more significant. Upon increasing β, the dimensions of both regions, l_s, h_s, l_r, and h_r, experience a notable reduction as shown in Figure 5.17.



(a) (b) (c)

Figure 5.16: Mean λ_2 at the top of the train (a) 0+0 (b) 15+0 (c) 30+0.



(a) (b) (c)

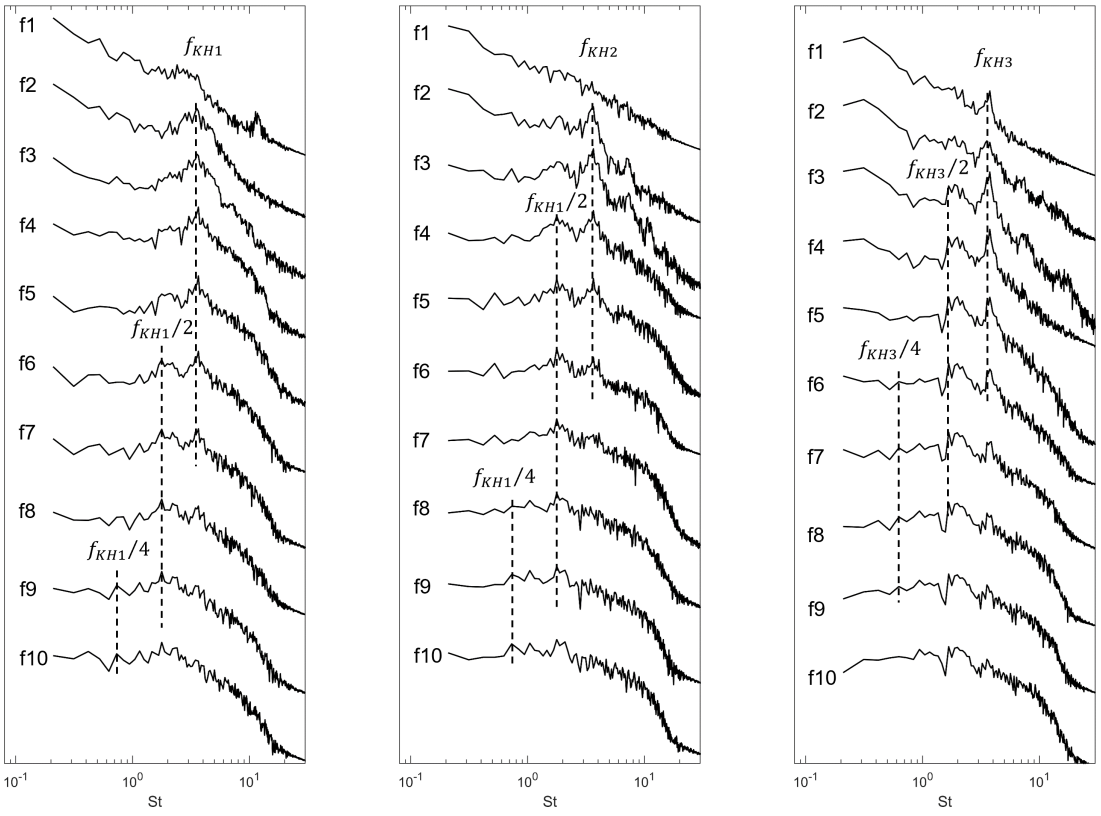
Figure 5.17: Mean λ_2 at the side of the train (a) 30+0 (b) 30+15 (c) 30+30.

Previous research has suggested that the vortex structures present on a train roof are sensitive to changes in the head bluffness, particularly variations in α. To further investigate the impact

of bluffness on vortex instability, a Fourier transform velocity frequency analysis was conducted on a set of points located just beyond the mean average shear layer edge. This methodology is proposed by Rocchio et al. [129] to analyse the Kelvin-Helmholtz instability onset. Specifically, measurements were taken at ten points along the x-axis (f1-f10 in Figure 5.18), with a spacing of 0.01 m between each point, covering a range from 0 to 0.09 m from the train head along the separated shear layer centreline. The amplitudes of the spectral density obtained from the Fourier transform were shifted linearly to allow for comparison among the set of measuring points, and to enable observation of the frequency changes associated with vortex evolution. The frequency are non-dimensionalised by W and train velocity $v_t r$, and expressed as Strouhal number $St = fW/V_{tr}$, which is the x-axis in Figure 5.18. As shown in the figure, the frequencies where the peak occurs changes from f_{KH} to $f_{KH}/2$ and $f_{KH}/4$ when measuring points moving from f1 to f10,indicating the pairing of vortical structures that originate from the roll up of the shear layer as the flow moves downstream. Here, f_{KH1}, f_{KH2} and f_{KH3} represent the Kelvin-Helmholtz frequency for α = 0, 15 and 30, respectively. Peaks for $f_{KH1}/f_{KH1}/2/f_{KH1}/4$ are found at measuring points f2-f7/f6-f9/f9-f10, corresponding to a distance to the leading edge in the range of [0.01,0.06]/[0.05,0.08]/[0.08,0.09]m. Similarly, peaks for $f_{KH3}/f_{KH3}/2/f_{KH3}/4$ are found at measuring points f1-f6/f3-f8/f6-f9, corresponding to a distance to the leading edge in the range of [0.0,0.05]/[0.02,0.07]/[0.05,0.08]m. These results indicate that the shear layer roll-up and form vortices earlier (closer to the leading separation edge) when α increases, which is consistent with the phenomenon observed in Figure 5.16. The magnitude of these Kelvin-Helmholtz frequencies does not exhibit a significant change with the alteration of α. Specifically, f_{KH1} and f_{KH3} slightly decreases from 3.54 and 3.34 when α increases from 0 to 30°.

5.6 Influence of Blockage Ratio

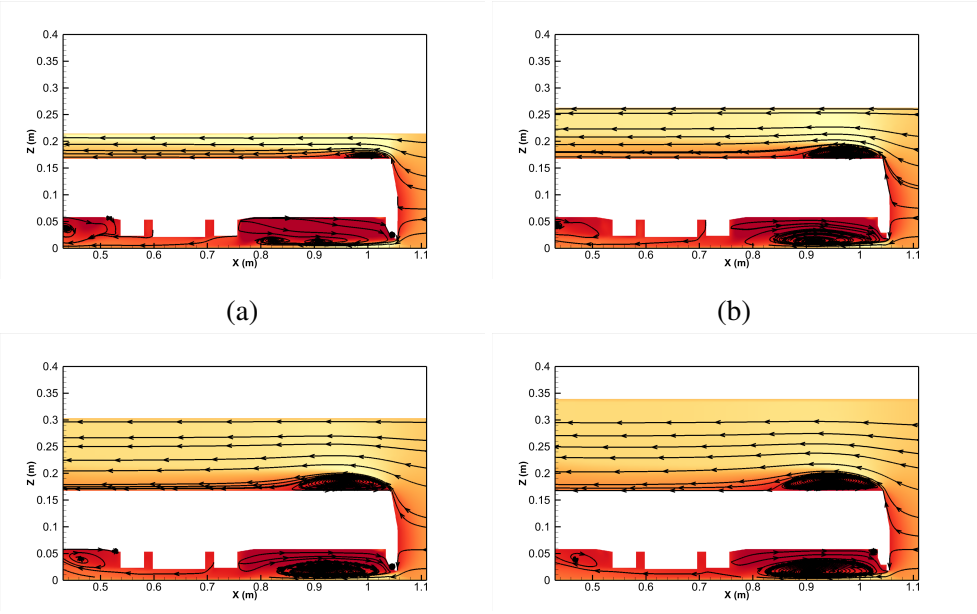
The separation bubble model, discussed in section 5.4.3, incorporates a scaling factor for the size of the separation region when transitioning from an open track to a tunnel. In order to establish the generalisability of the model across different scenarios, an investigation was carried out to



(a) (b) (c)

Figure 5.18: PSD of velocity fluctuations at positions near average shear layer edge (a) 0+0 (b) 15+0 (c) 30+0.

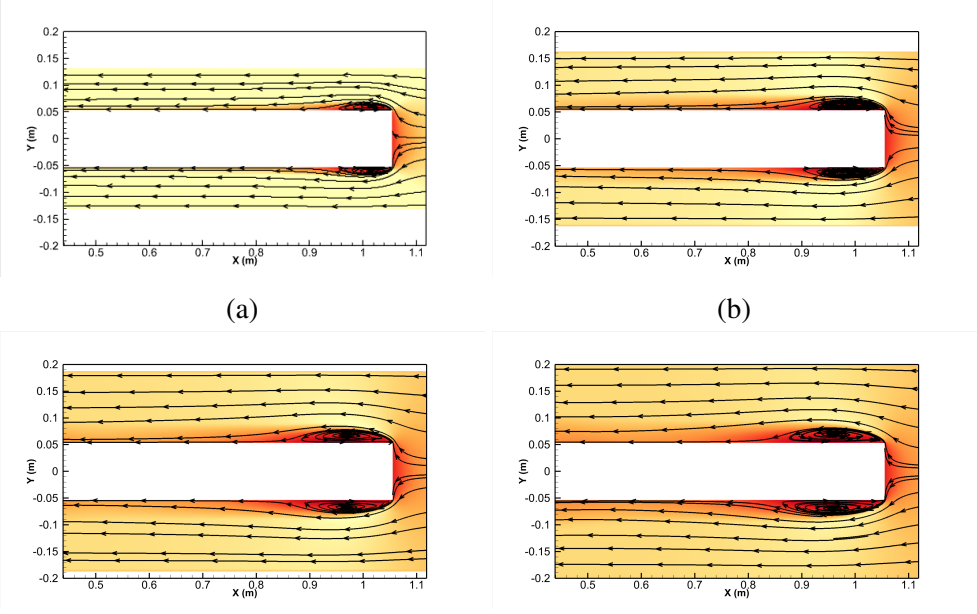
examine the correlation between the scale factor and the blockage ratio β_E. The investigation involved examining various tunnel cross-sectional areas (30/45/60/75 m^2), corresponding to β_E values ranging from 0.14 to 0.35, chosen to represent a range of tunnel sizes that necessitate accounting for the aerodynamic effect of freight trains.



(a) (b)

(c) (d)

Figure 5.19: H_R inside the tunnel (a) 30 m^2 (b) 45 m^2 (c) 60 m^2 (d) 75 m^2.



(a) (b)

(c) (d)

Figure 5.20: H_{S1} inside the tunnel (a) 30 m^2 (b) 45 m^2 (c) 60 m^2 (d) 75 m^2.

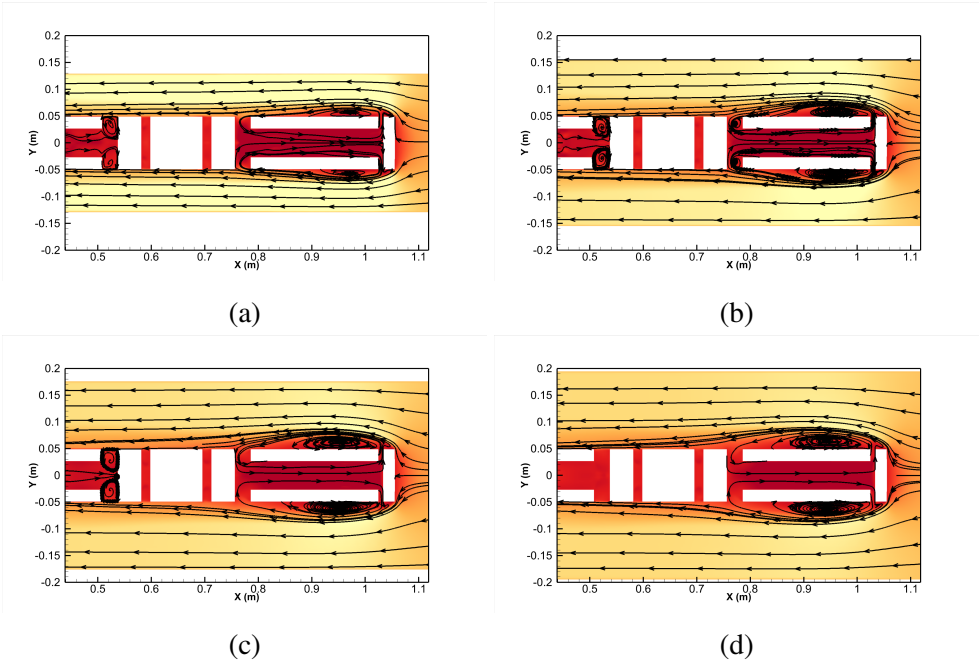


Figure 5.21: H_{S2} inside the tunnel (a) 30 m^2 (b) 45 m^2 (c) 60 m^2 (d) 75 m^2.

The streamline and velocity contour at different slices (Y= 0/ Z = 0.1/Z = 0.15 m) are depicted as shown in Figure 5.19, 5.20 and 5.21. It is clear that the velocity in the annulus region increases with the decrease of tunnel area, which is as expected following the continuity equation. Besides, in this investigation, the separation bubble height on the roof, side, and bottom of a freight train inside a tunnel was measured for each cross-sectional area. It clearly shows that both the height and length of the separation bubble decreases with the increase of blockage ratio, especially when the cross-sectional area is 30 m^2. It should be noted that while the cross-sectional area decreases linearly from 75 to 60/45/30 m^2 (as shown in Figure. 5.24(a)), with a difference of 15 between each value, the rate at which the blockage ratio increases is not proportional. In fact, as the area decreases to 60/45/30 m^2, the blockage ratio accelerates at a faster rate, increasing from 0.14 to 0.175/0.233/0.35. It explains the decrease on separation bubble size is more significant when the cross-sectional area is 30 m^2. Though both height and length of the separation region changes with the change of tunnel area, the length is always around ten times of the height of the separation bubble. Additionally, as shown in Figure. 5.8 that changing the length of the separation bubble doesn't influence the maximum magnitude of the pressure waves. Thus in this investigation, only the relationship equation of the height

of separation bubble and the blockage ratio is studied for a wider application of the proposed separation bubble model as analysed in section 5.7.

5.7 Summary of the Parameters to be Used in 1d Code

Parameterisation Equations

Now that the results for the influence of train nose bluffness and tunnel geometry have been considered, it is important for the development of the 1d model to draw all this information together into a parameterisation equation. A parameterisation equation is obtained by using polynomial fitting function to get the relationship between the bubble height on roof and the side of the train with the angles (α and β) controlling the bluffness of the head. The angles are transformed to radians before fitting into the equation. The equation used to fit the variables is given in Equation 5.5 and the fitting parameters are given in Table 5.3. The R-Square of both fitting functions fall in the range over 0.998, indicating a strong relationship between the fitting model for the bubble height and the variables that control the bluffness of the train head. The fitting domains that show the relationship between the height of the separation bubble (H_R and H_S) and the bluffness of the train (α and β) are shown in Figure 5.22. From the parameters and the fitting domain, it can be seen that, as analysed in Section 5.5.2, the size of the separation bubble on the roof is more sensitive to α. However, the height of the separation bubble on the side of the train exhibits a more obvious trend of decrease when β increases.

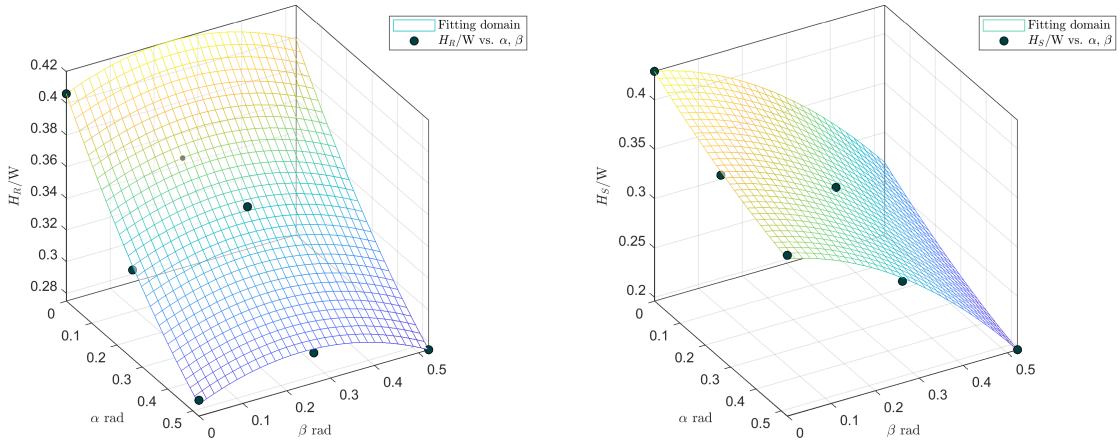
In order to assess the influence of α and β on the separation region, a sensitivity analysis is performed using Sobol indices [159]. Total-order Sobol indices are calculated to determine the extent to which the total variance of H_R and H_S can be attributed to α and β, taking into account both the direct and indirect effects. The range of α and β values considered is [0,0.0524] radians. The total-order Sobol indices of α and β for H_R are found to be 0.975 and 0.05, respectively. These results indicate that around 97.5% of the total variance in H_R can be explained by variations in α, indicating that α has a more dominant impact on the separation height at the roof of the train than β. For H_S, the total-order Sobol indices of α and β are

0.172 and 0.828, respectively, indicating that approximately 82.8% of the change in H_S can be attributed to variations in β.

$$\mathrm{H}(\alpha,\beta) = \mathrm{h0} + \mathrm{C}_{\alpha 1}\alpha + \mathrm{C}_{\beta 1}\beta + \mathrm{C}_{\alpha 2}\alpha^2 + \mathrm{C}_{\beta 2}\beta^2 \tag{5.5}$$

	h0	$C_{\alpha 1}$	$C_{\beta 1}$	$C_{\alpha 2}$	$C_{\beta 2}$	R-Square
H_R/W	0.406	-0.318	0.1213	0.1568	-0.259	0.9980
H_S/W	0.429	-0.1919	-0.1003	0.0985	-0.390	0.9985

Table 5.3: Fitting parameters for the parameterisation equation.

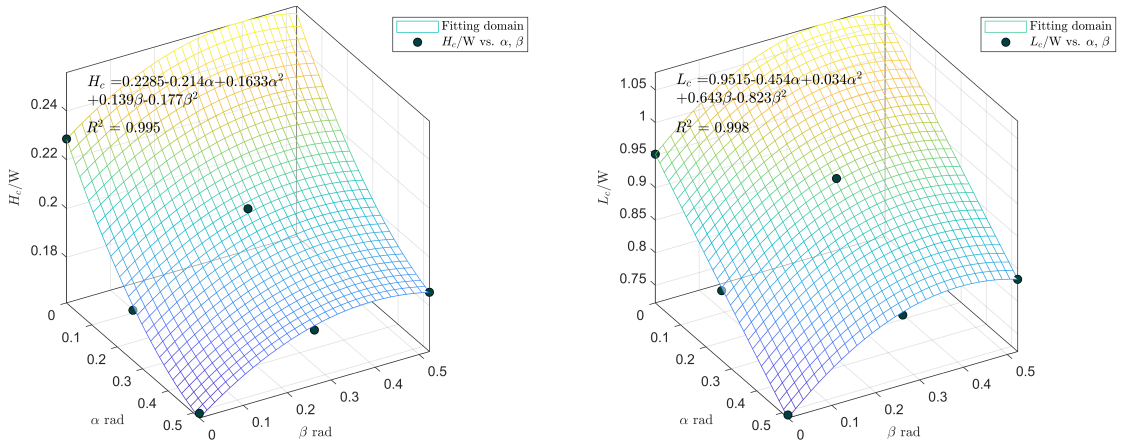


(a) (b)

Figure 5.22: Fitting domain for the height of separation bubble and bluffness (a) relationship between H_R and α, β (b) relationship between H_S and α, β.

Previous research has shown that the shape of locomotive head has a significant impact on the length and width of separation regions [160]. This study further analyses the height and length of the center of the separation bubble (H_c and L_c) at the top of the train. The relationship between H_c and L_c with α and β is presented in Figure 5.23. The results indicate that both H_c and L_c increase as α decreases and β increases. This trend is consistent with the influence of bluffness on the full height and length of the separation region (H_{R1} and L_{R1}) at the top of the train. Table 5.4 summarises the relative position of the vortex core with respect to H_c and L_c. The findings show that the relative height of the vortex core significantly increases with an increase in α and β, while the relative length of the vortex core does not change much with a

variation in bluffness. The relative length slightly increases as β increases and α decreases, with the percentage position change ranging from 40% to 50%.



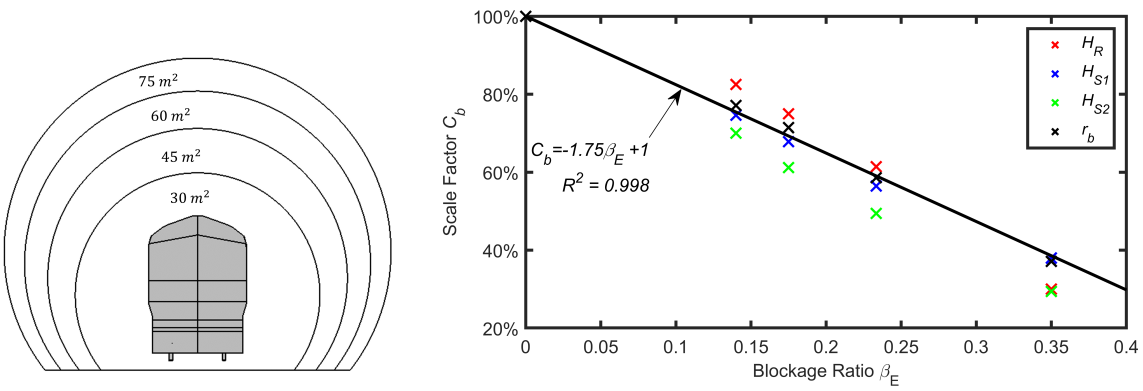
(a) (b)

Figure 5.23: Fitting domain for the height and length of the center of the separation bubble and bluffness (a) relationship between H_c and α, β (b) relationship between L_c and α, β.

$\alpha+\beta$	0+0	15+0	15+15	30+0	30+15	30+30
H_C/H_R	49.43%	54.93%	60%	57.38%	62.54%	67.46%
L_C/L_R	47.38%	46.44%	48.77%	42.94%	47.81%	48.06%

Table 5.4: The relative position of the vortex core with respect to the full height and length of the vortex (%).

The relationship between the scale factor C_b of $H_R/H_{S1}/H_{S2}$ and β_E was graphically depicted in Figure 5.24. Scale factor C_b is the reduction coefficient of the effective cross-sectional area from the open track to inside the tunnel. The configuration of the train and tunnel indicated that as the cross-sectional area of the tunnel decreases, the space between the roof of the freight train and the tunnel ceiling decreases at a faster rate than the space between the side of the freight train and the tunnel sidewall when the tunnel cross-section is circular. This limited space at the top exerts a stronger squeezing effect on the separated region above the roof, which may be the reason for the slightly faster decrease rate of H_R compared to H_{S1} and H_{S2} as β_E increases. In general, the results indicate that within the range examined, the scale factor of these three variables decreases linearly, with a similar decreasing rate, as β_E increases. As such, for ease of



(a) (b)

Figure 5.24: Influence of the blockage ratio on the scale factor. (a) Configuration of the tunnel cross section (dimensions given as full-scale) (b) Relationship between C_b and β_E.

model application, the radius of the separation bubble $r_b = \sqrt{\frac{E_{max}}{\pi}} - r_t$ (as shown in Figure 5.7), which accounts for the overall influence of the separation region on the effective cross-sectional area, was investigated instead. The relationship equation between the scale factor of r_b and β_E is given in Figure 5.24(b).

Validation of the Model

In order to test the applicability of the parameterisation equation detailed in Section 5.7 and the proposed separation bubble model outlined in Section 5.4.3, two additional simulations are conducted. The first case is to test the accuracy of the relationship equation between separation bubble size and head bluffness. Simulation of a generic freight locomotive with a length of 21 m (full scale) and a nose shape of $\alpha + \beta = 30 + 10$ entering a tunnel is conducted. The cross sectional area of the generic freight locomotive is 10.2 m^2 and the tail pressure loss is β_E^2, where β_E is the blockage ratio. The height of separation bubble at the coupling region stays the same as shown in Figure 3.1. The height of the separation bubble at roof and windshield region of the head are obtained from the parameterisation equation, and substituted into the separation bubble model to calculate the recirculation region on open track, before being then scaled down according to the reduction factor in Figure5.7 to get the effective blockage area inside tunnel. Pressure history curve at 2 m, 4 m, 8 m and 16 m inside tunnel are compared with the numerical

simulation result and shown in Figure 5.25. It can be seen that the magnitude of maximum pressure rise fits well with the simulation result for the test case. There is some discrepancy on the influence of reflected pressure wave, mainly at measuring point close to tunnel portal (2m to tunnel entrance) caused by the same strong 3d effect as shown previously for the Class 66 locomotive shape. For 8 m and 16 m inside tunnel, the peak values caused by compression and expansion waves are well-predicted. Thus it is concluded that the separation model proposed in Figure 3.1 and the parameterisation equation for the height of the separation bubble present a reasonable prediction on the effective blockage area of blunt freight train head.

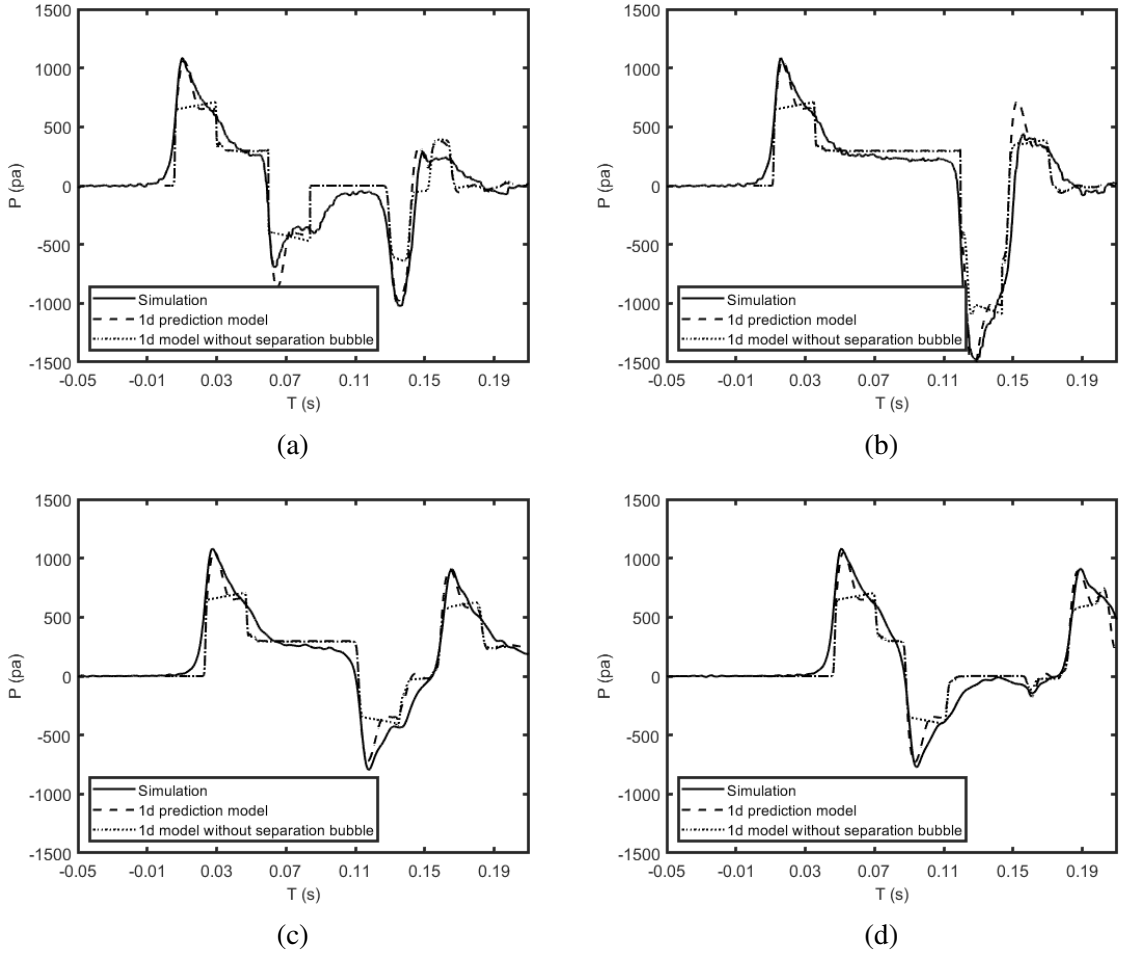


Figure 5.25: Comparison of pressure history curve obtained from 1d prediction model and simulation (a) 2m to the tunnel portal (b) 4m to the tunnel portal (c) 8m to the tunnel portal (d) 16m to the tunnel portal.

The second case is to assess applicability to a completely different train type and the validate the relationship equation between the size of separation bubble and blockage ratio for an

actual locomotive type. The simulation was conducted featuring a Class 70 locomotive (Figure 5.26(a)) passing through a 65 m^2 tunnel. The locomotive surface mesh and the dimensions for the roof/windshield/coupling regions required for the separation bubble model are illustrated in Figure 5.26(b). Due to the unique design of the Class 70 locomotive, as depicted in Figure 5.26(a), separate cross-sectional area are used for the locomotive's head (9.5 m^2) and body (8.5 m^2). It is worth noting that these dimensions are obtained directly from the locomotive CAD model.

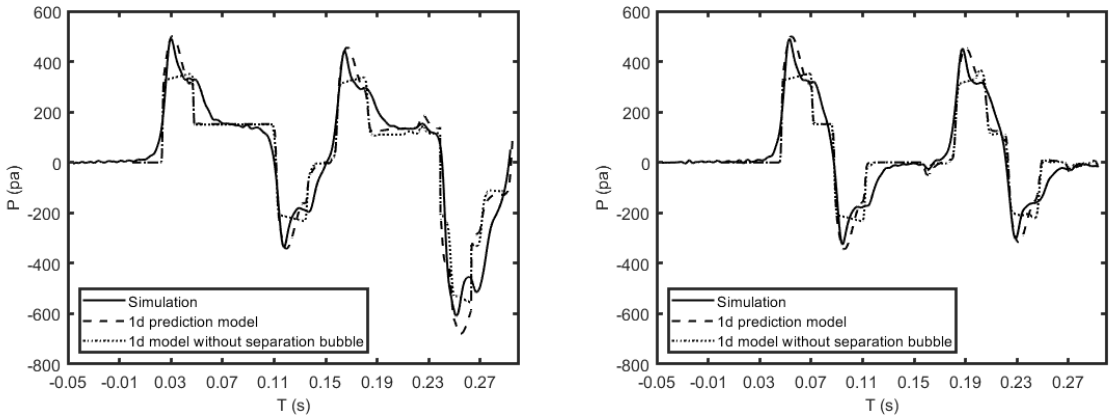
To calculate the height of the separation bubble at the roof and windshield regions of the Class 70 locomotive head, the parameterisation equation is utilised with values of α and β equal to 12°. The resulting separation bubble height values are then inputted directly into the separation bubble model to calculate the recirculation region in the open track, $H_R = 0.36W$ and $H_S = 0.355W$. Subsequently, the effective area within the tunnel is determined by scaling down the effective blockage area in the open track using the reduction factor C_b, specific to the 65 m^2 tunnel cross-sectional area, calculated using the equation presented in Figure 5.24. With $\beta_E = 0.146$, the calculated value of C_b is found to be 0.74.

To evaluate the performance of the proposed methodology, the pressure time history curves obtained from the redeveloped 1d numerical model are compared against the CFD results for distances of 8 m and 16 m from the tunnel entry portal, as shown in Figure 5.27. It can be observed that the magnitude of the maximum initial pressure rise obtained from the 1d model is in good agreement with the CFD simulation results for the validation case. Moreover, the peak values caused by compression and expansion waves, as well as the pressure changes caused by the reflected pressure waves, are also accurately predicted. Hence, it can be concluded that this additional simulation successfully validates the accuracy of the relationship equations and the separation bubble model in predicting the pressure wave formation and behavior for different blunt locomotive types passing through a tunnel. The ability to parameterize any locomotive shape using a simple methodology and the incorporate the influence of tunnel dimension provides important additional functionality to the 1d code to meet the requirement for modelling the initial train nose pressure rise accurately for bluff trains.



(a) (b)

Figure 5.26: The Class 70 validation case locomotive. (a) Class 70 locomotive (b) the CFD mesh and key dimensions, given here in the reduced 1/25th scale in m.



(a) (b)

Figure 5.27: Comparison of pressure time history curves for a Class 70 locomotive passing through a tunnel obtained from the 1d prediction model and CFD simulation for measuring positions (a) 8 m from the tunnel entry portal and (b) 16 m from the tunnel entry portal.

5.8 Methodological Contributions

This section outlines the methodological contributions to the research on separation bubbles around freight trains and summarizes the key conclusions drawn from this chapter. Numerical simulation of a freight locomotive entering a tunnel are conducted using LES and URANS numerical model. The pros and cons of the two methods are analyzed, and an appropriate consideration is taken to determine the suitable model used for freight aerodynamics and the further parameterisation study. The results obtained from the simulations are adopted to calculate the input parameters for a novel redeveloped 1d code which is capable of considering freight train

geometries. Then a parameterisation study of the size of the separation bubble is undertaken based on the simplified Class 66 locomotive. A series of important conclusions can be drawn as below:

(a) As a freight train enters a tunnel, the separation bubble induced by the blunt head of the freight train will increase the effective blockage ratio. It will influence the initial pressure rise and the subsequent pressure changes as the pressure wave propagates inside tunnel.

(b) A redeveloped 1d code is built by modifying the boundary conditions at the train nose and adding the term described area change in the continuity equation. Additionally, a separation bubble model is built to calculate the effective blockage area by dividing the head of the freight train into roof, windshield and coupling regions and using the separation bubble height for each region. The development of pressure waves calculated using the separation bubble model before and after modification of the code are compared with experimental results presented in previous works. Results indicate that the traditional code fails to predict the maximum initial pressure rise accurately. This issue is greatly improved after considering the influence of the separation bubble by reducing the error of the maximum pressure rise from 43% to 4%.

(c) The length and width of the vortex size on the top, corner, and side of the locomotive head are measured. The results show that increasing the leading edge angle can efficiently decrease the height and width of the separation bubble both at top and side of the train. When α increases from 0° to 30°, L_{R1}/L_{S1} decrease from $2.0W/1.78W$ to around $1.7W/1.3W$ and H_{R1}/H_{S1} decrease from $0.406W/0.429W$ to around $0.28W/0.196W$ separately.

(d) Increasing the sub-angle between the windshield and the roof cap causes the source node, where the separation length is the shortest on the side of the train surface, to tend to move from the corner to the middle height of the train. However, the sub-angle has only a minor influence on the separation bubble on the roof.

(e) To improve the 1d code to apply to various types of freight trains, a parameterisation study is conducted to get the fitting equation of the relationship between the parameters proposed

in the separation bubble model (the height of the separation bubble at different region) and bluntness of head. The accuracy and applicability of the parameterisation equation and the separation bubble model is tested and validated by comparing with simulation result using a new nose shape. The outputs of this research provide valuable information for tunnel and freight train design.

Chapter 6

Pressure Wave Induced by Loading Configurations

6.1 Introduction

This chapter contains a thorough comparative analysis of the flow field development as a partially loaded freight train enters a tunnel. The study assesses the accuracy of LES and URANS methodologies in simulating the pressure wave patterns concerning different container loading configurations. Additionally, it delves into analysing how the flow within the unloaded gap affects the pressure wave formation. Leveraging insights from numerical results, further redevelopments are made to the 1d code, enabling it to simulate the disruptions caused by the partially loaded containers on the flatbed wagon portion of the train and the impact of flow separation within gaps between loaded containers. These redevelopments involve mesh system reorganisation, modifications to governing equations, and the introduction of novel boundary conditions to calculate flow at the disruptions. Subsequently, a parameterization study is carried out to explore the impact of gap distance on the effective blockage area of the unloaded gap and the size of the separation bubble generated as air flows over the sharp edge of the container behind the gap. The study yields parameterization equations linking gap length with these predetermined parameters, enhancing the versatility of the 1d programme.

6.2 Modification of the 1d Code

6.2.1 Mesh System

This chapter introduces the modified mesh system of a locomotive with a partially loaded container entering a tunnel, as illustrated in Figure 6.1, in which the grid in the annulus space (X_2) is based on the train as the frame of reference. The annulus space around the train is further divided into sub-meshes by the ends of the gap between containers. The flow in each sub-mesh system is solved using MOC method (3.3) based on the corresponding different physical parameters (length, perimeter, cross-sectional area, etc) and the flow connecting different sub-meshes is solved by the boundary conditions illustrated in Chapter 6.2.2. Through this approach it can be seen from Figure 6.1 that although there are discontinuities along the train body, it doesn't have to separate the mesh at the annulus space when the train enters the tunnel, which avoids the excessive extending and extracting mesh when the reference frame is based on the ground.

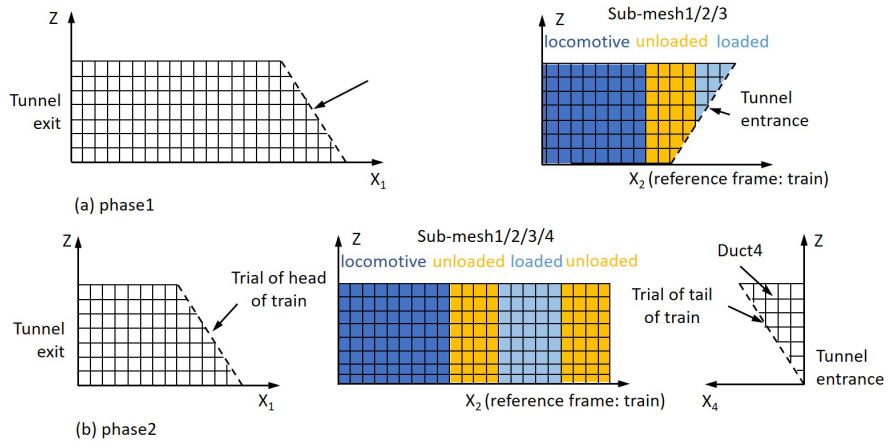


Figure 6.1: Mesh system for a partially loaded train.

6.2.2 Boundary Conditions

When the intermodal container freight train is partially loaded, there are potentially large gaps between the containers where pressure loss are generated, as the flow passes through. Both ends of these large gaps are considered as discontinuities in the 1-d code. Therefore, new boundary

conditions at the front and end of these gaps entering the tunnel are added to the code to describe these discontinuities, as illustrated in Figure 6.2. The air flow from the loaded/unloaded region to the unloaded/loaded region can be simplified as a duct flow from large/small cross-sectional area, to the small/large cross-sectional area. In summary, the flow characteristic at these position can be considered as ducts with a sudden area change. This is a similar concept to that applied to simulate the flow at train head and tail. The relationship of velocity, pressure and density between connected ducts and the deduction of continuity, momentum and energy equation for quasi-steady flow is similar as those illustrated in Chapter 3.2. The unknown variables are marked red in Figure 6.2. Thus in this chapter, only the equations used to directly solve the unknown Riemann variables are presented, as given in Equations. 6.1~6.3.

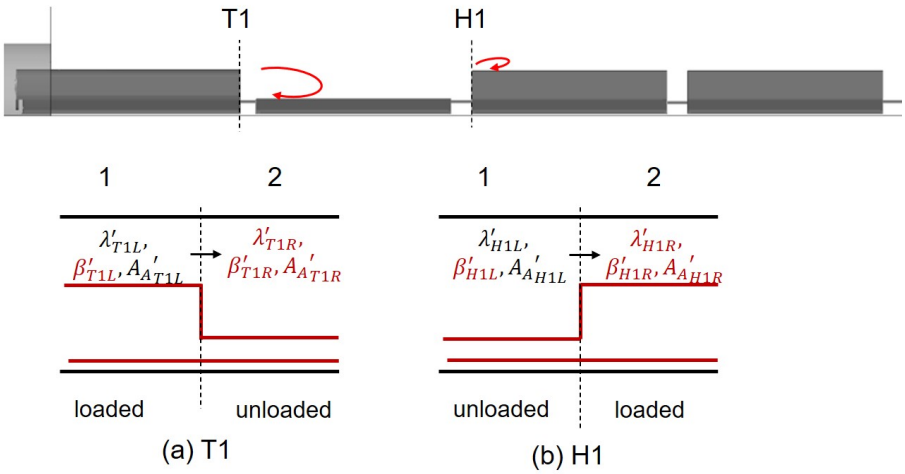


Figure 6.2: New boundary condition at the ends of containers for a partially loaded train.

$$\left(\lambda'_{T1L}+\beta'_{T1L}\right)^2-\left(\lambda'_{T1R}+\beta'_{T1R}\right)^2+\frac{2}{\kappa-1}\left[\left(\lambda'_{T1L}-\beta'_{T1L}\right)^2-\left(\lambda'_{T1R}-\beta'_{T1R}\right)^2\right]=0 \tag{6.1}$$

$$\left(\lambda'_{T1L}-\beta'_{T1L}\right)^2\left(\lambda'_{T1L}+\beta'_{T1L}\right)^{\frac{2}{\kappa-1}}\left(\frac{A_{A_{T1R}}}{A_{A_{T1L}}}\right)^{\frac{2\kappa}{\kappa-1}}-\frac{E_{T1R}}{E_{T1L}}\left(\lambda'_{T1R}-\beta'_{T1R}\right)\left(\lambda'_{T1R}+\beta'_{T1R}\right)^{\frac{2}{\kappa-1}}=0 \tag{6.2}$$

$$\frac{A_{A_{T1R}}}{A_{A_{T1L}}}=\left(1+\frac{\frac{2\kappa}{(\kappa-1)^2}\left(\frac{\lambda'_{T1R}-\beta'_{T1R}}{\lambda'_{T1R}+\beta'_{T1R}}\right)^2\zeta}{\left[1+\frac{2}{\kappa-1}\left(\frac{\lambda'_{T1R}-\beta'_{T1R}}{\lambda'_{T1R}+\beta'_{T1R}}\right)^2\right]^{\frac{\kappa}{\kappa-1}}}\right)^{\left(\frac{\kappa-1}{2\kappa}\right)} \tag{6.3}$$

Note that E_{T1L} and E_{T1R} are the areas of the left and right annular duct after considering the separation. ζ is the pressure loss coefficient at the discontinuities at the ends of the unloaded containers. The pressure loss at T1 ζ_{T1} is calculated based the same method (Borda-Carnot relationship [17]) to calculate the pressure loss at train tail, using the effective cross-sectional areas of the loaded and unloaded containers,

$$\zeta_{T1} = (\frac{E_{con} - E_{gap}}{E_{tu} - E_{con}})^2 \tag{6.4}$$

in which E_{con} is the cross-sectional area of the loaded container and E_{gap} is the effective cross-sectional area of the gap. Apart from the equations. 6.1 $\sim$ 6.3, an additional characteristic equation concerning β_{T1L} is required to solve the four unknown variables. The deduction of this characteristic equation can be guided by Equation. 3.33. Equations are solved using Newton Raphson method. For the equations to solve the flow from the unloaded region to loaded region, the subscript T1 is substituted by H1, and the pressure loss at H1 $\zeta_{T1} = 0.03$. Furthermore, due to the sharp front edge of the container, a separation bubble forms when then air flows over from the gap in front. The size of the separation bubble and the pressure loss coefficient changes with the distance of the gap. Details of the relationship between the parameters which need to be determined and the gap size are discussed in the following sections.

6.3 Reference Case

In order to establish an initial comprehension of the flow field and to derive essential parameters for input into the 1d code, a reference case featuring a 33% loaded intermodal container freight train entering a tunnel is subjected to numerical investigation. In a similar approach to the previous Chapter 5.2, both LES and URANS models are employed and subsequently compared to elucidate the efficacy of different numerical models in accurately calculating the pressure wave phenomena. The initial analysis of the flow field entails examining wall shear stress, velocity, and pressure contours derived from the LES simulations. Subsequently, a comparative study is conducted by comparing the pressure wave history curves obtained from both LES and URANS

simulations. Subsequently, the parameters derived from LES simulations are integrated into the modified 1d code to validate the suitability of the proposed algorithms outlined in Chapter 6.2.

6.3.1 Wall Shear Stress

In line with the demonstration provided earlier in Chapter 2.3.3 and as depicted in Figure 2.4, the second part of the pressure rise Δp_{fr} is induced by the frictional effect when the main part of the train body enters the tunnel. In the case of passenger trains or fully laden freight trains, the train body maintains a streamlined form, facilitating the steady development of the boundary layer along its surface [22]. Consequently, the wall shear stress within this boundary layer is uniformly oriented, actively contributing to the pressure amplification caused by the pressure wave. However, for partially loaded container freight trains, a distinctive scenario unfolds due to the boundary layer separating after each container and the consequent formation of a recirculation zone at the forefront of each blunt container. These factors lead to a reversal in the direction of the wall shear stress within these separation regions, profoundly affecting the frictional dynamics and thereby modifying the pressure change Δp_{fr}. To provide a comprehensive visualisation and analytical insight into the distribution of wall shear stress, the instantaneous wall shear stress on the train body during the process of a partially loaded freight train entering a tunnel is depicted from both a top-view (Figure 6.4) and a side-view perspective (Figure 6.3).

The positive wall shear stress, denoted by the red colouration, prominently characterises regions of recirculation or separation. The positive direction of the x-axis corresponds to the direction of the train's motion. As anticipated, the sections preceding each container and the inter-container gap exhibit this red hue, symbolizing areas of notable recirculation and separation. Upon comparative analysis of Figure 6.3 (a) and (f), it is evident that the blue and red regions on the train body appear darker when inside the tunnel, implying a higher magnitude of wall shear stress in comparison to when outside the tunnel. This disparity can be attributed to the increased freestream velocity inside the confined tunnel space, resulting in an elevated friction velocity u_τ. Moreover, the extensive coverage of red across the train body visually underscores that, in comparison to passenger trains, the impact of the frictional effect on the pressure change, Δp_{fr},

is relatively diminished for partially loaded freight trains. This explains the lower frictional coefficient adopted in the 1d code for partially loaded freight train.

6.3.2 Velocity Field and Vortex Structure

The side and top views of the instantaneous velocity contours during the freight train entry into the tunnel are depicted in Figure 6.5 and 6.6. The negative x velocities depicted in the figure flow from the train head to the train tail. Therefore, the green-shaded areas indicate recirculation zones. Consistent with conclusions drawn in preceding chapters, these zones are situated in the wake region of the leading container, at the front of the trailing container and around the former part of the containers, as illustrated in the figures. The separation bubbles formed at the top and sides of the containers are notably smaller than those generated around the locomotive. This disparity arises because the trailing containers reside in the near or far wake region of the leading container, where the incoming air velocity is lower than the operating velocity of the train. Furthermore, the approaching air velocity in front of the trailing container increases with a rise in the gap distance. This phenomenon is similar to that observed in a platoon of vehicles [161]. The dynamics of airflow within the gap significantly impact the effective blockage area of the unloaded section of the train and play a crucial role in simulating the 'step-like' pattern of the initial pressure wave, as shown in Figure 6.11. However, due to the transient and turbulent nature of the flow calculated from LES method, accurately determining the shape of the recirculation region is not possible. In Section 6.4, a quantitative analysis of this area will be carried out by analysing the mean flow field of a partially loaded train inside tunnel (train is stationary with velocity inlet at the tunnel entrance) using LES method.

Due to the restricted area inside the tunnel, the flow speed in the region between tunnel and train surface is accelerated when the train enters. The increasing air velocity and the restriction on flow motion caused by tunnel walls triggers a higher generation of turbulence. In order to better visualize the turbulent structures formed around the train, a λ_2 criteria is adopted to identify the votices as shown in Figure 6.7 and 6.8. Comparing the moments before and after the train enters the tunnel, a noticeable increase in turbulence around the train body is observed

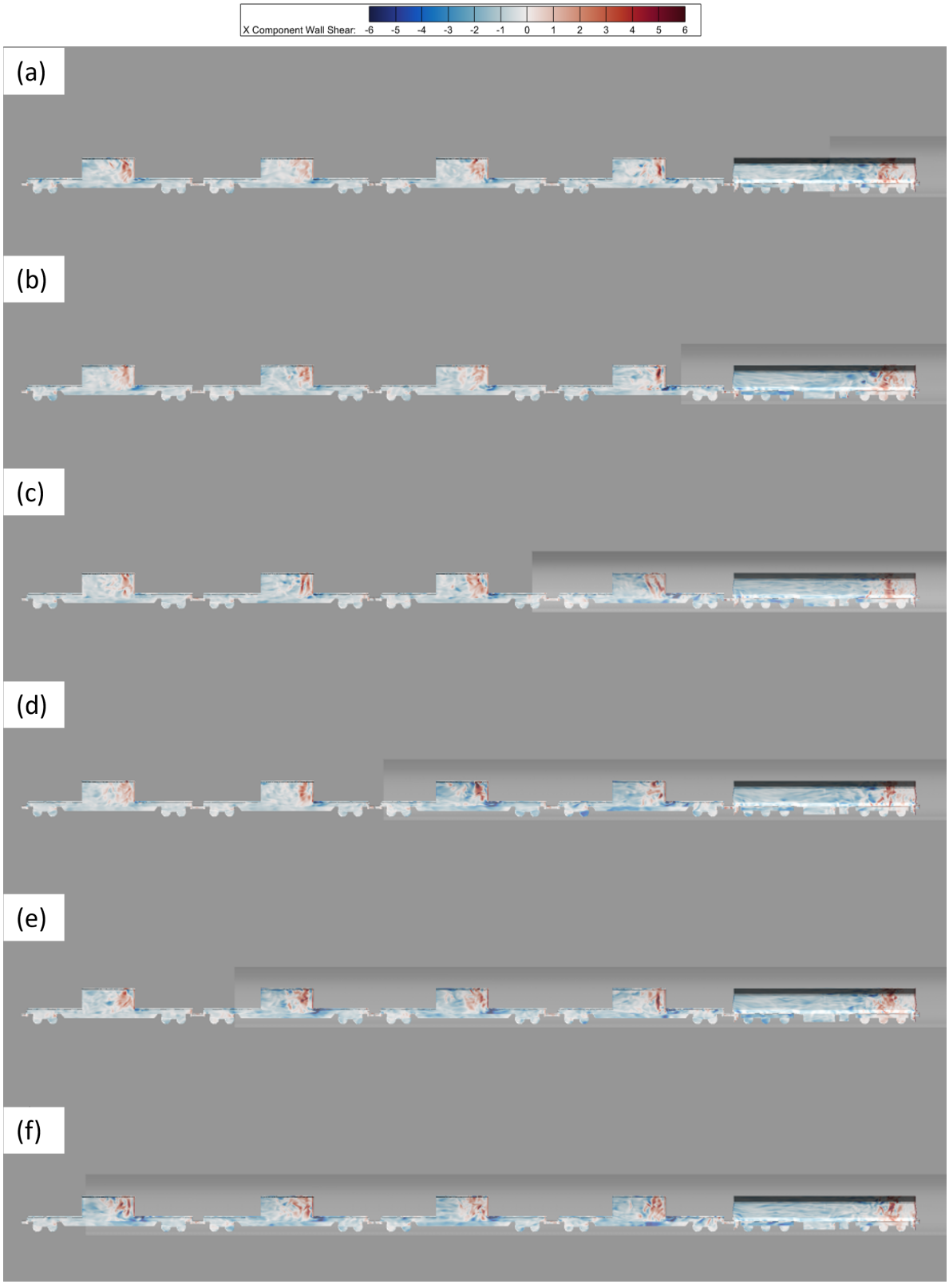


Figure 6.3: Side view of variations in wall shear stress on the train surface at different time instants during the train's entry into the tunnel.

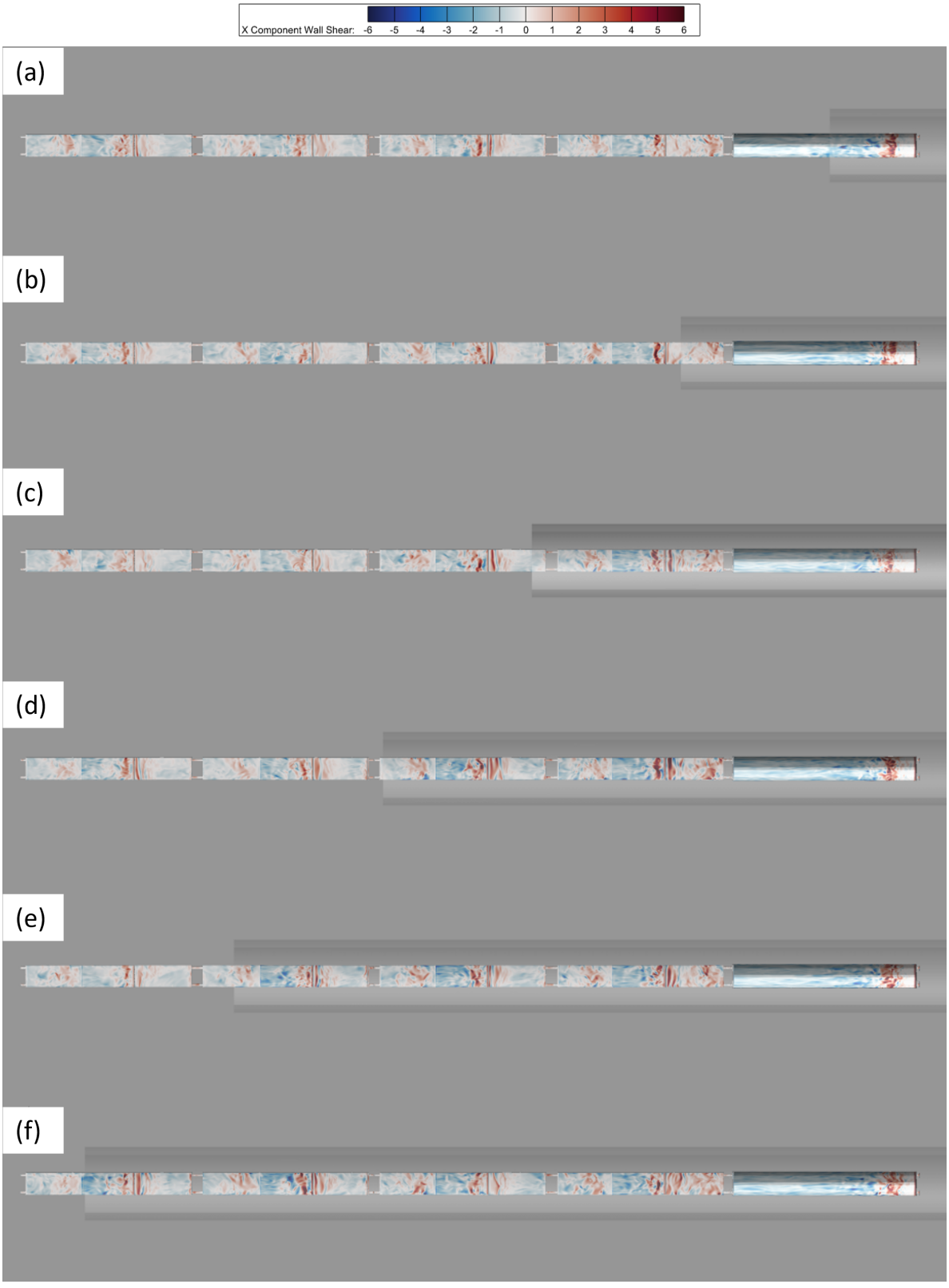


Figure 6.4: Top view of variations in wall shear stress on the train surface at different time instants during the train's entry into the tunnel.

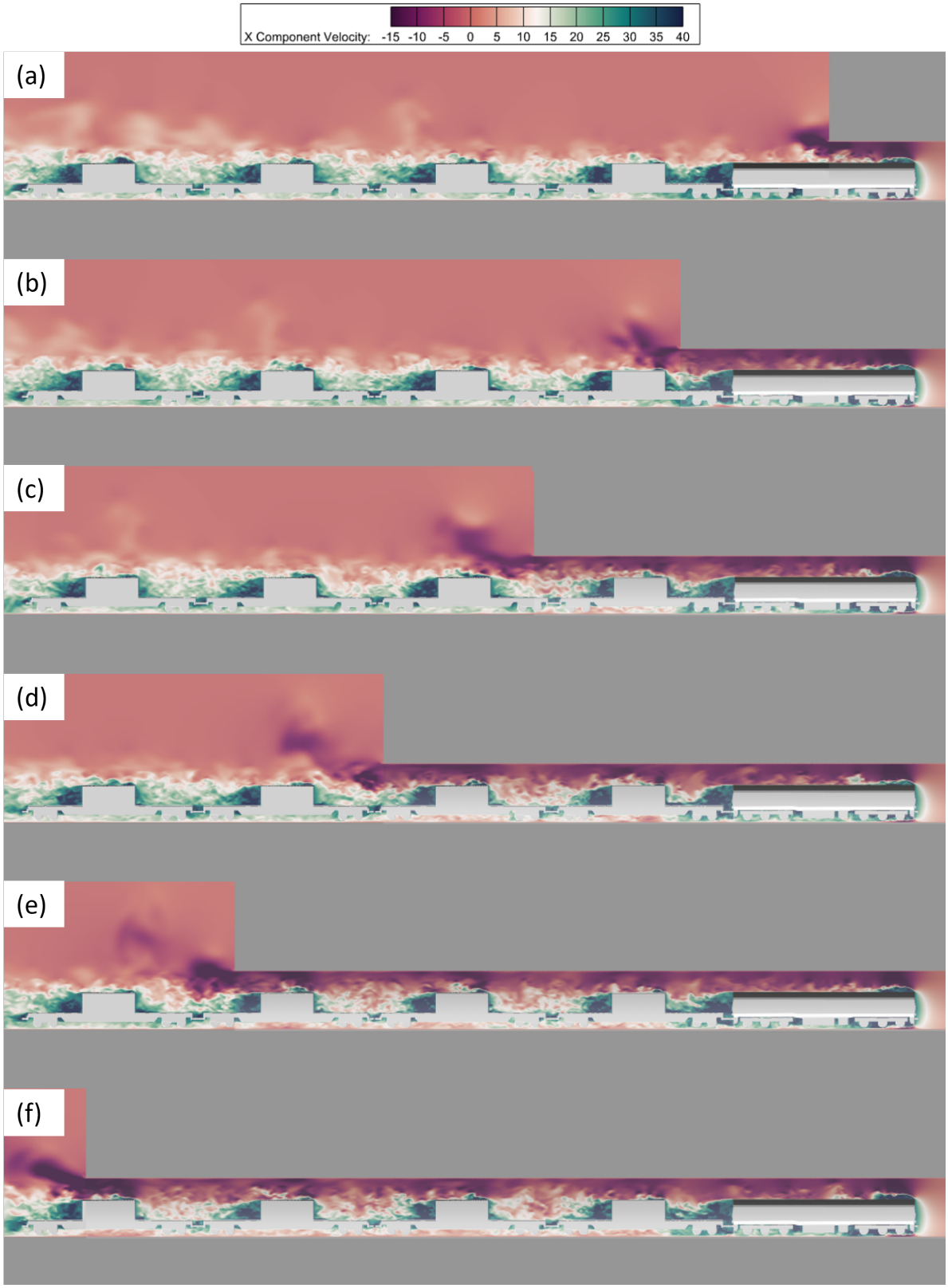


Figure 6.5: Side view of velocity distribution on plane Y = 0 m at different time instants during the train entry into the tunnel.

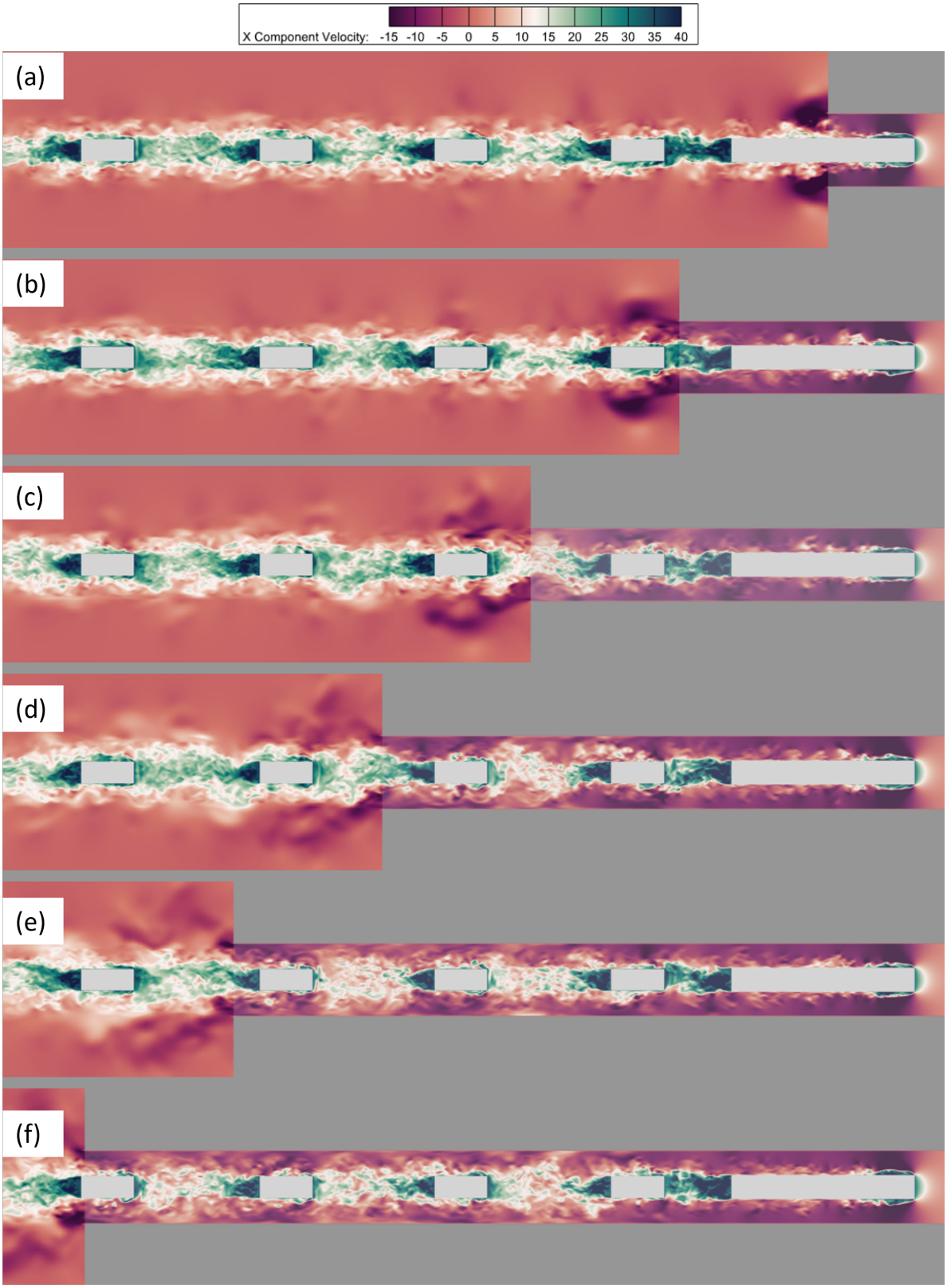


Figure 6.6: Top view of velocity distribution on plane Z = 0.09 m at different time instants during the train entry into the tunnel.

once the train is inside the tunnel.

6.3.3 Pressure Field and Pressure Waves

The side view and top view of the instantaneous pressure field at different time instants during the train entry into the tunnel are shown in Figure 6.9 and 6.10. The areas where negative pressure are high (coloured by dark blue), around the front part of each containers and after the containers, indicating the exits of each vortex core. These negative areas form a linearly developing pattern along the train body towards the rear, representing the shedding and development of vortices generated at the sharp edge of the blunt container front. Compared to the situation before the container enters the tunnel, there are more negative circles generated around the container after it enters the tunnel, indicating the splitting and broken nature of the vortices within the confined environment, leading to a more turbulent flow generated inside tunnel. The pressure inside the gap consists of a negative region, where the wake vortices generated from the separation of boundary layer at the rear of former container, and a positive region in front of the latter container. Due to the increasing velocity of the constrained flow inside tunnel, the absolute pressure values at both the negative and positive regions increases.

The time-history curve measured at the location 4 m inside tunnel obtained from LES and URANS are compared and summarised in Figure 6.11. The compression and expansion wave generated by the four partially loaded containers on the intermodal flatbed wagons entering the tunnel are clearly visible in the pressure trace and labelled as $c_{C1} \sim c_{C4}$ and $e_{C1} \sim e_{C4}$ in the Figure. It can be seen from the LES result that these pressure waves contribute to a 'step-like' pressure rise of ~350 Pa overall. However, contradictory to the conclusions drawn in Chapter 5.2 that URANS is acceptable to study the influence of separation bubble at locomotive head, in the case concerning the influence of flatbed wagons it is clear that the URANS is not able to model the change on pressure wave caused by partially loaded containers entering the tunnel. This is because the pressure wave change caused by the separation bubble at the head of the locomotive or from each container is primarily influenced by the height of the separation region; however, the accurate prediction of pressure waves caused by separation vortices in the region between

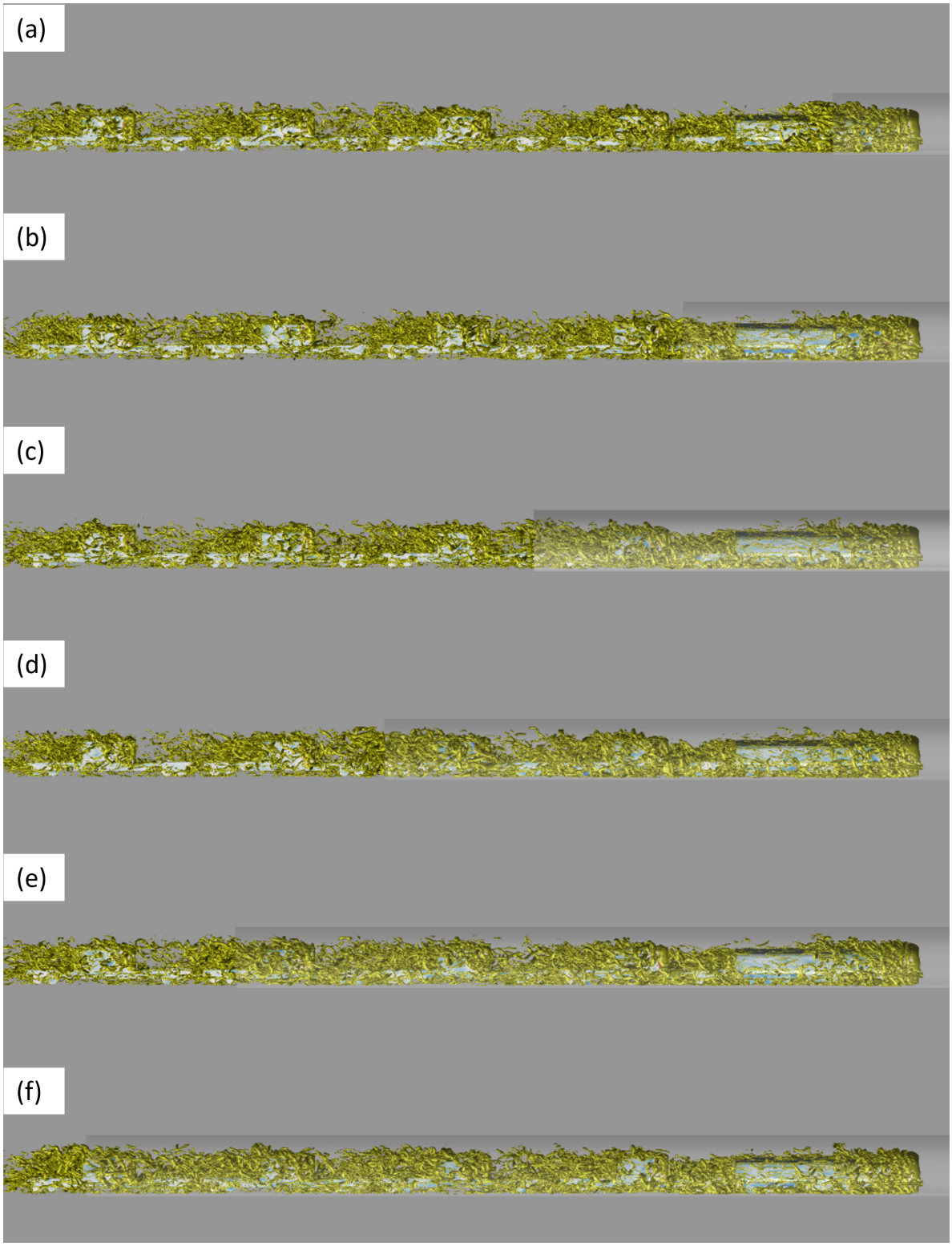


Figure 6.7: Side view of iso-surface of $\lambda_2 = -80000$ at different time instants during the train entry into the tunnel.

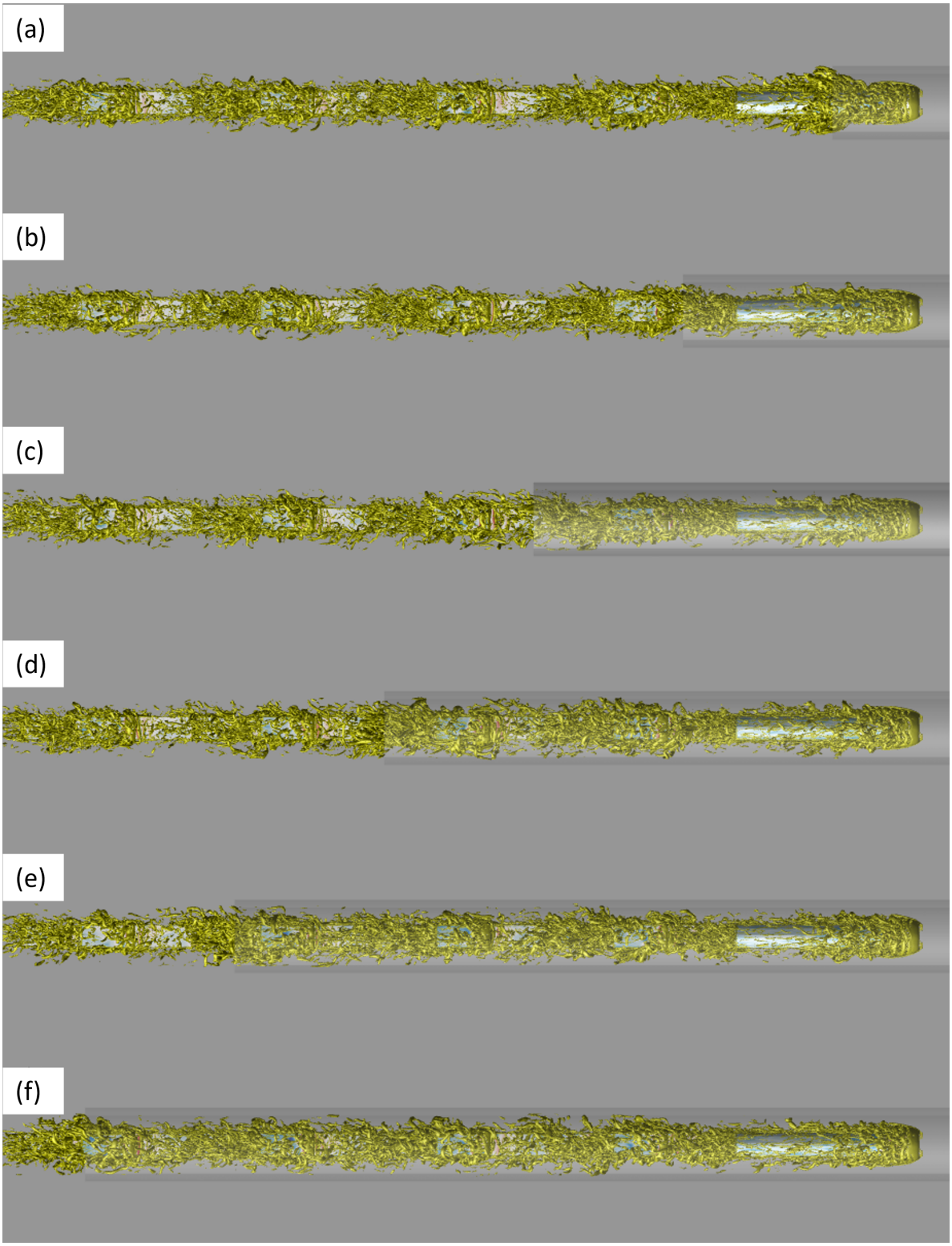


Figure 6.8: Top view of iso-surface of $\lambda_2 = -80000$ at different time instants during the train entry into the tunnel.

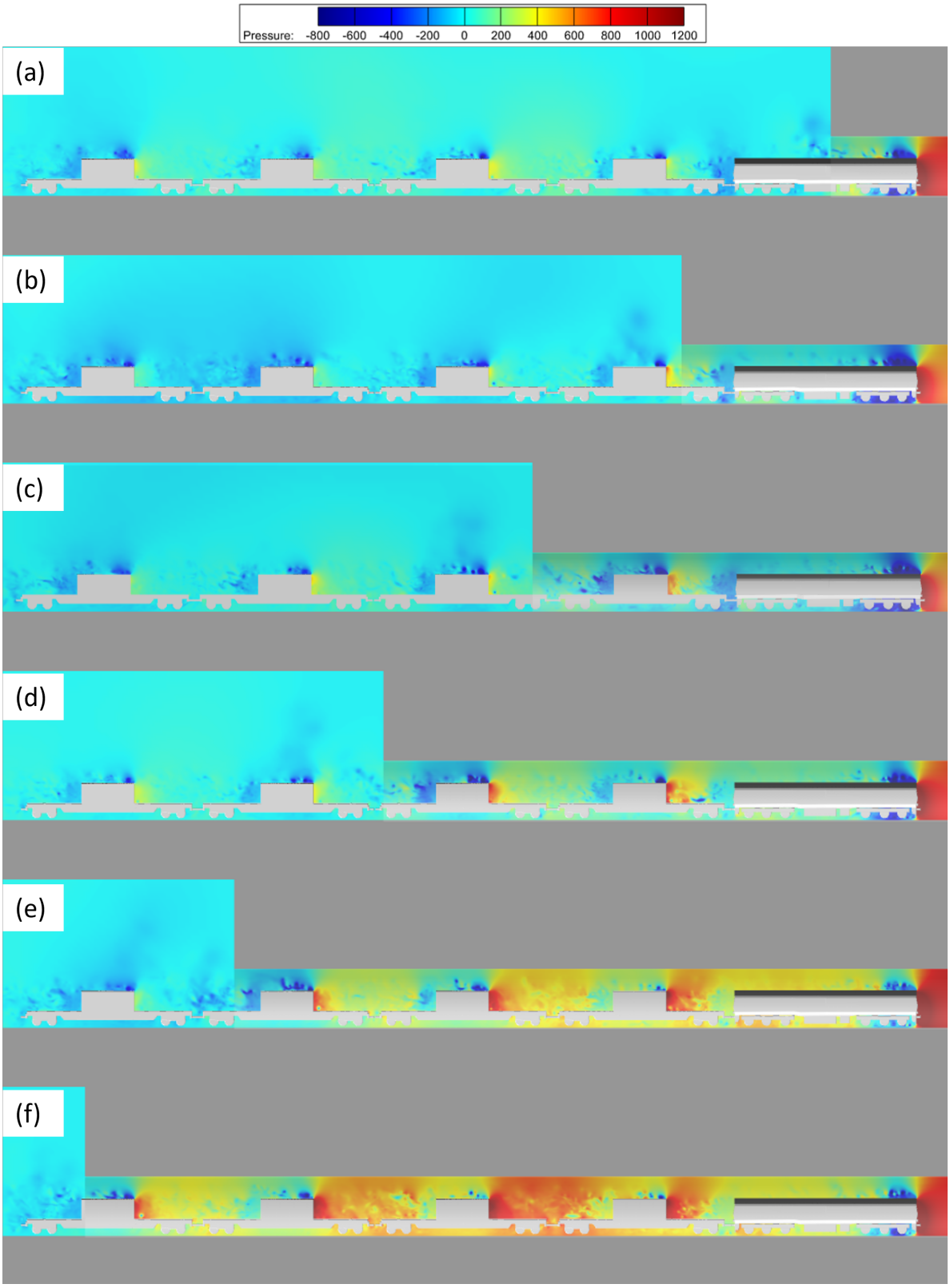


Figure 6.9: Side view of pressure distribution on plane Y = 0 m at different time instants during the train entry into the tunnel.

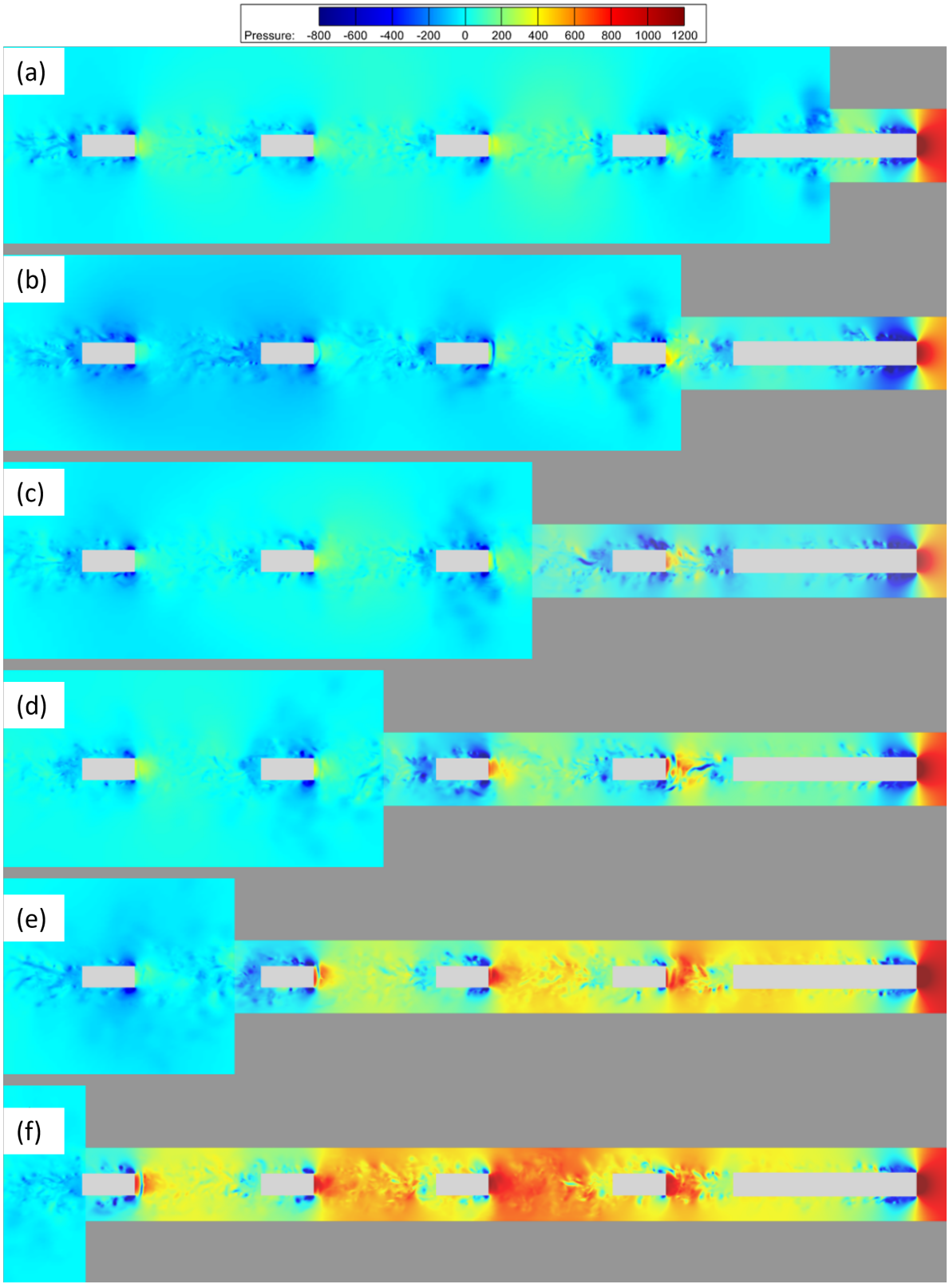


Figure 6.10: Top view of pressure distribution on plane Y = 0 m at different time instants during the train entry into the tunnel.

containers hinges not only on the separation region height but also on the wake vortex length and the flow development between containers. This is due to the fact that the the gap length may not be long enough for the flow to become fully developed, leading to the air becoming trapped in the gap and moving along with the train. This phenomenon influences the effective blockage area at the gap between containers, thereby exerting an impact on the magnitude of the expansion and compression waves upon entry into the tunnel. Furthermore, the length of the recirculation region is also important to be accurately calculated, since the recirculation region features high negative wall shear stress along the train surface, which has the effect of decreasing the pressure rise caused by frictional effect Δp_{fr}. Since $k-\omega sst$ URANS model tends to overpredict both the vortex reattachment length and the length required for the flow to be fully developed in the gap, this leads to a substantial underestimation of the pressure rise caused by frictional effects during the train tunnel entry.

In conclusion, the URANS model demonstrates inadequacy in calculating the flow field of interest and fails to capture the pressure wave pattern, as well as the maximum pressure rise associated with the entry of a 33% loaded container freight train into a tunnel. This deficiency primarily originates from the substantial discrepancy between the predictions of the URANS method and the LES approach concerning the phenomenon of separation in the 'wake region' in between the gap. Consequently, for the subsequent inquiries into the effects of varying loading configurations, the LES method is employed, despite its higher demand for computational resources.

6.3.4 Implement the Parameters in the Modified 1d Code

Given that the locomotive and tunnel geometries remain consistent with the reference case detailed in Chapter 5.4.3, the parameters utilised in the 1d code for the locomotive (Class 66 for the initial reference design case) and the tunnel stay the same as those presented in Table 3.1 and Table 3.2. Notably, from the depiction of the container, it can be seen that the container cross-sectional area (without considering the separation bubble region) is marginally smaller than that of the locomotive, estimated to be approximately 9.5 m^2 in the code.

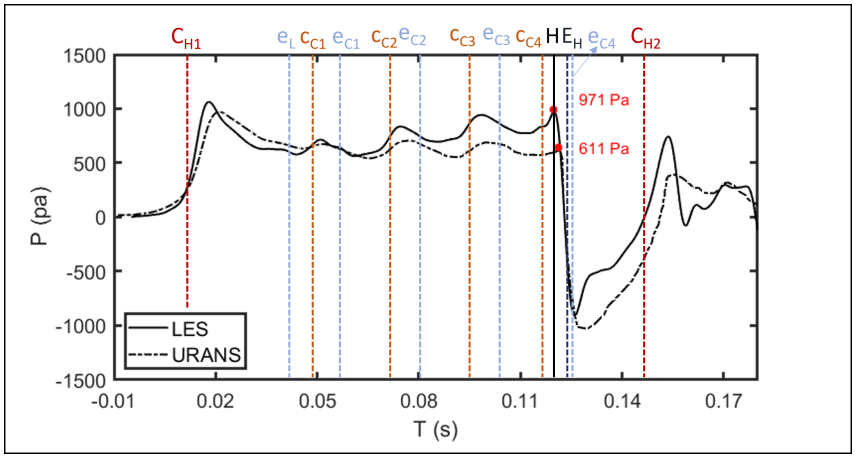


Figure 6.11: Pressure history curve generated by a locomotive with four 33% partially loaded freight train at 4 m inside tunnel (C_{H1}: the first compression wave induced by the train head entering the tunnel;e_L: Expansion wave generated by the rear of the locomotive entering the tunnel; c_{C1}: Compression wave generated by the front of the containers entering the tunnel; e_{C1}: Expansion wave generated by the rear of the containers entering the tunnel; E_{H1}: Expansion wave when C_{H1} reflected back from the tunnel exit; C_{H2}: the second compression wave when E_{H1} reflected from the tunnel entrance; H: the head of the train).

Considering the recirculation "wake region" within the gap, where the large region of negative wall shear stress is observed, the pressure rise stemming from the train body entrance into the tunnel is diminished. Consequently, this reduces the effective frictional coefficient of the entire train. Moreover, the perimeter of the unloaded section is smaller in comparison to the loaded portion of the train. Equation 3.6 demonstrates that both these parameters play a role in the computation of the frictional force. For the reference case, where the loaded and unloaded sections of the train are nearly evenly distributed and the respective total lengths are relatively short (within 1 L_{car}), both influences are approximated by decreasing the effective frictional coefficient to 0.005 in this study. It is important to note that in future iterations of the model, the influence of these two parameters could be separately simulated and examined in more detail to develop a more refined understanding. This approach not only provides a simplified initial representation but also offers the potential for more nuanced investigations as the model evolves.

Building upon the discussions in the previous sectors, it becomes apparent that the length of the gap significantly influences the internal flow structure within the gap itself, as well as the separation bubble generated by the airflow over the container behind it. For a 33% partially loaded freight train, the gap between the locomotive and the first container is around 20 feet

(33% of a carriage) and the gap between the containers for the following containers are 40 feet (66% of a carriage length). For the sake of simplicity and clarity, the length of a whole carriage will be denoted as L_{car} in the subsequent discussions. Consequently, it follows that the parameters allocated for the first gap (33% L_{car}) within the 1d code differ from those employed for the subsequent gaps (66% L_{car}). In the case of the first gap, the gap length is shorter than the reattachment length. Subsequently, the following container restricts the wake development, causing a significant portion of the airflow to be trapped within the gap. This distinction from the 40-foot gap results in a comparatively larger effective cross-sectional area in the 20-foot gap configuration. Consequently, this configuration exhibits reduced pressure loss, particularly in tandem with both the leading and trailing parts of the train. Moreover, the transition of air from the gap to the subsequent container occurs more smoothly in the 20-foot gap configuration.

This smoother flow transition leads to a smaller separation bubble size forming at the front of the container located after the 20-foot gap. It is important to note that unlike Chapter 5.4.3, where the bubble size could be directly measured using URANS simulations, the transient and highly turbulent nature of the flow field makes capturing the precise separation bubble shape challenging. Given that the relationship between separation bubble size and the pressure rise induced by pressure waves during train tunnel entry has been previously established and analysed, a best-fit method [17] is employed to deduce the parameters governing the separation bubble sizes for the containers after the 33% L_{car} and 66% L_{car} gaps. The predetermined parameters are implemented into the 1d code. Following modifications to the mesh system and boundary conditions, the 1d program is rerun to compute the pressure variation induced by a 33% loaded freight train with 4 containers. Pressure history curves inside the tunnel at 2 m, 4 m, 8 m, and 16 m from the tunnel portal, calculated from the modified 1d code, are compared with LES results, as shown in Figure 6.12. It is evident that the step-wise pressure rise caused by the partially loaded containers entering the tunnel is accurately simulated after modification. Moreover, the propagation and magnitude of these sub-pressure waves align well with the LES results. It is worth noting that parameters obtained from the best-fit method are utilised for validating the feasibility of the proposed algorithms in Section 6.2, while more comprehensive

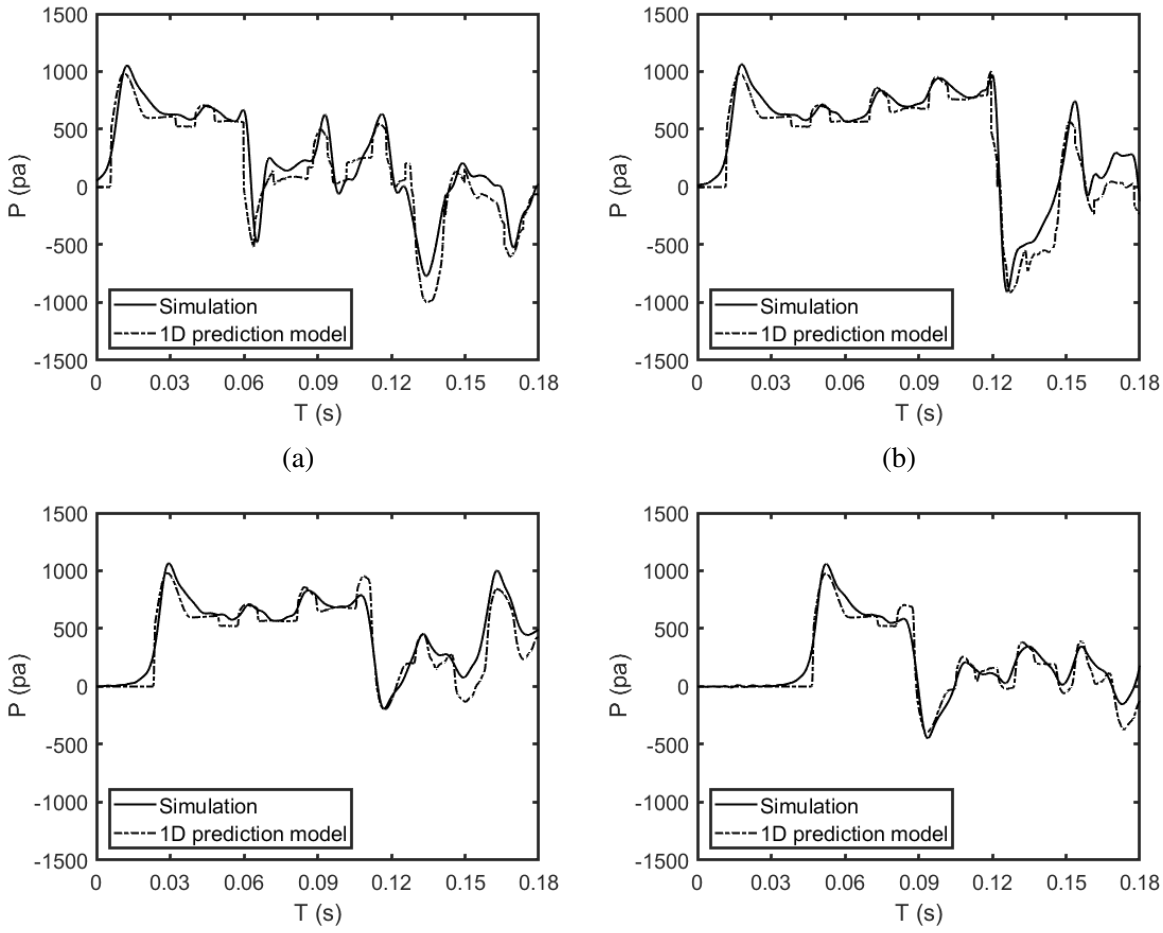


Figure 6.12: Comparison of pressure history curve obtained from 1d result and LES simulation (a) 2 m (b) 4 m (c) 8 m (d) 16 m.

analysis will be conducted in subsequent chapters through the examination of mean flow fields from LES simulations in freight trains featuring diverse loading configurations.

6.4 Parameterisation Study on Loading Configurations

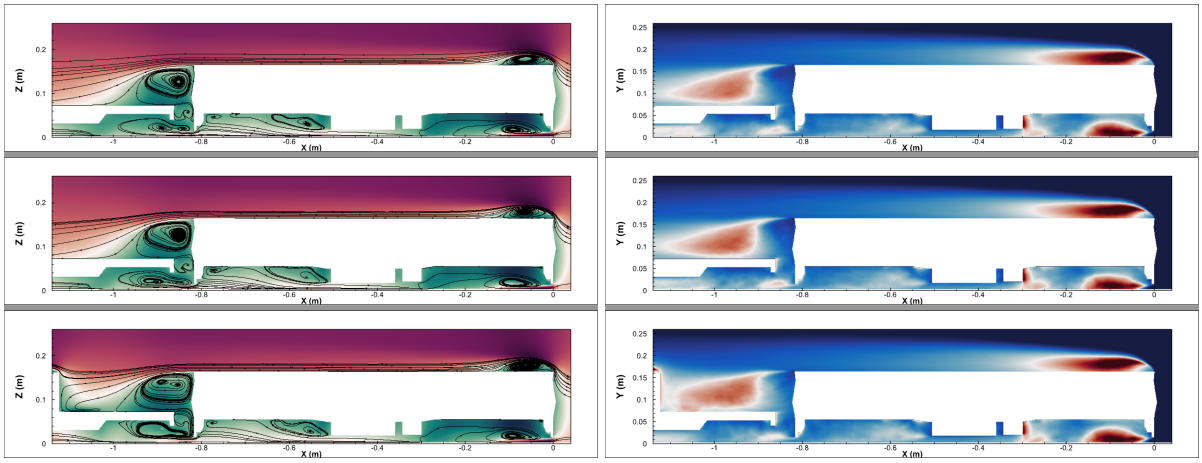
6.4.1 Streamline and Velocity field

Locomotive

Figure 6.13 and Figure 6.14 present the contours of the mean velocity field and TKE at Y=0 m and Z=0.09 m. The three sub-figures in each of these figures correspond to three loading configurations, where the rear carriage is fully unloaded, 0.66 loaded, and 0.33 loaded, resulting in gap distances between the locomotive and the loaded part equivalent to 1 L_{car}, 0.66 L_{car}, and 0.33 L_{car}, respectively. The subsequent figures in this chapter maintain the same order. The left side of the contours is colour by $\bar{u}$ (mean stream-wise velocity), while the right side is colour by TKE. TKE is calculated as the sum of root-mean-square velocity fluctuations in three directions (as defined in equation 6.5). This TKE parameter serves as a measure of the turbulence generation and overall turbulence intensity surrounding the train.

$$TKE = 0.5 \times (u'^2 + v'^2 + w'^2) \tag{6.5}$$

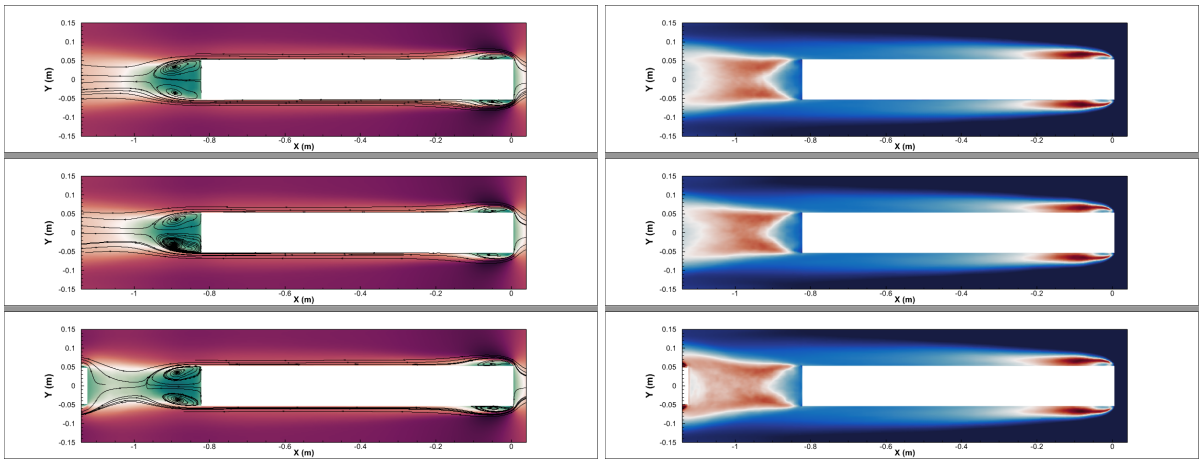
In the present study, it is observed that the loaded carriage is situated downstream of the locomotive, which leads to a very limited impact of the loading condition on the flow field in the vicinity of the locomotive. Three loading configurations are examined, and it is noteworthy that the recirculation at the head of the train and the wake, where the boundary layer separates (indicated by green shading in the velocity contours), exhibit a similar distribution and spatial extent across all these configurations. Moreover, an examination of the TKE reveals higher values at locations where vortices are generated and along the trajectory of vortex shedding. The region where turbulence is predominantly distributed at the head of the train extends from 0 m to approximately 0.3 m from the leading separation edge. Further investigation on the wake



(a) (b)

Figure 6.13: Velocity field of the locomotive at contour Y=0 m (From top to bottom corresponding to gap distances of 1 L_{car}, 0.66 L_{car}, and 0.33 L_{car} respectively) (a) mean u and streamline (b) TKE.

region of the locomotive will be provided in Section 6.4.1.



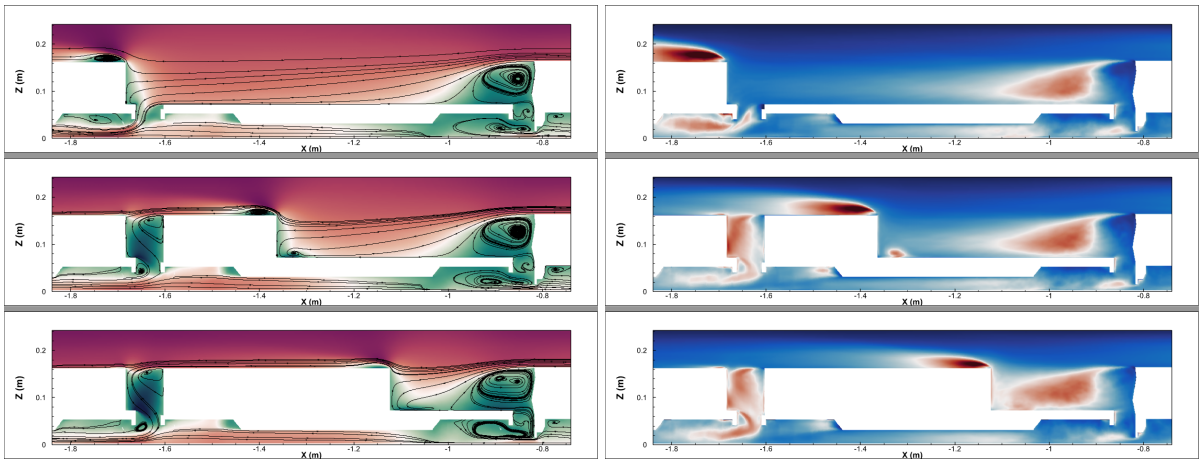
(a) (b)

Figure 6.14: Velocity field of the locomotive at contour Z=0.09 m (From top to bottom corresponding to gap distances of 1 L_{car}, 0.66 L_{car}, and 0.33 L_{car} respectively) (a) mean u and streamline (b) TKE.

Loaded Container 1

The mean velocity distribution and streamlines for container 1 at various contour positions are depicted in Figure 6.15 and 6.16. Each loading configuration of container 1 is presented separately to visualize the wake vortex formation as air flows over the leading carriage.

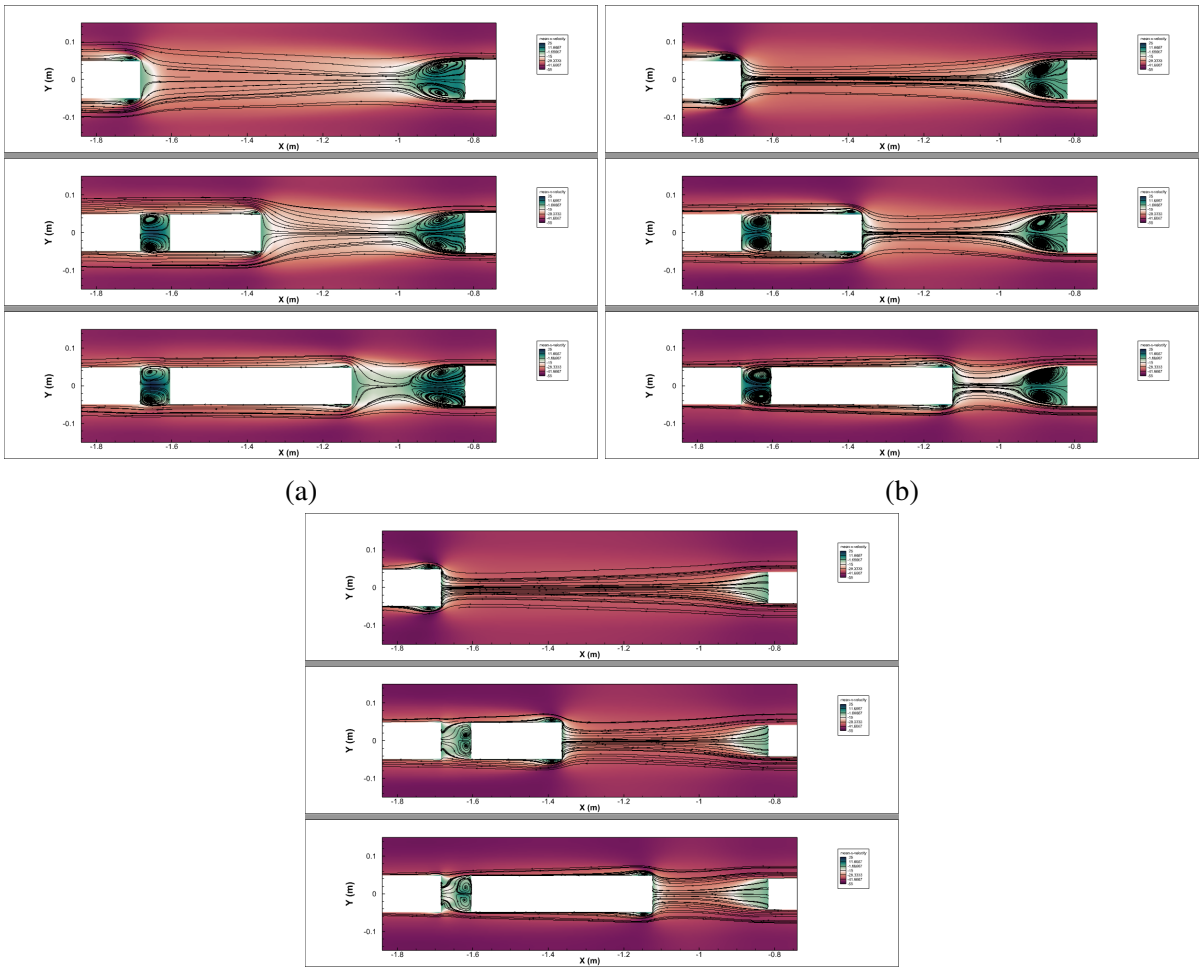
A consistent observation across all three loading configurations is the separation of the boundary layer at the end of the locomotive, resulting in the formation of large vortices. The length of the recirculation wake region is approximately 0.25 times the length of the container (0.25 L_{car}), which is shorter than the smallest gap size (0.33 L_{car}). In the cases with gap lengths of 0.33 and 0.66 L_{car}, the trailing container is positioned at the wake reattachment zone. Some of the air downwash from the leading container is obstructed by the trailing container, leading to the formation of a backflow region in front of it. For the 0.33 L_{car} gap case, where the gap is quite short, this backflow region connects with and influences the wake recirculation region. The contours in the figures illustrate that the length of the wake vortex is larger, with higher TKE compared with the other two cases.



(a) (b)

Figure 6.15: Velocity field of the second container at contour Y=0 m (a) mean u and streamline (b) TKE.

Figure6.17 provides a quantitative comparison of the mean velocity inside the gap. It is evident that the recirculation velocity at the wake vortex in the 0.33 L_{car} gap case is larger, while there is no difference between the other two cases. The velocity distribution profiles at measurement lines in front of the trailing container are similar for the 0.33 and 0.66 L_{car} gap cases (lines 4 and 8 in Figure6.17). Examining the velocity profile at lines 4 to 12 of the fully empty container provides insights into the flow development influenced by the leading container. As the distance from the leading container increases, the lower part of the air velocity (near the flatbed) gradually rises, approaching a value closer to the freestream velocity. This trend



(a) (b)

(c)

Figure 6.16: Velocity field of the second container (a) at contour Z=0.09 m (b) at contour Z=0.12 m (c) at contour Z=0.15 m.

indicates that the impact of the leading container on the trailing container diminishes with a larger gap distance.

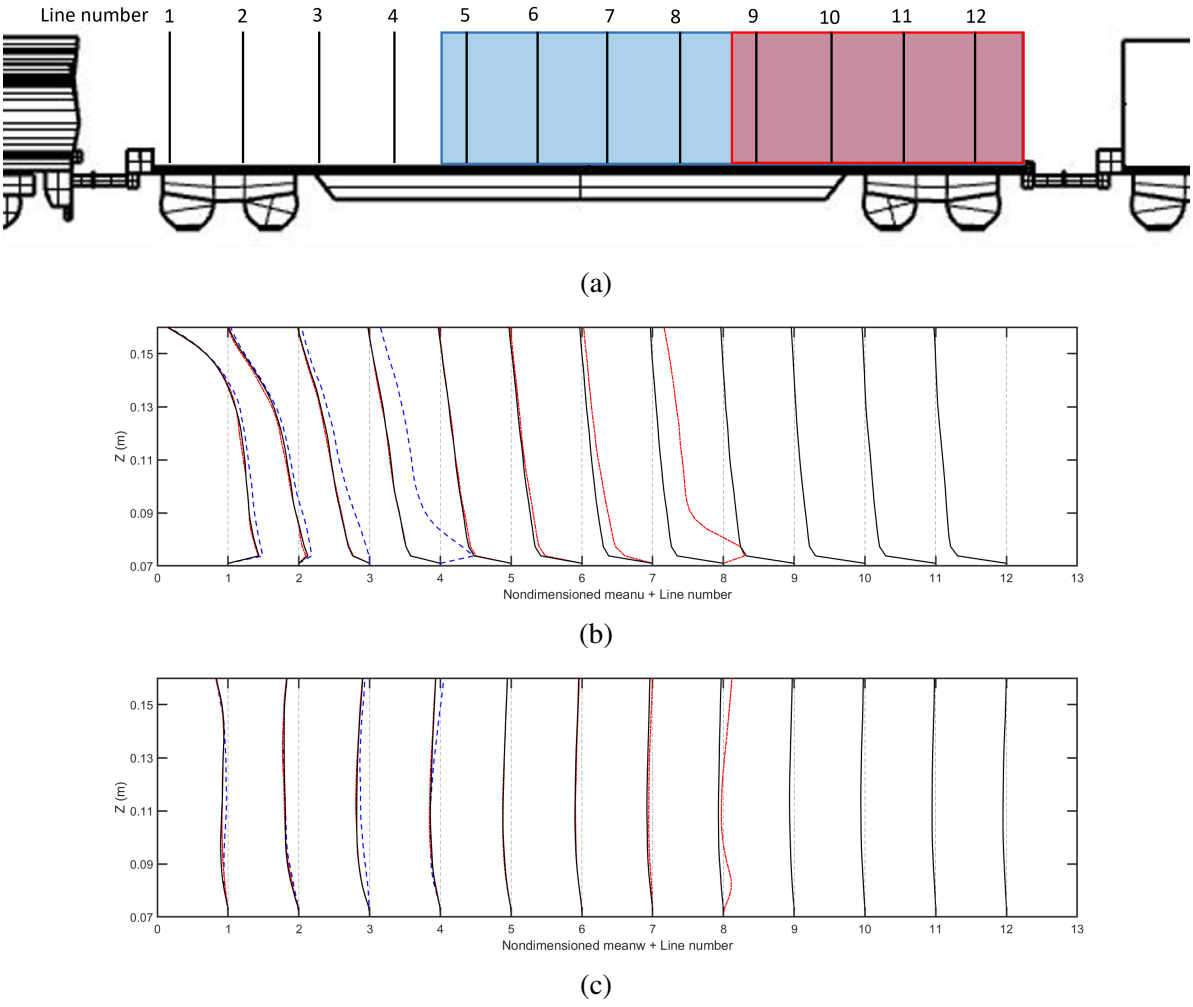


Figure 6.17: Comparison of velocity distribution at different measuring lines inside the gap (a) position of the 12 measuring lines (b) $\bar{u}$ (c) $\bar{w}$ (blue dash line: Gap = 33% L_{car}; red line: Gap = 66% L_{car};black line: Gap = 1 L_{car}).

Additionally, since the container itself constitutes a bluff body with a sharp leading edge, separation bubbles form at the top and sides of the container. The size of the separation bubble around the head of the trailing container significantly increases with a longer gap length. This observation aligns with the earlier discussion, where it was established that the oncoming flow velocity increases as the gap length becomes longer. Similar to the analytical approach outlined in Chapter 5.4.3, the heights of the separation bubbles at the top and sides of the container are summarised in Table 6.1. The position of the slices used to measure H_{R_c}/W_C and H_{S_c}/W_C are

at Y=0 m and Z=0.12m, which are approximately at the middle of container width and height. These heights are non-dimensionalised using the width of the container, denoted as W_c. These values will play a crucial role in calculating the effective blockage area at the containers. The separation bubble model for containers and the parameterization equation correlating H_{R_c}, H_{S_c}, and the gap length are further explored in Chapter 6.5.

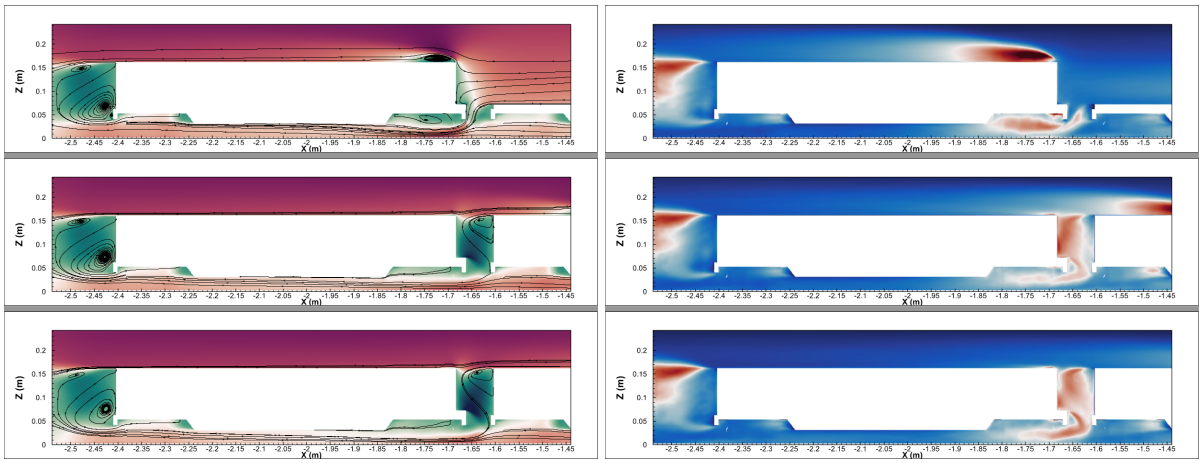
Gap Length	0.33 L_{car}	0.66 L_{car}	1 L_{car}
H_{R_c}/W_C	0.082	0.1327	0.158
H_{S_c}/W_C	0.071	0.1122	0.154

Table 6.1: The height of the separation bubble at the top and height of the container.

Loaded Container 2

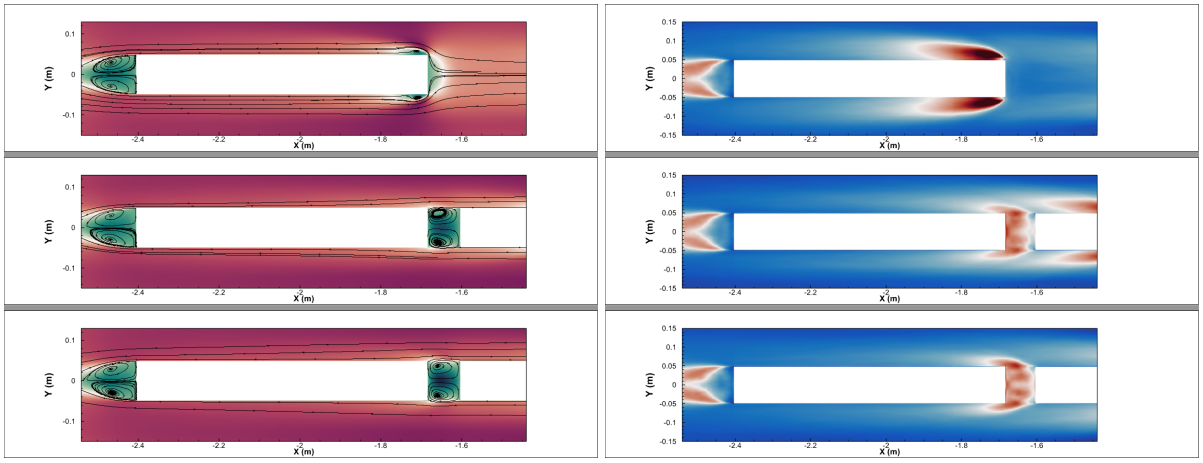
Figure 6.18 and Figure 6.19 display the contours of the mean velocity field and TKE distribution for the second container, taken at Y=0 m and Z=0.09 m. It is worth noting that despite the diverse loading configurations of the first container, the vortices engendered during the separation of the boundary layer at the tail of the second container manifest negligible disparities. In a broader context, both the velocity field and TKE distribution within the wake region of the last container demonstrate merely marginal fluctuations across the spectrum of loading configurations. To be more specific, wherein the TKE in the wake region exhibits a slightly higher magnitude for the freight train of which the gap of first container is 33% L_{car}. This phenomenon can be ascribed to the length disparity between cases with varying loading levels. Notably, in scenarios where wagons are more heavily laden, the distance from the leading edge of the container to the end of the train becomes more extensive. Consequently, the thickness of the boundary layer at the rear of the train, just before its separation, are different. It is conceivable that this variation in boundary layer thickness contributes to the slightly amplified TKE observed in the wake region of the less loaded freight train. These findings suggest the potential applicability of parameterisation equations that establish a relationship between the effective cross-sectional area and the gap size calculated from the first container to other sections of the freight train. The consistency observed

in the wake characteristics indicates that such parameterisation equations could potentially be extended and generalised for broader use for other parts of the train configuration in the 1d code.



(a) (b)

Figure 6.18: Velocity field of the second container at contour Y=0 m (From top to bottom corresponding to gap distances of 1 L_{car}, 0.66 L_{car}, and 0.33 L_{car} respectively) (a) mean u and streamline (b) TKE.



(a) (b)

Figure 6.19: Velocity field of the second container at contour Z=0.09 m (From top to bottom corresponding to gap distances of 1 L_{car}, 0.66 L_{car}, and 0.33 L_{car} respectively) (a) mean u and streamline (b) TKE.

To conduct a quantitative analysis of the velocity magnitude across various loading configurations, the variation of $\bar{u}$ is plotted along distinct lines positioned along the entire length of the freight train (Figure 6.21). Note that the stream wise direction of $\bar{u}$ is negative. From the figures, it is evident that the velocity characteristics in freight trains with partially loaded containers

differ from those observed in passenger trains due to the discontinuity of the train body caused by the varying loading conditions. Referenced by the method to identify the flow regions of passenger trains [22, 30], the velocity distribution around a intermodal container freight train can be characterised by a series of zones as follows:

1. Starting from the blunt head of the locomotive, the first separation bubble zone ($Zone_{S1}$) is formed, where the magnitude of the velocity is primarily influenced by the relative position of the measuring points with respect to the separation bubble.

2. Subsequently, a boundary layer zone ($Zone_{B1}$) follows, in which the magnitude of $|\bar{u}|$ gradually increases due to the development of the boundary layer.

3. As the airflow reaches the tail of the locomotive, the boundary layer separates, leading to the formation of a quasi-wake region ($Zone_{W1}$) at the gap.

4. The airflow then flows over the partially loaded container and generates the second separation bubble zone ($Zone_{S2}$).

5. Similarly, a second boundary layer zone ($Zone_{B2}$) develops along the body of the fully-loaded containers.

This pattern of velocity characterisation can be similarly deduced for scenarios involving more gaps and containers in a partially loaded freight train. Besides, it could be observed from the figure that there is an obvious 3d effect on $\bar{u}$ at $Zone_{S1}$ and $Zone_{S2}$. In the subsequent paragraph, a more detailed analysis and comparison of the velocity distribution among different loading scenarios at various positions are conducted.

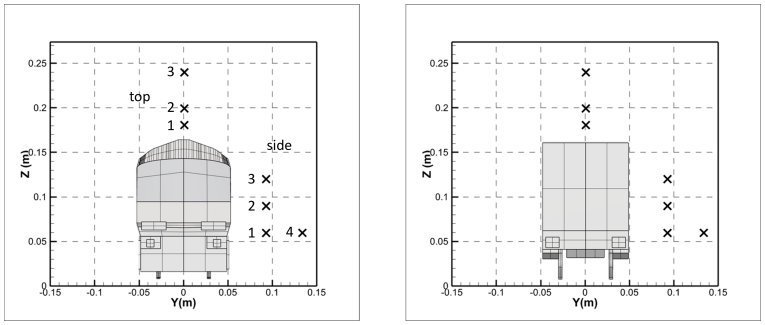


Figure 6.20: Position of measuring lines relative to the locomotive and container

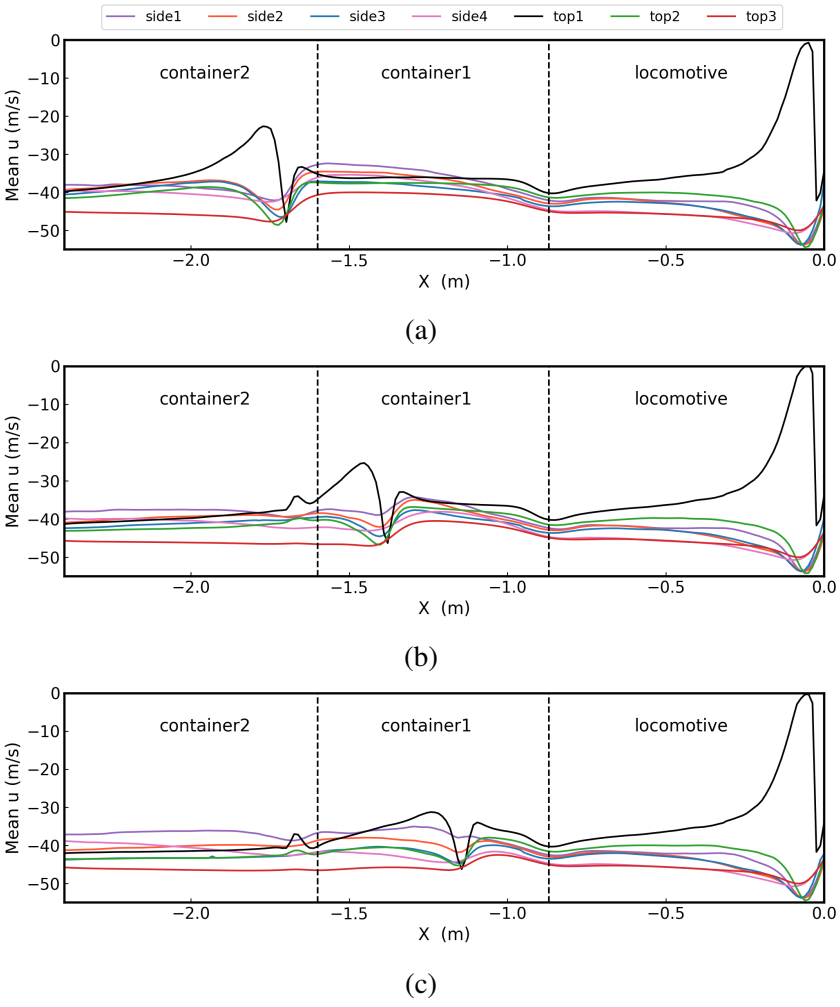


Figure 6.21: Distribution of mean u at different lines positioned along the train (a) 1 container empty (b) 0.66 container gap (c) 0.33 container gap.

The lines labelled as top1/2/3 are positioned at heights of 0.02/0.04/0.08 m above the train roof, respectively. Additionally, the lines labelled sides1/2/3 are situated 0.04m away from the train side, with varying heights of 0.06/0.09/0.12 m, respectively. Considering Z=0.6m

corresponds to a full scale of 1.5m, which is crucial for human safety, an additional measuring position (side4) is introduced at this height, located 0.08m away from the train side. The positions of these lines relative to the locomotive and container are clearly depicted in Figure 6.20. An intriguing observation emerges with regard to the velocity distribution along line top1, which is situated within the separation bubble ($Zone_{S1}$). This line passes through the centre of the separation bubble generated at the front of the locomotive, resulting in a velocity close to zero. Conversely, for the lines positioned outside the separation bubble, an acceleration is observed as the airflow passes over them.

To facilitate a comprehensive investigation of the velocity characteristics among train carriages with different loading configurations, the three carriages are demarcated as shadow regions in each sub-figure. In agreement with the conclusions drawn from the velocity contours, $\bar{u}$ at the locomotive exhibits minimal discrepancy across different loading configurations. Regarding the flow characteristics at the partially loaded containers, line top1 traverses the upper part of the separation bubble generated as the airflow passes over the container gap.

As anticipated, the larger gap induces a larger separation bubble at the top of the container, leading to line1 in Figure 6.21(a) being closer to the vortex centre and the velocity closer to zero. Conversely, line1 in Figure 6.21(b) and (c) is situated closer to the upper edge of the vortex, resulting in $\bar{u}$ being closer to the upstream flow velocity. The peak value of $\bar{u}$ of line top1 at the the separation bubble generated by the container changes from around -20/-24/-30 m/s when the gap changes from 1/0.66/0.33 of wagon length. Line top2 is positioned beyond the recirculation zones in each separation bubble region, while remaining within the boundary layer along the locomotive and container body.

The rest of the measuring lines, positioned outside the boundary layer and separation bubble, exhibit a uniform manner of velocity distribution and similar magnitudes. At the separation bubble zones ($Zone_{S1}$ and $Zone_{S2}$), noticeable velocity peak is observed due to flow acceleration around the separation bubble. At the boundary layer zones ($Zone_{B1}$ and $Zone_{B2}$), $|\bar{u}|$ gradually increases due to the thicken of the boundary layer, then gradually decreases at $Zone_{W1}$ as the distance to the locomotive tail increases.

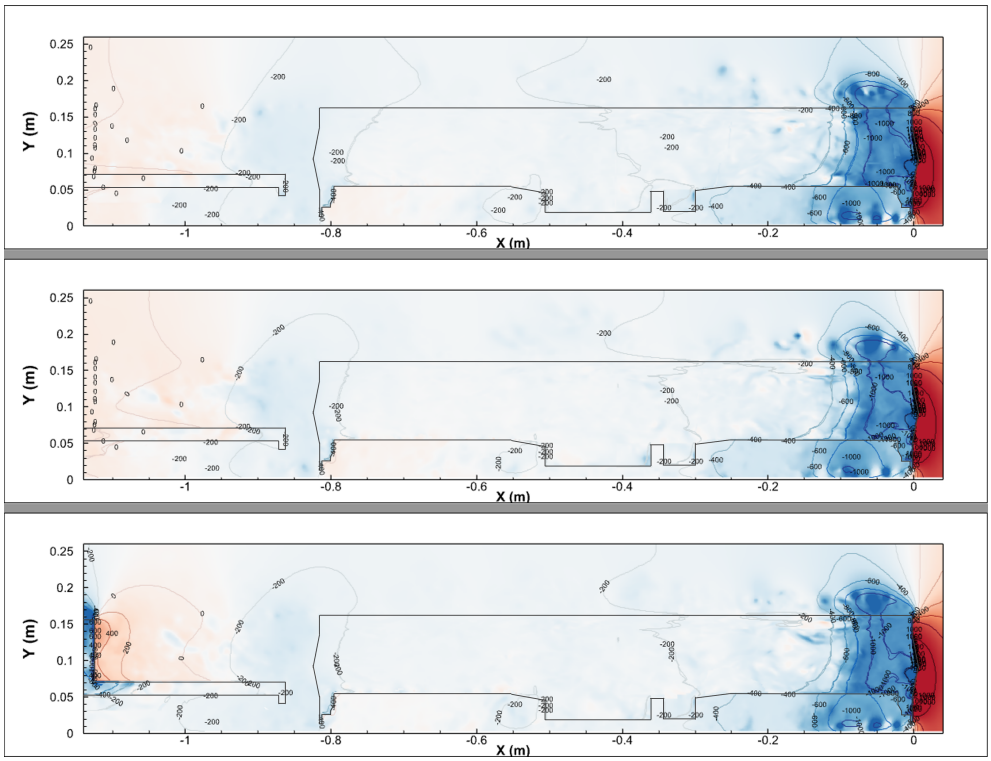


Figure 6.22: Pressure distribution around the locomotive (From top to bottom corresponding to gap distances of 1 L_{car}, 0.66 L_{car}, and 0.33 L_{car} respectively).

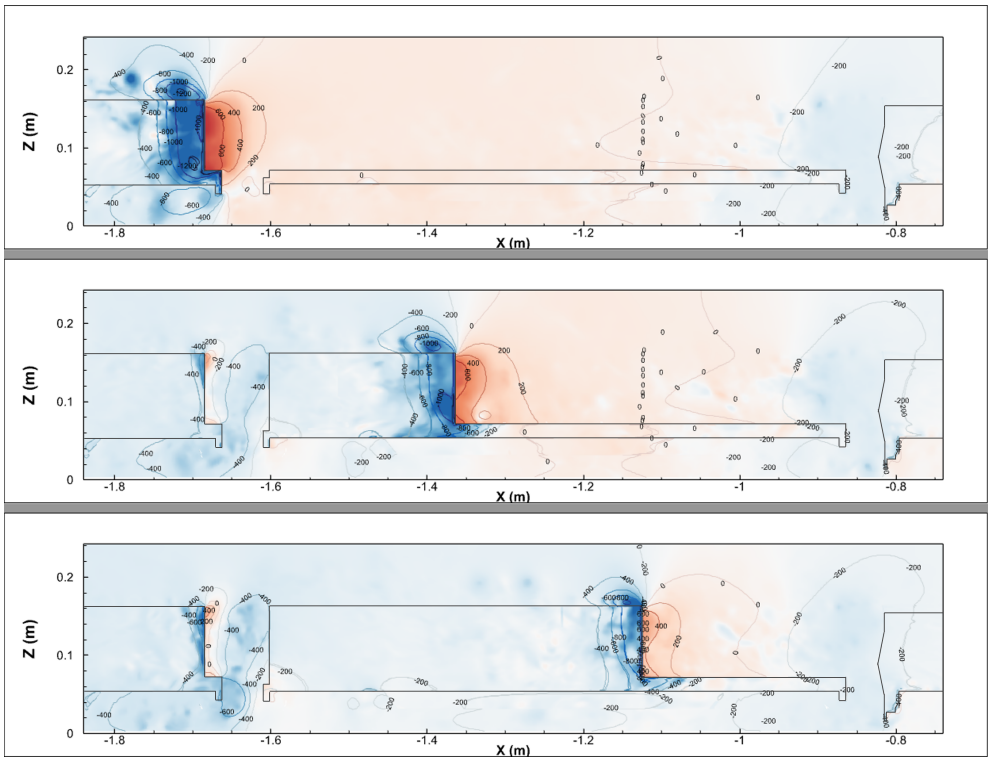


Figure 6.23: Pressure distribution around the first container (From top to bottom corresponding to gap distances of 1 L_{car}, 0.66 L_{car}, and 0.33 L_{car} respectively).

6.4.2 Pressure Distribution

The pressure distribution at each carriage is depicted in Figure 6.22 to 6.24. The pressure contours are color-coded based on instantaneous pressure, and contour lines are drawn using mean pressure data. Similar to the observations from velocity contours, the pressure distribution around the locomotive remains largely consistent across various loading configurations. The maximum pressure zone in front of the locomotive exceeds 1500Pa. The presence of a negative pressure region around the locomotive's head indicates the presence of a separation bubble.

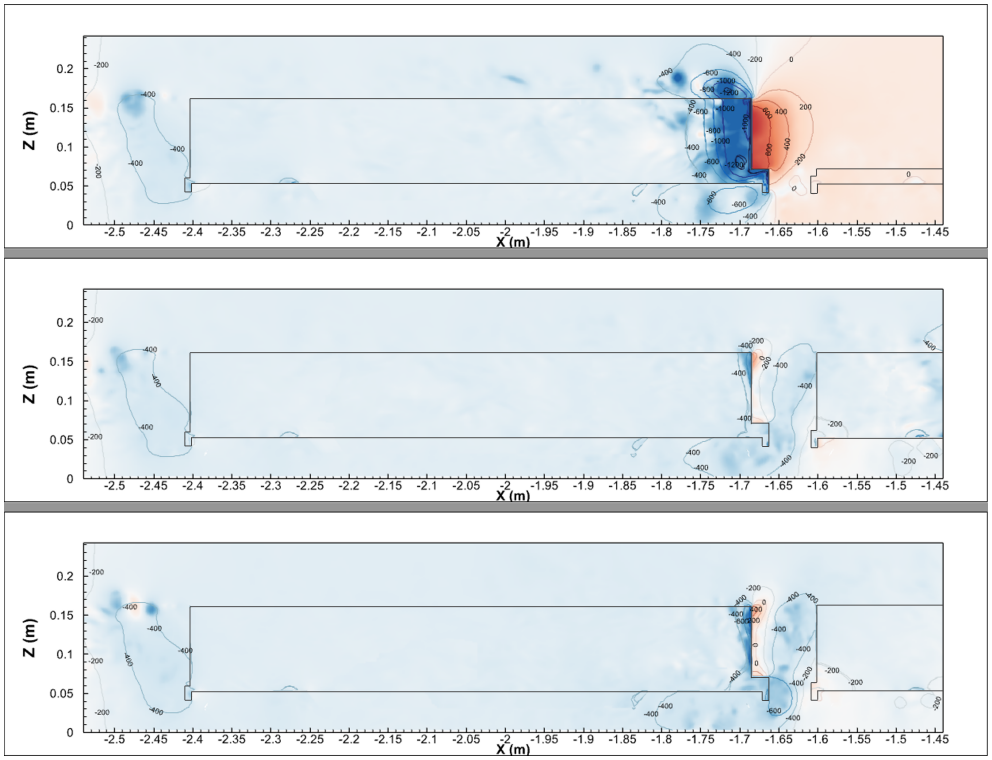


Figure 6.24: Pressure distribution around the second container (From top to bottom corresponding to gap distances of 1 L_{car}, 0.66 L_{car}, and 0.33 L_{car} respectively).

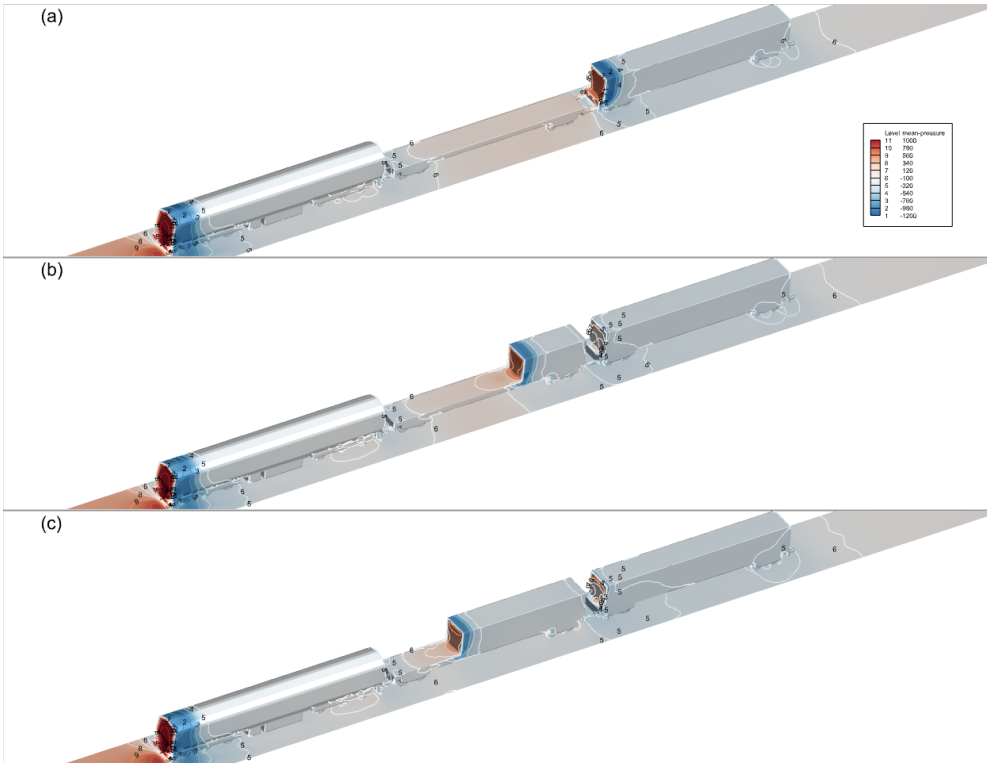


Figure 6.25: Distribution of mean pressure on train surface (a) 1 container empty (b) 0.66 container gap (c) 0.33 container gap.

In the case of the second carriage, illustrated in Figure6.23, a weak negative pressure zone can be observed behind the locomotive, corresponding to the wake recirculation ($Zone_{W1}$). Following this, a positive pressure region is observed in front of the loaded container. The maximum pressure ahead of the container increases with the gap length. Specifically, it rises from approximately 200 to 400/600 Pa as the gap increases from 33 to 66/100 % L_{car}. Furthermore, the length and magnitude of the negative pressure region around the head of the loaded container, corresponding to the second separation bubble region $Zone_{S2}$, also increase significantly with the unloaded gap's extension. To quantitatively compare the pressure variance, the mean pressure variance at different positions along the measuring lines is presented in Figure6.26. The positions of these measuring lines are illustrated in Figure6.20.

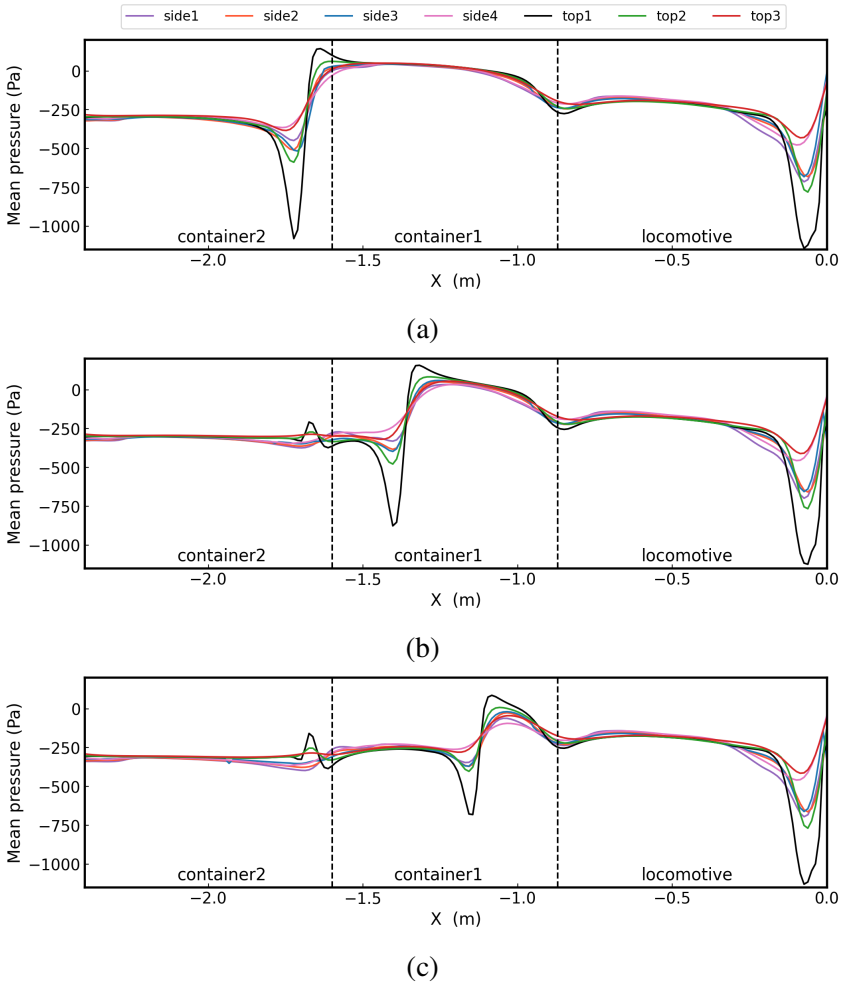


Figure 6.26: Distribution of mean pressure at different lines positioned along the train (a) 1 container empty (b) 0.66 container gap (c) 0.33 container gap.

6.5 Summary of the Parameters to be used in 1d Code

6.5.1 Parameterisation Equations

Following the discussion above, the model of flow motion over and inside the gap between two containers can be characterised into three parts, and a diagram visualising these regions is illustrated in Figure 6.27.

1. The recirculation region dominated by large wake vortices generated from the separation of the boundary layer from the leading container.

2. The air flow downwash from the tail of the leading container, blocked by the trailing

container, forming a recirculation in front of the trailing container and moving with the train as trapped air in the gap.

3. The outer part of the air can escape the gap and flow over the trailing container, forming a separation bubble region behind the sharp leading edge of the trailing container.

It is important to highlight that both region I and II contribute to the increase in the effective cross-sectional area of the unloaded part of the train. In Chapter 6.4, through flow visualisation and analysis, it was observed that for the case with a gap of 33 % L_{car}, the bottom of the trailing container is positioned at the transition between region I and II. Furthermore, for the case with a gap of 66 % L_{car}, the bottom of the trailing container is within region II. Consequently, the total effective blockage area for both cases is the sum of regions I and II. In Chapter 6.2, the effective blockage areas for 33 % L_{car} and 66 % L_{car} were determined using the best fit method, resulting in values of $0.85 \times E_{con}$ and $0.7 \times E_{con}$ respectively. Additionally, for a fully loaded freight train (gap length is zero), the effective cross-sectional area equals $1 \times E_{con}$. Assuming the upper edge of the trapped air flow trajectory is approximately a straight line, indicating an approximately linear relationship between the gap length and the effective blockage area, Thus one could estimate the fitting equation between gap length L_{gap} and effective blockage area at the gap,

$$E_{gap} = (1 - 0.4\frac{L_{gap}}{L_{car}})E_{con} \tag{6.6}$$

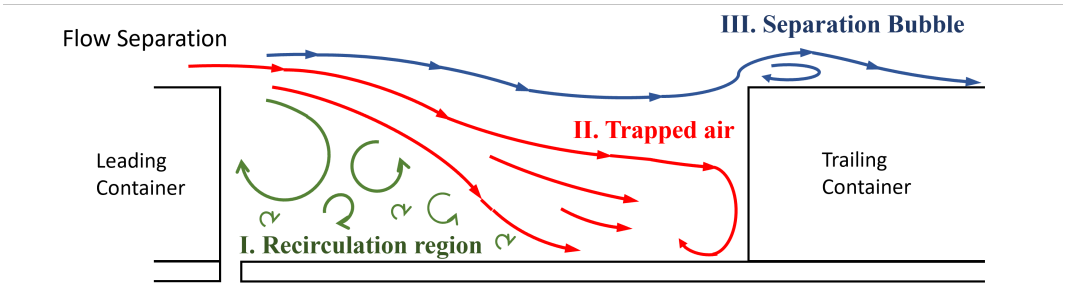
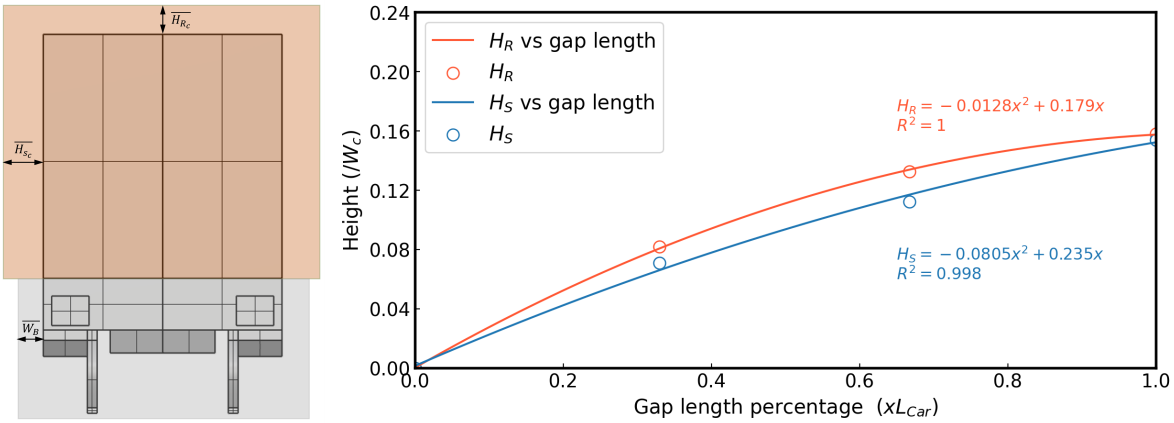


Figure 6.27: Diagram of flow characteristics inside the gap.

Region III represents the separation bubble region around the trailing container, and its size significantly impacts the pressure wave rise when the container enters the tunnel, especially for

sufficiently long gaps where the bubble size cannot be neglected. The separation bubble model for the containers is similar to that for the locomotive. The methodology to estimate the cross-sectional area of the loaded wagon considering the influence of separation bubble is illustrated in Figure 6.28(a). The effective cross-sectional area of bogie is the same as that used for the locomotive as given in chapter. 5.4.3. For the case this paper studied, the cross-sectional shape of the container is a rectangular. The effective blockage area of the container part is estimated to be a larger rectangular considering the separation bubble height H_R and H_S. Using the data in Chapter 6.4.1, the relationship equations among the heights of separation bubbles at the top and side of the container and the percentage gap length are consolidated in Figure 6.28(b). Thus by utilising the separation bubble height at different positions, one can estimate the effective radius of the separation bubble at the trailing container, denoted as r_{b_C}, after a certain distance of an unloaded gap. The squeezing effect induced by the tunnel cross-sectional area on r_{b_C} can be considered analogous to that on r_b. Consequently, the scale factor for the separation bubble formed at the container C_{b_C} effectively shares the same relationship equation for the locomotive, as given in Section 5.7.



(a) (b)

Figure 6.28: Estimation of the container's effective area

6.5.2 Validation of the Model

To evaluate the performance of the proposed methodology, the pressure time history curves

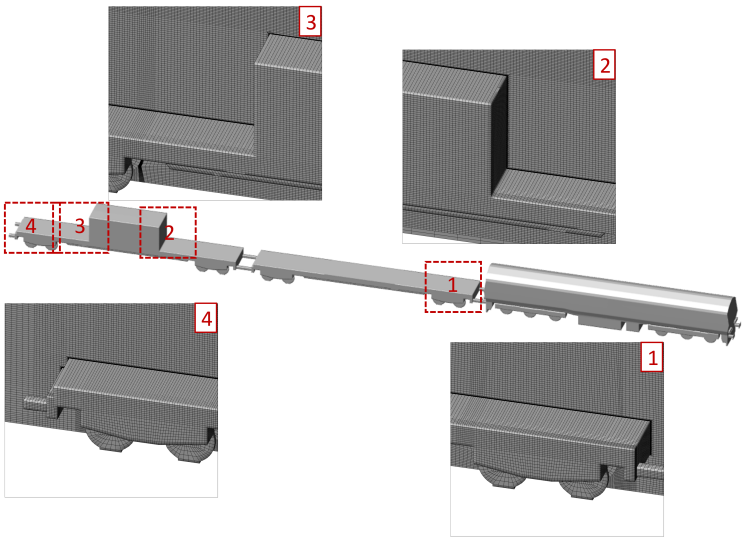


Figure 6.29: Surface mesh of freight train for validating loading configuration

obtained from the redeveloped 1d numerical model are compared against the CFD results using LES model. A freight train with new loading configuration, which is the first carriage fully unloaded and the second carriage 33% loaded, is adopted in the simulation. Besides, new tunnel configuration is adopted, of which cross-sectional area is $70m^2$. The mesh of the train surface and the loading situation of the freight train are illustrated in Figure 6.29.

The cross-sectional area, length and separation bubble r_b of the locomotive 66 used in the 1d programme are the same as given in Chapter. 5.4.3.The effective cross-sectional area of the gap between the locomotive and the first loaded container is calculated using the fitting equation. 6.6, which is approximately $0.418 \times E_{\text{con}}$. The separation bubble heights at the top and side of loaded container behind the gap are calculated using the parameterisation equation given in Figure 6.28. The reduced scale factor C_{b_C} for the effective blockage area of the container inside a $70m^2$ tunnel is calculated using equation. 5.24, which is found to be 0.76 with $\beta_E = 0.136$. Subsequently, r_{b_C} can be obtained from the effective blockage area of the container.

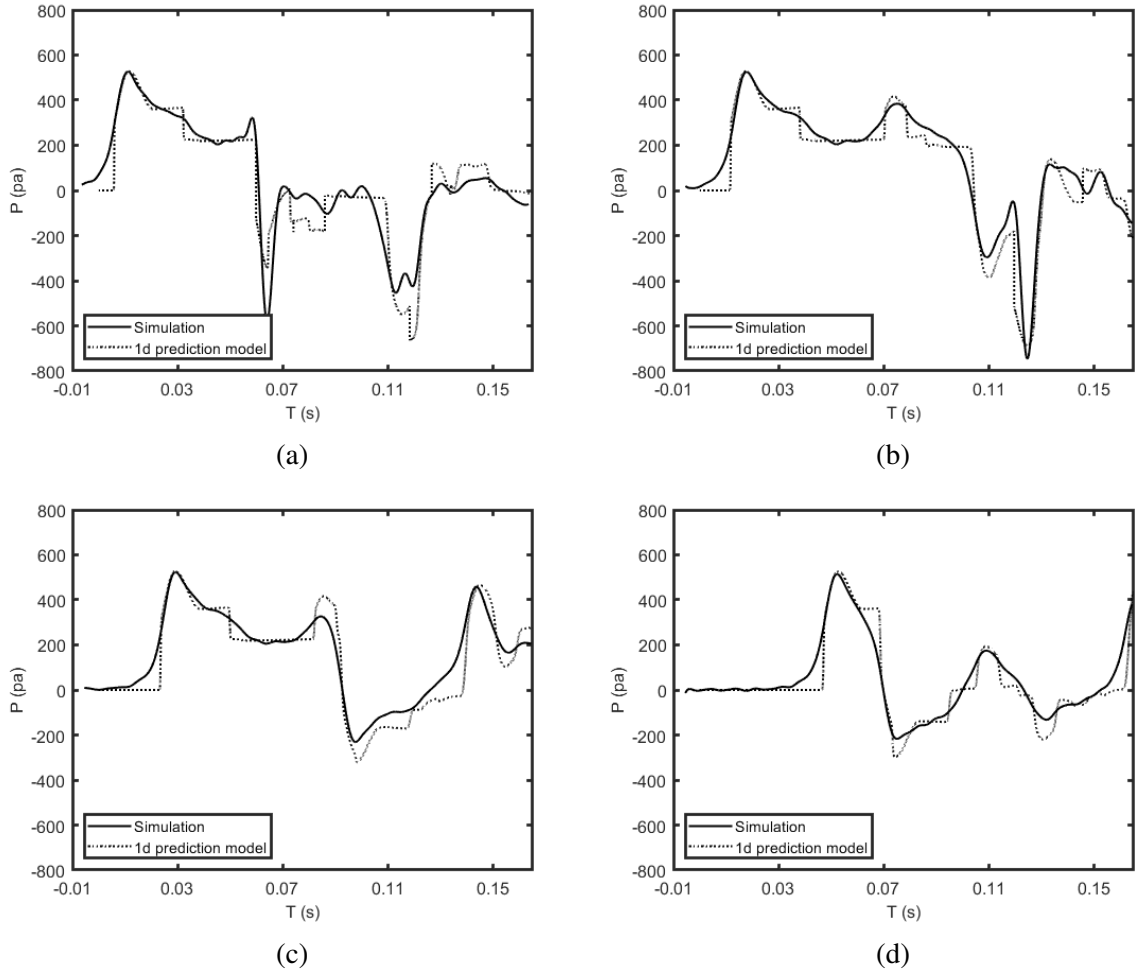


Figure 6.30: Comparison of pressure history curve for the validation case predicted by the redeveloped 1d programme and LES simulation (a) 2 m (b) 4 m (c) 8 m (d) 16 m from tunnel entrance.

Incorporating the predetermined parameters into the 1d programme, the comparison of pressure history curves at measuring points at 2 m, 4 m, 8 m, and 16 m inside the tunnel are illustrated in Figure 6.30. With the integration of these parameterization models into the modified 1d programme, it could be seen that the program can accurately predict the pressure wave patterns generated by freight trains under a certain range of loading configurations. However, limitations exist in the broader application of this parameterization model due to computational and experimental constraints. Nonetheless, this code serves as a foundational framework for further development of the model under various working conditions in future research.

6.6 Methodological Contributions

This section delineates the methodological contributions to the research concerning various loading configurations of freight trains and summarizes the principal findings drawn from this chapter. In this chapter, a thorough assessment was conducted to ascertain the suitability of different numerical models for accurately simulating the pressure waves generated as a partially loaded freight train enters a tunnel. The intricacies and crucial need for precise representation of separation regions and flow dynamics within the gap were elaborated upon. Subsequently, a redeveloped 1d programme was introduced, enhancing its capabilities to simulate the discontinuities in the train body and consequent pressure wave alterations induced by partial loading. Furthermore, a comprehensive parameterization study was executed, involving the relationship between predetermined parameters and gap length, through LES simulations. The flow regions are categorised, providing deeper insights into the pressure wave variations, and to conduct a quantitative investigation to expand the programme versatility across a spectrum of loading configurations. In summary, the study in this chapter yielded several noteworthy contributions:

(a) The 'step-like' increase in pressure rise (Δp_{fr}) resulting from the entry of a partially loaded freight train into the tunnel is linked to the compression and expansion pressure waves produced by the abrupt area change as unloaded gaps enter the tunnel. The flow pattern within these gaps can be categorised into three regions:

   (i) The recirculation region, dominated by large vortices separated from the leading container.

   (ii) The airflow down-wash from the leading container.

   (iii) The outer airflow passing over the trailing container, forming a separation bubble.

   The first two regions influence the effective blockage ratio of the unloaded part, subsequently affecting the separation bubble at the trailing container and the strength of the pressure waves. Therefore, accurately calculating these separations and flow patterns is crucial.

(b) The URANS model fails to accurately capture the pressure wave pattern and is not suitable for studying aerodynamic issues related to intermodal container freight trains in tunnels. URANS model tends to overestimate the length of the recirculation region separated from the leading container, where the direction of wall shear stress on the train surface aligns with the operational velocity of the train. Consequently, URANS underestimates the pressure rise caused by the frictional effects on the train surface. Additionally, the overestimation of wake vortex development within the gap by the URANS model leads to a larger effective blockage area, reducing the influence of area change on the generation of pressure waves resulting from the unloaded gaps.

(c) The direction of wall shear stress on the flatbed wagon, where wake recirculation region formed due to boundary layer separation at the end of leading container, is the same as the direction of train operation. Thus will result in a lower effective frictional coefficient, comparing to fully loaded containers without gaps and separation regions on train body.

(d) A redeveloped 1d program has been coded. This program introduces a new mesh system to address the complexity arising from moving containers with different loading configurations. Additionally, new boundary conditions have been implemented at the ends of containers to simulate airflow transitions from loaded to unloaded and vice versa. The program's ability to predict the pressure rise caused by a 33% partially loaded container entering a tunnel has been validated by comparing its results with LES simulations.

(e) The influence of loading configurations on flow patterns has been investigated using the LES method. Specifically, the boundary layer region typically identified for passenger trains, has been divided into quasi-'nose, boundary layer, and wake' regions, segmented by the loaded and unloaded parts of the containers. Differences in velocity peaks at the quasi-nose region of the container are observed due to variations in separation bubble sizes among different loading configurations.

(f) As the unloaded gap length increases, the effective blockage area of the gap decreases. When the gap length is approximately 33% of the locomotive length (L_{car}), a significant

amount of air becomes trapped in the gap, corresponding to an effective blockage area of 0.85 times the container's width (E_{con}). This value decreases approximately linearly to 0.7/0.55 E_{con} as the gap length increases to 66/100% L_{car}. Furthermore, the air velocity in front of the trailing container increases with longer gap lengths, approaching the free stream velocity (train speed). This generates a larger separation bubble where the air flows over the trailing container. The height of the separation bubble is measured, and its relationship with gap length is quantitatively studied.

(g) To enhance the versatility of the 1d code for different loading configurations, a parameterization study was conducted to derive equations describing the relationship between pre-determined parameters and gap length. The parameterization equation, summarised in this study, is applicable to a spectrum of loading configurations achieved by combining different unloaded gap lengths. This equips the code to swiftly and accurately estimate the pressure waves generated in freight train tunnel aerodynamics, accommodating various scenarios.

Chapter 7

Conclusions and Future Work

7.1 Introduction

This study has shown that the prediction of pressure wave patterns is highly sensitive to the accurate numerical resolution of the separation region occurring at the blunt train nose, within containers, and at gaps of unloaded sections. Achieving this accuracy necessitates exceptional mesh quality, substantial computational resources, and careful selection of appropriate numerical models. One of the primary objective of this research is to address these challenges by evaluating various numerical models and assessing their competence in capturing the intricacies of the separation regions. Quantitatively analyze and understand how alterations in head shape and loading configurations of freight trains influence the resulting pressure patterns as they traverse a tunnel. Furthermore, the primary goal is to synthesize these insights to develop an innovative 1d computational framework. This advanced programme is designed to tackle these problems and accurately simulate the pressure waves generated by partially loaded freight trains.

The conclusions drawn from this research are framed within the aims and objectives outlined in Chapter 1.3. Subsequently, this chapter delves into the existing limitations of this work and explores potential avenues for future research on freight train tunnel aerodynamics, elaborated further in Section 7.3.

7.2 Conclusions

Objective1: Undertaking a comprehensive literature review on freight train aerodynamics, and previous research on how freight trains have been considered in relation to the development of pressure waves when the train passes through a tunnel.

The review effectively collated current research on freight train tunnel aerodynamics, illuminating the research gap and the computational challenges associated with solving this problem.

- It was highlighted that a significant gap in research exists between the treatment of train tunnel aerodynamics for freight trains compared to passenger trains. While substantial research exists for passenger trains, there is a notable lack of studies focused on freight trains passing through tunnels.
- Due to the requirement of high mesh quality, restriction of computational resources, and the strict selection of numerical models, there is a complexity of numerically predicting pressure waves induced by a partially loaded intermodal container freight trains passing through tunnels, leading to a gap of research.
- The development of the 1d models are thoroughly summarised, showing that previous 1d models have shown inadequacies in accounting for the influence of a blunt train nose shapes and significant gaps on pressure waves, emphasizing the need for this research.

Objective2: Write a code based on the 1d unsteady compressible non-homotropic model, which is able to calculate the tunnel pressure wave generated by a passenger train. The accuracy of the code is validated by comparing with results presented in published research.

A 1d computational programme is developed based on the traditional 1d unsteady compressible non-isentropic model. Since the code is self-written, efforts are made to validate

the model accuracy within this 1d programme. To confirm the precise implementation of the model, the results are validated against previously published findings.

- The physical numerical model incorporated in this 1d programme considers the heat transfer and frictional effects between the air and the train, as well as tunnel walls. This model aligns with the approach utilised in widely adopted 1d commercial simulation programme in the global research community.
- The 1d programme encompasses the formulation of boundary conditions at the moving ends (train head and tail) and tunnel portals. The computational mesh is divided into several contracting and expanding sections, with lengths adapting as the train passes through the tunnel. Temporal discretization for time propagation is accomplished using the MOC method.
- Given that the 1d solver is self-developed, the programme accuracy is validated by comparing the results with previously published research on the pressure wave generated by a Talgol train passing through a tunnel. The results demonstrate that the code accurately predicts the magnitude of the pressure rise and drop caused by the train head and tail upon entering the tunnel. Furthermore, it effectively models the propagation and reflection of the pressure wave, affirming the successful implementation of the algorithm in the programme.

Objective3: Conduct 3D CFD simulations for freight trains entering a tunnel and validate results by comparing with the experimental results. The flow field around the blunt freight train head is analysed for the separation bubble model to be built into the 1d code.

LES and k-ω SST URANS models were utilised to simulate the development of the flow field. The obtained results were then compared with experimental data to validate their applicability in simulating the influence of the separation bubble on the initial pressure wave. Furthermore, a separation bubble model was developed to characterize the shape change of the effective cross-sectional area.

- Both numerical models were employed to analyze the flow field around the freight Class 66 locomotive in both open field and inside the tunnel. The results indicated that while the k-ω SST URANS model predicted a similar height of the separation bubble around Class 66 locomotive, it tended to over predict the length.
- The pressure wave curve predicted numerically using the URANS model was compared with experimental results from prior research. The maximum pressure rise, predicted using the k-ω SST URANS model, was found to be within an acceptable error range of 6%. This could be attributed to the additional pressure rise caused by the separation bubble, resulting from an increase in the effective blockage area, being closely related to the height rather than the length of the separation bubble.
- A separation bubble model was proposed to describe the separation bubble region. The model was developed by referencing the locomotive geometry and the flow field characteristics around the locomotive. The separation region was divided into three parts to calculate the total effective blockage area. This model provided the foundation for the parameterization study concerning the height of the separation bubble for each part and served as the physical model to be modified in the 1d programme.

Objective4: Modify the 1d code to consider the effective area change caused by the separation bubble. The pressure history curve measured from the modified 1d code is compared with experimental result.

The 1d programme written in Objective2 has been redeveloped. Modifications have been made on boundary conditions, equations governing flow around the train, and adaptive mesh sizes. The proposed separation bubble model, a key component identified in Objective 3, has been integrated into the code and thoroughly validated against experimental results. The robustness and applicability of this 1d code have been tested across various train shapes and tunnels.

- The governing equations for solving the boundary conditions at the train head have

been deduced and modified to account for the influence on velocity and pressure due to changes in area. Furthermore, additional terms have been incorporated to address flow characteristics in the annulus space between the train and tunnel.

- The separation bubble profile is represented using sine functions. Predefined parameters, including effective radius (r_b), length (L_b) and scale factor (C_b) of the separation bubble, have been integrated into the programme. The head mesh is designed to be adaptive to different mesh sizes, achieving mesh refinement in specific regions for a better fit to the shape without significantly increasing the total number of mesh points that need solving.
- Validation of the pressure history curve at various measuring points inside the tunnel, calculated using the redeveloped 1d programme, has been performed against experimental data. The results demonstrate the accurate prediction of the separation bubble influence on the pressure wave. Compared to the traditional 1d code, the maximum error has reduced from 43% to 4%, and the discrepancies in subsequent pressure changes caused by reflected pressure waves have also significantly decreased.
- Leveraging the results obtained from the parameterisation study on the pre-determined factors in Objective5, the robustness of the proposed model and the modified 1d programme have been tested by comparing with simulation results using the Class 70 locomotive and under different working conditions. The outcomes from the redeveloped code align well with the simulation results, providing valuable insights for the initial design of tunnels and freight locomotives.

Objective5: A parameterisation study is conducting using a generic freight train head model to obtain the relationship between the bluntness of the train head and the parameters used in the separation bubble model. The applicability of the model is tested and validated.

For achieving a wide range of applicability, a comprehensive parameterisation study involving predefined parameters (r_b, L_b, and C_b) has been conducted. The study aimed

to analyze the influence of bluntness and blockage ratio on these parameters, resulting in the relationship equations that were then tested on new working conditions.

- To quantitatively analyze the bluntness of the locomotive, the bluffness was controlled by adjusting the leading separation angle α and the sub-angle β. These angles represent the angles between the windward side and the vertical line of the roof and windshield region, respectively. The angle ranges were determined by referencing a wide array of freight locomotive types. Additionally, the influence of blockage ratio was investigated by choosing a tunnel cross-sectional area varying from 30 to $75m^2$, covering a range of single-line tunnel sizes that needed to account for the aerodynamic effect of freight trains.

- The impact of bluntness on separation bubble size was investigated through locomotive operation in an open field using the LES model. The LES model was chosen to ensure a more accurate fitting function for both the height and the length of the separation area. Flow field analysis around the locomotive revealed that increasing the leading edge angle effectively decreased the height and width of the separation bubble on both the roof and the sides of the train. Sensitivity analysis showed that 97.5 % of the total variance in the height of the separation bubble on the roof (H_R) could be explained by variations in α, and 82.8 % of the change in the separation bubble on the roof side (H_S) could be attributed to variations in β.

- The influence of blockage ratio on the scale factor C_b was explored through locomotive operation inside tunnels of various cross-sectional areas using the URANS numerical model. The URANS model was chosen due to its ability to clearly identify the shape of the separation bubble and its accuracy in simulating the maximum effective blockage area, as validated. The results showed that the separation bubble exerted a stronger squeezing effect on the separated region above the roof compared to that at the sides and bottom of the train. Overall, within the examined range, C_b decreased linearly with the increase of β_E.

- To ensure the 1d programme could simulate a wider range of locomotive types, fitting relationship equations among H_R, H_S, L_R, and L_S of the separation bubble with angles α and β were summarised. Additionally, to make the code suitable for more tunnel configurations, the relationship equation between C_b and blockage ratio β_E was obtained. The applicability of these fitting equations was validated on the simulation results of a Class 70 locomotive passing through a cross-sectional area of $60m^2$.

Objective6: To understand the flow field at the large gaps between containers and how it influences the pressure wave, 3d CFD simulations of a partially loaded freight train entering a tunnel are conducted using different numerical models.

Similar to objective3, both LES and k-ω SST URANS models were utilised to simulate the pressure wave generated when a 33 % partially loaded freight train passing through a tunnel. The obtained results were then compared to understand their applicability in simulating the flow separation at the end of the container and the vortices in between the gap. The mechanism of how loading configurations influence the initial pressure change is analysed through the numerical results.

- The freight train used in the parameterization study comprises a locomotive and two containers, with the first container being 33/66/100% unloaded. As the gap length increases, the air velocity ahead of the trailing container also increases, approaching the free stream velocity. Consequently, this leads to a higher pressure field in front of the trailing container and a larger separation bubble formed at the leading edge of the trailing container.
- Results demonstrate that the pressure rise (Δp_{fr}) exhibits a 'stepwise' pattern, caused by compression and expansion waves generated when the loaded and unloaded parts of the container enter the tunnel. Furthermore, the separation bubble generated due to the leading edge separation at the trailing container increases the magnitude of the compression wave when the container enters the tunnel. The size of the wake vortex

and the air trapped in the gap influence the effective blockage area of the unloaded part, subsequently affecting the strength of the pressure waves.

- Both LES and URANS numerical models are utilised for the simulations mentioned above. Upon comparing the obtained results, the URANS numerical model tends to overpredict the length of the vortex separated from the tail of the leading container, as well as the length for the wake to be fully developed. Thus it overestimates the effective cross-sectional area at the gap, significantly diminishing the influence of the unloaded gap on the pressure wave pattern. Consequently, it is not capable of accurately simulating the pressure rise caused by the partially loaded containers entering the tunnel, especially when the gap size is not long enough (less than 33/66% L_{CAR}). Therefore, subsequent numerical investigations on loading configurations are conducted using the LES numerical method.

Objective7: Add new boundary conditions and change the mesh and coordinate systems of the 1d code to simulate the discontinuities of the train body. The result obtained after modification is compared with the validated numerical result.

New boundary conditions have been incorporated into the code to model the airflow passing through gaps resulting from sudden changes in cross-sectional area due to varying load conditions. These discontinuities in the train body necessitated a partitioning of the mesh into numerous segments, the positions and lengths of which vary as the train moves. This complexity prompted the development of a new mesh system in the code. The pressure history curve at various measurement points within the tunnel, calculated using this refined code, has been validated against LES results.

- New boundary conditions have been introduced into the 1d programme to accurately represent the airflow transitioning between loaded and unloaded segments of the train. This addresses the discontinuities caused by partially loaded train bodies. The effective cross-sectional area at an unloaded gap (E_{gap}) encompasses the cumulative area of the platform, bogies, and the air trapped within the gap.

- The presence of discontinuities necessitated a modification of the mesh system surrounding the train. This alteration transformed the mesh system from being relatively stationary with respect to the ground to being relatively stationary with respect to the train itself. This change aimed to mitigate excessive expansion and contraction of meshes in each sub-mesh component during train movement. Corresponding adjustments were made to the governing equations to solve the flow at grid points within each sub-mesh component.
- The redeveloped 1d programme is validated by comparing the numerical result of a locomotive with four 33 % loaded containers passing through a tunnel using LES method. Due to the fact that the flow field calculated using LES method consists a high number of turbulent flow and transient coherent structures, which masks the overall shape of the core vortex. The effective cross-sectional area at the 33 % L_{car} and 66 % L_{car} gap and the effective frictional coefficient are estimated using a best-fit method. Results show that the stepwise increase pattern of pressure waves caused by the discontinuities of the partially loaded train body are well reproduced after the redevelopment of the 1d code.

Objective8: A parameterisation study is undertaken using a freight train with different loading configurations, to investigate the relationship among the predetermined parameters and the distance of the gap.

To improve the adaptability of the 1d code for various loading configurations, we conducted a parameterization study to investigate its influence on flow field and to characterise the correlation between effective blockage ratio of the gap, separation bubble size at the trailing container and gap length.

- The freight train used for parameterisation study consists of a locomotive and two containers, with the first container 33/66/100 % unloaded. With the increase of gap length, the upcoming air velocity in front of the trailing container increases and becomes closer to the free stream velocity. Thus leading to a higher pressure field

in front of the trailing container and larger separation bubble separated from the leading edge of the trailing container.

- The velocity distribution within the boundary layer region, as typically defined for passenger trains, is subdivided into specific zones due to the presence of partially loaded containers. These zones include the separation bubble zone at the container ($Zone_{S1}$), quasi-boundary layer zone ($Zone_{B1}$) along the container, and quasi-wake zone ($Zone_{W1}$) at the gap.
- Regardless of the different loading configurations, the size of the vortex generated at the wake region after the last container shows negligible disparities. This suggests the potential applicability of the parameterization equation obtained for the first container to other sections of the train. Moreover, there is more turbulence generated for a 33% loaded freight train due to the thicker boundary layer before separation.
- With an increase in the unloaded gap length, the effective blockage area of the gap linearly decreases. Additionally, the heights of the separation bubbles at the top and side of the trailing container are measured and summarised. Equations describing the relationship between these parameters and gap length are derived for the broader application of this 1d program to various loading configurations.

7.3 Limitations and Future Works

1. This study has developed a fundamental 1d programme, providing a foundational platform for the rapid simulation of pressure waves generated by partially loaded freight trains transiting through tunnels. Future research in freight train tunnel aerodynamics should endeavour to consider more intricate working conditions and diverse tunnel configurations, such as freight trains interacting within tunnels or tunnels equipped with ventilation shafts and entrance hoods.

2. A noteworthy research gap is evident in experimental investigations concerning freight trains passing tunnels, particularly in the context of partially loaded freight trains. The

available experimental data in this domain is markedly sparse, presenting substantial challenges for validating the numerical work expounded upon in Chapter 6. Existing experimental studies primarily involve 4 and 8 containers passing through a tunnel, demanding considerable computational capacity due to stringent mesh quality and resolution requisites for adequately resolving the influence of separation regions within the gaps. This demand on the computational resources makes achieving a numerical solution nearly unattainable. Subsequent research stands to benefit significantly from a more comprehensive range of experiments involving freight trains of varying lengths and diverse loading configurations.

3. Previous research has primarily relied on empirical parameters obtained through the 'best-fit' method to define the magnitude of the friction coefficient in 1d models. These empirical parameters have been derived from investigations on passenger trains. As discussed in chapter 6.3.1, for partially loaded freight trains, the presence of several separation regions at the front of locomotives/containers and on flatbed wagons significantly impacts wall shear stress, consequently affecting the friction coefficient. Due to the intricacies of the train model and time constraints in this study, a quantitative analysis of this influence was not conducted. However, further exploration of this phenomenon is warranted to enhance the proposed 1d model and gain deeper insights.

4. This research shows that URANS is insufficient in accurately considering the influence of diverse loading configurations on the initial pressure wave. Given the limitations of computational resources, conducting a thorough parameterization study using LES in this aspect is challenging. Since this research demonstrates that changes on pressure wave is intimately connected to separations within the gaps, it is clearly important that this is appropriately considered moving forward. Moreover, prior research on passenger trains has indicated that boundary layer separation at the end of the train is highly sensitive to the shape of the train tail and the train length. Consequently, further investigations on parameterization study of loading configurations are expected to comprehend the effects

of varying container types, the total length of upstream carriages, blockage ratio, and other relevant parameters.

References

[1] Times. *COMPULSORY PURCHASE SYSTEM REFORM FOLLOWING HYBRID BILL*. [Online; accessed 10-October-2013]. URL: https://www.kslaw.co.uk/site/library/kslaw_legal_news/Compulsory_Purchase_System_Reform_Following_Hybrid_Bill.

[2] CEN. *BS EN 14067-5:2021. Railway applications. Aerodynamics - Requirements and assessment procedures for aerodynamics in tunnels.* 2021.

[3] T. Liu, Z. Jiang, X. Chen, J. Zhang, and X. Liang. "Wave effects in a realistic tunnel induced by the passage of high-speed trains". In: *Tunnelling and Underground Space Technology* 86 (2019), pp. 224–235.

[4] Z. Liu, G. Chen, D. Zhou, Z. Wang, and Z. Guo. "Numerical investigation of the pressure and friction resistance of a high-speed subway train based on an overset mesh method". In: *Proceedings of the Institution of Mechanical Engineers, Part F: Journal of Rail and Rapid Transit* 235.5 (2021), pp. 598–615.

[5] G. Bouladon. "Technological forecasting applied to transport". In: *Futures* 2.1 (1970), pp. 15–23.

[6] J. A. Schetz. "Aerodynamics of high-speed trains". In: *Annual Review of fluid mechanics* 33 (2001), p. 371.

[7] G. railfreight. *UK FIRST RAIL FREIGHT ELECTRIFICATION TRIAL BOOSTS INDUSTRY NET ZERO AMBITIONS*. URL: https://www.gbrailfreight.com/uk-first-rail-freight-electrification-trial-boosts-industry-net-zero-ambitions/.

[8] D. Soper, C. Baker, and M. Sterling. “Assessing crosswind effects on a container freight train with differing container loading configurations”. In: *First International Conference in Numerical and Experimental Aerodynamics of Road Vehicles and Trains, Bordeaux, France*. 2014.

[9] X.-h. Li, J. Deng, D.-w. Chen, F.-f. Xie, and Y. Zheng. “Unsteady simulation for a high-speed train entering a tunnel”. In: *Journal of Zhejiang University-SCIENCE A* 12.12 (2011), pp. 957–963.

[10] M. Howe, M. Iida, and T. Fukuda. “Influence of an unvented tunnel entrance hood on the compression wave generated by a high-speed train”. In: *Journal of Fluids and Structures* 17.6 (2003), pp. 833–853.

[11] T.-h. Liu, H.-q. Tian, and X.-f. Liang. “Aerodynamic effects caused by trains entering tunnels”. In: *Journal of transportation engineering* 136.9 (2010), pp. 846–853.

[12] J.-L. Peters. “Aerodynamics of very high speed trains and maglev vehicles: state of art and future potential”. In: *Int. J. of Vehicle Design, Technological Advances in Vehicle Design Series, Impact of Aerodynamics on Vehicle Design* 3 (1983), pp. 308–341.

[13] Q.-S. Yang, J.-H. Song, and G.-W. Yang. “A moving model rig with a scale ratio of 1/8 for high speed train aerodynamics”. In: *Journal of Wind Engineering and Industrial Aerodynamics* 152 (2016), pp. 50–58.

[14] T. Ogawa and K. Fujii. “Numerical investigation of three-dimensional compressible flows induced by a train moving into a tunnel”. In: *Computers & Fluids* 26.6 (1997), pp. 565–585.

[15] D. Cross, B. Hughes, D. Ingham, and L. Ma. “A validated numerical investigation of the effects of high blockage ratio and train and tunnel length upon underground railway aerodynamics”. In: *Journal of Wind Engineering and Industrial Aerodynamics* 146 (2015), pp. 195–206.

[16] W. Woods and C. Pope. “A generalised flow prediction method for the unsteady flow generated by a train in a single-track tunnel”. In: *Journal of Wind Engineering and Industrial Aerodynamics* 7.3 (1981), pp. 331–360.

[17] A. Vardy and P. Reinke. “Estimation of train resistance coefficients in tunnels from measurements during routine operation”. In: *Proceedings of the Institution of Mechanical Engineers, Part F: Journal of Rail and Rapid Transit* 213.2 (1999), pp. 71–87.

[18] M.-P. William-Louis and R. Gregoire. “1-d calculations of pressure fluctuations outside and inside a pressure sealed high-speed trainset travelling through tunnels”. In: *TRANSAERO—A European Initiative on Transient Aerodynamics for Railway System Optimisation*. Springer, 2002, pp. 342–357.

[19] J. Fox and D. Henson. “THE PREDICTION OF THE MAGNITUDES OF PRESSURE TRANSIENTS GENERATED BY A TRAIN ENTERING A SINGLE TUNNEL.” In: *Proceedings of the Institution of Civil Engineers* 49.1 (1971), pp. 53–69.

[20] R. S. Raghunathan, H.-D. Kim, and T. Setoguchi. “Aerodynamics of high-speed railway train”. In: *Progress in Aerospace sciences* 38.6-7 (2002), pp. 469–514.

[21] P. Iliadis, D. Soper, C. Baker, and H. Hemida. “Experimental investigation of the aerodynamics of a freight train passing through a tunnel using a moving model”. In: *Proceedings of the Institution of Mechanical Engineers, Part F: Journal of Rail and Rapid Transit* 233.8 (2019), pp. 857–868.

[22] C. Baker, S. Dalley, T. Johnson, A. Quinn, and N. Wright. “The slipstream and wake of a high-speed train”. In: *Proceedings of the Institution of Mechanical Engineers, Part F: Journal of Rail and Rapid Transit* 215.2 (2001), pp. 83–99.

[23] M. Sterling, C. Baker, S. Jordan, and T. Johnson. “A study of the slipstreams of high-speed passenger trains and freight trains”. In: *Proceedings of the Institution of Mechanical Engineers, Part F: Journal of Rail and Rapid Transit* 222.2 (2008), pp. 177–193.

[24] D. Soper, C. Baker, and M. Sterling. “Experimental investigation of the slipstream development around a container freight train using a moving model facility”. In: *Journal of Wind Engineering and Industrial Aerodynamics* 135 (2014), pp. 105–117.

[25] S. Huang, H. Hemida, and M. Yang. “Numerical calculation of the slipstream generated by a CRH2 high-speed train”. In: *Proceedings of the Institution of Mechanical Engineers, Part F: Journal of Rail and Rapid Transit* 230.1 (2016), pp. 103–116.

[26] C.-H. Shin and W.-G. Park. “Numerical study of flow characteristics of the high speed train entering into a tunnel”. In: *Mechanics Research Communications* 30.4 (2003), pp. 287–296.

[27] D. Flynn, H. Hemida, D. Soper, and C. Baker. “Detached-eddy simulation of the slipstream of an operational freight train”. In: *Journal of Wind Engineering and Industrial Aerodynamics* 132 (2014), pp. 1–12.

[28] G. Chen, X.-B. Li, Z. Liu, D. Zhou, Z. Wang, X.-F. Liang, and S. Krajnovic. “Dynamic analysis of the effect of nose length on train aerodynamic performance”. In: *Journal of Wind Engineering and Industrial Aerodynamics* 184 (2019), pp. 198–208.

[29] Z. Liu, D. Zhou, D. Soper, G. Chen, H. Hemida, Z. Guo, and X. Li. “Numerical investigation of the slipstream characteristics of a maglev train in a tunnel”. In: *Proceedings of the Institution of Mechanical Engineers, Part F: Journal of Rail and Rapid Transit* 237.2 (2023), pp. 179–192.

[30] C. J. Baker, A. Quinn, M. Sima, L. Hoefener, and R. Licciardello. “Full-scale measurement and analysis of train slipstreams and wakes. Part 1: Ensemble averages”. In: *Proceedings of the Institution of Mechanical Engineers, Part F: Journal of Rail and Rapid Transit* 228.5 (2014), pp. 451–467.

[31] S. Krajnović. “Optimization of aerodynamic properties of high-speed trains with CFD and response surface models”. In: *The Aerodynamics of Heavy Vehicles II: Trucks, Buses, and Trains*. Springer, 2009, pp. 197–211.

[32] X.-D. Chen, T.-H. Liu, X.-S. Zhou, W.-h. Li, T.-Z. Xie, and Z.-W. Chen. "Analysis of the aerodynamic effects of different nose lengths on two trains intersecting in a tunnel at 350 km/h". In: *Tunnelling and Underground Space Technology* 66 (2017), pp. 77–90.

[33] Munoz-Paniagua, J. Jorge, A. García, and Crespo. "Genetically aerodynamic optimization of the nose shape of a high-speed train entering a tunnel". In: *Journal of Wind Engineering and Industrial Aerodynamics* 130 (2014), pp. 48–61.

[34] Munoz-Paniagua, J. Jorge, and A. García. "Aerodynamic drag optimization of a high-speed train". In: *Journal of Wind Engineering and Industrial Aerodynamics* 204 (2020), p. 104215.

[35] J. Niu, Y. Wang, D. Wu, and F. Liu. "Comparison of different configurations of aerodynamic braking plate on the flow around a high-speed train". In: *Engineering Applications of Computational Fluid Mechanics* 14.1 (2020), pp. 655–668.

[36] Z. Guo, T. Liu, Z. Chen, Z. Liu, A. Monzer, and J. Sheridan. "Study of the flow around railway embankment of different heights with and without trains". In: *Journal of Wind Engineering and Industrial Aerodynamics* 202 (2020), p. 104203.

[37] J. Zhang, A. Adamu, X.-c. Su, Z.-h. Guo, and G.-j. Gao. "Effect of simplifying bogie regions on aerodynamic performance of high-speed train". In: *Journal of Central South University* 29.5 (2022), pp. 1717–1734.

[38] H. Hemida and C. Baker. "Large-eddy simulation of the flow around a freight wagon subjected to a crosswind". In: *Computers & Fluids* 39.10 (2010), pp. 1944–1956.

[39] Z. Guo, T. Liu, Z. Liu, X. Chen, and W. Li. "An IDDES study on a train suffering a crosswind with angles of attack on a bridge". In: *Journal of Wind Engineering and Industrial Aerodynamics* 217 (2021), p. 104735.

[40] H. Hemida and S. Krajnović. "LES study of the influence of a train-nose shape on the flow structures under cross-wind conditions". In: (2008).

[41] C. Baker. "The simulation of unsteady aerodynamic cross wind forces on trains". In: *Journal of wind engineering and industrial aerodynamics* 98.2 (2010), pp. 88–99.

[42] Z. Guo, T. Liu, M. Yu, Z. Chen, W. Li, X. Huo, and H. Liu. "Numerical study for the aerodynamic performance of double unit train under crosswind". In: *Journal of Wind Engineering and Industrial Aerodynamics* 191 (2019), pp. 203–214.

[43] C. E. A. Reyes, D. Rocchi, G. Tomasini, M. I. Sánchez, and M. Artano. "Effects of different aerodynamic configurations on crosswind stability of a conventional train". In: *Journal of Wind Engineering and Industrial Aerodynamics* 242 (2023), p. 105588.

[44] D. Zhou, C. Xia, L. Wu, and S. Meng. "Effect of the wind speed on aerodynamic behaviours during the acceleration of a high-speed train under crosswinds". In: *Journal of Wind Engineering and Industrial Aerodynamics* 232 (2023), p. 105287.

[45] Z. Chen, T. Liu, Z. Jiang, Z. Guo, and J. Zhang. "Comparative analysis of the effect of different nose lengths on train aerodynamic performance under crosswind". In: *Journal of Fluids and Structures* 78 (2018), pp. 69–85.

[46] G. Matschke and C. Heine. "Full scale tests on side wind effects on trains. Evaluation of aerodynamic coefficients and efficiency of wind breaking devices". In: *TRANSAERO—A European Initiative on Transient Aerodynamics for Railway System Optimisation*. Springer. 2002, pp. 27–38.

[47] X. He and S. Zou. "Advances in wind tunnel experimental investigations of train–bridge systems". In: *Tunnelling and Underground Space Technology* 118 (2021), p. 104157.

[48] D. Ouyang, W. Yang, E. Deng, Y. Wang, X. He, and L. Tang. "Comparison of aerodynamic performance of moving train model at bridge–tunnel section in wind tunnel with or without tunnel portal". In: *Tunnelling and Underground Space Technology* 135 (2023), p. 105030.

[49] Z. Sun, H. Dai, H. Hemida, T. Li, and C. Huang. "Safety of high-speed train passing by windbreak breach with different sizes". In: *Vehicle system dynamics* 58.12 (2020), pp. 1935–1952.

[50] T. Gilbert, C. Baker, and A. Quinn. "Aerodynamic pressures around high-speed trains: the transition from unconfined to enclosed spaces". In: *Proceedings of the Institution of Mechanical Engineers, Part F: Journal of Rail and Rapid Transit* 227.6 (2013), pp. 609–622.

[51] M. Bellenoue, V. Moriniere, and T. Kageyama. "Experimental 3-D simulation of the compression wave, due to train–tunnel entry". In: *Journal of Fluids and Structures* 16.5 (2002), pp. 581–595.

[52] M. L. MUNJAL, M. Vorländer, P. Költzsch, M. Ochmann, A. Cummings, W. Maysenhölder, and W. Arnold. *Formulas of acoustics*. Springer Science & Business Media, 2008.

[53] P. Iliadis. "Aerodynamics of a freight train passing through a tunnel". PhD thesis. University of Birmingham, 2019.

[54] C.-R. Chu, S.-Y. Chien, C.-Y. Wang, and T.-R. Wu. "Numerical simulation of two trains intersecting in a tunnel". In: *Tunnelling and Underground Space Technology* 42 (2014), pp. 161–174.

[55] B. P. Rochard and F. Schmid. "A review of methods to measure and calculate train resistances". In: *Proceedings of the Institution of Mechanical Engineers, Part F: Journal of Rail and Rapid Transit* 214.4 (2000), pp. 185–199.

[56] A. Baron, M. Mossi, and S. Sibilla. "The alleviation of the aerodynamic drag and wave effects of high-speed trains in very long tunnels". In: *Journal of wind engineering and industrial aerodynamics* 89.5 (2001), pp. 365–401.

[57] Z. Cao, S. Yao, D. Chen, P. Lin, and X. Deng. "An Aerodynamic Force Computation Method of High Speed Trains Based on Pressure Distribution". In: *Science Technol Eng* 17.5 (2017), pp. 289–297.

[58] A. Vardy. "Aerodynamic drag on trains in tunnels part 1: synthesis and definitions". In: *Proceedings of the Institution of Mechanical Engineers, Part F: Journal of Rail and Rapid Transit* 210.1 (1996), pp. 29–38.

[59] T. W. Muld, G. Efraimsson, and D. S. Henningson. “Wake characteristics of high-speed trains with different lengths”. In: *Proceedings of the Institution of Mechanical Engineers, Part F: Journal of Rail and Rapid Transit* 228.4 (2014), pp. 333–342.

[60] J.-K. Choi and K.-H. Kim. “Effects of nose shape and tunnel cross-sectional area on aerodynamic drag of train traveling in tunnels”. In: *Tunnelling and Underground Space Technology* 41 (2014), pp. 62–73.

[61] J. HE, Z.-g. YANG, X.-m. TAN, D.-j. ZHANG, and X.-l. WU. “Aerodynamic drag optimization of subway train head with speed of 160 km/h”. In: *Journal of ZheJiang University (Engineering Science)* 51.10 (2017), pp. 2030–2038.

[62] J. Moon, S. Kim, and H. Kwon. “A study on the aerodynamic drag reduction of high-speed train using bogie side fairing”. In: *Journal of computational fluids engineering* 19.1 (2014), pp. 41–46.

[63] A. Ido, Y. Kondo, T. Matsumura, M. Suzuki, and T. Maeda. “Wind tunnel tests to reduce aerodynamic drag of trains by smoothing the under-floor construction”. In: *Quarterly Report of RTRI* 42.2 (2001), pp. 94–97.

[64] TSI. “Commission Regulation (EU) No 1302/2014 of 18 November 2014 concerning a technical specification for interoperability relating to the rolling stock — locomotives and passenger rolling stock subsystem of the rail system in the European Union”. In: (2023).

[65] M. Rabani and A. K. Faghih. “Numerical analysis of airflow around a passenger train entering the tunnel”. In: *Tunnelling and Underground Space Technology* 45 (2015), pp. 203–213.

[66] Y.-Y. Ko, C.-H. Chen, T. Hoe, and S.-T. Wang. “Field measurements of aerodynamic pressures in tunnels induced by high speed trains”. In: *Journal of wind engineering and industrial aerodynamics* 100.1 (2012), pp. 19–29.

[67] H. Zhang, C. Zhu, M. Liu, W. Zheng, S. You, B. Li, and P. Xue. "Mathematical modeling and sensitive analysis of the train-induced unsteady airflow in subway tunnel". In: *Journal of Wind Engineering and Industrial Aerodynamics* 171 (2017), pp. 67–78.

[68] J. Mok and J. Yoo. "Numerical study on high speed train and tunnel hood interaction". In: *Journal of wind engineering and industrial aerodynamics* 89.1 (2001), pp. 17–29.

[69] M. Howe. "On the design of a tunnel-entrance hood with multiple windows". In: *Journal of sound and vibration* 273.1-2 (2004), pp. 233–248.

[70] M. Bellenoue, B. Auvity, and T. Kageyama. "Blind hood effects on the compression wave generated by a train entering a tunnel". In: *Experimental Thermal and Fluid Science* 25.6 (2001), pp. 397–407.

[71] X.-t. Xiang and L.-p. Xue. "Tunnel hood effects on high speed train-tunnel compression wave". In: *Journal of Hydrodynamics, Ser. B* 22.5 (2010), pp. 940–947.

[72] T.-h. Liu, H.-q. Tian, and X.-f. Liang. "Design and optimization of tunnel hoods". In: *Tunnelling and Underground Space Technology* 25.3 (2010), pp. 212–219.

[73] D. Uystepruyst, M. William-Louis, and F. Monnoyer. "3D numerical design of tunnel hood". In: *Tunnelling and underground space technology* 38 (2013), pp. 517–525.

[74] P. Xue, S. You, J. Chao, and T. Ye. "Numerical investigation of unsteady airflow in subway influenced by piston effect based on dynamic mesh". In: *Tunnelling and Underground Space Technology* 40 (2014), pp. 174–181.

[75] J.-Y. Kim and K.-Y. Kim. "Effects of vent shaft location on the ventilation performance in a subway tunnel". In: *Journal of Wind Engineering and Industrial Aerodynamics* 97.5-6 (2009), pp. 174–179.

[76] M.-T. Ke, T.-C. Cheng, and W.-P. Wang. "Numerical simulation for optimizing the design of subway environmental control system". In: *Building and Environment* 37.11 (2002), pp. 1139–1152.

[77] S. Krajnovic and L. Davidson. “Large-eddy simulation of the flow around a bluff body”. In: *AIAA journal* 40.5 (2002), pp. 927–936.

[78] S. Krajnović and L. Davidson. “Flow around a simplified car, part 1: large eddy simulation”. In: (2005).

[79] S. Krajnović and L. Davidson. “Flow around a simplified car, part 2: understanding the flow”. In: (2005).

[80] Y. Zhuang and X. Lu. “Numerical investigation on the aerodynamics of a simplified high-speed train under crosswinds”. In: *Theoretical and Applied Mechanics Letters* 5.5 (2015), pp. 181–186.

[81] K. He, X. Su, G. Gao, and S. Krajnović. “Evaluation of LES, IDDES and URANS for prediction of flow around a streamlined high-speed train”. In: *Journal of Wind Engineering and Industrial Aerodynamics* 223 (2022), p. 104952.

[82] S. Maleki, D. Burton, and M. C. Thompson. “Assessment of various turbulence models (ELES, SAS, URANS and RANS) for predicting the aerodynamics of freight train container wagons”. In: *Journal of Wind Engineering and Industrial Aerodynamics* 170 (2017), pp. 68–80.

[83] Y. Liu, W. Yang, E. Deng, Y. Wang, X. He, Y. Huang, and Y. Zou. “Aerodynamic characteristics of the train–SENB (semi-enclosed noise barrier) system: A high-speed model experiment and LES study”. In: *Journal of Wind Engineering and Industrial Aerodynamics* 232 (2023), p. 105251.

[84] W. Yang, H. Yue, E. Deng, X. He, Y. Zou, and Y. Wang. “Comparison of aerodynamic performance of high-speed train driving on tunnel-bridge section under fluctuating winds based on three turbulence models”. In: *Journal of Wind Engineering and Industrial Aerodynamics* 228 (2022), p. 105081.

[85] A. Yamamoto. “Aerodynamics of a train and tunnel”. In: *In Proceedings of the International Conference on Vehicle Mechanics*. 1968.

[86] M. Schultz. “Pressure transients in short tunnels”. In: *Aerodynamics and Ventilation of Vehicle Tunnels* (1991).

[87] K. Kage, H. Miyake, and S. Kawagoe. “Numerical Study of Compression Waves Produced by High-Speed Trains Entering a Tunnel: Effects of Shape of Hood”. In: *JSME International Journal Series B Fluids and Thermal Engineering* 38.2 (1995), pp. 191–198.

[88] A. E. Vardy. “On the use of the method of characteristics for the solution of unsteady flows in networks”. In: *Proceedings of the 2nd International Conference on Pressure Surges, BHRA Fluid Engineering, London*. Vol. 2. 1. 1976, pp. 15–30.

[89] A. Vardy and J. Fox. “Compressible and leaky trains in tunnels”. In: *Proceedings of the Institution of Mechanical Engineers, Part D: Transport Engineering* 201.3 (1987), pp. 209–215.

[90] M. William-Louis, C. Tournier, and C. Crnojevic. “Theoretical evaluation of the friction coefficient in the zone between a train and a tunnel: application to the propagation of pressure waves”. In: *Proceedings of the ITTG* 2 (1993), pp. 1025–1036.

[91] M. Schultz. “The influence of unsteady friction on the propagation of pressure waves in tunnels”. In: *Proc. of 6th Int. Symp. on Aerodynamics and Ventilation of Vehicle Tunnels*. Vol. 123. 1988.

[92] M. William-Louis and C. Tournier. “Non-homentropic flow generated by trains in tunnels with side branches”. In: *International Journal of Numerical Methods for Heat & Fluid Flow* (1998).

[93] Y. Mei. “A generalized numerical simulation method for pressure waves generated by high-speed trains passing through tunnels”. In: *Advances in Structural Engineering* 16.8 (2013), pp. 1427–1436.

[94] Y.-G. Mei, Y.-X. Jia, and Y. Liu. “Numerical method of pressure waves produced by a high-speed train through a tunnel with perforated wall”. In: *Acta Aerodynamica Sinica* 29.6 (2011), pp. 789–794.

[95] Y. Jia. "Study on numerical simulation of pressure wave of perforated wall in high-speed railway tunnel". In: *Master's Degree Dissertation of Lanzhou Jiaotong University* (2009).

[96] A. Vardy. *ThermoTun–Overview*. 2012.

[97] A. E. Vardy. "Aerodynamic drag on trains in tunnels part 2: prediction and validation". In: *Proceedings of the Institution of Mechanical Engineers, Part F: Journal of Rail and Rapid Transit* 210.1 (1996), pp. 39–49.

[98] R. Gawthorpe, C. Pope, and R. Green. *Analysis of train drag in various configurations of long tunnel*. Tech. rep. 1979.

[99] C. Somaschini, T. Argentini, E. Brambilla, D. Rocchi, P. Schito, and G. Tomasini. "Full-scale experimental investigation of the interaction between trains and tunnels". In: *Applied Sciences* 10.20 (2020), p. 7189.

[100] F. Liu and S. Yao. "Analysis on aerodynamic pressure of tunnel wall of high-speed railways by full-scale train test". In: *Journal of Zhejiang University (Engineering Science)* 50.10 (2016), pp. 2018–2024.

[101] A. Martinez, E. Vega, J. Gaite, and J. Meseguer. "Pressure measurements on real high-speed trains travelling through tunnels". In: *Proceedings of BBAA VI International Colloquium on Bluff Bodies Aerodynamics & Applications, Milano, Italy*. Citeseer. 2008, pp. 20–24.

[102] A. Sasoh, K. Matsuoka, K. Nakashio, E. Timofeev, K. Takayama, P. Voinovich, T. Saito, S. Hirano, S. Ono, and Y. Makino. "Attenuation of weak shock waves along pseudo-perforated walls". In: *Shock Waves* 8.3 (1998), pp. 149–159.

[103] T. Aoki, J. Yamamoto, and K. Nagatani. "Characteristics of a compression wave propagating over porous plate wall in a high-speed railway tunnel". In: *Journal of Thermal Science* 17.3 (2008), pp. 218–223.

[104] J. Zonglin, K. Matsuoka, A. Sasoh, and K. Takayama. "Numerical and experimental investigation of wave dynamic processes in high-speed train/tunnels". In: *Acta Mechanica Sinica* 18.3 (2002), pp. 209–226.

[105] P. Ricco, A. Baron, and P. Molteni. "Nature of pressure waves induced by a high-speed train travelling through a tunnel". In: *Journal of Wind Engineering and Industrial Aerodynamics* 95.8 (2007), pp. 781–808.

[106] M. C. Swarden. "Vehicle-tunnel entry at subsonic speeds". In: (1973).

[107] D. Zhou, H.-q. Tian, J. Zhang, and M.-z. Yang. "Pressure transients induced by a high-speed train passing through a station". In: *Journal of Wind Engineering and Industrial Aerodynamics* 135 (2014), pp. 1–9.

[108] F. Liu, S. Yao, J. Zhang, and Y.-b. Zhang. "Effect of increased linings on micro-pressure waves in a high-speed railway tunnel". In: *Tunnelling and Underground Space Technology* 52 (2016), pp. 62–70.

[109] M. Yang, J. Du, Z. Li, S. Huang, and D. Zhou. "Moving model test of high-speed train aerodynamic drag based on stagnation pressure measurements". In: *Plos one* 12.1 (2017), e0169471.

[110] D. Soper. *The aerodynamics of a container freight train*. Springer, 2016.

[111] L. Zhang, M.-z. Yang, X.-f. Liang, and J. Zhang. "Oblique tunnel portal effects on train and tunnel aerodynamics based on moving model tests". In: *Journal of Wind Engineering and Industrial Aerodynamics* 167 (2017), pp. 128–139.

[112] D. Heine, K. Ehrenfried, G. Heine, and S. Huntgeburth. "Experimental and theoretical study of the pressure wave generation in railway tunnels with vented tunnel portals". In: *Journal of Wind Engineering and Industrial Aerodynamics* 176 (2018), pp. 290–300.

[113] L. Zhang, H. Liu, N. Stoll, and K. Thurow. "Influence of tunnel aerodynamic effects by slope of equal-transect ring oblique tunnel portal". In: *Journal of Wind Engineering and Industrial Aerodynamics* 169 (2017), pp. 106–116.

[114] S. Meng, D. Zhou, and Z. Wang. "Moving model analysis on the transient pressure and slipstream caused by a metro train passing through a tunnel". In: *Plos one* 14.9 (2019), e0222151.

[115] P. Iliadis, H. Hemida, D. Soper, and C. Baker. "Numerical simulations of the separated flow around a freight train passing through a tunnel using the sliding mesh technique". In: *Proceedings of the Institution of Mechanical Engineers, Part F: Journal of Rail and Rapid Transit* 234.6 (2020), pp. 638–654.

[116] J. Östh and S. Krajnović. "A study of the aerodynamics of a generic container freight wagon using Large-Eddy Simulation". In: *Journal of Fluids and Structures* 44 (2014), pp. 31–51.

[117] Z. J. Taylor, E. Palombi, R. Gurka, and G. A. Kopp. "Features of the turbulent flow around symmetric elongated bluff bodies". In: *Journal of Fluids and Structures* 27.2 (2011), pp. 250–265.

[118] C. Li, D. Burton, M. Kost, J. Sheridan, and M. C. Thompson. "Flow topology of a container train wagon subjected to varying local loading configurations". In: *Journal of Wind Engineering and Industrial Aerodynamics* 169 (2017), pp. 12–29.

[119] C. Li, M. Kost, D. Burton, J. Sheridan, and M. C. Thompson. "Wind tunnel investigation of a double stacked wagon in free-stream". In: *Fluids Engineering Division Summer Meeting*. Vol. 57212. American Society of Mechanical Engineers. 2015, V001T16A002.

[120] S. Maleki, D. Burton, and M. C. Thompson. "Flow structure between freight train containers with implications for aerodynamic drag". In: *Journal of Wind Engineering and Industrial Aerodynamics* 188 (2019), pp. 194–206.

[121] A. Kocoń and A. Flaga. "Critical velocity measurements of freight railway vehicles roll-over in wind tunnel tests as the method to assess their safety at strong cross winds". In: *Journal of Wind Engineering and Industrial Aerodynamics* 211 (2021), p. 104559.

[122] S. Giappino, S. Melzi, and G. Tomasini. "High-speed freight trains for intermodal transportation: Wind tunnel study on the aerodynamic coefficients of container wagons". In: *Journal of Wind Engineering and Industrial Aerodynamics* 175 (2018), pp. 111–119.

[123] S. Watkins, J. Saunders, and H. Kumar. "Aerodynamic drag reduction of goods trains". In: *Journal of Wind Engineering and Industrial Aerodynamics* 40.2 (1992), pp. 147–178.

[124] H. C. Lim, T. Thomas, and I. P. Castro. "Flow around a cube in a turbulent boundary layer: LES and experiment". In: *Journal of Wind Engineering and Industrial Aerodynamics* 97.2 (2009), pp. 96–109.

[125] Y. Gao and W. K. Chow. "Numerical studies on air flow around a cube". In: *Journal of Wind Engineering and Industrial Aerodynamics* 93.2 (2005), pp. 115–135.

[126] Y. J. Chen and C. P. Shao. "Suppression of vortex shedding from a rectangular cylinder at low Reynolds numbers". In: *Journal of Fluids and Structures* 43 (2013), pp. 15–27.

[127] J. Paik, F. Sotiropoulos, and F. Porté-Agel. "Detached eddy simulation of flow around two wall-mounted cubes in tandem". In: *International Journal of Heat and Fluid Flow* 30.2 (2009), pp. 286–305.

[128] L. Bruno, M. V. Salvetti, and F. Ricciardelli. "Benchmark on the aerodynamics of a rectangular 5: 1 cylinder: an overview after the first four years of activity". In: *Journal of Wind Engineering and Industrial Aerodynamics* 126 (2014), pp. 87–106.

[129] B. Rocchio, A. Mariotti, and M. Salvetti. "Flow around a 5: 1 rectangular cylinder: Effects of upstream-edge rounding". In: *Journal of Wind Engineering and Industrial Aerodynamics* 204 (2020), p. 104237.

[130] P. Richards and S. Norris. "LES modelling of unsteady flow around the Silsoe cube". In: *Journal of Wind Engineering and Industrial Aerodynamics* 144 (2015), pp. 70–78.

[131] Z. Liu, Z. Yu, X. Chen, R. Cao, and F. Zhu. "An investigation on external airflow around low-rise building with various roof types: PIV measurements and LES simulations". In: *Building and Environment* 169 (2020), p. 106583.

[132] J. Keogh, T. Barber, S. Diasinos, and G. Doig. "The aerodynamic effects on a cornering Ahmed body". In: *Journal of Wind Engineering and Industrial Aerodynamics* 154 (2016), pp. 34–46.

[133] B. Havel, H. Hangan, and R. Martinuzzi. "Buffeting for 2D and 3D sharp-edged bluff bodies". In: *Journal of Wind Engineering and Industrial Aerodynamics* 89.14-15 (2001), pp. 1369–1381.

[134] H. Hangan and B. Vickery. "Buffeting of two-dimensional bluff bodies". In: *Journal of Wind Engineering and Industrial Aerodynamics* 82.1-3 (1999), pp. 173–187.

[135] M. Zdravkovich. "Review of flow interference between two circular cylinders in various arrangements". In: (1977).

[136] R. S. Iyer, D. H. Kim, and H. D. Kim. "Propagation characteristics of compression wave in a high-speed railway tunnel". In: *Physics of Fluids* 33.8 (2021), p. 086104.

[137] C. H. Zhou and Y. G. Mei. "The one-dimensional unsteady flow prediction method for pressure waves in high-speed subway and its applications". In: *Applied Mechanics and Materials*. Vol. 94. Trans Tech Publ. 2011, pp. 1967–1970.

[138] R. Rennie and J. Law. *A dictionary of physics*. Oxford University Press, 2019.

[139] A. Tony and E. Marcel. *A Dictionary of Mechanical Engineering*. Oxford University Press, 2013.

[140] R. S. Benson and N. D. Whitehouse. *Internal combustion engines: a detailed introduction to the thermodynamics of spark and compression ignition engines, their design and development*. Vol. 1. Elsevier, 2013.

[141] W. Woods and R. Gawthorpe. "The train and tunnel-A large scale unsteady flow machine". In: *2nd International JSME Symposium on Fluid Machinery and Fluidic*. 1972, pp. 249–258.

[142] W. Woods and C. Pope. *On the range of validity of simplified one dimensional theories for calculating unsteady flows in railway tunnels*. Tech. rep. 1979.

[143] A. Hellsten, S. Laine, A. Hellsten, and S. Laine. "Extension of the k-omega-SST turbulence model for flows over rough surfaces". In: *22nd atmospheric flight mechanics conference*. 1997, p. 3577.

[144] D. C. Wilcox. "Turbulence modeling for CFD. La Canada, CA: DCW Industries". In: *Inc, November* 34 (2006).

[145] C. Liu, W. Bu, D. Xu, Y. Lei, and X. Li. "Application of hybrid RANS/LES turbulence models in rotor-stator fluid machinery: a comparative study". In: *International Journal of Numerical Methods for Heat & Fluid Flow* 27.12 (2017), pp. 2717–2743.

[146] P. Ji, T.-t. Wang, and F. Wu. "Calculation grid and turbulence model for numerical simulating pressure fluctuations in high-speed train tunnel". In: *Journal of Central South University* 26.10 (2019), pp. 2870–2877.

[147] Y. Xia, T. Liu, H. Gu, Z. Guo, Z. Chen, W. Li, and L. Li. "Aerodynamic effects of the gap spacing between adjacent vehicles on wind tunnel train models". In: *Engineering Applications of Computational Fluid Mechanics* 14.1 (2020), pp. 835–852.

[148] A. Premoli, D. Rocchi, P. Schito, and G. Tomasini. "Comparison between steady and moving railway vehicles subjected to crosswind by CFD analysis". In: *Journal of Wind Engineering and Industrial Aerodynamics* 156 (2016), pp. 29–40.

[149] G. Kalitzin, G. Medic, and G. Xia. "Improvements to SST turbulence model for free shear layers, turbulent separation and stagnation point anomaly". In: *54th AIAA Aerospace Sciences Meeting*. 2016, p. 1601.

[150] A. E. Benchikh Le Hocine, R. J. Lacey, and S. Poncet. "Turbulent flow over a D-section bluff body: a numerical benchmark". In: *Environmental Fluid Mechanics* 19.2 (2019), pp. 435–456.

[151] CEN. "EN 14067-4 Railway applications-aerodynamics. Part 4: requirements and test procedures for aerodynamics on open track". In: *Technical report* (2013), pp. 14067–14074.

[152] P. Ding, X. Zhou, H. Wu, and Q. Chen. "An efficient numerical approach for simulating airflows around an isolated building". In: *Building and Environment* 210 (2022), p. 108709.

[153] Z. Wu, J. Li, and Q. Wen. "Heat release and transfer of premixed propane/air flames in high g-load centrifugal force fields". In: *Fuel* 327 (2022), p. 125196.

[154] F. R. Menter. "Two-equation eddy-viscosity turbulence models for engineering applications". In: *AIAA journal* 32.8 (1994), pp. 1598–1605.

[155] C. Liu, D. Guo, S. Yao, and G. Yang. "The influence of different cross-section shapes of train body on aerodynamic performance". In: *Proceedings of the 1st International Workshop on High-Speed and Intercity Railways: Volume 2*. Springer. 2012, pp. 19–30.

[156] Y.-y. Zhao, Z.-g. Yang, Q.-l. Li, and C. Xia. "Analysis of the near-field and far-field sound pressure generated by high-speed trains pantograph system". In: *Applied Acoustics* 169 (2020), p. 107506.

[157] A. E. Perry and M. S. Chong. "A description of eddying motions and flow patterns using critical-point concepts". In: *Annual review of fluid mechanics* 19.1 (1987), pp. 125–155.

[158] J. Jeong and F. Hussain. "On the identification of a vortex". In: *Journal of fluid mechanics* 285 (1995), pp. 69–94.

[159] I. M. Sobol. "Global sensitivity indices for nonlinear mathematical models and their Monte Carlo estimates". In: *Mathematics and computers in simulation* 55.1-3 (2001), pp. 271–280.

[160] G. Lunghi, E. Pasqualetto, B. Rocchio, A. Mariotti, and M. V. Salvetti. "Impact of the lateral mean recirculation characteristics on the near-wake and bulk quantities of the BARC configuration". In: *Wind and Structures* 34.1 (2022), pp. 115–125.

[161] P. Vegendla, T. Sofu, R. Saha, M. M. Kumar, and L.-K. Hwang. *Investigation of aerodynamic influence on truck platooning*. Tech. rep. SAE Technical Paper, 2015.

Appendix A

Authors publications

During my PhD, I authored three journal papers and contributed to a potential upcoming publication. The three published papers are presented in the appendix for reference. The first paper focuses on numerically investigating the aerodynamic drag of a metro train. It was initially written and submitted during my Master's study. It underwent the review process during my PhD and was accepted in 2020. Through this process I developed skills in CFD modelling, which have been further developed throughout my PhD and applied in the development of the work presented in this study.

The second paper involved the numerical simulation of a maglev train entering a tunnel using the IDDES method, with a specific focus on studying the influence of nose length on slipstream characteristics. This research provided valuable insights into numerical modeling, shedding light on how the flow field changes and develops with varying nose lengths.

The third paper revolved around the redevelopment of a code to explore the impact of a separation bubble on the pressure wave generated by a freight train entering a tunnel. This work is closely related to the content in Chapter 5 of this thesis.

Additionally, the fourth paper deals with the redevelopment of a code to assess the influence of different loading configurations on tunnel pressure waves. The results from this paper are closely related to Chapter 6 of this thesis and are currently in the preparation stage for a full journal publication.

In addition to these publications, I was actively involved in analyzing open-field train aerodynamics studies during my PhD. This involvement led to co-authorship on two journal papers. These experiences significantly contributed to the development of my skills in conducting parameterization studies on freight train aerodynamics throughout my PhD.

1. *Zhen Liu*, Guang Chen, Dan Zhou, et. al. (2020). Numerical Investigation of the pressure and friction resistance of a high-speed subway train based on an overset mesh method. Part F: Journal of Rail and Rapid Transit.

2. *Zhen Liu*, Dan Zhou, David Soper, et. al. (2022). Numerical investigation of the slipstream characteristics of a maglev train in a tunnel. Proceedings of the Institution of Mechanical Engineers. Part F: Journal of Rail and Rapid Transit.

3. *Zhen Liu*, David Soper, Hassan Hemida, et. al. (2023). A study of the influence of separation bubbles around a generic freight train on pressure waves inside tunnels using 1d and 3d numerical methods. Journal of Wind Engineering and Industrial Aerodynamics

4. *Zhen Liu*, David Soper, Hassan Hemida, et. al. A numerical investigation on the influence of loading configurations on freight train/tunnel aerodynamics. Journal of Wind Engineering and Industrial Aerodynamics (In preparation)

5. Zijian Guo, Tanghong Liu, *Zhen Liu*, et. al. (2021) An IDDES study on a train suffering a crosswind with angles of attack on a bridge. Journal of Wind Engineering and Industrial Aerodynamics.

6. Zijian Guo, Tanghong Liu, Yutao Xia, *Zhen Liu* (2022) Aerodynamic influence of the clearance under the cowcatcher of a high-speed train. Journal of Wind Engineering and Industrial Aerodynamics.

Check for updates

Original Article

Institution of MECHANICAL ENGINEERS
Journal of RAIL AND RAPID TRANSIT

Proc IMechE Part F:
J Rail and Rapid Transit
2021, Vol. 235(5) 598–615
© IMechE 2020
Article reuse guidelines:
sagepub.com/journals-permissions
DOI: 10.1177/0954409720951290
journals.sagepub.com/home/pif
SAGE

Numerical investigation of the pressure and friction resistance of a high-speed subway train based on an overset mesh method

Zhen Liu[1,2], Guang Chen[1], Dan Zhou[1], Zhe Wang[1,3] and Zijian Guo[1]

Abstract

The aerodynamic resistance induced by a high-speed metro train entering and operating in a tunnel with a speed of 120 km/h is simulated using a three-dimensional, compressible turbulence model. An overset mesh method is adopted to solve the moving boundary problem, and the flow field around the train is simulated with a k-omega SST turbulence model to obtain accurate stress values at the walls. The selected model is verified with experimental and numerical data from the literature. Then, numerical simulations are performed to analyse the formation mechanisms of the pressure and friction drags. The aerodynamic drag basically stabilizes after the expansion wave passes the train head. The results reveal that the variations in friction resistance are related to the direction of the Mach wave, and this trend differs from that observed for pressure resistance. Mach wave influences the velocity where it passes, and further influences the friction drag. Result shows that friction drag of the train increases when encounter with compression wave propagated from the front or expansion wave propagated from the back, and decreases otherwise. The effects of the blockage ratio on the maximum and average pressure and friction resistance values of each train section are evaluated based on fitting functions. The predicted aerodynamic drag varies with the blockage ratio and for each train section, and the results are summarized and compared with predictions and experimental data from the literature. The variations in tunnel resistance and the overall trend are in good agreement with the previous results. Therefore, the findings presented in this study may provide a reference for the design of high-speed subway tunnels.

Keywords

Blockage ratio, high-speed subway, friction drag, computational fluid dynamics

Date received: 2 March 2019; accepted: 12 July 2020

Introduction

Subway transportation is becoming a crucial part of city transportation networks because subways are fast, can transport many people, emit little pollution, and are highly efficient. With rapid increases in the population density and the continuous expansion of urban areas, the need to improve the transport efficiency has become an urgent issue. The current operating speed of 60∼100 km/h cannot meet the capacity demands of some medium and large cities.[1] However, increasing the operating speed to increase the volume of passenger transported will significantly increase the aerodynamic drag, which is approximately proportional to the train speed squared.[2] In addition, the cross-sectional area of most subway tunnels is generally small, and the blockage ratio (the ratio of the cross-sectional area of the train to the cross-sectional area of the tunnel) can reach 0.5.[3] When a train enters a narrow subway tunnel at high speed, the interaction between the train and air will be intensified. The strengthening of compression waves and expansion waves will increase the stress upon vehicle and transient load on ear, leading to

[1]Key Laboratory of Traffic Safety on Track of Ministry of Education, School of Traffic & Transportation Engineering, Central South University, Changsha, PR China
[2]School of Civil Engineering, University of Birmingham, Birmingham, UK
[3]Institute of Industrial Design, Zhaoqing University, Zhaoqing, PR China

Corresponding author:
Dan Zhou, School of Traffic & Transportation Engineering, Central South University, Changsha 410075, PR China.
Email: zd_lzj@126.com

Check for updates

Original Article

Institution of MECHANICAL ENGINEERS
Journal of RAIL AND RAPID TRANSIT

Proc IMechE Part F:
J Rail and Rapid Transit
2023, Vol. 237(2) 179–192
© IMechE 2022
Article reuse guidelines:
sagepub.com/journals-permissions
DOI: 10.1177/09544097221100658
journals.sagepub.com/home/pif
SAGE

Numerical investigation of the slipstream characteristics of a maglev train in a tunnel

Zhen Liu[1], Dan Zhou[2], David Soper[1], Guang Chen[2], Hassan Hemida[1], Zijian Guo[1] and Xianli Li[2]

Abstract

High-speed maglev trains operate at higher speeds than conventional high-speed trains. This has implications on intensified aerodynamic issues, such as the transition between open air running and entering into a tunnel. In this paper, numerical simulation of a maglev train entering a tunnel is carried out using IDDES methods (based on SST k-omega model) to analyze the changing slipstream. The peaks and fluctuations of the slipstream are analyzed, together with the transient wake characteristics and TKE (turbulent kinetic energy) distributions. The influence of train nose length on the slipstream and its associated characteristics inside tunnels is also investigated in this paper. It was found that as the maglev train enters the tunnel, the wake slipstream at measuring points close to tunnel entrance increases significantly then decreases slightly with the increase of distance to tunnel entrance. Overall, the fluctuation and magnitude of slipstream inside tunnel is larger than that on open line, more specifically, the maximum TKE generated inside tunnel is. 7.62% larger than that on the open line at contour X = 3 H behind the train tail. Besides it takes longer time for the slipstream inside tunnel to return to the initial condition. These phenomena could be explained by that the scale of vortex structure formed behind the train tail is larger, the developing distance of the wake vortices in the streamwise direction is longer and the TKE generated is more significant inside tunnel. It was also found that increasing the nose length could effectively decrease the spatial scale and TKE of the wake vortices, which resulted on reducing the peak and pulsation of wake slipstream. Comparing to that of 5.4 m, the peak of the wake slipstream of the maglev trains with the 7.4 m and 9.4 m nose lengths at Y = 0.235 m(0.385) is reduced by approximately 23.7%(58%) and 35.9%(82.2%) on open field, and by about 3.6%(4.7%) and 14%(18.5%) inside tunnel. Besides, the maximum TKE at contour X = 2H/3H/5H behind the train tail decreases about 14.4%/10.7%/11.3% and 51%/31.5%/18% as the nose length increase to 7.4 m and 9.4 m respectively.

Introduction

Compared with conventional high-speed trains, the maglev train completely eliminates the adverse effects caused by wheel-rail contact, which greatly raises the opportunity for higher operating speeds. In recent years, research on maglev systems have been carried out mainly in China, Japan, Germany, USA and other countries, with a view to trial operation lines under construction or recently opened. Due to the environmental limitations and the requirement to achieve the desired operation speed, it typically required that up to 50% of a journey to be within a tunnel.[1] For example, the central Shinkansen project in Japan, started in 2013, includes a tunnel length of 24.6 km, and the total proportion of the line in a tunnel totals 86%. However, it is known that train aerodynamic problems are intensified in tunnel, due to the relative confinement, including the increasing slipstream magnitude that could cause damage to tunnel infrastructures and danger to trackside workers.

Train slipstream are formed by the movement of a train through the air as the surrounding flow moves with the train due to viscosity.[2,3] According to previous research, the slipstream of a high speed train (HST) operating on open line has a typical profile including a nose region (upstream and nose region), boundary-layer region and wake region (near-wake and far-wake region).[4–6] The near-wake region is dominated by an unsteady gust peak created by a pair of counter-rotating vortices, which brings the major adverse effect and receives special attention from researchers. A great number of experiments and numerical simulations has been done to investigate the characteristics of the vortex street (frequency, length scale, motion, etc.) and slipstream profile of HST, passenger train and freight trains operating on open field.[3,7–12] Results indicated that the characteristic large-scale vortex structure varies from train-to-train due to a sensitive to the shape of tail train, as well as being influenced by the track as it extends.[3,5,13] Besides, the instantaneous flow structure and aerodynamic performance of high-speed trains under cross-wind are also been widely investigated.[14–16] The influence of geometry of the train and objects around the

[1]School of Civil Engineering, University of Birmingham, Birmingham, UK
[2]Key Laboratory of Traffic Safety on Track of Ministry of Education, School of Traffic & Transportation Engineering, Central South University, Changsha, PR China

Corresponding author:
Dan Zhou, Key Laboratory of Traffic Safety on Track of Ministry of Education, School of Traffic & Transportation Engineering, Central South University, Changsha 410075, PR China.
Email: zd_lzj@126.com

Journal of Wind Engineering & Industrial Aerodynamics 240 (2023) 105461

Contents lists available at ScienceDirect

Journal of Wind Engineering & Industrial Aerodynamics

journal homepage: www.elsevier.com/locate/jweia

A study of the influence of separation bubbles around a generic freight train on pressure waves inside tunnels using 1D and 3D numerical methods

Zhen Liu *, David Soper, Hassan Hemida, Boyang Chen

School of Engineering, University of Birmingham, Birmingham, B15 2TT, UK

ARTICLE INFO

Keywords:
Freight train
Computational Fluid Dynamics
One-dimensional numerical method
Train/tunnel aerodynamics
Large Eddy Simulation

ABSTRACT

Due to the increased effective blockage area caused by the bluff nature of a freight train, traditional one-dimensional (1D) numerical modelling techniques struggle to predict the initial pressure wave formation for these train types. This paper presents, for the first time, a detailed study of this phenomenon for typical freight train locomotives, and a redeveloped 1D code capable of solving for bluff freight vehicles. Firstly, a 1D numerical model for tunnel pressure development is written and validated with previous research. Then, 3D simulations using computational fluid dynamics (CFD) have been carried out to model a freight train entering into a tunnel, with a view to characterising the key regions of flow separation. According to this, the 1D code is redeveloped to simulate the changing effective blockage area of the freight train, caused by flow separation at the blunted train head. A separation bubble model is built to calculate the effective blockage area. Results show that the error between the results obtained from the modified 1D model and the experiment is significantly reduced in relation to traditional 1D numerical models. To provide further functionality through the ability to apply the model to various types of freight train locomotives, a parameterisation study is conducted to obtain the relationship between the vehicle shape (bluntness) and new input parameters for the separation bubble model. Finally, the separation bubble model and parameterisation equation is tested to validate its applicability, with results indicating good agreement for a range of train designs.

1. Introduction

The UK government aims to double the volume of rail freight cargo on the UK rail network by 2030 (DfT, 2007). Opportunities highlighted to achieve this aim include the introduction of dedicated high-speed freight. However, increasing train speeds can cause a series of aerodynamic issues, including slipstream effects for platform passengers and trackside workers, as well as tunnel pressure magnitudes, which act as barriers to the implementation of higher freight train speeds. For example, the amplitude of pressure change increases approximately proportional to the square of train speed (Li et al., 2011). Furthermore, aerodynamic problems are more obvious when the train is running in a confined space, such as a tunnel (Liu et al., 2021). Though numerous studies have been conducted to consider the aerodynamics of trains in tunnels, the majority have purely focused on passenger trains, due to the speed at which these vehicles travel. Although traditionally travelling at much lower speeds, there are still aerodynamic issues that need to be considered for freight trains passing through a tunnel, due to the 'bluff' nature of these vehicles.

As a train enters into a tunnel, the nose of the train pushes the air ahead of it, generating a compression wave that propagates to the tunnel exit with the speed of sound (Howe et al., 2003; Liu et al., 2010). This compression wave leads to a sudden pressure rise where it passes. This can lead to safety concerns in the tunnel environment, especially in relation to aural discomfort for passengers/workers in the locality. With the improvement of computational ability, massive computational fluid dynamics (CFD) simulations can be undertaken using commercial software to achieve a better knowledge and characterisation of the flow field when trains pass through tunnels (Liu et al., 2021; Howe et al., 2003; Ogawa and Fujii, 1997; Cross et al., 2015). The simulation of a moving train is however very computationally expensive and time-consuming. Munoz-Paniagua et al. (2014) conducted optimisation of the train nose shape to minimise the maximum pressure gradient and drag during tunnel entry. This was achieved using a surrogate-based optimiser, which employed a surrogate model to substitute CFD solver calls, thereby reducing computational costs. Since the length of the tunnel is much larger than the diameter of the tunnel section, the pressure fluctuation over a certain cross-section of the tunnel can be neglected compared to its variation with time (Woods and Pope, 1981). Subsequently many researchers have developed one-dimensional (1D) numerical models to calculate a quick, less computationally intensive

* Corresponding author.
E-mail address: 15581666545@163.com (Z. Liu).

https://doi.org/10.1016/j.jweia.2023.105461
Received 8 December 2022; Received in revised form 4 April 2023; Accepted 20 May 2023
Available online 12 June 2023
0167-6105/Crown Copyright © 2023 Published by Elsevier Ltd. This is an open access article under the CC BY license (http://creativecommons.org/licenses/by/4.0/).

In addition to the aforementioned journal papers, I contributed to the publication of four conference papers during my PhD.

1. *Zhen Liu*, David Soper, Hassan Hemida. (2022) Effect of separation bubbles around the head of a freight train on pressure waves inside tunnels using 1d and 3d numerical methods. The fifth International Conference on Railway Technology, Montepellier, France.

2. *Zhen Liu*, David Soper. (2023) Numerical Modelling of Freight Trains in Tunnels: A Redeveloped 1D Model and Separation Bubble Parameterisation. Fifth international conference in numerical and experimental aerodynamics of road vehicles and trains, Poitiers, France.

3. *Zhen Liu*, Bruno Fraga. (2024) Optimizing Ventilation Efficiency: Exploring the Impact of Opening Posi-tions. Indoor Air 2024, Hawaii, USA.

4. *Zhen Liu*, David Soper. (2024) Numerical Modelling of Partially Loaded Freight train Entering a Tunnel. The Sixth International Conference on Railway Technology: Research, Development and Maintenance, Prague, Czech Republic.